

**THE STRUCTURE AND PROPERTIES OF MILL SCALE IN
RELATION TO EASY REMOVAL**

WENGAI YANG

FEBRUARY 2001

Submitted for the degree of Doctor of Philosophy

Department of Engineering Materials

University of Sheffield



IMAGING SERVICES NORTH

Boston Spa, Wetherby
West Yorkshire, LS23 7BQ
www.bl.uk

BEST COPY AVAILABLE.

VARIABLE PRINT QUALITY

ABSTRACT

Oxide scale must be removed before cold drawing wire, otherwise it will cause bad surface quality, inferior die life and many wire ruptures. The nature of oxide scales and the methods of scale removal are reviewed, with particular emphasis on mechanical descaling. This is the major concern of the research, therefore a cantilever bending test has been developed to assess the ease of removal of the scale on commercial steel rod surface in the laboratory. A scanner method and a Finite Element model have been developed to evaluate the critical strain for scale cracking and removal after cantilever bending. Scanning electron microscopy (SEM), together with electron backscattered diffraction (EBSD), energy diffraction spectrum (EDS) and X-ray element mapping analysis, was used to characterize the scale before and/or after bending test.

The effects of laying temperature, cooling conditions, ageing time, relative humidity and temperature, and coil positions on scale cracking and removal behaviour were studied. It was found that laying temperature has a larger effect on descalability than cooling conditions. The effect of relative humidity and temperature on descalability depended on a critical holding time. Beyond it, relative humidity and temperature had no further effect on descalability. The higher the environmental temperature, the less the critical holding time. Ageing time had an effect on descalability, but the effect was relatively small.

Failure in tension started with first cracks formed at the places with high stress concentration. As tensile strain increased, new cracks formed midway between the existing cracks. Crack spacing stayed uniform but decreased until the scale segments spalled off the rod surface. The crack spacing increased with scale thickness and decreased with strain applied. Scale cracking and spallation mechanisms in compression depended on the relative shear strength of the oxide, the buckling stability of the layer and the relative shear strength of the interface. Spallation always required the propagation of a crack at the interface.

The residual sub-layer left on the rod surface of EAF steel after the bending test was identified as magnetite. On the same sample, copper enrichment was found at the scale/metal interface, but within the metal side, and silicon enrichment was found at the scale/metal interface, but within the scale side.

ACKNOWLEDGEMENTS

I would like to acknowledge the financial support received from an ORS award and the Materials Forum.

My sincere thanks go to my supervisors, Prof. C. M. Sellars and Dr. Y. H. Li. for their help and guidance throughout my PhD and during the preparation of this thesis. Thanks are also due to Mr. Henry Marston and Mr. Andy Bell of Corus group and Mr. Graeme Manning of Tinsley Wire Industry Ltd for their kindly advice at the regular three monthly meetings during last three years, for sending me copious quantities of steel rods, and arrangements for plant visits.

I would like to express my gratitude to all members of the Department of Engineering Materials who have helped me over the past three years and to everyone in the D-floor office (past and present) who put some life into the world of metallurgy.

I would like to thank my friends, both in and out of the university, for putting up with me when things got rough and making Sheffield a place to remember, particularly to Ms Hong Zheng, Mrs Xiaoxue An, Dr. Yingxu Yang, Dr. Sujiuan Zhang, Dr. Lihong Zhang, Dr. Zhiran Wang for kindly advice in my daily life and study; to Dr Qiang Zhu, Mr. Wanhua Yu, Dr. Shaowei Zhang, Dr Gongqi Shi, Dr. Yungui Zheng and Dr. Yun Wang for their friendly help when I had difficulty in computer-related work; to Dr. Dongliang Cheng for helping me learn how to use Finite Element code Marc 7.2; to Dr. R. L. Higginson for helping me doing EBSD and to the girls of our department female football team for giving me the opportunity to touch football during the first year of my PhD.

Special thanks go to my parents who have always been there for me, have given me constant love and support and don't mind that I'm still be a student after all these years.

This thesis could not have been written without help from these and many other people who I have neglected to mention, to everyone who has spent time convincing me I could do this, read on...

Nomenclature

b	A constant, ≈ 3
c	Defect size
d	Wire rod diameter
d_0	Rod diameter before shot blasting
D	Bending diameter
D_i	Distance along the neutral plane and from the fixed end of the sample in cantilever bending
E	Young modulus; subscript ox for oxide
E_0	Modulus of the fully compact solid
F	A constant
G_{IC}	Critical energy release rate
h	Scale thickness
H	Sample length
h_c	Critical oxide thickness
K	A constant
k	A constant
K_{IC}	Critical stress intensity factor of the oxide
k_1	A factor related to the fraction of stored energy within the layer that is used for the fracture process
k_2	A factor related to the stored energy in the volume $\zeta^2 h$ used in the fracturing process
l_0/l	Distance between the scribed lines before and after bending, respectively.
L	Crack spacing
p	Porosity
ρ_{Ox}	Average scale density
Q	Activation energy
R_{ten}/R_{com}	Local radius of the tensile/compressive surface of a bent rod sample
R_{coil}	Radius of the coil from which rod was taken

R	Gas constant
R'	A constant
R_d	Initial radius of the zone of decohesion
r	Roughness height
s	Distance between the inner and outer rollers in 4-point bending
t	Time
T	Temperature
u	Distance between the outer rollers in 4-point bending
w_0	Sample weight before shot blasting
w_1	Sample weight after shot blast
W^*	Stored energy per unit volume of the layer
χ	Interfacial roughness index
δ	Deflection of the specimen in 4-point bending
$\delta_{ten}/\delta_{com}$	Relative height of the chord on the tensile/compressive surface of a bent rod sample
γ	Surface fracture energy; subscripts m , ox and interface for metal, oxide and the interface between oxide and scale
γ_0	Energy value for a smooth interface
γ_r	Energy value for the interface with roughness
γ_s	True surface energy
γ_p	Energy associated with plastic deformation around a crack tip
λ	Roughness length
ζ	Length of a single shear crack
σ_{ox}	Stress; subscripts ox for oxide
σ_I	Principle stresses
σ_y	Yield stress
τ_{max}	Maximum shear stress
ϵ	Strain
ϵ_I	Principle strains
ϵ_c	Critical strain
ϵ_I^{init}	Critical strain for initiation of Route I failure

- ε_I^{spall} Critical spallation strain for Route I failure, i.e. critical strain for crack propagation at the interface
- ε_{II}^{init} Critical strain for initiation of Route II failure
- ε_{II}^{spall} Critical spallation strain for Route II failure

CONTENTS

	Page No.
Abstract	I
Acknowledgement	II
Nomenclature	III
1. Introduction	1
1.1. The importance of mechanical descaling	1
1.2. Descaling methods	1
1.3. Objectives of the present research	2
1.4. Outline of the thesis	2
1.5 Terminology	4
2. Literature Review	5
2.1. Introduction	5
2.2. Oxide scale formation	6
2.2.1. Primary scale formation	6
2.2.1.1. 'Classical' three layer scale	6
2.2.1.2. Deviations from 'classical' scaling mechanism	7
2.2.2. Secondary scale	8
2.2.3. Tertiary scale	8
2.3 Failure mechanism of oxide scale	9
2.3.1 Options for stress relief in oxide scale	10
2.3.2 Failure of oxide scale in tension	11
2.3.3 Failure of oxide scale in compression	15
2.3.4 Critical parameters for prediction of oxide scale failure at room temperature	18
2.4 Descaling methods used in industry	21
2.4.1 Chemical pickling	22
2.4.2 Mechanical descaling	22
2.5 Methods for simulating scale cracking in mechanical descaling	24
2.5.1 3-point bending test	24
2.5.2 4-point bending test	24

2.5.3	Uniaxial tensile test	24
2.6	Factors affecting the descaling properties of scale	25
2.6.1	Laying temperature	25
2.6.2	Cooling condition	26
2.6.3	Steel grades	29
2.6.4	Rod surface roughness	31
3.	Experimental Methods	33
3.1.	Introduction	33
3.2.	Experimental materials	33
3.2.1.	Processing route	33
3.2.2.	Chemical compositions of steel grades	35
3.2.3.	State of materials	35
3.3.	Experimental methods	37
3.3.1.	Oxide scale produced in the laboratory	37
3.3.2.	3-point bending test	37
3.3.3.	4-point bending test	38
3.3.4.	Cantilever bending test	38
3.3.5.	Constrained bending test	39
3.3.6.	Observation of scale	39
3.4.	Evaluation of plastic strain variation	39
3.4.1.	Objective	39
3.4.2.	Evaluating strains after cantilever bending test in the laboratory	40
3.4.2.1.	Scriber method	40
3.4.2.2.	Shadowgraph method	42
3.4.2.3.	Scanning method	44
3.4.3.	Evaluating strains by the Finite Element Method	45
3.4.3.1.	Introduction	45
3.4.3.2.	FE model of 4-point bending	46
3.4.3.3.	FE model of cantilever bending	48
3.4.3.4.	FE model of constrained bending	48
3.5.	Characterisation of the effects of process variables	49
3.5.1.	Objective	49
3.5.2.	Laying temperature test	49

3.5.3. Ageing time test	50
3.5.4. Cooling condition test	50
3.5.5. Positions in coil test	50
3.5.6. Relative humidity and temperature test	51
3.6. Scale characterisation techniques	52
3.6.1. Introduction	52
3.6.2. Optical metallography and scanning electron microscopy	52
3.6.2.1. Sample preparation	52
3.6.2.2. Evaluation of scale thickness	54
4. Results	56
4.1. Primary scale growth, microstructure and cracking & removal in 3-point bending test	56
4.2. Scale cracking and removal behaviour of commercial steel rod in 3-point bending test	57
4.3. Scale cracking and removal behaviour of commercial steel/copper rod in 4-point bending test	57
4.4. Scale cracking and removal behaviour of commercial steel rod in cantilever bending test	59
4.5. Scale cracking and removal behaviour of commercial steel rod in constrained bending test	60
4.6. Strains measurement and calculation	60
4.6.1. Scriber/shadowgraph methods for copper sample	60
4.6.2. Shadowgraph/scanner methods for steel rod sample	61
4.6.3. The repeatability and reliability of scanner method	61
4.6.4. Scanner method/FE modelling	61
4.6.5. Strain calculated for copper sample in 4-point bending	62
4.6.6. Strain calculated for steel rod in 4-point bending	62
4.6.7. Strain calculated for copper rod in cantilever bending	62
4.6.8. Strain calculated for steel rod in cantilever bending	62
4.6.9. Strain calculated for steel rod in constrained bending	63
4.7. Effects of processing variable	63
4.7.1. Laying temperature	63
4.7.2. Ageing time	63

4.7.3. Cooling condition	64
4.7.4. Positions in coil	64
4.7.5. Relative humidity and temperature	64
4.8. SEM results of scale cracking and removal behaviour	65
4.8.1. Oxide scale cracking in tension and compression	65
4.8.2. Residual scale at different laying temperatures	65
4.9. EBSD results of scale structure/residual scales	66
4.10. EDS and X-ray element mapping results	66
5. Discussion	68
5.1. The characteristics of primary scale	68
5.2. Evaluation of 3-/4-point bending, cantilever bending and constrained bending tests	68
5.3. Comparison of the methods for evaluating strains	72
5.3.1. Comparison of scribe and shadowgraph methods on copper sample	72
5.3.2. Comparison of shadowgraph and scanner methods on steel rod sample	73
5.3.3. Comparison of scanner method and FE modelling	74
5.3.4. Comparison of strain evaluated by scanner method in cantilever bending and calculated in constrained bending tests	75
5.3.5. Summary	75
5.4. Comparison of the methods used for sample preparation for metallographic examination	76
5.5. Comparison of the methods for scale thickness measurement	76
5.6. Scale failure mechanisms at room temperature	77
5.7. Factors affecting the descaling properties	80
5.7.1. Laying temperature	81
5.7.2. Cooling condition	81
5.7.3. Steel grade	83
5.7.4. Position in the coil	85
5.7.5. Ageing time	86

5.7.6. Relative humidity and temperature	86
6. Conclusions and Future Work	88
6.1. Conclusions	88
6.2. Future work	90
References	91
Appendix: Micro-FE model of steel rod with oxide scale on its surface in cantilever bending	
Tables	
Figures	

CHAPTER ONE

INTRODUCTION

1.1 The reason for descaling

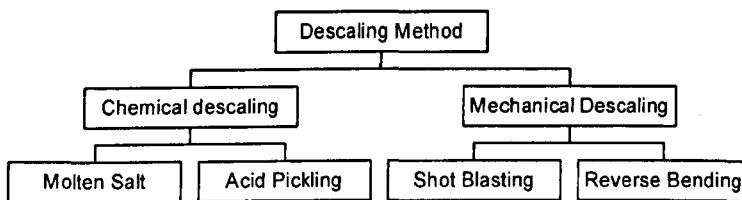
The hot rolling process produces a coiled product capable of being drawn by the wire drawer, but possessing an oxidised surface which has to be removed prior to the drawing operation. Because the formation of mill scale on the rod surface is unavoidable during the hot rolling process, it is necessary to remove the rolling scale before wire drawing.

If not: - hard oxide layer impressed in the wire surface causes bad surface quality

- inferior die life
- many wire ruptures

1.2 Descaling methods

The alternative methods of descaling are summarised [Stalson et al. 1965] in the following:



Pickling has so far been mainly employed to descale wire rods prior to drawing. However, because of the severe pollution control regulations concerning waste acid treatment, mechanical descaling has been put into industrial use and there is a tendency toward the spread of this process since it provides advantages in terms of operating cost. In mechanical descaling, reverse bending has so far been used widely.

1.3 Objectives of the present research

In view of the industrial importance of descaling, work has been carried out in the past to investigate the manufacturing conditions for reducing scale losses and obtaining scale with good descaling properties and structures. However, most researches use total amount of scale removed and the residual scale after mechanical descaling as the evaluating standard. For mechanical descaling in industry, if the bending strain and bending radius for the scale removal for a certain condition are known, it will save much energy and cost. But little work has been done in this field. As will be described in Chapter two, descalability depends on many variables, such as laying temperature, cooling condition, ageing time, steel grade, etc.. Some of the effects of these variables have been investigated experimentally, but others are still ambiguous and need to be further identified. Therefore, in the present research, experimental study and numerical modelling are carried out to optimise the conditions in relation to easy scale removal. Emphasis is put on the effects of laying temperature, cooling conditions, ageing time, relative humidity and temperature, and steel grade on scale removal. The final objective is to develop physically based models to reveal the scale cracking and removal mechanisms at room temperature.

1.4 Outline of the thesis

The whole thesis consists of six chapters.

In Chapter two, the latest researches related with oxide scale formation and failure have been reviewed. These include oxide scale formation mechanisms composed of 'classical' three layer scale theory and deviations from 'classical' scale growth, oxide scale failure mechanisms in tension and compression, industrial descaling methods such as chemical descaling and mechanical descaling, methods for simulating scale cracking in mechanical descaling, and factors influencing descalability such as laying temperature, cooling condition, steel grade and rod surface roughness.

On the basis of the review of published work, selective experiments have been carried out in the present investigations. These include the formation of oxide scale in a laboratory furnace, the development of scale removal technique and strain evaluation

methods in the laboratory, scanning electron microscopy (SEM) observations and analysis of scale structure. Details of the methods used to remove scale and evaluate strain in the laboratory and SEM analysis, together with energy diffraction spectrum (EDS), electron backscattered diffraction (EBSD) and X-ray element mapping analysis of the structure and composition of residual scale and scale have been described in Chapter three. In order to compare with the strain measured in the laboratory, Finite element modelling (FEM) was used to calculate the strain distribution after 4-point bending, cantilever bending and constrained bending. Commercial FE code MARC7.2 was available for strain computations of rod samples after bending tests. In Chapter three, details are given of the establishment of the 2-D and 3-D numerical models (without scale layer).

In Chapter four, the results of experimental observation and mathematical modelling are presented. These include the results of preliminary works, scale cracking and removal behaviour in the cantilever bending test, strains evaluated by different experimental methods and calculated by FE modelling, factors influencing descalability and the results of SEM observation, together with the results of EDS, EBSD and X-ray element mapping analysis.

In Chapter five, on the basis of experimental observations and numerical modelling, discussions are carried out. These include comparison of scale removal techniques used in the laboratory (3-point bending, 4-point bending, cantilever bending and constrained bending tests), comparison of methods for evaluating strains (scriber method, shadowgraph method, Cyclone scanner method and FEM), and effects of process variables on descalability. Then, scale failure mechanisms in tension and compression have been developed according to experimental observation. Finally the factors influencing descalability have been discussed.

From these investigations, several conclusions are drawn, and some important issues for further investigations are pointed out in Chapter six.

1.5 Terminology

Laying temperature: a water trough is installed between the finishing mill and the laying head to cool the wire rod to a predetermined temperature in about 1 sec. The temperature after this cooling is usually called the laying temperature.

Relative humidity: the amount of water vapour in the air compared with the amount of vapour needed to make the air saturated at the air's current temperature.

CHAPTER TWO

LITERATURE REVIEW

2.1 Introduction

The oxidation and scale formation of steel is an unavoidable phenomenon during industrial hot rolling processes which involve reheating of steel in a furnace, multipass hot rolling and air-cooling in the interpass delay times and after rolling. The formation of oxide scale not only results in a significant loss of metal yield, but also worsens the surface quality of the steel product caused by rolled-in scale defects or roughened surface. In addition, the presence of a hard scale layer on the steel could have an adverse effect on roll wear and working life.

In order to produce steel products with high surface quality and to reduce roll wear, hydraulic descaling is normally applied to remove the primary scale formed during the reheating operation before hot rolling. However, secondary scales will continue to form on the descaled steel surface during the interpass delay time in the roughing and intermediate rolling mills. Therefore, in many industrial hot rolling processes such as hot strip rolling, secondary descaling is applied to remove the secondary scales before the steel strip enters the finishing mill. Even though a complete secondary descaling is applied, tertiary scales will be further produced on the hot steel during the interpass delay time of finishing rolling and during air cooling after hot rolling. It is therefore necessary to know the oxide formation and fracture mechanism. In addition, in order to remove the tertiary scale before wire drawing by bending, some fundamental issues such as stress in the oxide scale and stress relief in oxide scale should be understood. Moreover, the methods for detecting scale cracking should be rationalised.

During the past few decades, there is a large body of published information available on oxides and oxidation of metallic materials. Most of these focus on the oxidation behaviour of different alloys under specific conditions. In this review, only publications on the structure and properties of mill scale were considered with particular emphasis on their relation to easy removal. Descaling methods used in industry and in the laboratory, and the factors which influence the scale structure and

properties, such as, laying temperature, cooling process, ageing time, humidity and temperature, steel grade, etc., are reviewed.

2.2 Scale Formation

For this project, tertiary scale is the most important and relevant, but in order to understand scale thoroughly, primary scale and secondary scale are also introduced here.

2.2.1 Primary Scale Formation

Primary scale is formed during the reheating operation before hot rolling, and is removed by hydraulic descaling before hot rolling. Primary scale is also called furnace scale. There are many theories about the formation of oxide scale at high temperature, which are discussed in the following sub-sections.

2.2.1.1 'Classical' three layer scale growth mechanism

It is generally agreed that pure iron will form a classic three layer scale upon heating above 850°C in pure oxygen or air. Phases within the scale are shown in the Fe-O phase diagram Fig. 2.1. This three layer scale described by Sachs and Tuck in 1967, is schematically illustrated in Fig. 2.2, and is best summarised as follows: the innermost layer with the lowest oxygen content is wüstite, FeO, and takes up 95% of the scale thickness; the intermediate layer is magnetite, Fe₃O₄, and accounts for 4% of the scale thickness; and the outer layer is hematite, Fe₂O₃, and occupies about 1% of the scale thickness. Hopkinson [1993] described the visual and microscopical appearances of the three iron oxides as shown in Table 2.1. The proportions of the three oxides change with temperature. Fig. 2.3 shows the relative thickness of the oxide layers at different temperatures [Garber and Sturgeon, 1961]. At constant temperature the thickness of oxide increases with the square root of the exposure time [Kubaschewski and Hopkins, 1962], consistent with a mechanism in which diffusion is the slowest, and therefore the rate-control process. Mathematically this relationship is expressed as:

$$h = K\sqrt{t} \quad (2.1)$$

where h is the scale thickness, t is the time, and K is a constant. Scaling is, of course, fast at higher temperatures, the rate increasing exponentially.

$$K=k\exp(-Q/RT). \quad (2.2)$$

T is temperature, Q is the activation energy, R is the gas constant, and k is a constant

2.2.1.2 Deviations from 'classical' scaling mechanism

Commercial steels in atmospheres formed by the combustion of oil or gas with a reasonable amount of excess air are likely to form a porous, fissured and compact adherent three-layer scale at a rate substantially slower than the ideal parabola for control by vacancy diffusion, owing to fissuring of the scale and stabilization of the fissures by inert gases. Tables 2.2 and 2.3 summarize the main effects in terms of the deviation from the classical oxidation of iron in pure oxygen [Sachs and Tuck, 1967]. The presence of alloy elements further complicates the oxidation of steels. The nature of the scale is strongly dependent on the steel composition. Sulphur at the level normally present in steel has no significant effect, but at high levels rapid scaling may occur due to the presence of a liquid phase [Schell and Kiwit, 1936]. Phosphorus lowers the oxidation resistance of iron slightly [Schell & Kiwit, 1936 and Hessenbruch & Rohn, 1923]. Manganese can substitute for iron in wüstite and magnetite, and the effects attributed directly to manganese have been slight [Schell & Kiwit, 1936 and Hessenbruch & Rohn, 1923]. At temperature above 1170°C silicon killed steels form the liquid phase fayalite ($2\text{FeO} \cdot \text{SiO}_2$), which binds the innermost layer of the scale to the steel surface [Sachs & Tuck, 1967, Marston, 1995 and Asai et al, 1997]. Nickel has been shown to prompt the growth of fibrous scale, which entangles the metal-scale interface [Marston, 1995]. A further investigation on the effect of Ni on descaling showed that the steels with high Ni content are found to have thicker residual scale [Asai et al, 1997]. Copper enrichment of the surface layer can lead to the precipitation of molten copper causing intergranular attack, hot shortness and surface defects. In steels containing up to 1% Molybdenum the oxidation rate may be reduced by the formation of a spinel, Fe_2MoO_4 , at the scale-metal interface [Sachs & Tuck, 1967]. Chromium forms a similar spinel, which maybe a significant part of the scale and inhibits the outward diffusion of iron. Less iron is therefore present in the scale, which consists mostly of magnetite and hematite. Scaling may be depressed by increasing the amount of Cr, Ni and Mo in the steel [Cook and Rasmussen, 1970].

2.2.2 Secondary Scale

The above thick scale formed during re-heating is easily removed by primary descalers before the roughing operations and is therefore of less interest than the secondary and tertiary scales.

Once the steel has been removed from the furnace, it is descaled prior to rolling. However, the steel is still hot, the temperature is around 1100°C, and the surface immediately oxidises again to form secondary scale or residual scale. Secondary scale is formed on the descaled surface during the interpass delay time in the roughing and intermediate rolling mills. Residual scale is secondary scale, which forms on a surface where primary scale could not be fully removed. Because the steel temperature at this stage is lower than when it is in the furnace and the time is shorter, the secondary scale is thinner than the primary scale, but it still can be found that there is a gap between metal and scale (Fisher, 1998), which means that the secondary scale could be easily removed by further descaling. The real difference in secondary scale is found whether silicon is present [Marston, 1995]. The primary scale could not be totally removed by first hydraulic descaling, an inner residual scale is left which is “glued” to the surface of the metal. This residual scale oxidises further to form the secondary scale, and in this case, there is no gap between the secondary scale and metal, which means that the secondary scale cannot be removed totally even by second hydraulic descaling. Luyckx and Lorang [1965] found that the secondary scale was rolled out with the steel. This secondary scale does not crack or spall off; indeed it can be pushed into waves by the slip in the roll gap and the tops of these waves can be pushed into the surface, causing defects.

2.2.3 Tertiary Scale

After the secondary scale is removed by the secondary hydraulic descaling, the steel temperature is still around 900-1000°C, and tertiary scale could still be formed on the steel surface.

Usually, primary scale refers to furnace scale, and secondary scale is considered to be the scale that forms, after first hydraulic descaling, either on the residual scale or on the clean metal surface during the interpass delay time in the roughing and intermediate rolling mills. However, sometimes the interface between secondary scale and tertiary

scale and the definition of tertiary scale are less clear. But, it is generally accepted that the tertiary scale is further formed on the hot steel during the interpass delay time in finishing rolling mills and during air cooling after hot rolling, even when a complete secondary descaling is applied.

2.3 Failure mechanism of oxide scale

There are mainly three sources of stresses in the oxide-metal system. Among them, the first one arises from external mechanical or thermal load, the second one comes from the oxidation process itself and the third one derives from geometrically induced stresses.

Thermal stress

Thermal stresses are due to cooling/heating or thermo-cycling as a result of differences in thermal expansion coefficients of metal and oxide [Armitt et al, 1978]. During cooling, compressive stresses usually develop in the oxide layer since the expansion coefficient of the oxide is usually less than that of the metal substrate. Temperature transients above the notional oxidation temperature will, thus, usually generate in-plane tensile stresses within the oxide layer [Evans, 1995]. Tien and Davidson [1975] calculated this thermal stress.

Growth stress

Growth stresses arise mainly from the volume change during formation of the oxide. It is originally suggested by Philling and Bedworth [1923] that if the ratio of volume of oxide to that of metal which it replaced exceeded unity, the oxide grew under compressive stress, or vice versa, but this only applies to oxide formed at the metal/oxide interface. Tien & Davidson [1974] and Huntz [1988] thought that growth stresses were mainly compressive because most materials exhibited a volume expansion during oxidation. There are many methods to measure the growth stress such as specimen extension tests [Wasilewski 1953, Seybolt 1954, Buresch and Bollenrath 1962, Noden et al. 1968, Roy and Burgess 1970, Burton 1982, Rhines and Wolf 1970, Davidson and Tien 1981 and Donaldson 1991], deflection method [Pawel and Campbell 1966, Stringer 1970, Roy and Burgess 1970, Pawel and Campbell 1975,

Weirick 1975, Delauney et al. 1980, Zhao and Huntz 1984, Moulin 1989 and Tiefan & Meishuan 1989], catenary specimen [Zhao and Zhang 1989], and X-ray diffraction [Borie et al 1962, Francis and Whitton 1965, Huntz and Zhao 1987, Aurby et al. 1988, Huntz 1988, Hou and Stringer 1991, Huntz et al. 1993, Banks et al. 1994 and Goedjen et al 1994]. Quantitative modelling of this process has also been made by Donaldson and Evans in a series of papers [Donaldson and Evans 1981].

Stress developed during the oxidation of the curved surface

The third source of stresses develops during the oxidation of curved surface. These stresses will be high when the oxide thickness is large relative to the radius of curvature of the substrate and can then have a pronounced effect on oxide integrity. However, for cases where the oxide layer is relative thin, geometrically induced stresses are small compared with these developed by temperature changes [Evans, 1995&1996]. The thermal strains induced in the oxide layer on curved surfaces can be calculated readily from standard elasticity texts [Timosheko and Goodier 1951]. Application of such solutions has been made to evaluate the stress developed in oxidised circular cylinders [Timosheko and Gooder 1951, Schütze 1988 and Evans et al. 1983] during cooling.

For difference cases, different stress source plays a key role, such as for the oxide formed on the containers used in nuclear power plant; the stress caused by thermal load plays a main role. For the oxide on the surface of the steel grade rods used for cold drawing, external mechanical load is the main stress source of the oxide scale. When these stresses exceed critical values, various types of scale damage may occur, such as micro-crack formation, through scale cracking, formation of cracks at interfaces between oxide partial layers, stable growth of delaminations at the scale-metal interface, and/or sudden spalling of parts or of the entire scale [Schütze, 1988].

2.3.1 Options for stress relief in oxide scale

Oxide scale often displays brittle characteristics, at least at intermediate and room temperature [Williams et al. 1965, Crouch & Dooley 1976, Hancock & Nicholls 1988&1994, Nagl et al 1963 & 1993, Schütze 1991, Banks et. al. 1957&1994]. The substrate/oxide system can accommodate strain by elastic deformation. If the elastic limit is exceeded, stress relaxation can take place by mechanical failure of the oxide.

Failure can start within the oxide, the substrate or at the interface by delamination [Eisenblatter, 1979]. At high temperature, oxide scale often shows plastic or ductile properties. In these cases, stress relaxation can also happen by (i) stress induced oxide growth processes [Armitt et al. 1978, Schütze 1985&1991 and Walter 1991], (ii) diffusional-related processes (“creep”) [Manning 1981, Evans et al. 1995 and Saunders et al. 1997], and (iii) plastic deformation of oxide and/or metal [Berchtold 1980, Frost and Ashby 1982, Borbehön 1988, Barnes 1989, Schütze 1990 and Zhang et al. 1997]. But (i), (ii) and (iii) can happen only at high temperature. There are a number of publications available on the stress relaxation mechanisms of oxide scale at high temperature, but the present project is concentrated on scale removal at room temperature. The following sections focus on the stress relaxation mechanisms at room temperature.

2.3.2 Failure of oxide scale under tensile stress

Armitt et al [1978] proposed an approach to express the oxide failure under tensile stress based on the critical energy release rate G_{IC} . Accordingly fracture occurs when the energy release exceed a critical value, i.e. $G_{IC}=2\gamma$, where “2” means that two new surfaces are created within the oxide scale when a through-thickness crack forms. This gives the following equation:

$$\epsilon_c = \sqrt{\frac{2\gamma}{F^2 \pi E c}} \quad (2.3)$$

where ϵ_c is the critical applied tensile strain needed to produce unstable crack growth, γ the surface fracture energy, F a constant factor, E Young modulus and c defect size. Robertson and Manning [1990] based on the same assumption consider the failure of a uniform scale which lies on a massive metal substrate under a rapidly applied external strain so that creep may be neglected, and obtained an equation the same as equation (2.3).

Evans [1988] proposed another failure mechanism for oxides under tensile stress. In his model, first through-scale cracks develop at the area of high stress concentration, i.e. the oxide breaks up into a finite number of fragments. According to linear elastic fracture mechanics, the critical applied tensile strain needed to produce unstable crack growth is [Evans, 1988]:

$$\varepsilon_c = \frac{K_{IC}}{EF\sqrt{(\pi c)}} \quad (2.4)$$

Both approaches are related via:

$$G_{IC} = \frac{K_{IC}^2}{E} \quad (2.5)$$

for the plane stress condition.

Evans and Cannon [1989] calculated the lateral extension of a crack initiated at tensile stress concentration sites, e.g. holes, pores, voids and concave undulations at edges. Stable crack propagation occurs when

$$h_c = \frac{2}{\pi} \left(\frac{K_{IC}}{\sigma_{ox}} \right)^2 = 0.6 \left(\frac{K_{IC}}{\sigma_{ox}} \right)^2 \quad (2.6)$$

where K_{IC} is the critical stress intensity factor of the oxide, σ_{ox} is the stress and h_c is the critical oxide thickness. This is effectively equation (2.4) when $c=h/2$ and with a value of $F=1$.

After the forming of through-thickness cracks, further stress relief due to high strains can happen by [Armitt, Holmes and Manning, 1978] (Fig. 2.4):

[i] multiple cracking with pure elastic stress relaxation

[ii] multiple cracking with interfacial slip and/or plastic deformation of the substrate at the base of through-scale cracks

[iii] delamination at suitable interface.

In the following, cases [i] and [iii] are discussed in detail. But for the case [ii], because the interfacial slip/plastic deformation will happen when the oxide is under tensile stress at high temperature [Armitt et al. 1978, Riedel 1982, Berchthold 1980, Manning 1981, Evans 1989, Hertzner 1990, Schütze 1989 and Robertson & Manning 1990], they are not discussed here.

Multiple cracking with pure elastic stress relaxation

Under tensile load, the ductility of such layers is usually much less than 0.02% [Hancock 1994] and the fracture process can be described by linear elastic fracture

mechanics. As soon as the through-thickness cracks form, the elastic stress concentration in the vicinity of through-thickness cracks relaxes and reduces the local stress concentration within the oxide segment and along the interface between metal and oxide scale. The in-plane stress must reduce to zero at crack faces because the stress cannot be transmitted across these places. Without relaxation, this tensile stress will increase as the distance from the crack face increases and will, due to symmetry, reach a maximum value midway between cracks [Nicholls et al. 1997] and new cracks will form here if tensile strain increases further.

Grosskreutz and McNeil [1969] first calculated the crack density, i.e. regularly spaced cracks appear in the coating based on the assumption that the substrate deforms continuously. The spacing L at any strain ϵ is given by:

$$\ln \frac{\epsilon}{\epsilon_0} = k \left(\frac{1}{L} \right) \left(\frac{1}{L_0} \right) \quad (2.7)$$

where L_0, ϵ_0 are any convenient set of data points. k is a constant and must be determined by experiment.

The formation of a tensile crack will introduce shear stresses along the oxide/metal interface because within the scale fragment the strain distribution significantly relaxes the level of deformation of the oxide scale compared with the surface layer of the metal [Nagl, 1992]. If there is no stress relaxation, this shear stress will be highest at the edges of the tensile cracks. It is these stresses that keep the islands of oxide in their stretched position. Tien and Davidson [1974] made a first attempt to calculate the shear stress distribution along the oxide-metal interface. They assumed that a linear shear stress reached a maximum value at the interface next to the tensile cracks. This gives a limiting crack spacing of:

$$L = \frac{4h}{\tau_{\max}} \sigma_{\text{ox}} \quad (2.8)$$

where τ_{\max} is the maximum shear stress at metal-oxide interface, σ_{ox} is the stress of oxide. If stresses are higher than that τ_{\max} or σ_{ox} , fracture will happen along the oxide-metal interface or within the oxide respectively.

Evans [1989] compared the prediction made by this model with another made by Nichols et al for a 10 μm thick Cr_2O_3 layer on a 400 μm thick stainless steel sample and

found that the maximum shear stress predicted by Nicholls et al was an order of magnitude smaller than that predicted by Tien and Davidson for a crack spacing of 100 μ m (Fig. 2.5a). Evans [1989] also reviewed the model proposed by Grosskreutz & McNeil and Nicholls et al and revealed that there was a significant difference between the two models for the shear stress (Fig. 2.5b). In addition, the stress normal to the crack surface drops to zero when a through-thickness crack has formed, therefore the tensile stress will vary with position (Fig. 2.5c) and reach a maximum midway between cracks.

Delamination on suitable interfaces

A final option for stress relief following through-thickness cracking is crack deflection along a suitable interface, thereby initiating delamination of some or all of the scale [Armitt and Manning, 1978]. Cracks can develop either at the metal/oxide interface or parallel to it within the oxide layer. However, deflection of the crack will occur along the surface of lowest release rate G_{IC} [Robertson and Manning, 1990]. The shear stresses along the interface between metal and oxide can be relaxed by interface cracking and spallation of the scale fragment when the strain increases to a critical level. Tien and Davidson [1974] also state that once cracks in the oxide are initiated, the loss of adherence becomes more likely, i.e. nucleation is the more difficult stage. Other researchers have investigated the deflection of tensile cracks at interface. There is general agreement that the interfacial fracture energy must be less than the cohesive fracture energy [Armitt and Manning 1978 and Heizer 1990].

Summary:

The failure of oxide scale in tension includes the formation of through-thickness cracks and interface delamination of oxide scale segments. From the previous analysis, it was found that even though the start point or the initial assumptions of the different proposed models were different, they were related with each other. In general, the fracture mechanics based on the critical energy release rate can be used to predict any thickness scale failure. But linear elastic fracture mechanism can be used to predict failure except for very thin scale, which will fracture in ductile way at high temperature. Several mechanisms were also proposed for the process of interface delamination.

Even though the problem of oxide failure in tension has been discussed in many publications, most of them are for high temperature. The oxide scale failure mechanism at room temperature is not fully understood yet.

2.3.3 Failure of oxide scale under compressive stress

Table 2.4 shows the observed failure mechanisms, together with the designation and the critical condition for initiation. Cases B and E are similar except that for Case E the oxide delimitates along a line of least cohesive strength within the oxide. In Case C a shear crack develops at 45° as a result of shear failure [Barbehön, 1988]. In Case D the oxide delaminates as a result of grain boundary sliding in the substrate adjacent to the interface [Grosskreutz and McNeil, 1969]. Cases A and B are discussed in the following. Case A, also termed Route I or wedging was originally proposed by Evans [1988]. It is characteristic of a strong interface and a weak oxide. Case B, also termed Route II or buckling, was originally proposed by Wells et al. [1974]. It is the result of a weak interface and a relatively strong oxide.

U. R. Evans [1948] first studied the spallation process. He proposed that if the strain energy within the oxide layer was equal to, or exceeded, the interfacial fracture energy, oxide-metal debonding would occur. The idea was supported by a number of researchers [Tien and Davidson 1974, Armitt et al. 1978, Evans and Lobb, 1984 & 1987, Evans 1988 & 1989 and Robertson & Manning 1990].

The stored energy W^* per unit volume of the layer is:

$$W^* = \frac{1}{2} \sigma_1 \varepsilon_1 + \frac{1}{2} \sigma_2 \varepsilon_2 = \frac{\sigma_{ox}^2}{E_{ox}} (1 - \nu) \quad (2.9)$$

where σ_i and ε_i are the principle stresses and strains, respectively. The energy release rate G_{IC} is:

$$G_{IC}^{cohesive} = 2\gamma_{ox} \quad (2.10)$$

where γ_{ox} is the fracture surface energy of the oxide and the '2' arises from the fact that two surfaces are created when delamination takes place within the oxide. However, in the more likely case, the delamination happens at the oxide-metal interface, so the energy release G_{IC} becomes:

$$G_{IC}^{int\ erface} = (\gamma_{ox} + \gamma_m - \gamma_{int\ erface}) \quad (2.11)$$

Since $G_{IC}^{int\ erface}$ accounts for both the fresh oxide and the metal surfaces, it is not necessary to include a factor of 2 [Evans and Lobb, 1984].

In Route I (case A) failure (Fig. 2.6a), it is assumed that the oxide-metal interface is intrinsically strong and has not been weakened by void formation or segregation of trace elements. Initial failure occurs by shear cracking. Evans and Lobb [1984] deduced the strain ε_I^{init} to produce a single shear crack with the length ζ as:

$$\varepsilon_I^{init} = \sqrt{\frac{G_{IC}^{cohesive}}{k_1 \zeta E_{ox} (1-\nu)}} \quad (2.12)$$

where k_1 ($\ll 1$) is a factor related to the fraction of stored energy within the layer that is used for the fracture process. When the initial shear crack is deflected at the interface and the oxide is driven away from the substrate by the wedging effect of the shear crack surface, spallation will proceed. Thus a second criteria standing for the loss of adherence or the initiation of spallation, ε_I^{spall} is derived as [Evans and Lobb 1984]:

$$\varepsilon_I^{spall} = \sqrt{\frac{G_{IC}^{int\ erface}}{k_2 E_{ox} h (1-\nu)}} \quad (2.13)$$

where h is the oxide thickness and k_2 (~ 1) is a factor related to the stored energy in the volume $\zeta^2 h$ used in the fracturing process.

In Route II (case B) (Fig. 2.6b), it is assumed that the oxide-metal interface is weak. Spallation is the result of proceeding decohesion at the scale/metal interface and buckling of the oxide layer leading to through thickness cracks or to unstable growth of the interfacial decohesion zone. In this case, of failure, it is assumed that buckling precedes through-thickness cracking, the latter leading to spalling of parts of the scales. Similarly, Route II failure behaviour can also be described by two equations. The critical strain for buckling is given by Evans et al. [1993],

$$\varepsilon_{II}^{init} = \frac{1.22}{(1-\nu^2)} \left(\frac{h}{R_d}\right)^2 \quad (2.14)$$

with R_d being the initial radius of the zone of decohesion.

Wells et al. [1974] defined the spallation criterion as that to initiate unstable propagation of the buckle. This gives an upper limit to the spallation strain ε_{II}^{spall} of [Evans and Lobb, 1984, Wells et al. 1974 and Evans et al. 1990]:

$$\varepsilon_{II}^{spall} = \sqrt{\frac{1.052h^4}{R^4} + \frac{1.041G_{IC}}{E_{ox}h}} \quad (2.15)$$

where the value of G_{IC} is the energy release rate at the plane of delamination. The first expression in equation (2.15) governs the initiation and the second spallation. A comparison of the second term with equation (2.13) shows that they differ only by a small factor, indicating that spallation is governed in both cases by the propagation of a tensile crack at the interface [Evans et al. 1990]. Equation (2.14) and (2.15) also indicate that it becomes more difficult to buckle as the oxide thickness increases. In addition, the presence of an initial delamination does not disturb the stress field until the oxide layer has buckled, i.e. a driving force for buckling must exist [Tien and Davidson, 1974]. Likewise, compositional changes in a single layer can induce differential stress and bending moments. Using equations (2.12) and (2.14) scale failure mode diagrams were calculated for different oxide-metal systems [Schütze, 1995] (Fig.2.7).

A similar scale failure mode diagram has been drawn by Robertson and Manning [1990] (Fig. 2.8). This diagram uses two criteria for scale failure. One criterion is the same as that of Equation (2.12), i.e. spallation resistance is determined by the energy for separation at the oxide-metal interface. The other one assumes that plastic oxide yield occurs at a stress of [Kelly and McMillan 1986]

$$\sigma_y \approx E_{ox} / 10 \quad (2.16)$$

Since brittleness is regarded as a size-dependent concept, a critical scale thickness h_c is calculated from the yield stress σ_y below which the oxide does not fail by cracking, but in a ductile manner (material comminution limit [Walter, 1991]):

$$h_c = \frac{2.8\gamma_0 E_{ox}}{\sigma_y^2} \quad (2.17)$$

Using equations (2.12) and (2.17), the scale failure mode diagram in Fig. 2.8, which contains data for most of the oxides relevant as surface oxide scales, was established.

In the above analysis the scale-metal interface was treated as smooth, i.e. γ_0 is the energy value for a smooth interface. For many practical oxide scales, the interface is, however, rough, which influences the adherence of the scale and, thus, the spalling behaviour. Interfacial roughness can be taken into account when using Equation (2.12) by replacing γ_0 by γ_r according to Robertson and Manning [1990], and Zhao & Huntze [1984].

$$\gamma_r = \gamma_0 \left(1 + \frac{0.1E_{ox}}{2\gamma} \frac{r}{\lambda} \right) \quad (2.18)$$

r the roughness height and λ the roughness length (Fig. 2.9). From Equations (2.12) and (2.18), it can be deduced that if r increases and/or λ decreases, the interfacial roughness will increase, thus the energy necessary for scale separation increases and adherence increases.

Summary:

From the above analysis, for the different oxide failure mechanisms, they all have an initiation condition and a spallation condition. The spallation condition is the same in all cases. It needs crack propagation along the interface or within the oxide parallel to the interface. Initiation can only occur when the stress exceeds the shear strength of the oxide (Case A and C), the buckling stability of the oxide layer (Case B and E) or when the substrate yields (Case D). But there has been little experimental data to support one or the other failure mechanism.

2.3.4 Critical parameters for prediction of oxide scale failure at room temperature

From the above analysis, it is illustrated that the critical parameters governing tensile and compressive oxide failure at room temperature are Young's modulus, the fracture surface energy of the oxide and oxide-metal interface, and the composite void size etc.. Table 2.5 gives a summary of oxide parameters [Robertson and Manning, 1990]. There is some scatter in the values of the oxide parameters found in different literature.

Young's Modulus (E)

Robertson and Manning [1990] proposed that the moduli of the oxides in scales should be similar or slightly less than those of the bulk oxides. The elastic moduli of solids depend primarily on their interatomic bonding. They are not affected significantly by work hardening, grain boundaries, etc., and are only reduced by porosity [Robertson and Manning, 1990]. The effect of porosity can be represented by various semiempirical formulae [Spriggs 1961, Rice 1977, Wang 1984 and Phani 1986] such as:

$$E = E_0(1 - p)^3 \quad (2.19)$$

and

$$E = E_0 \exp(-bp) \quad (2.20)$$

as reviewed by Rice [1977], where E_0 is the modulus of the fully compact solid, p is the porosity, and $b \approx 3$. Birchall et al. [1981] have shown that when porosity consists of both large and small pores, the small pores reduce E as in equations (2.19) and (2.20) and the large pores act as flaws or stress concentrators and weaken the materials towards fracture.

Surface Fracture Energy (γ)

Robertson and Manning [1990] proposed that the surface fracture energy of the ideal oxide-metal interface is equal to that of the bulk oxide. For the surface fracture energy of oxide bulk, quoted values can vary over one order of magnitude for a given oxide. It is considered as the work of fracture. Therefore it is the sum of the true surface energy γ_s and the energy associated with plastic deformation around the crack tip γ_p , plus further terms for polycrystalline solids. For brittle solids, the deformation term is small because dislocations are not easily emitted by the crack tips. This is the case for highly ionic or covalent compounds, thus for their single crystals

$$\gamma = \gamma_s \quad (2.21)$$

Polycrystallinity has a large effect on γ , often increasing it by an order of magnitude. Robertson and Manning [1990] studied the effect of polycrystallinity on the surface fracture energy of oxides in detail, which are listed in Table 2.5.

Porosity also decreases γ . Empirical equation similar to those used for elastic moduli are often used [Rice 1977 and Birchall 1981].

$$\gamma = \gamma_0(1-p)^3 \quad (2.22)$$

or

$$\gamma = \gamma_0 \exp(-bp) \quad (2.23)$$

again with $b \approx 3$.

Armitt et al [1978] and Manning [1981&1983] have made extensive use of the empirical correlation

$$\frac{\gamma}{E} = k \approx 0.04nm \quad (2.24)$$

found by Mecholsk et al [1976] for polycrystalline materials in which γ varied between 4 and 40J/m². The relationship between γ and E was also found by Robertson and Manning [1990] for polycrystals, but with a constant value of 0.02nm. On the other hand, Kelly and MacMillan [1986] analysed the theoretical strength in terms of cohesion between adjacent atomic planes and found a different relationship.

$$\gamma \approx \frac{ER'}{10} \quad (2.25)$$

This gives $k \approx 0.02$, if $R' \approx 0.2nm$, here R' is a constant.

Nature of the scale-metal interface

In all models, spalling will occur along the surface of lowest energy release rate G_{IC} , which can be either within the scale or along the scale-metal interface. This leads to the question of whether or not the interface is intrinsically weak. Robertson and Manning [1990] have pointed out that the scale-metal interface is intrinsically strong on an atomic scale. On the other hand, the scale-metal interface is also a site for segregation of elements which are relatively insoluble in the scale or for oxides. Sulphur segregation at the interface was assumed to have a negative influence on the interface strength [Evans and Cannon, 1989]. It is difficult to separate each of these aspects with the present state of experimental knowledge [Robertson and Manning 1990 and Schütze 1991].

Robertson and Manning [1990] proposed that the surface energy of this ideal oxide-metal interface is equal to that of the bulk oxide. So, even though the experimental data are limited, the assumption proposed by Robertson and Manning [1990] make some calculation by using some of the equations listed in this chapter possible, such as the calculation the spalling strain for Route I and II failure under compressive stress.

Composite void size

Until now, little attention has been paid to the effects of voids within the oxide or at the oxide-metal interface on the failure process, although it is an important factor in all the quoted models for through-scale cracking and spalling. Hancock and Nicholls [1988] proposed a new simple method for determining the dimensions of a 'composite defect' in surface scale by summing the actual defects present in the scale using well established techniques of linear elastic analysis. From such estimates, fracture toughness can be assessed and the stress intensity factor for growing surface oxide scale can be calculated. The effects of pores on the fracture strength were investigated by Birchall et al. [1981] for cement and by Rice [1984] for bulk ceramics. It seemed apparently that the defect size is a crucial factor for the determination of the strength of oxides. It was also suggested that a major role of active element additions is to reduce the macro defects present within the oxide scales with consequent benefit on scale adherence and spalling resistance [Robertson & Manning 1990 and Nicholls & Saunders 1990]. Hancock and Nicholls [1988] also found that thicker oxide layers failed at lower levels of applied stress than thin films. This was thought to be due to a higher probability of finding larger composite defects in the thicker oxides.

2.4 Descaling methods used in industry

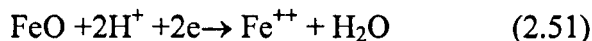
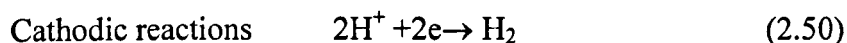
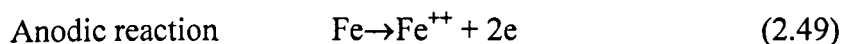
The alternative methods of descaling are summarised in Fig. 2.10.

Chemical pickling has so far been mainly employed to descale wire rods prior to drawing. However, because of the severe pollution control regulations concerning waste acid treatment, mechanical descaling has been put into industrial use and there is

a tendency toward the spread of this process since it provides advantages in terms of operating cost [Tominaga et al., 1982].

2.4.1 Chemical Descaling

Chemical pickling uses an acid solution to dissolve the oxide scale. In the acid solution, the solubility of FeO is the highest, that of Fe₃O₄ next, and Fe₂O₃ scarcely dissolves [Hopkinson, 1993]. The dissolution of the iron base is followed by the reduction dissolution of the oxides. The following reactions [Hopkinson, 1993] are considered in this connection:



In ordinary pickling operations, it may be considered qualitatively that the dissolution takes place in the order of (2.49), (2.50), (2.51), (2.52), (2.53) [Hopkinson, 1993]. The pressure of H₂ generated by the reaction (2.50) contributes to the mechanical peeling of scale [Hopkinson, 1993].

The acid chemical descaling process involves high costs with regard to proper installation, operation and maintenance [Fresnedo and Ruiz, 1996].

2.4.2 Mechanical Descaling

Although the principles were known long before, mechanical descaling began gaining popularity in the 1950s and there has been a tendency toward the spread of this process since then. At that time, in general, the concern about contamination and waste disposal was much less prevalent than it is today [Fresnedo and Ruiz, 1996]. The incentives for adoption of mechanical cleaning are the high costs of pickling acids and the difficulties of disposing of spent pickle liquor [Stalson and Hurat, 1965]. However, there are some costs and disadvantages related to mechanical descaling that must be recognised. These include: (1) increased wear of the dies, especially in the first pass; (2) the heavy wear to which some equipment parts are subjected; (3) lower surface

quality of the product; (4) material hardening due to mechanical deformation and (5) more stringent lubrication requirement [Hopkinson, 1993]. As a result of these limitations, mechanical descaling is not recommended for especially stringent quality product, i.e., for steel with more than 0.64 carbon, or for products requiring a specific surface quality [Fresnedo and Ruiz, 1996].

Three mechanical descaling methods have been used in the industry [Tominaga et al., 1982]:

Reverse Bending Process: In this process, scale which is far more brittle than steel is cracked and removed by the tensile and compressive deformation of the rod surface produced by bending and reverse bending of the rod around two rollers whose axes are perpendicular to each other (Fig. 2.11).

The strain of the rod surface is given by

$$\varepsilon = \frac{d}{D+d} \quad (2.54)$$

where d is the wire rod diameter, D is the diameter of bending (Fig. 2.12). In general, the proper amount of strain necessary for scale removal is considered to be 6 to 8%. Permanent elongation may be produced in the wire rod due to reverse bending under a constant tension. Descaling by simple tension required 10% elongation of the material. By the repeated bending method, however, even 5% elongation suffices, and more elongation proves no more effective for the purpose [Tominaga et al., 1982]. Complete removal cannot be achieved simply by elongation of the material, and the residual scale needs to be brushed off by passing the rod through whisker boxes.

Shot Blast Process: Scale is broken and removed by blasting shot against the rod surface. At present, steel shot or cut wires of 0.3 to 0.6mm in diameter (the latter having longer life but its cost being higher) are blasted against the rod from three to four directions using high-speed impellers (4000rpm), and it has become possible to connect shot blasting equipment directly to drawing machines.

Air Blast Process: Abrasive grains of silica sand, alumina, etc. are blasted against the rod by compressed air blown through nozzles. A process of injecting water together with abrasive grains is called liquid honing.

2.5 Methods for simulating scale cracking in mechanical descaling

2.5.1 3-Point Bending Test.

A 3-point bending test was used by Hall et al [1988] for preliminary work at room temperature in tension and compression. They used flat specimens with the scale on only one side. In this way tensile and compression forces could simply be applied by placing the layer on the bottom or top side within the bending jig without modification of jig or specimen. The work produced good results. However the experimental arrangement had drawbacks:

(1) The oxide stress and strain varied with position along the length of the beam in the 3-point bending which leads to different stages of the failure process overlapping.

(2) The upper roller was at the position of highest stress, i.e. in the fracture zone during loading in compression, which might have influenced the failure mechanism.

2.5.2 4-Point Bending Test.

Nagl et al [1992, 1993 and 1994] used a 4-point bending test at both room temperature and high temperature, with Acoustic Emission to identify the oxide fracture mode. They used a flat sample with the oxide on one side only.

In the 4-point bending test, there is an area between the two upper rollers, where stress and strain are constant, which can be used to study the relationship between the strain and scale cracking and removal behaviour.

2.5.3 Uniaxial Tensile Test.

In Swinden Technology Centre of Corus Group, tensile test is used to remove the scale on the steel rod surface. Before the test, chemical picking is used to remove the scale on the two ends of the sample in order to avoid the influence of the grips. This is also a good method to study the relationship between the strain and the scale removal percentage.

Murahashi [1993] used the tensile test to study the descalability of wire rod by evaluating the residual scale amount stated in mass percent after a four percent elongation exerted in a tensile testing machine. This method allows a simple

comparison between the values, without paying attention to differences in design of a mechanical descaler, since it offers inherent descalability qualities of a given wire rod [Baroux, 1979].

Queiroga et al. [1995] used the tensile test to study the influence of cooling conditions of steel wire rod on scale formation and its application on mechanical descaling.

2.6 Factors influencing descalability

The hot rolling process produces a coiled product capable of being drawn by the wire drawer, but possessing an oxidised surface which has to be removed prior to the drawing operation. The amount of scale formed is dependent on the rolling conditions, particularly the billet reheating temperature, the laying temperature and the cooling rate. The three oxide phases present in the scale are wüstite (FeO), magnetite (Fe₃O₄), and hematite (Fe₂O₃). The composition and visual appearance of each phase are listed in Table 2.7 [Hopkinson, 1993].

The study of the influence of rolling conditions on descalability of high carbon steel wire rod carried out by Murahashi et al. [1993] showed that the billet reheating temperature does not seem to largely affect the initial scale amount, although there is a small increase in the scale amount recognizable with increased reheating temperature.

Tominaga explained this phenomenon early in 1982 that the billet passes through many stands, scale is repeatedly formed and peeled. Scale remaining on the wire rod in the stage of laying is about several micrometers in thickness and is negligible. Therefore, the laying temperature and cooling after laying have the largest effect on the formation of scale.

2.6.1 Laying temperature

[Tominaga et al, 1982] studied the effect of laying temperature (650°C, 750°C, 850°C and 900°C) on scale properties of mild steel wire rods, such as the scale constitution, the amount of scale (wt%) before bending and the amount of scale removed (wt%) after bending. It was found that the laying temperature has a large effect on the composition of scale. Above 850°C, Fe₃O₄ becomes thick and the amount

of scale increases. Therefore, they thought that laying temperatures above 850°C were not desirable. The proper amount of scale recommended is about 0.5% below 750°C and about 1% at 800°C to 850°C after bending. For mechanical descaling about 1% scale is sufficient if the laying temperature is fairly high and the cooling rate is sufficiently high.

A study of the influence of laying temperature (850°C, 900°C, 950°C and 1000°C) on descalability was also carried out by Murahashi et al. [1993] on high carbon steel rod. It was found that the initial scale amount became greater with increasing laying temperature.

In order to optimise the cooling cycles of low carbon steel wire rod after hot rolling, Genève & Francois [1994] and Confente et al [1995] used an experimental radiation furnace to simulate industrial cooling conditions. The study conducted by Genève & Francois [1994] shows that an increase in laying temperature can reduce the scale adhesion. And the study carried out by Confente et al [1995] found that in order to improve the mechanical descaling of grade SAE 1008 low carbon steel rods, it was necessary to ensure high-laying temperatures above 850°C, together with low initial cooling rates to promote scale growth. But both parameters - laying temperature and initial cooling rate – have to be adjusted in order to avoid excessive scale thickness and also blisters.

Queiroga et al. [1995] studied the effect of cooling conditions of steel wire rod on scale formation and its application in mechanical descaling. The procedures used to obtain the scale were divided into two steps. In the first one, the goal was to compare two cooling speeds for the same laying temperature. In the second one, the objective was to apply the better condition of cooling for two laying temperatures (875°C and 900°C). Their results show that the laying temperature is more efficient than cooling rate in generating more scale, in the interval of Stelmor cooling applied. The highest laying temperature also provided a greater amount of FeO in the scale.

2.6.2 Cooling rate

Table 2.6 shows processes for cooling wire rod from the rolling heat. From the historical viewpoint, water quenching of the coil in cold water (no.3) was among the early steps. This process was efficient enough to be maintained in Germany for 70

years. The next step in the development was based on the realization that conventionally the coil cooled too slowly, and scale rich in iron was formed that could not be pickled completely and quickly enough. Therefore, descaling with acid or by mechanical means had to be improved, which could be achieved by cooling the smaller rod sizes with water more effectively. The bigger sizes may be cooled faster by blowing air into the reel during and after coiling, which results in a 100°C reduction in the rod temperature [Beck, 1981].

To further reduce scale formation and at the same time replace air patenting the Stelmor process was developed. In this process the wire rod is laid via the laying tube in non-concentric rings on moving conveyor chains rather than into the reel as a compact coil. Thus the single rings are separated and cooled faster in a controlled manner in several consecutive zones by adjustable air volumes. With the conveyors at full speed and with the highest air volume, 5.5mm diameter rod is cooled between 800°C and 500°C at 20°C/s. By shutting off the air and with the conveyor moving slowly at 0.2m/s, the cooling speed is decreased to about 4°C/s. By reason of this range, the Stelmor process in its standard version makes it feasible to adjust the structure and mechanical properties of the wire rod to the demands of processing to a great degree. The scale is so reduced by the fast cooling below 850°C that mechanical descaling or pickling does not pose problems. The Stelmor process is suited to low and high carbon steels [Beck 1981].

Sachs et al [1959] examined in detail the scale on mild steel in various stages of rolling wire rod by using X-ray and metallographic techniques. (The production flow is: the billets are heated to about 1200-1120°C in a furnace fired with enriched blast-furnace gas. The billets are in the furnace for about 2h altogether and are at the temperature for about 15-20 min. They enter the roughing train fairly slowly, so that a piece can be cut off the back end. The roughing train consists of 10 stands; at stand 10 the material emerges as 5/8-in. rod and there is a flying shear at this point. The rods then pass through the finishing train of 5 stands emerging as 5 swg rods at temperatures of the order 950-1000°C. The rod are cooled to 850°C by water circulating in the guide tubes and reeled into 480-lb coils). Sachs et al [1959] found that the mill variables,

particularly the cooling rate, have a profound influence on the thickness and structure of the scale, particularly on the extent of decomposition of wüstite below 570°C.

Tominaga et al. [1982] studied the effect of cooling conditions on descaling properties. The experiments with actual wire rods on the effect of cooling conditions such as a difference between tight coils reeled by the conventional process and loose coils reeled by the Stelmor process on the descaling property has demonstrated that loose coils show a good mechanical descaling property at high temperature. An investigation of more effective cooling conditions was conducted in the laboratory. The results show that cooling to below 600°C after laying is very important for preventing transformation to Fe₃O₄. Cooling rates above 1°C/s are desirable for mechanical descaling.

The study of the influence of cooling rate (in the Stelmor process) on descalability was also carried out by Murahashi et al. [1993] on high carbon steel rod. It was found that the initial scale amount became greater with decreased cooling rate.

Genève & Francois [1994] and Confente et al [1995] conducted laboratory simulations with the aid of a radiation furnace on eutectoid steel rod, permitting rapid heating and cooling speeds, in order to better understand the effect of the different stages of cooling on the aptitude for the mechanical descaling process. The simulations allowed them to study the influence on the oxide layer of several parameters:

- The laying temperature at the wire rod mill,
- The duration of slow cooling in calm air at the beginning of the conveyor; the cooling speed in the growth zone was fixed at 4°C/s for all the trials,
- The cooling speed before the pearlitic transformation,
- The cooling speed during the phase transformation, and
- The cooling speed after the phase transformation.

It was found that the main factors contributing to a reduction in scale adhesion are [Genève & Francois, 1994]:

- An increase in the laying temperature (up to the point that blisters appear)
- The careful application of a well-adapted growth time at the beginning of the cooling phase
- A not too rapid cooling before the pearlitic transformations, and

- A not too rapid cooling after the pearlitic transformation (until the decomposition of wüstite).

So it is possible to obtain a slight scale adhesion, satisfactory to the users, without significant increase in the amounts of scale, while conserving the protective effect of the oxide layer on the metal [Genève & Francois, 1994]. Confente et al [1995] found that in order to improve the mechanical descaling of grade SAE 1008 low carbon steel rods, it was necessary to ensure high cooling rates at temperatures from 570°C to 300°C to prevent FeO transformation to Fe₃O₄.

Queiroga et al. [1995] studied the influence of cooling conditions (in the Stelmor process) of low carbon steel wire rod on scale formation and its application on mechanical descaling. The main controlled variables were:

- Opening of the fan;
- Conveyor speed; and
- Retarded cooling system.

It was found that cooling rate is less efficient to control the scale thickness than laying temperature.

2.6.3 Steel grade

Sachs and Tuck [1967] reviewed the effect of elements on the oxidation of commercial steels. However, this was for furnace (or primary) scale, which has been discussed in detail in section (2.2.1.2).

Murahashi et al [1993] studied the influence of constituent elements on descalability of high carbon steel wire rods. According to their results, the elements tested can be divided into three categories: those which enhance descalability such as Cu and S, those which deteriorate descalability such as Si, Ni and Co, and those which do not have much influence such as Cr. They explained the influence of constituent elements on descalability according to the equation proposed by Robertson and Manning [1990]:

$$\varepsilon_c = \left[\frac{2\gamma_0(1 + \chi^2)}{hE} \right]^{1/2} \quad (2.55)$$

where ϵ_c is the critical strain beyond which scale spalling occurs, h is the scale thickness, E is Young's modulus of the scale, γ_0 is the surface fracture energy for a smooth interface, and χ is an interfacial roughness index.

It is known that elements other than iron and carbon contained within steel form enriched surface layers at high temperatures between the matrix and usual iron oxides through selective oxidation mechanisms due to their difference in affinity for oxygen [Yasuhiko, 1971]. Furthermore, elements such as Si with a higher affinity for oxygen than iron can form internal oxides underneath the matrix surface [Ruth, 1978]. These layers are considered to influence descalability by changing such interfacial properties as defined by χ and γ_0/E ratio in the above equation. The Cu existing in such an enriched layer is said to be metallic Cu due to its low affinity for oxygen, and plays a role in suppressing decarburization [Hideo, patent]. Less decarburization will lead to less roughening of the interface, that is, a better descalability owing to a low value of χ . Si and S are said to form enriched layers consisting of fayalite ($2\text{FeO}\cdot\text{SiO}_2$) and FeS, respectively [Yasuhiko, 1971]. The descalability worsening effect of Si and descalability enhancing effect of S may be explained in terms of γ_0/E ratio. The γ_0/E ratio for SiO_2 is greater than that for FeO, while the γ_0/E for FeS is smaller than that for FeO [Robertson and Manning, 1990]. In the case of Si, however, the unevenness with which oxidation penetrates into the matrix may also be responsible for its effect of worsening descalability. Si is one of the typical elements causing internal oxidation, and possibilities are strong that the scale/matrix interface is roughened simultaneously with oxidation.

Murahashi et al [1993] thought that it would be possible to explain the descalability data obtained with other elements in this way. However, a full understanding of the observations is thought to require further study of the influences of these elements on the behaviour of their enriched surface layers.

Electric arc furnace (EAF) steels are increasingly being used in wiredrawing applications previously supplied by BOS (basic oxygen steel), but the main disadvantages of a scrap-based route as opposed to BOS are in two areas:

- The scrap-based route generally produces higher levels of residual elements in the steel.

- Electric arc steelmaking tends to produce higher levels of nitrogen in the steel than the BOS process.

Franks and Kirkcaldy [1997] studied the effect of boron additions on the properties of electric arc-sourced plain carbon wiredrawing qualities, including the descalability, and found that:

- Boron treated electric arc steel can be used to successfully replace BOS steels in low carbon drawing application.

- Boron additions to electric arc drawing quality rods have been shown to be effective in reducing rod strength, reducing work hardening rate and reducing strain ageing.

- Boron treated electric arc steels with relatively high residual levels can give drawing behaviour similar to BOS steels providing other factors such as internal cleanness and surface quality are also controlled.

Yalamanchili et al [1999] studied the effect of residual elements on low carbon rod quality and implications to the end user. There are three distinct paths to control the residual elements. The most common approach is to exclude the residuals by selecting high grade scrap. The second approach has been to dilute the effect by adding high percentages of alternate iron units. The amount of dilution depends upon the end product being made. The third method was to compensate by adding elements such as boron to control the effect of elements such as nitrogen because electric arc steelmaking tends to produce higher levels of nitrogen in the steel than the BOS process. When boron is added to low carbon heats in the appropriate levels, the mechanical properties of the rods can in some instances be improved.

2.6.4. Rod surface roughness

The condition of the surface of wire rod after hot working and just before scale formation also has an effect on adhesion. These factors determine the conditions for scale removal and the resulting finishing surface, which in turn governs the wiredrawing process.

The study carried out by Tominaga et al. [1982] found that the rod surface roughness had a large effect on the mechanical descaling property. This reflected in the unexpectedly large difference in the mechanical descaling property of scale between

rolling on a conventional mill and rolling on a non-twist mill. When the steel base is smooth, the mechanical descaling property is very satisfactory, so it is important to pay sufficient attention to the service time and material of rolls.

CHAPTER THREE

EXPERIMENTAL METHODS

3.1 Introduction

The main aims of the present experimental work can be defined as two parts. The first is to investigate the development and removal mechanisms of scale on wire rod of commercial steels by experimental simulation tests and metallurgical observations. The second is to investigate optimum manufacturing conditions for the easy removal of scale.

Although the main aim of the present experimental work is to remove the tertiary scale on commercial steel rod surface, some preliminary tests were carried out on primary scale. Several different types of bending tests, such as 3-/4-point bending, cantilever bending and constrained bending, have been conducted to follow the work in the literature and to simulate industrial mechanical descaling. In order to assess the ease of removal of scale, the strain for scale cracking and removal has been used as an evaluation standard. Several methods, such as a scribe method, shadowgraph method and Cyclone scanner method have been applied to evaluate the critical strain for scale cracking and removal. The effects of process variables, such as laying temperature, cooling condition, ageing time, and humidity and temperature on descalability have been studied. Also, in order to investigate the scale microstructure, an EBSD technique was used to characterize the multicomponent layers of scale, and X-ray element mapping was used to identify the element enrichment in scale/metal interface. In the following sections, the details of the experimental materials and methods are described.

3.2 Experimental Materials

Here the materials used were commercial steel rods supplied by Scunthorpe Rod Mill, Roundwood Rod mill and Cardiff Rod Mill.

3.2.1 Process route

Tertiary scale is formed on the hot steel during the interpass delay time in finishing rolling mills and during air cooling after hot rolling. The process route,

especially the cooling process therefore has an important influence on the scale thickness and structure.

Fig. 3.1 shows the process flow of Scunthorpe Rod Mill, where billets are heated in a walking beam reheating furnace, then pass through roughing and intermediate stands. The rod then undergoes finishing rolling, passes through water boxes and the laying head, and then travels down a Stelmor cooling conveyor and passes into a reform tub. The coil is then compacted, and a compacting band is put on.

Fig. 3.2 shows the process flow of Roundwood Rod Mill, where after finishing rolling, the rod passes through water boxes and forms coil, which further cools, in blow stations. The main difference between Scunthorpe Rod Mill and Roundwood Rod Mill is the cooling process. In Roundwood Rod Mill, it is conventional cooling. The compact coil cools slowly, so thick scale forms during the slow cooling. By mechanical descaling, it can be removed but mechanical descaling increases the metal loss. In Scunthorpe Rod Mill, there is Stelmor cooling in which the wire rod is laid via the laying tube in non-concentric rings on moving conveyor chains rather than into the reel as a compact coil. Thus the single rings are separated and cooled faster in a controlled manner in several consecutive zones by adjustable air volumes. With the conveyors at full speed and with the highest air volume, 5.5mm-diameter rod is cooled between 800°C and 500°C at 20°C/s. By shutting off the air and with the conveyor moving very slowly at 0.2m/s, the cooling speed is decreased to about 4°C/s [Beck, 1981]. Because of this wide cooling range, the Stelmor process in its standard version makes it feasible to adjust the structure and mechanical properties of the wire rod to meet the demands of subsequent processing. At the same time, it also can control the scale structure and thickness.

The process flow of Cardiff Rod Mill is similar to that of Scunthorpe Rod Mill, but there are still some differences between them. In Cardiff Rod Mill, the rods are rolled in a two-strand mill, which was built in 1975 by Morgan Construction Co. The mill has two Morgan No-twist finishing blocks, followed by water boxes and Stelmor cooling lines. The water boxes are of relatively recent design, and incorporate feedback control, so that it is possible to control the coil laying temperature to within +/-10°C of the required temperature. The Stelmor conveyors are 55m long. They are chain

conveyors, with slotted deck plates to distribute the air across the width of the coil. Originally, the air-cooling consisted of 5×9m long zones, each with a single fan rated at 87,6000m³/h capacity. The original zones 1 and 2 on each conveyor have been split into two, and an additional fan (of the same capacity) installed in each.

3.2.2 Chemical compositions of steel grades

Table 3.1 lists the chemical compositions of all steel grades used in the experimental tests and the related information, such as rod diameters, steelmaking processes, applications and suppliers etc.. For Scunthorpe Rod Mill and Roundwood Rod Mill, Basic Oxygen Steelmaking (BOS) steels are used. For Cardiff Rod Mill, Electric Arc Furnace (EAF) steels are used. The chemical compositions of the first four steel grades were analysed in the university laboratory, but the rest of the steel grades were analysed in the industry laboratory. Here, only the main elements are listed in the table. The steel grades supplied by Scunthorpe Rod Mill are BOS steels. Among them, K58 and D12 have the same Si and Mn contents, while their S and C contents are different. R09 and K08 have the same Si content, but their S, C and Mn contents are different. For D12 and K08, whereas their Si and Mn contents are same, their C and S contents are different. K58 and R09 have the same Si content although their S and Mn contents are different. In addition K58 has the highest carbon content 0.59%, R09 has the lowest carbon content 0.032%, K58 has the lowest sulphur content 0.011% and D12 has the highest sulphur content 0.041%. Both R09 and B03 have similar chemical composition. The steel grades provided by Cardiff Rod Mill are EAF steels, which used steel scrap as raw materials and caused high residual elements in the steel, such as high Cu content in K08B and K08-F.

3.2.3 State of materials

Samples supplied by Scunthorpe Rod Mill, Roundwood Rod Mill and Cardiff Rod Mill was taken from different positions in the rod mills. Therefore the states of the materials were different.

Fig. 3.3 shows a schematic diagram of the rolling and coiling process in Scunthorpe Rod Mill. The steel grade rod samples were taken at the trimming stage. After the rod has travelled down the Stelmor conveyor and passed into the reform tub, a

back end trim is taken, and the samples were then taken from the back end trim. The samples of different steel grades supplied by Scunthorpe Rod Mill were used in 3-/4- point bending tests, laying temperature tests, ageing time tests, coil positions tests, and relative humidity and temperature tests. For 3-/4- point bending tests, the samples were taken for one laying temperature 950°C. For laying temperature tests, samples of steel grade K08 but from different casts were taken for three laying temperatures, such as, 950°C, 890°C, 830°C. For ageing time test, samples were taken for two laying temperatures 950°C and 890°C. For coil positions tests, the samples were taken for one laying temperature, 890°C. For relative humidity and temperature tests, the samples were taken for one laying temperature, 830°C.

Fig. 3.4 is a schematic diagram of the positions where the rod samples are taken in Roundwood Rod Mill. These steel rod samples with diameter of 14mm were taken from three different positions, such as: inner (I), middle (M) and outer (O) positions, at the same level (such as Front, MA, MB, and Back level) of the coil. Overall, samples were taken from 12 different positions in the coil, and were labelled: FO, FM, FI, MAO, MAM, MAI, MBO, MBM, MBI, BO, BM, and BI. Some of these samples, such as the samples marked FO, FM and FI, had surface damage when they were received, i.e. the scale were already off the rod surface. The rod temperatures at different positions are shown below:

After blow top 620°C
middle 650°C
bottom 650°C

In Cardiff Rod Mill, the wraps were also taken from different strands at the trimming stage. These rod samples were cooled under 4 different conditions, i.e.:

Laying temperature 900°C, fans on the conveyor.

Laying temperature 900°C, fans off the conveyor.

Laying temperature 870°C, fans on the conveyor.

Laying temperature 870°C, fans off the conveyor.

At each cooling condition, within each batch of rings, there may be rod from different strands, although they should have been cooled under the same nominal conditions. The colours of the rods from each batch were different, which can be divided into three groups: dark red, blue grey, and light grey colour.

3.3 Experimental methods

3.3.1 Oxide scale produced in the laboratory

Some preliminary tests were carried out in order to understand the characteristic of primary scale. Thin flat strip of low carbon steel with a geometry of approximately 12×3mm in cross section were first cut into short samples of approximately 100mm in length. The steel samples were then surface ground with SiC paper to 800-grit finish. After cleaning with pure alcohol and acetone, the samples were oxidised in a furnace with and without gas protection to obtain different thickness of scale layers.

Three different procedures were used in oxidation treatment. The first one was to compare three holding times for the same reheating temperature. The second one was to compare three different reheating temperatures for the same holding time. In the third procedure, the reheating temperature and holding time were held constant, but the furnace atmosphere was changed, with and without gas protection in order to investigate the effect of furnace atmosphere on scale formation. With these considerations, the reheating temperature and holding time were finally chosen as the following combinations: 820°C×6min, 900°C×5, 10, 20min, and 1000°C×2, 5, 10, 20min. After being reheated, the samples were cooled outside the furnace to room temperature for bending tests.

3.3.2 3-point bending test

Two different types of specimens were used in 3-point bending test: flat samples of low carbon steel on whose surface oxide scale was formed in the laboratory, and circular cross-section commercial D12 steel rod samples provided by SRM. Their chemical compositions are shown in Table 3.1.

Fig. 3.5 shows a schematic illustration of 3-point bending test and its bending moment distribution. 3-point bending tests of flat and rod specimens with overall

length about 100mm were carried out on a Hounsfield 100KS 100kN Capacity Tensile Testing Machine with a 3-point bending jig. Different strains were obtained by changing the deflections for the same span between two anvils set on the bottom horizontal beam, and also by changing the spans for the same deflection to examine the scale cracking behaviour at different stages (Table 3.2-3.3). During a bending test, deformation load was recorded against deflection.

3.3.3 4-point bending test

Fig. 3.6 shows a schematic diagram of the 4-point bending test and its bending moment distribution. 4-point bending tests of commercial steel rod samples, whose chemical compositions are shown in Table 3.1, with overall length about 100mm, were carried out on the H100 machine with a 4-point bending jig. Parameters used in 4-point bending tests, such as, u (the distance between inner and outer rollers, mm), s (the distance between outer rollers, mm), δ (deflection, mm) and f (cross head speed, mm/min), for the rod samples of steel grades K08, R09, B03, K08+B and K58 are shown in Table 3.4 – 3.6 respectively. A steel grade K08 ($\phi 5.5\text{mm}$) rod samples was used to study the effect of parameters, such as, u , s and f , on the scale cracking and removal behaviour (Table 3.4). The effect of steel grades on the scale cracking and removal behaviour was studied by using rod samples of steel grades R09, B03, K08+B and K58 ($\phi 6.5\text{mm}$) (Table 3.4 – 3.6). For the rods of diameter 14mm supplied by Roundwood, samples of about 100mm long were cut from different coil positions, and tested under the same condition, i.e. $u=20\text{mm}$, $s=80\text{mm}$, $\delta=4.57\text{mm}$ and $f=5\text{mm/min}$. Finally, a copper rod sample ($\phi 6.5\text{mm}$) of 100mm long was also used to test 4-point bending, where $u=20\text{mm}$, $s=80\text{mm}$, $f=5\text{mm/min}$.

3.3.4 Cantilever bending test

A 300mm long rod sample was cut from the coil, with an initial curvature forming the coil diameter of about 1 metre. This was fixed in a vice horizontally at one end, and a load was applied to the other end by hand to bend the steel rod in the direction, which increases the original curvature. Fig. 3.7 shows a schematic representative of (a) the cantilever bending test, (b) the definition of critical area, (c) the bending moment distribution and (d) the stress distribution in the rod cross section. With bending of the rod, the oxide scale on the tensile and compressive sides of the rod surface undergoes

continuous cracking and removal along the length of the rod. Once part of a circle with a constant radius is formed in the bent part of the rod, releasing the loaded end stops the bending. Therefore, there is always a transient region on the rod where the oxide scale undergoes initial cracking, crack development and complete scale removal from the rod surface (after brushing). Before and after the test, the curvatures of the tensile surface and the compressive surface of the sample were measured and used to evaluate the critical strain for scale cracking and removal.

3.3.5 Constrained bending test

To simulate industrial bending round a pulley, 300mm long rod samples were cut from the coil with an initial curvature forming the coil diameter of about 1 metre. One end of the sample and a cylinder were fixed in a vice, and another end of the sample was bent around the cylinder. Fig. 3.8 is a schematic diagram of constrained bending. A series of cylinders, whose diameters are 51mm, 74mm, 92mm, 102mm, 143mm, 160mm, 180mm, and 215mm respectively, was used in the constrained bending tests.

3.3.6 Observation of scale

In order to simulate industrial conditions, bent rods were subjected to brushing before the scale removal was assessed. Brushing was carried out using a brush with plastic bristles.

3.4 Evaluation of plastic strain variation

3.4.1 Objective

In order to assess the effects of manufacturing conditions on the ease of removal of scale, a plastic strain is used as a comparison standard, i.e., by comparing the strain for the same amount of removal of scale after the bending, the good manufacturing conditions can be found. In the laboratory, in order to measure the strain accurately, many methods, such as a scribe method, shadowgraph method and scanner method, have been tried to obtain the plastic strain after the cantilever bending test. On the other hand, in order to compare with measured strain, the strain in 4-point bending, cantilever bending and constrained bending have been calculated by the FE method

respectively. In this section, two parts of work will be described in detail. The first part is to measure the stain in the laboratory. The second part is to calculate the stain by the FE method.

3.4.2 Evaluating strains after cantilever bending in the laboratory

3.4.2.1 Scriber method

The aim of the scriber method is to obtain a standard sample with known plastic strain. Then other samples' strains can be obtained by comparing with the standard sample. Because the scale on the steel rod surface is brittle, a copper rod sample was used for this method.

Fig. 3.9 illustrates scriber method schematically. This method was to use a scriber to draw lines around and along the rod surface. A scriber with digital control (with $\pm 0.01\text{mm}$ accuracy) was used to draw lines along and around the straight rod sample surface. Photographs of lines on the rod surface were taken into the PC image analyser using a camera ($\times 3.3$) connected with the optical microscope whose objective lens' magnification are $\times 5$. A Graticule was photographed in the PC image analyser under the same magnification as the rod sample. The Graticule was divided into 100 parts, so the accuracy of the stage micrometer is $\pm 0.005\text{mm}$. The distance between the scribed lines before and after bending can be measured. By using the following equation (3.1), the strain can be calculated.

$$\varepsilon = \ln\left(\frac{l}{l_0}\right) \quad (3.1)$$

where l_0 and l are the distance between the scribed lines before and after bending, respectively.

By the PC image analyser, four methods have been used to measure the line spacing before and after a cantilever bending test:

(1) Use the PC image analyser to measure a single object length automatically. It needs to treat the image in Paintbrush, i.e. to pick up or separate the single object from the others in the image, and then the PC image analyser can measure the single object length automatically. The PC image analyser calculates the length by single object

colour. There are two colours, one is the single object, one is the background, and can be changed by the operator.

(2) The computer has its own co-ordinate system, the line spacing was obtained by subtracting the corresponding two lines co-ordinates, such as $L_{ab}=X_b-X_a$, the length unit used is a pixel (1micron=5.2356pixel), and each photograph just contained two lines. Six photographs were opened on the screen at the same time. Three of photographs were taken before the cantilever bending test, and three of photographs were taken after cantilever bending test. The lines on the three photographs before/after test are consecutive. Because the corresponding relationship of lines before and after the cantilever bending test were shown on the screen at same time under same setting of the computer, the accuracy of this method was relative higher than that of method (1).

(3) Use the Zoom function to enlarge the image of a photograph of line spacing as large as possible. Even though the computer has its own ruler in three units: cm, inch and pixel, a Graticule was photographed and saved into the computer under the same magnification. The image of the Graticule was enlarged under the same condition as that of the image of the photograph with line spacing, and then the stage micrometer was copied onto the image of the photograph with line spacing. By comparison, the line spacing was obtained. The line length unit is mm. Because the image of a photograph of line spacing was enlarged as much as possible by using the Zoom, just one photograph was shown on the screen each time, the relative relationship of the line spacing before and after cantilever bending was easily lost. The measurement accuracy of this method is higher, but the accuracy of the real strain calculated from the line spacing obtained by this method was lower than that of the last two methods.

(4) Use a replication material to obtain the trace of line spacing. A replication material was used to obtain the line trace on the rod surface, and then the film was peeled from the rod surface. The film was observed under the optical microscope and finally the line spacing on the film was measured. In the other methods, because the sample was deformed, most parts of the sample surface were not perpendicular to the light beam of optical microscope. If the sample surface forms an angle of 10° with the horizontal stage of the optical microscope, the relativity error of line spacing caused by

this angle is 2%. The replication method avoids this problem. But extra strain was caused by tearing the film from the deformed sample surface.

3.4.2.2 Shadowgraph method

This method was to use a shadowgraph, in which an enlarged image of the bent sample is projected on a screen, to measure the local radius of curvature of a sample after a cantilever bending test. The stain was then calculated from the local radius. Copper and steel rod samples were used in this method.

With the shadowgraph, two methods have been used to obtain the curvature. One was to use AutoCAD to draw a series of circles, which were printed out and photocopied to a transparency, and then a transparency was put on the screen of the shadowgraph. Circles of different radius on the transparencies were used to match the profile of the deformed sample and then the local curvature was obtained. Another method was as shown in Fig. 3.10, i.e., to set $L=300\text{mm}$ at a magnification $\times 50$ first, (for $3/4$ point bending $L=200\text{mm}$ and magnification $\times 10$ was used) and then d was measured by using a ruler on the screen. The local radius R value can be obtained by equation (3.2a) - (3.3b).

$$R_{ten}^2 = (R_{ten} - \delta_{ten})^2 + \left(\frac{L}{2}\right)^2 \quad (3.2a)$$

$$R_{com}^2 = (R_{com} - \delta_{com})^2 + \left(\frac{L}{2}\right)^2 \quad (3.2b)$$

$$R_{ten} = \frac{\delta_{ten}^2 + \frac{L^2}{4}}{2\delta_{ten}} \quad (3.3a)$$

$$R_{com} = \frac{\delta_{com}^2 + \frac{L^2}{4}}{2\delta_{com}} \quad (3.3b)$$

On the screen of shadowgraph, initially a ruler with a minimum interval of 0.5mm was first used to measure the value of δ and L . Because of the measurement error caused by the ruler minimum interval and the difficulty in keeping the operator sight and the line to be measured at a horizontal, a travelling microscope was then used

instead of a common ruler. The travelling microscope stands 2 metres away from the screen of shadowgraph and the height of the eye lens of the travelling microscope can be adjusted to keep the operator sight and the line to be measured at a horizontal. The minimum interval of the travelling microscope is 0.01mm, so the measurement accuracy was improved, but the efficiency of using travelling microscope is very low.

With this method, a small sample, which covers the entire length from cracking beginning to 100% scale removal, was cut from the 300 mm long steel rod ($\phi 5.5$ mm) after the cantilever bending test. A number of lines with 1 mm interval were then marked on the rod surface along the geometrical neutral plane. The rod sample was then placed on the stage of the shadowgraph machine for measuring local radius of the bent region. The stage of the shadowgraph machine is about 5mm by 100mm with a hole of 10mm diameter at its centre. It has a maximum magnification of 50. Two straight lines at right angle which cross the central point of the hole of the stage were drawn on the shadowgraph for use as reference lines in measuring the length and height of each arc section with the travelling microscope. For each sample, complete measurements were made for the entire length of the critical region, which is about 5 mm. Also, for each line section, three repeated measurements were made to reduce measurement errors. Therefore, it usually takes almost a half-day to complete the measurement of one sample. Also, since many manual operations are involved, significant errors are included in the data measurements.

When local radius R was obtained, equation (3.4a) or (3.4b) was used to calculate the tensile strain and the compressive strain.

$$\varepsilon_{ten} = \ln\left(\frac{R_{ten}}{d}\right) - \ln\left(\frac{R_{coil}}{d}\right) \quad (3.4a)$$

$$\frac{R_{ten} - \frac{d}{2}}{R_{coil} - \frac{d}{2}}$$

$$\varepsilon_{com} = \ln\left(\frac{R_{com}}{d}\right) - \ln\left(\frac{R_{coil}}{d}\right) \quad (3.4b)$$

$$\frac{R_{com} + \frac{d}{2}}{R_{coil} + \frac{d}{2}}$$

where R_{ten} is the local radius of the tensile surface (mm),

δ_{ten} is the height of the relative chord on the tensile surface (mm),

R_{com} is the local radius of the compressive surface (mm),

δ_{com} is the height of the relative chord on the compressive surface (mm),

d is the diameter of rod (mm),

R_{coil} is the radius of the coil from which rod was taken (mm).

Because the rod sample was taken from a coil, it had initial curvature, in equation (3.4a) or (3.4b), the apparent strain caused by initial curvature of the rod was subtracted.

3.4.2.3 Scanner method

Fig. 3.11(a) shows a schematic representation of the Cyclone scanner system (Renishaw plc.). This method was to use a Cyclone scanner to obtain the profile of a steel rod sample after the cantilever bending test. The scanner has a stylus “pen” which can move against the rod continuously. A rod sample was fixed on the horizontal stage. The movement of the “pen” gives the profile of the rod sample. The image of the rod sample was saved in the computer. Even though the “pen” has a small diameter, the computer itself processes the data before it forms the true image of the rod sample. The image scale was 1:1.

With this method, using the stylus scanning system, with technical specifications listed in Table 3.7 first scanned the profile of the bent rod sample. This can be finished in a few minutes. For example, for a 70mm long rod sample, it just takes about 5 minutes to finish the entire scanning of the rod profile. Fig. 3.11(b) shows the schematic illustration of the data evaluation of the scanner method. After scanning, the continuous profile of the rod was transformed into a geometrical image composed of many very short lines and arcs, and a data file including the co-ordinates of the points at the end of each line and arc was created within the computer. This data file was then analysed by using software, AutoCAD, to determine the local radius of the arc, the starting and end angles of the arc, or the co-ordinates and length of the straight line. For most of the regions of the profiles scanned, only two consecutive arcs were used as a group to obtain a local radius. For larger arcs, however, the computer tool for generating a circle with 3 points was used. The arc radius R_j , starting angle θ_{sj} and end angle θ_{ej} . were again calculated by AutoCAD automatically. In this way, the

relationship between local radius R_i and the distance from the fixed end of the sample (D_i) along the neutral plane can be built up continuously.

When $R_{i(ten)}$ is the local radius of the tensile surface, Equation (3.5) was used to calculate the distance along the neutral plane and from the fixed end of the sample

$$D_i = \sum_1^n \left(R_{i-1(ten)} - \frac{d}{2} \right) \times (\theta_{e(i-1)} - \theta_{s(i-1)}) + \frac{1}{2} \times \left(R_{i(ten)} - \frac{d}{2} \right) \times (\theta_{ei} - \theta_{si}) \quad (3.5)$$

where d is the diameter of the rod, and n is the number of the arc and line sections that are taken into account.

When $R_{i(com)}$ is the local radius of the compressive surface, Equation (3.6) was used to calculate the distance along the neutral plane and from the fixed end of the sample.

$$D_i = \sum_1^n \left(R_{i-1(com)} + \frac{d}{2} \right) \times (\theta_{e(i-1)} - \theta_{s(i-1)}) + \frac{1}{2} \times \left(R_{i(com)} + \frac{d}{2} \right) \times (\theta_{ei} - \theta_{si}) \quad (3.6)$$

Equation (3.4a) or (3.4b) was then used to calculate the tensile strain or the compressive strain. So the relationship between the real strain and the distance along the neutral plane and from the fixed end of sample can be established.

In order to check the reliability of the data manipulation of the scanner method, attempts have been also made to use one arc, three arcs or four arcs as a group to evaluate the local radius and strain.

3.4.3 Evaluating strains by the Finite Element Method

3.4.3.1 Introduction

In order to compare with the strain measured in the laboratory and to identify whether the neutral plane moves, finite element (FE) models are used to calculate the strain distribution of copper/steel rod in 4-point bending, cantilever bending and constrained bending. For 4-point bending test, several FE models are developed in

order to study the effects of the parameters used in the tests (u : the distance between the inner and outer rollers; s : the distance between the outer rollers) and materials on strain distribution. In these macro-FE models, oxide layers on the rod surface are ignored because scale is totally removed after bending for most steel grades. Because the FE models were developed on the base of commercial FE code MARCK7.2, the descriptions below follows the MARC programming sequence.

3.4.3.2 2D FE model of 4-point bending test

Mesh generation:

Fig.3.12 illustrates the basic model set-up. The mesh of a half of the specimen was generated because of the symmetrical loading about the specimen central axis. A series of 4-point bending FE model geometry were developed in order to study the effect of the distance between the inner and outer rollers (u) and the distance between the outer rollers (s) on the deformation of the specimen in a 4-point bending test. In the annual book of ASTM standards [1994], for the 4-point bending test (symmetrical loading), the standard setting is $u=s/6$, i.e. $s=90\text{mm}$, $u=15\text{mm}$, deflection $\delta=10\text{mm}$. For the 4-point bending FE models of the copper sample, the effect of the parameters u and s on the deformation of the sample was studied. The settings are $u=30\text{mm}$, $s=90\text{mm}$ and $\delta=10\text{mm}$; $u=20\text{mm}$, $s=80\text{mm}$ and $\delta=10\text{mm}$; and $u=15\text{mm}$, $s=90\text{mm}$, and $\delta=10\text{mm}$. For the 4-point bending FE models of steel rod sample, the effect of the parameters u and s on the deformation of rod sample was also studied. The setting of u , s and δ are $u=30\text{mm}$, $s=90\text{mm}$ and $\delta=10\text{mm}$; $u=20\text{mm}$, $s=80\text{mm}$ and $\delta=10\text{mm}$; and $u=15\text{mm}$, $s=90\text{mm}$, and $\delta=10\text{mm}$; $u=10\text{mm}$, $s=90\text{mm}$ and $\delta=8\text{mm}$. For the different FE models, the meshes are all made of four-node plane strain quadrilateral axisymmetric elements and the nearer to the rollers, the finer the mesh.

Boundary condition:

Because of the axisymmetry about the specimen central axis, for the half of specimen shown in Fig.3.12, x direction displacements are fixed for all the nodes at $x=0$, i.e. $u_x(0,y)=0$. And for the node at $x=0$, $y=0$, y direction displacement is fixed, i.e. $u_y(0,0)=0$.

Materials properties:

Because all of the 4-point bending tests were done at room temperature, for the materials properties used in the model, the temperature effect was ignored.

For steel rod samples:

Young's modulus, $E=207\text{GPa}$

Poisson's ratio $\nu=0.3$

Work-hardening curve see Fig 3.13

Here the work-hardening curve was obtained from a uniaxial tension test using $L_0/D_0=5$ tension specimen made from K08 steel rod ($\phi 5.5\text{mm}$). Three specimens were tested.

For copper rod ($\phi 6.5\text{mm}$) samples:

Young's modulus, $E=110\text{GPa}$

Poisson's ratio $\nu=0.3$

Work-hardening $\sigma=320\varepsilon^{0.54}$ ($\sigma_0=65\text{Mpa}$)

Contact

Here rod is deformable and rollers are all rigid. The loading roller moves down at a constant speed, such as 5mm/min . After a period of time, it moves up at a speed 1mm/min , which generates the release of the load. The contact tolerance is 0.0001mm .

Load case

Here solution control is Full Newton-Raphson.

The contribution of initial stress to stiffness is Full

Job

Here analysis options are Large Displacement and Updated Lagrange Procedure.

Result

Here the outputs are total equivalent elastic and plastic strains against arc length.

3.4.3.3 3D FE model of cantilever bending test

Mesh generation

Fig 3.14 shows a schematic representation of the finite element mesh in the 3D FE model of the cantilever bending test. The mesh element type is 3D solid 8 nodes hex. Here finer meshes are used near the two ends of the specimen and coarser meshes are generated in the middle and away from the critical area of the specimen.

Boundary condition

At the fixed end of the specimen, i.e. for all of the nodes at $z=0$, z direction displacement is zero, i.e. $u_z(x, y, 0)=0$. Because of symmetry about $y-z$ plane, x direction displacements are fixed as zero for all of the nodes at $y-z$ plane, i.e.

$u_x(0, y, z)=0$. At node $x=0, y=0, z=0$, y direction displacement is zero, i.e.

$u_y(0, 0, 0)=0$.

Materials Properties

The same materials properties as used in the FE model of the 4-point bending test were applied.

Contact

The load is applied by a cylinder whose centroid movement trace is a quarter of a circle. The cylinder continuously moves until a part of a circle with a constant radius is formed in the bent part of the rod. The bending is stopped by the release of the load by moving the cylinder in an opposite direction within a short time. The contact tolerance is 0.0001mm.

Load case, Job and Result

These were the same as those used in the FE model of the 4-point bending test.

3.4.3.4 2D FE model of constrained bending test

Mesh generation

Fig.3.15 illustrates the basic FE model set-up for the constrained bending test. Fine mesh is used for the whole specimen. Element type is same as the one used in the FE model of the 4-point bending test.

Boundary condition

At the fixed end of the specimen, for the nodes at $x=0$, x direction displacements are all zero, i.e. $u_x(0,y)=0$. For the node at $x=0$ and $y=0$, y direction displacement is fixed as zero, i.e. $u_y(0,0)=0$.

Materials Properties

The same materials properties as used in the FE model of the 4-point bending test were applied.

Contact

The rod sample is deformable. Cylinder A is rigid, motionless and keeps contact with the fixed end of the sample. Cylinder B is also rigid and contacts the other end of the sample. Its movement is just like the cylinder's movement in cantilever bending. Here the moving of cylinder B forces the sample to deform around cylinder A, which forms the constrained bending.

Load case, Job and Result

These were the same as those used in the FE model of 4-point bending test.

3.5 Characterisation of the effects of process variables

3.5.1 Objective

The following work is to assess the effects of manufacturing conditions for scale easy removal, i.e., to study the effects of laying temperature, ageing time, cooling condition, coil positions, and relative humidity and temperature on descalability by using the cantilever bending test.

3.5.2 Laying temperature test

K08-B, K08-C and K08-D steel rods supplied by SRM with three laying temperatures (950°C, 890°C and 830°C) were used in the test. The compositions and diameters of the steel rods are shown in Table 3.1. The tests were carried out in the laboratory at Sheffield University. At each laying temperature, three samples were tested from positions in the waps, which were random in relation to Stelmor cooling.

3.5.3 Ageing time test

K08-E steel rods provided by SRM with two laying temperatures 950°C and 890°C were used to study the ageing time effect. The composition and diameter of the steel rods are shown in Table 3.1.

For the steel rod with laying temperature 950°C, the bending tests for the effect of ageing time were carried out in the laboratory of SRM. The coil was at room temperature by the time the waps had been taken to the laboratory where the individual samples were prepared. For each ageing time, three samples were tested. The ageing time is ½, 1, 2, 4, 8, 16, 24, 48, 72, 96 and 120 hours respectively (Table 3.8).

For the steel rod with laying temperature 890°C, totally 12 waps were taken at the trimming stage at SRM. After marking the centre and edge positions of the coil (Fig. 3.16), each ring of steel rod was cut into four parts (Fig 3.17). The 1/2 hour ageing test was carried out in the laboratory of SRM, and the other bending tests were carried out in the laboratory at Sheffield University. Ageing times were 2, 4, 16, 24, 48, 72, 96, 120 hours, 15 days and 21 days (Table 3.8). At each ageing time, 5 samples were tested.

3.5.4 Cooling condition test

The steel rods K08-F supplied by CRM were cooled under 4 different conditions (Table 3.9). The tests were carried out in the laboratory at the university. For each cooling condition, 3 samples were taken from each of the two strands.

3.5.5 Positions in coil test

In coil position tests, two diameters of rods were used. The steel rod samples with diameter 5.5mm were cut from different positions of a ring of the waps supplied by SRM, such as: centre, near centre, near edge, and edge (Fig. 3.16). The composition of the steel rod (K08-F) is shown in Table 3.1.

Another diameter of steel rod (ϕ 14mm) provided by RRM was also used in the coil position tests. Their chemical compositions are shown in Table 3.1. The sampling positions were described in Section 3.2.3.

The scale thickness of the samples taken from different coil positions was measured. Fig 3.18 shows a schematic representation of 4 positions for scale thickness

measurement in rod samples. For each sample, measurement was made in 4 different positions, 1, 2, 3, and 4. For each condition, 5 small samples were tested.

3.5.6 Humidity and temperature test

Here, salt solutions were used to control the relative humidities of the atmosphere for steel rod. Distilled water, potassium sulphate (K_2SO_4), sodium chloride (NaCl), sodium iodide dihydrate ($NaI \cdot 2H_2O$) over-saturated salt and silica gel were used simulate 100%, 97%, 70%, 40% and 5% relative humidity respectively.

Salt solution preparation

Warm water (about $40^\circ C$) is used to make a salt solution. Salt is added until no more salt can be dissolved. When the water cools down to room temperature, the salt solution is over-saturated.

250mm long steel rod samples were cut from the coil with an initial curvature forming the coil diameter of about 1 metre. Several steel rod samples and a container of diameter 100mm with potassium sulphate over-saturated salt solution inside and a lid with many holes of diameter 2 mm in its top were put into a large desiccator. The desiccator and another sample were put into an oven in order to compare the effect of dry air with 97% relative humidity. The temperature of the oven is controlled at $30^\circ C$ and $46^\circ C$ respectively, and holding time is 0.5, 1, 2, 3, 4, 5, 7 days respectively. At each condition, one sample was tested. After a sample was taken off the oven, one end of the sample was fixed in a vice and another end was bent to 180° by hand immediately. Only potassium sulphate over-saturated salt solution was used to test the effect of relative humidity and temperature on descalability.

Distilled water, sodium chloride over-saturated salt solutions, sodium iodide dihydrate over-saturated salt solutions and silica gel were also used to study the effect of relative humidity at room temperature on descalability. At each condition, 3 samples were tested.

Only one grade of steel rod (K08, laying temperature $830^\circ C$) was used in the humidity and temperature test.

3.6 Scale characterisation techniques

3.6.1 Introduction

Oxide scale is very brittle. In order to keep it perfect without damage during the sample preparation, many sample mounting materials/methods have been tried, such as by using bakelite under high pressure, common resin in air, low viscosity resin under vacuum and Woods metal. In addition to SEM observation of scale cracking, its related techniques, such as EBSD technique was used to identify the multicomponent layers of scale and X-ray element mapping was applied to investigate the element enrichment in the scale/metal interface.

3.6.2 Optical metallography and scanning electron microscopy

3.6.2.1 Sample preparation

A small piece of rod sample was cut from the coil. Before being polished, the sample was mounted first to protect the scale from damage. All specimens were ground and polished using standard metallographic techniques, finishing with a 0.25 μm colloidal silica (Silco) polish. Optical specimens were observed using a Reichart-Jung Polyvar optical microscope. Scanning electron microscopy (SEM) was carried out using a Camscan Series 2 or a Jeol 6400 microscope.

For optical microscopy and SEM, small pieces of rod samples were mounted using different materials, such as conducting bakelite powder, epoxy resin, low viscosity resin and Woods metal. For the specimens mounted in the resins and used in the SEM, after being polished, they were ultrasonically cleaned to remove the debris which maybe be generated during sample polishing and trapped in the gap within the scale, and carbon coated in order to reduce charging in the microscope. Before being put into the sample chamber of the SEM, the specimens were painted with conducting silver from their top surfaces continuously to the bottom surfaces on one side of the samples and then put into a copper sample holder with a fastenable screw in its side. The screw was kept in touch with the painted side of the samples and fastened prior to inserting in the SEM. For EDS, X-ray element mapping and EBSD analysis, the specimens were mounted in Woods metal. After being polished with a 0.25 μm colloidal silica (Silco), the specimens were put into a small copper holder and then put

into the sample chamber of SEM – JSM 6400. X-ray element mapping was conducted in Hallam University using SEM-Philip SL40 with Link ISIS commercial software.

Mounting sample using a conducting bakelite powder under high pressure

First make sure that the compression is switched on. And then turn the water on. After place a small piece of rod sample face down on the top of the ram, lower the ram. Then cover the sample with bakelite (2 scoops for a 40mm diameter, approx. 1 scoop for 30mm), slide the top cover into place and screw down until tight. After release screw top by ½ a turn, rise the ram and set heating and cooling times (8 minutes heating, 4 minutes cooling). Then switch power on (red switch), press rocker switch to start process, and wait for the sequence of lights as well as the Buzzer to indicate the process has finished. After turn power off, low the ram and unscrew the top. And then raise ram and remove sample. Finally turn off the water.

Mounting sample by epoxy resin

A small piece of rod sample was put in a plastic holder. A mixer of epoxy resin and hardener in a proportion of 4:1 was poured in the holder. It was cooled in air until the resin was hard and then hand polished to 1/4 micron, carbon coated and observed under SEM – Camscan Series 2.

Mounting sample in low viscosity Epo-thin resin and Epo-thin hardener

After a small piece of sample was put in a plastic holder, an amount of the mix of Epo-thin resin and hardener in a weight proportion: 100:36 was poured in the plastic holder. Then the plastic holder was moved into a chamber with a vacuum switching on and off button on its lid. After being turned on for 10-15 minutes until no bubbles came off, the vacuum was released for a while to allow the low viscosity resin to be absorbed in the gap between the scale and substrate metal. And then the lid was removed. After a smaller amount of the mixer was filled in the plastic holder, the vacuum was switched on again until no bubbles were rising up from the resin. Then it was switched off again for a while. After the plastic holder was removed from the chamber, the mounted sample was cured overnight at room temperature or at 32-38°C cooled for 3-4 hours. Then the mounted sample surface was ground down to 2-3mm

and hand polished gently and carefully, or automatically polished to 1/4 micron. After carbon coating, it was observed under SEM – Camscan Series 2.

Mounting sample in Woods metal

A small rod sample was cut in the longitudinal direction. A small beaker was put in a large beaker, which contained water. A small amount of Woods metal whose melting point is 70°C was put in the beaker. The large beaker was put on an electrical heater to keep the water boiling. After being melted, Woods metal was poured into an aluminium holder who contained a small piece of steel rod. Then the Woods metal solidified rapidly at room temperature. After being polishing to 1 micron, the sample was polished in Silica, and washed by warm water, and then immediately put into the sample chamber of the JSM 6400 SEM.

3.6.2.2 Evaluation of scale thickness

Optical microscope method

For the laying temperature test and different coil position test, this method was used. A sample was mounted by low viscosity resin under vacuum. The technique was described in 3.6.2.1, and then the scale thickness was measured under an optical microscope ‘Olympus’ CH-2. For laying temperature tests, at each laying temperature, 5 samples were taken, and for each sample, measurements were made in 4 different positions, 1, 2, 3, 4, see Fig 3.9 the schematic representation of 4 positions for scale thickness measurement of the rod sample. For different coil position tests, small size samples were cut from FO, FM, FI, MAO, MAM, MAI, MBO, MBM, MBI, BO, BM, and BI positions respectively. These samples were mounted in epoxy resin in air. The technique was explained in 3.6.2.1. For each sample, measurement was made in 4 different positions, 1, 2, 3, 4 (Fig. 3.9). For each position, 5 small samples were cut.

Weighing method

For the test of different positions in a ring of coil, this method was used.

The weight of rod samples of about 200mm length was measured before and after shot blasting by using a weighing scale Osertling GC62, which has a minimum interval of 0.01g. Scale thickness was then calculated by the following equations.

$$\pi \times d_0 \times H \times h \times \rho_{ox} = w_0 - w_1 \quad (3.7)$$

$$h = \frac{w_0 - w_1}{\pi \times d_0 \times H \times \rho_{ox}} \quad (3.8)$$

where d_0 rod diameter before shot blasting (cm)

ρ_{Ox} average scale density (5.7 g/cm³)

H sample length (cm)

h scale thickness (cm)

w_0 sample weight before shot blasting (g)

w_1 sample weight after shot blast (g)

For the test of different positions in a ring of coil, 4 samples were taken from each of 4 different coil positions, such as: centre, near centre, near edge, and edge (Fig.3.6).

CHAPTER FOUR

RESULTS

4.1 Primary scale growth, microstructure, cracking and removal in 3-point bending test

Some phenomena that took place during the growth of the primary oxide scale on the flat sample surface in the laboratory furnace are described in Table 4.1. It was found that at 900°C without gas protection, the oxide scale separated from all of the sample surfaces when the samples were in the furnace. At 1000°C, even with gas protection, when heating time was 5min, the oxide scales separated from the sample surfaces when the samples were in the furnace. At 1000°C, without gas protection, when heating time was 2min, the oxide scale also separated from the sample surfaces even in the furnace. At 820°C×6min with gas protection, some oxide scale separated from the sample surfaces.

Fig. 4.1 shows the primary scale formed on the low carbon steel flat sample surfaces at 900°C in the laboratory furnace without gas protection. The holding time was 5min, 10min and 20min respectively. It was found that the primary scales (furnace scale) were loose, brittle, and easily separated from the sample surface. In addition to the cracking of the scale on the surface, some scale had spalled off the surface.

Cross sectional SEM (back-scattered electron image) examination of the scale on the flat sample surface (heated at 1000°C ×2min with gas protection and then cooled in air) revealed that the scale consisted of two layers (Fig. 4.2). The outer layer has a thickness of about 4.5µm and the inner layer has a thickness of about 75µm.

The first cracking of the scale on the low carbon steel flat sample surface in 3-point bending tests and the corresponding conditions are recorded in Table 4.2. Fig. 4.3 shows the scale cracking and removal behaviour of samples under different deflections in 3-point bending tests. It indicates that cracking first begins under small deflection (or strain) (Fig. 4.3a). As the deflection increases, some scale falls off the sample surface (Fig. 4.3b), and scale is removed from the sample surface on further increasing the deflection (Fig.4.3c).

4.2 Scale cracking and removal behaviour of commercial steel rods in 3-point bending test

The cross-sectional analysis of the scale on commercial steel K58 and K08 rod surfaces showed typical two-layer scale structures (Fig. 4.4). The outer layer has a thickness of about $6\mu\text{m}$ for K58 and $4\mu\text{m}$ for K08, and the inner layer has a thickness of about $28\mu\text{m}$ for K58 and $30\mu\text{m}$ for K08.

Fig. 4.5 shows the scale cracking and removal behaviour of D12 steel rod samples in 3-point bending tests (Table 4.3). It was found that the scale first cracked in the middle area of the sample where the loading rollers contacted with the sample surface. Then as the deflection (or strain) increased, the scale was removed around the middle area of the sample.

4.3 Scale cracking and removal behaviour of commercial steel rods in 4-point bending tests

The study of the effects of the parameters used in 4-point bending tests on the scale cracking and removal behaviour of K08 steel rod revealed that for this steel grade rod, even though the conditions under which the tests were carried out were different, there was one thing in common, which was the occurrence of plastic hinges in all of the tests (Fig. 4.6-4.8). When the deflection is small, scale cracks develop at uniform intervals. As deflection increases, the scale removal area extends from the inner roller-sample contact area to the middle of the sample. From Fig. 4.7, it was found that as the distance between inner and outer rollers decreased, the undeformed area of the sample increased and the plastic hinges can be seen more obviously. Fig. 4.8 suggests that the crosshead speed have no effect on the scale cracking and removal behaviour. Fig. 4.9 - 4.10 show the scale cracking and removal behaviour of R09 and K08+B steel grades in 4-point bending test respectively. The parameters used in the bending test were the same and plastic hinges formed for both steel grades.

During the bending test, it was found that the scale on the compressive surface began to crack and fall off first and then the scale at the tensile surface started to crack

and fall off the surface. The scale cracking behaviour can be divided into two kinds for the four grades of steel rods (K08, R09, B03 and K08+B): i) fine cracking can be seen on the sample surface, such as K08+B and K08, and the scale comes off in a powder state; ii) coarse cracking can be seen on B03 and R09 rod surfaces, and the scale comes off in a flaky state. In most of cases, cracking began from the sample area, which is near the inner rollers. Sometimes cracking first began in the sample middle area, and then concentrated on the sample area, which is near the inner rollers. During the plastic deformation, as the strain increased, there were few new cracks in the undeformed horizontal area of the sample, but the scale removal area extended gradually from the sample-inner roller contact area to the sample middle.

Fig. 4.11 is the scale cracking and removal behaviour of steel grade K58 rod in 4-point bending tests. Plastic hinges formed during the bending test, but they were not so serious as in steel grades B03, K08, K08+B and R09 rods. The scale comes off in larger flakes compared with K08 and K08+B steel rods.

Fig. 4.12 shows the scale cracking and removal behaviour of steel rod (ϕ 14), supplied by Roundwood Rod Mill, in 4-point bending tests. The scale comes off in larger flakes compared with K58 and R09 rods, and no plastic hinges formed for this mild steel rod.

Fig. 4.13 is the photograph of copper rod in 4-point bending test. It can be seen that copper rod deforms homogeneously in the area between two upper rollers, which means that there is no plastic hinge formed in copper rod in 4-point bending.

The variation of removed scale weight percentage with strain for steel grades K08, K08+B, R09 and K58, shown in Fig. 4.14 - 4.17, revealed that for a high carbon steel, such as K58, the scale was more difficult to remove than that of low carbon steel grades R09 and K08+B. For the low carbon steel rods R09 and K08+B, the scale on the low silicon steel grade R09 rod is easier to remove than that on the high silicon steel grade K08+B rod. For K08 and K08+B steel rods, there are two differences between them, which make the descalability of the steel rod different. One is without or with B element, the other is that the steelmaking processes are different, i.e. K08 is BOS steel and K08+B is EAF steel.

4.4 Scale cracking and removal behaviour of commercial steel rods in cantilever bending tests

Fig. 4.18 shows the side view (a), top view (b), and bottom view (c) of the scale cracking and removal of K08 steel rod samples under gradually increased strain (stage 1-3) in the cantilever bending tests. During the tests, when the load was applied, the rod sample deformed gradually. As the strain increased, the scale was removed from the rod surface continuously, i.e., scale began to crack when the strain was small and as the strain increased, cracking began to extend, and finally the scale fell off the rod surface. In the meanwhile, new cracking also formed further along the rod. It can be seen from the photographs that cracking forms in different ways on the tensile/compressive sides of the rod sample. Through-thickness cracking at a larger interval is formed under a small compressive strain. As the compressive strain increases, new cracking forms between the existing scale cracking and also forms further towards the loading end of the sample. A similar scale cracking process was observed on the tensile surface of the rod steel, except that the scale cracked under the tensile strain (stress). In other areas of the rod surfaces, except for the neutral plane, the cracking was formed in ± 45 angle with the geometrical neutral plane, where the shear stress was the highest. In some cases, it was found that through-thickness cracked scale was still attached on the tensile side of sample under high strain. By brushing by hand, the scale fragments could be easily removed from the rod surface.

In the cantilever bending test, the scale could be seen to crack and fall off the sample surface under tensile and compression stress conditions at the same time. It was found that the strain for initial scale cracking at the compressive side was slightly smaller than that obtained from the tensile side. From the tests, it was also found that for the similar strains applied, the scale removal degrees were similar, which means that the test results can be reproduced reasonably well and easily.

Unfortunately, there were 3 samples, which still had scale patches or islands on top or bottom surface after the cantilever test.

4.5 Scale cracking and removal behaviour of commercial steel rod in constrained bending tests

Fig. 4.19 – 4.20 show the scale cracking and removal behaviour of the samples supplied by Scunthorpe Rod Mill (K08 steel, $\phi 5.5\text{mm}$, laying temperature 830°C) in constrained bending tests before and after brushing. It can be concluded that for the rod samples, as the cylinder diameter increases, i.e. as strain decreases, the amount of residual scale islands left on the rod surface after constrained bending increases. From Fig. 4.20a, it can be seen that when cylinder diameter is 74mm, i.e. plastic strain is 6.5%, the scale can be removed totally from the rod top/bottom surfaces. When the cylinder diameter is 92mm, i.e. the plastic strain is 5.2%; the scale can be partially removed. When the cylinder diameter is 102mm, i.e. the plastic strain is 4.7%; most of the scale is left on the rod surface. From Fig. 4.19d and Fig. 4.20d, it can be found that when the cylinder diameter increases further, i.e. the plastic strain is less than or equal to 3.3%, the amounts of residual scale is almost the same before and after brushing, i.e. scale just begins cracking and is still attached to the rod surface even after brushing.

Fig. 4.21 shows the side view of the scale cracking behaviour of the rod samples with different scale thickness in constrained bending tests. It can be found that as laying temperature increases, or at the same laying temperature, as the cooling rate decreases, the cracking spacing increases, i.e. as scale thickness increases, the cracking spacing increases.

4.6 Strain measurement and computation

4.6.1 Scriber/shadowgraph methods for copper sample

Fig. 4.22(a) is the true strains obtained by the scriber and shadowgraph methods on copper sample showing that for small strain, the error of the scriber method is larger than that of the shadowgraph method. Even though many methods have been tried to measure the line spacing, the problem of large error still existed. Because for small strain, sometimes equipment error and operator error are in the same order as the strain. Fig. 4.22(b) shows the sums of tensile & compressive strains obtained by the scriber

and shadowgraph methods. For the shadowgraph method, the sum of tensile and compressive strains was near zero.

4.6.2 Shadowgraph/scanner methods for steel rod sample

Fig. 4.23(a)-(b) show the local radius and true strain measured by using the scanner method, together with those obtained by using the shadowgraph method. It can be seen that the results obtained by using the two methods are generally in good agreement. As the position along the neutral plane increases, the local radius gradually increases from a constant value (determined by the sample length and radius) to the initial coil radius, and that the absolute value of tension/compression strain decreases gradually from a constant value to zero. The critical strain for 100% scale removal is around 0.05 for tension and 0.04 for compression.

4.6.3 The repeatability and reliability of the scanner method

Once the Cyclone method had been selected to measure the strain, its reliability and repeatability were examined further. The reliability of the data manipulation of the scanner method, i.e. the local radius and strain evaluated by using one arc, three arcs or four arcs as a group, together with those obtained by using two arcs as a group, are shown in Fig. 4.24. This indicates that all results were in good agreement.

The relationship between the true strains and the position along the neutral plane obtained from three repeated measurements of one sample by using the scanner method, plotted in Fig. 4.25, shows that the repeatability of the scanner technique is quite good. In particular, the 95% confidence limit of the true strain is ± 0.0015 for the tensile surface and ± 0.0018 for the compressive surface, respectively.

4.6.4 Scanner method/FE modelling

Fig. 4.26 shows local radius and strains obtained by FE modelling and the scanner method. It reveals that at the critical area, i.e. from 100% to 1% scale removal area, the strains obtained by the scanner method and FE modelling are in good agreement.

4.6.5 Strain calculated for copper sample in 4-point bending

The relationship between the total equivalent plastic strain and the position along the neutral plane from the centre of copper rod in different settings of 4-point bending

tests shows that, for the setting such as $u=20/30\text{mm}$, $u=80/90\text{mm}$ and $\delta=10\text{mm}$, plastic deformation is uniform at the area between two inner rollers in the copper sample after the bending (Fig. 4.27a and Fig. 4.27b). But in the 4-point bending tests with the standard setting ($u=s/6$, i.e. $u=15\text{mm}$, $s=90\text{mm}$ and $\delta=10\text{mm}$) according to the annual book of ASTM standards (symmetrical loading), local plastic deformation at the sample-roller contact region is higher than at the other regions (Fig. 4.27c).

4.6.6 Strain calculated for steel rod in 4-point bending

Fig. 4.28 shows the strains calculated for K08 steel rod in 4-point bending tests with different settings. It was found that plastic deformation was uniform at the part of the sample between two inner rollers in Fig. 4.28a and Fig. 4.28b. But in Fig. 4.28c and Fig. 4.28d, the plastic deformation in the inner roller and sample contact area is much higher than in other areas, and plastic deformation is not uniform in the region of the sample between two inner rollers. Fig. 4.28 also shows that as the parameters (u , s and δ) change, the deformation degrees of the steel rod after the bending tests are different. For the same deflection δ and s , when u is large, the sample plastic deformation is small and plastic hinges don't form (Fig. 4.28a and Fig. 4.28b). On the contrary, for fixed δ and s , when u is small, sample plastic deformation is serious and plastic hinges form at the sample-roller contact area (Fig. 4.28c). For the same s , as u decreases, even though the deflection decreases, plastic hinge becomes more serious (Fig. 4.28d).

4.6.7 Strain calculated for copper rod in cantilever bending

The relationship between local radius/total equivalent plastic strain and the position along the neutral plane in Fig. 4.29 shows that the local radius and the plastic strain gradually change in the cantilever bending. From Fig. 4.29a, it can be seen that the local radius increases from a constant radius to infinite because the sample was bent to 90 degree in the model. From Fig. 4.29b, it is seen that the total equivalent plastic strain decreases from a constant value to zero.

4.6.8 Strain calculated for steel rod in cantilever bending

Fig. 4.30 shows the variation of local radius/total equivalent plastic strain with the position along the neutral plane. Compared with Fig. 4.29, the plastic strain of steel rod

after the cantilever bending is larger than that of copper rod, i.e. bending is more localised.

4.6.9 Strain calculated for steel rod in constrained bending

The local radius/total equivalent plastic strain is plotted as a function of the position along the neutral plane in Fig. 4.31 showing that the local radius increases from a constant value to infinite and the total equivalent plastic strain decreases from a constant value to zero. In the constrained bending, the sample was bent to around 180°, after release, the spring back of the sample was very limited.

4.7 Effects of processing variables

4.7.1 Laying temperature

The results expressed as the variation of the true strain for 1% and 100% scale removal with laying temperature that were evaluated for three samples are shown in Fig. 4.32. The results averaged for the three repeat samples (plus 95% confidence limit) described in Fig. 4.32 are shown in Fig. 4.33 and Fig. 4.34. It can be seen that with the increase of laying temperature, the critical strains for 100% scale removal at the tensile and compressive sides decrease significantly, and the critical strains for 1% scale removal also shows decrease. Here, 1% scale removal corresponds to the strain when the first cracking line can be seen on the rod sample surface by eye.

The effect of laying temperature on the scale thickness is shown in Fig. 4.35. This reveals that as the laying temperature increases, the scale thickness increases.

4.7.2 Ageing time

Fig. 4.36a shows the variation of the true strain for 100% scale removal with the ageing time, averaged for 3 samples (plus 95% confidence limits). For a laying temperature of 950°C. It suggests that ageing time has an effect on scale removal, but its effect is relatively small. There are some benefits in 8 and 120 hours ageing compared with 20-40 hours. But ageing time 8h, i.e. 8h after rolling, is not a practical time for industry.

Fig. 4.36b shows the relationship between the true strain for 100% scale removal and the ageing time, averaged for three samples (plus 95% confidence limits) for a laying temperature of 890°C. There are some benefits in ageing time 48 hours compared with the others. By comparing Fig. 4.36a with Fig. 4.36b, it found that for different laying temperatures, the time for better scale removal appears to be different.

4.7.3 Cooling condition

The effect of cooling condition on the scale thickness and the true strain for 100% scale removal (plus 95% confidence limits) is plotted in Fig. 4.37. Here, the true strain is averaged for 6 samples and the scale thickness is averaged for 9 samples. It can be seen that as the cooling rate decreases, the true strain for 100% scale removal decreases, and scale thickness increase. The steel rod samples for the cooling condition test were taken from Cardiff Rod Mill, where the rods were rolled is a two-strand mill. The steel rod samples surface colours for the two strands are different, even though they were taken from the same laying temperature and the same cooling process, but two strands. Fig. 4.38 shows the relationship between the scale colour and the average true strain for 100% scale removal in the cooling condition test, averaged for 3 samples (plus 95% confidence limit). It revealed that, except one cooling condition (laying temperature 870°C, fans on), as the scale colour became dark, i.e. from light to medium to red, the true strain for 100% scale removal decreased.

4.7.4 Positions in coil

The average scale thickness expressed as a function of coil positions is shown in Fig. 4.39. Here the symbols used were explained in detail in 3.2.3. No common trend can be found.

Fig. 4.40 shows the effect of the positions in one ring of coil on the scale thickness. It revealed that the scale thickness was slightly different at different positions in the coil, i.e. it is thinner at the centre of the coil than that at the edge of the coil.

4.7.5 Relative humidity

Fig. 4.41 illustrates the effect of relative humidity on the descalability of K08 steel rod. It can be seen that for the silica gel (Fig. 4.41a), as holding time increases, the

strain for 100% scale removal decreases. From Fig. 4.41b, it is found that the 40% relative humidity has an effect on the strain for 100% scale removal, but the effect is relative small. From Fig. 4.41c, it reveals that as holding time increases, the strain for 100% scale removal increases, until the fourth day, it reaches the maximum. After that day, as the holding time increases, relative humidity has no effect on the average strain for 100% scale removal. From Fig. 4.41b, for the 100% relative humidity, it can find the same trend as that shown in Fig. 4.41c. From Fig. 4.41e, for the 97% relative humidity, the holding time for the maximum strain for 100% scale removal is the third day. And, in general, the higher the oven temperature (at the same relative humidity), the higher the strain for 100% scale removal.

4.8. SEM results of scale cracking and removal behaviour

4.8.1 Oxide scale cracking in tension and compression

From the SEM micrograph shown in Fig. 4.42a, it can be seen that there are through thickness cracks within the scale. This sample was cut after 4-point bending test and observed in longitudinal direction on the tensile side. In Fig. 4.42a, a gap between the metal and scale can be seen.

From Fig. 4.42b and Fig. 4.42c, it can be seen there are 45° cracks within the scale under high magnification.

Fig. 4.43a shows the “wedge” formed at small strain in compression, and Fig. 4.43b shows the “buckling” formed at small strain in compression.

Fig. 4.44 shows a blister presented in the upper layer of the scale in compression.

4.8.2 Residual scale at different laying temperatures

Figures 4.45 shows the steel surfaces after descaling at three laying temperatures. For the samples taken at laying temperature 890°C, the steel surfaces observed under a low magnification, such as ×200, are clean after descaling. But under a higher magnification, such as ×430, some fine scales are still left on the surface. For the sample taken at laying temperature 830°C, under low magnification, scale patches can be seen on the sample surface after descaling.

4.9 EBSD analysis of scale structure

EBSD results are shown in Fig. 4.46. Fig 4.46a is the data collecting area used correspondingly in EBSD. Fig. 4.46b-4.46e identifies the scale layers on the K08 rod surfaces with laying temperature 950°C, laying temperature 890°C, laying temperature 900°C with fans off during Stelmor cooling and laying temperature 950°C with ageing 30 minutes respectively. At these conditions, the scale is composed of magnetite and wüstite. But hematite, which lies at the outer surface of the scale, is too thin to be detected by EBSD, so it cannot be shown in the EBSD maps. In Fig. 4.46e, magnetite is found to form at the interface of scale and metal and the grain boundaries of wüstite. The Kichuchi pattern of the residual scale left on K08 steel rod surface (LT 900°C, fans off, rod colour is red) is shown in Fig. 4.47a. By comparing with Fig. 4.47b, the standard Kichuchi pattern of magnetite, the residual scale is identified as magnetite.

4.10 EDS and X-ray element mapping results

Fig. 4.48a shows the EDS spot scanning results of the sample used for the cooling condition test (laying temperature 900°C, fans off, rod colour is red) within the metal, the scale and near the interface between the scale and metal. It is very clear that there is silica and chromium, a little copper and sulphur near the interface, but silicon cannot be found in metal or scale. Fig. 4.48b shows the spot scanning results of the sample used for the cooling condition test (laying temperature 870°C, fans on, rod colour is light grey) within the metal, the scale and near the interface between the scale and metal. It can be seen that there is no silicon, sulphur, copper, etc. detectable in the metal, scale and interface.

Fig.4.49a and 4.50a show the SEM micrographs of the scale layers formed on the rod supplied by Scunthorpe Rod Mill with laying temperature 890°C and on the rod provided by Cardiff Rod Mill with laying temperature 870°C, fans off, respectively. Fig. 4.49b and 4.50b show the elements mapping of the scale shown correspondingly in Fig.4.49a and 4.50a. For the sample taken from Cardiff Rod Mill, copper enriches in the interface of scale and metal and lies within the metal, and silica also enriches in the interface of scale and metal, but within the scale. For the sample supplied by

Scunthorpe Rod Mill, only silicon enriches in the interface of the scale and metal and is within the scale.

CHAPTER FIVE

DISCUSSION

5.1 The characteristics of primary scale

From the observations of primary scale formed in the laboratory, the evidence was convincing that furnace scale was brittle. Because of the different thermal expansion/contraction coefficients between the steel and scale, it is easy for scale to spall off the steel surface during the heating/cooling process. After reheating in air, cracked scale spalls off the sample surface more easily than that with gas protection (i.e. in natural gas), because the oxygen potential is lower. This has been already explained well in reference [Sachs and Tuch, 1967], so it is not discussed again here.

5.2 Evaluation of 3-/4-point bending, cantilever bending and constrained bending tests

The 3-point bending tests were carried out before the 4-point bending jig was ready for use. The distribution of bending moment in 3-point bending in Fig. 3.5 shows that the moment is largest in the middle of the sample and gradually changes from the middle to the two ends of the sample, i.e. in 3-point bending, the upper roller is at the position of highest stress. The contact of the upper roller with the sample surface makes the scale fracture mechanism in compression complicated.

The distribution of bending moment in 4-point bending in Fig. 3.6 shows that the moment is constant in the middle area of the sample between the two inner rollers, which can be used to study the relationship between the strain and scale removal. As soon as the 4-point bending jig was ready, the 4-point bending test was used to replace the 3-point bending test.

Unfortunately, because of the material yield point, a plastic hinge took place in most of the 4-point bending tests, i.e., rod sample began to deform locally in the area where the inner rollers contacted the rod sample and scale began cracking and spalling off the rod surface in the same area. There was no deformation in the constant strain

area, which was intended to be used to study the relationship between the scale removal and strain when 4-point bending was chosen to replace 3-point bending. Here the contact of the rollers with the sample surface also complicated the scale cracking and removal processes.

By comparing the FE modelling results with the experimental results of 4-point bending tests on K08 steel rod samples, it was found that they agreed with each other well for the setting such as $u=10/15\text{mm}$, $s=90\text{mm}$ and $\delta=8/10\text{mm}$ (Fig. 4.7a, Fig. 4.28c and Fig. 4.28d). But for the setting such as $u=20/30\text{mm}$, $s=80/90\text{mm}$ and $\delta=10\text{mm}$, there is a little discrepancy between them (Fig. 4.7a, Fig. 4.28a and Fig. 4.28b). The reason is that for the different setting of 4-point bending tests, as the distance between inner and outer rollers (u) decreases, the deformation of the rod sample becomes more difficult and friction plays a more important role during the sample deformation. But the friction between the roller and steel rod sample has not been considered in the FE modelling, therefore for the hard deformation setting of 4-point bending tests such as $u=10/15\text{mm}$, $s=90\text{mm}$ and $\delta=8/10\text{mm}$, because friction has larger effect on the sample deformation, there is a discrepancy between the modelling and experiential results without the consideration of friction in FE modelling. For the easy deformation settings such as $u=20/30\text{mm}$, $s=80/90\text{mm}$ and $\delta=10\text{mm}$, the deformation of the rod sample is more easier than that of the hard setting, and friction plays a less important role in the sample deformation. Even though friction hasn't been considered in FE modelling, the modelling results agree with experimental results well.

In order to calibrate the 4-point bending test, copper rod ($\phi 6.5$) was used in 4-point bending. By comparing the experimental results of copper rod with K08 steel rod for the same setting of the 4-point bending test ($u=20\text{mm}$, $s=80\text{mm}$ and $\delta=10\text{mm}$) (Fig. 4.13 and Fig 4.7a), it was found that because copper work hardened normally, the plastic deformation was uniform in the area between two inner rollers of the sample, i.e. there was no plastic hinge formed in copper rod after the bending. For the steel rod, a plastic hinge appeared in the upper roller and the rod contact area after the bending. By comparing the FE modelling results of the copper rod sample and K08 steel rod sample in the same settings of 4-point bending tests (Fig. 4.27(a)-(c) and Fig. 4.28(a)-(c) correspondingly), plastic deformation is uniform in the area of copper sample between

two upper rollers for the three settings, but for steel rod, when the setting is hard, plastic hinge formed in the steel rod sample.

At NPL, a 4-point bending test was used to study the failure of oxide scale formed on flat sample surface [Nagl, 1992]. Because the oxide failure generally occurred during elastic sample deformation or at the beginning of the plastic deformation, i.e. strains <0.5%, plastic hinges never formed in their bending tests. In order to avoid the influence of loading rollers, only a raft of oxide scale was left in the middle of one side of the flat sample surface, the rest of scale was removed before the bending test. This method was also tried in our 4-point bending test, but due to the plastic hinge, only the part of the sample near the upper rollers deformed after load was applied, the middle part of the sample was still undeformed, so 4-point bending was finally abandoned.

The distribution of bending moment in the cantilever bending in Fig. 3.7 shows that as the distance from the fixed end of the sample increases, the bending moment decreases, i.e. the strain and stress decreases. This is one of the advantages of the cantilever bending, i.e. the strain in the sample after cantilever bending gradually changes, which can overcome the plastic hinge occurred in 4-point bending. Another advantage of the cantilever bending is that it is a free bending, which can avoid the contact problem, which took place in 3/4-point bending. In the cantilever bending test, once a part of a circle with a constant radius is formed in the bent part of the rod, releasing the loaded end stops the bending. Therefore, there is always a transient region on the rod where the oxide scale undergoes initial cracking, crack development and complete removal from the rod surface. For the study of the scale cracking and removal mechanism, this makes it the best method, because the cantilever bending not only overcomes the disadvantages of 3/4-point bending, but it is also simple and easy to carry out in the laboratory or works.

In the cantilever bending test, the scale can be seen to crack and fall off the sample surface under tensile and compression stress conditions at the same time. It is also found that the strains for scale cracking at the compressive side are slightly smaller than that obtained for the tensile side. The reasons for this difference are because (1) most materials exhibit a volume expansion during oxidation, (2) the substrate steel contracts much more than scale during cooling [Huntz and Schüze, 1995], the residual

stress which formed between the scale and substrate during oxidation or cooling after rolling is compressive, which reduces the tensile stress to some degree and increases the compressive stress in the cantilever bending test. This agrees with the literature [Nicholls et al, 1997] that the oxide scale fails more easily in compression than in tension.

In Swinden Technology Centre of Corus group, tensile testing is used to remove the scale on the steel rod surface. Before the test, chemical pickling is used to remove the scale on the two ends of the sample in order to avoid the influence of the grips. This is also a good method to study the relationship between the strain and the scale removal percentage, but compared with cantilever bending, preparation of the standard tensile test sample is needed and the cost is high. Also during the mechanical descaling used in industry, the oxide scale is removed not only by pure tension but also by bending, so cantilever bending test is better than the tensile test for studying the scale removal mechanism.

In industrial mechanical descaling, the scale on the commercial steel rod surface is removed by reverse bending, i.e., the scale which is far more brittle than steel is peeled and removed by giving the rod surface tensile and compressive deformation produced by bending and reverse bending using two of rollers whose axes are perpendicular to each other [Tominaga et al, 1982]. In order to simulate industry mechanical descaling process further, constrained bending is used to remove the scale on the steel rod surface. In constrained bending, there is a spring back after releasing the load. For our laboratory bending, the sample was bent to nearly 180° around the cylinder, the plastic deformation is very serious, so the spring back is very small, but it is still visible. FE modelling results of 2D constrained bending also proved this (Fig. 4.31), i.e. the local radii before and after releasing the load in constrained bending are almost the same, but there is a difference in the total equivalent strain before and after releasing the load. Elastic strain of the order of 10^{-3} is released after releasing the load. From the observation of constrained bending, in tension, the scale cracking and removal behaviour is similar with in cantilever bending, but in compression, because of the contact of cylinder surface with the rod surface, the situation is different. Only one strain can be obtained in one constrained bending test, i.e. there is an area in the bent

sample where the strain is constant, which can be used to study the relationship between the tensile strain and through-thickness cracking spacing. From Fig. 4.19a/d and Fig. 4.20a/d, it can be seen that as the strain increases or the cylinder diameter decreases the cracking spacing decreases.

Summary

A cantilever bending test is the best bending test compared with 3-/4-point bending and constrained bending. First, it is free bending which can avoid the contact problem between upper rollers and rod sample in 3/4-point bending. Second, there is always a transient region on the rod after cantilever bending where the oxide scale undergoes initial cracking, crack development and complete removal from the rod surface, so there is no problem with deformation of a plastic hinge. Third, it is a faster way to obtain a series of strains in one bending test compared with the constrained bending where a series of strains can be achieved by bending the rod samples around cylinders with a series of diameters.

5.3 Comparison of the methods for evaluating strains

5.3.1 Comparison of strain obtained by scriber method and shadowgraph method on copper sample

The comparison of the true strain obtained by the scriber and shadowgraph methods on copper sample shows that for small strain, the error of the scriber method is bigger than that of the shadowgraph method (Fig. 4.22a). It can be seen that the random scatter involved in the scriber method is much larger than in the shadowgraph method. For the scriber method, the errors came from several aspects. First there is systematic error, because the sharpness of the point of the scriber and the force applied on the scriber when the lines are being drawn cannot be kept exactly the same every time, the depths and widths of the lines drawn by the scriber on the rod sample cannot be guaranteed to be equal to each other. It is also not easy to draw lines on the exactly top/bottom surface of the rod. When the rod sample is fixed in a vice, it is also difficult to keep the top/bottom line on the exact top/bottom position of the rod. The error is about 0-5°. Second there is measurement error. After the cantilever bending test, it is

difficult to focus on two lines on the deformed sample surface at one time by optical microscopy. If the angle is 10° , the relative error caused by the curvature of the deformation sample is 0.46%. Even though many methods have been tried to measure the line spacing, the problem of large error still existed. For small strain ($< 8\%$), sometimes equipment error and operator error is of the same order as the strain. The comparison of the sum of tensile and compressive strains obtained by the scriber method and shadowgraph method plotted in Fig. 4.22b indicates that for the shadowgraph method, the sum of tensile and compressive strains was near zero and can be ignored in practice. For the scriber method, the sum of tensile and compressive strains is not near zero, which maybe derives from the systematic errors. Another explanation is that the neutral plane may move during plastic bending, but from the results obtained by the shadowgraph method, this explanation is not possible. After comparison of the scriber and shadowgraph methods, the shadowgraph method replaced the scriber method.

5.3.2 Comparison of strain obtained by shadowgraph and scanner method on steel rod sample

The comparison of the true strain and local radius measured by the scanner and shadowgraph methods shown in Fig. 4.23(a) and (b) indicated that the results obtained by using the two methods are generally in good agreement. For the shadowgraph method, an enlarged image of the bent sample is projected on a screen and it can be assumed that there is no system error. The only error of the shadowgraph method comes from the measurement of the chord height and the line length. In order to improve the accuracy of the measurement, a travelling microscope was used to keep the eyesight with the measured line at one horizontal position. However, by the shadowgraph method, for each sample, complete measurements were made for the entire length of the critical region, which is about 5 mm, and, for each line section, three repeated measurements were made to reduce measurement errors. Therefore, it usually takes almost a half-day to complete the measurement of one sample. Also, since many manual operations are involved, significant errors are included in the data measurements. For the scanner method, there is no system error because the movement of the “pen” gives the profile of the rod sample. The image of the rod sample was

saved in the computer. Even though the “pen” has a small diameter, the computer itself processes the data before it formed the true image of the rod sample. There is also no measurement error, because the data file was analysed by using software, AutoCAD, to determine the local radius of the arc automatically, which avoids error caused by the operator. Sometimes, due to the discontinuity of the rod sample profile caused by the spallation of the scale or roughness of the rod sample profile caused by inhomogeneous deformation during hot rolling, the local radii at these special positions are far away from the real value and should be ignored during the data processing.

In order to check the reliability of the data manipulation of the scanner method, attempts have been also made to use one arc, three arcs or four arcs as a group to evaluate the local radius and strain. The results, together with those obtained by using two arcs, are shown in Fig.4.24. It can be seen that all results are in reasonable agreement.

The true strains obtained for three repeated measurements of the same sample by using the scanner method revealed that the repeatability of the scanner technique is good (Fig. 4.25). In particular, the 95% confidence limit of the true strain is ± 0.0015 for the tensile surface and ± 0.0018 for the compressive surface, respectively.

Compared with the shadowgraph method, the scanner method has proved to be a more accurate and efficient procedure for measurement of local radius and strain since much less time is needed for scanner measurement and data evaluation, together with its high accuracy of measurement, the scanner method has been used for the measurements of local radius and strains in the further tests.

5.3.3 Comparison of strain obtained by scanner method and FE modelling

In order to compare with the strain measured in the laboratory and also to identify whether the neutral plane moves after the cantilever bending, FE modelling is used to calculate the strain distribution in the rod sample after the bending.

Comparison of the local strain obtained by FE modelling and the scanner method shown in Fig.4.26 revealed that all results are in reasonable agreement. It can also be seen that at the critical area, i.e. from 1% to 100% scale removal area, the tensile strain and compressive strain values obtained by the scanner method and FE modelling are

nearly the same. So at this area, the neutral plane can be assumed to be still at the geometrical middle plane.

5.3.4 Comparison of the strains evaluated by the scanner method in cantilever bending and calculated in constrained bending tests

Fig. 5.5 shows the comparison of the strains calculated after constrained bending and measured by the Cyclone scanner after cantilever bending. In constrained bending, the tensile strain is calculated by the following equation:

$$\varepsilon = \ln\left(\frac{D+2d}{D+d}\right)$$

where d is the diameter of the rod sample (mm), D is the diameter of the cylinder (mm). It is a true strain in the bend. For the strain evaluated by the scanner method in cantilever bending is true strain also, the middle point of the arc is defined as the local point, whose local radius is the arc radius. In general, the length is around 5mm, so there is a small discrepancy between the strains evaluated by the scanner method in cantilever bending and calculated in constrained bending on the sample taken from the same condition. Another aspect causing the discrepancy between two methods is that in constrained bending tests, the definite numbers of cylinders used limits the accuracy of the strain for 100% scale removal. For an example, for K08 steel rod with the laying temperature of 830°C, when the cylinder diameter is 74mm, the scale can be totally removed from tensile/compressive sides of the rod; when the cylinder diameter is 92mm, 50% scale can be removed from tensile/compressive sides of the rod. So the cylinder diameter used to remove 100% scale should be somewhere between 74 and 92mm. But in the laboratory constrained bending tests, only two diameters of cylinder were used. So in order to know the exact strain for 100% scale removal, the interval between the cylinder diameters should be decreased. It is difficult to say how narrow the gap between the cylinder diameters should be for accurate estimates.

5.3.5 Summary

Four methods: the scribe method, shadowgraph, Cyclone scanner and Finite Element methods have been used to obtain the strain after the cantilever bending. Among them, the scribe method is a classic method used to determine the strain after deformation. It is the simplest way to obtain strain, but for small strain, the error is of

the same order as the strain. For the shadowgraph, it is used to obtain the local radius of the rod sample. At high magnification, it is accurate, simple, and easy to use, but time consuming. For the critical area, such as from 100% to 1% scale removed area, the local radius changes sharply, the Cyclone scanner is accurate and quicker. Strain calculation by FE modelling of the cantilever bending shows that the simple assumptions used to relate radius and local strain in the above methods are valid.

5.4 Comparison of the methods used for sample preparation for metallographic examination

Because the scale is very brittle, it is easy to cause some damage on the scale during sample mounting and polishing. For the method of mounting a sample using a conducting bakelite powder under high pressure, the pressure in the radial direction may cause through thickness cracking during the sample preparation. For the method of mounting a sample in epoxy resin, during the mixture of the resin and hardener, the air is absorbed in the mixer. And because the high viscosity of the resin, it is difficult for the resin to fill in the gap between the scale and metal substrate caused by sample cutting. Mounting a sample in a mixer of low viscosity Epo-thin resin and Epo-thin hardener under vacuum overcomes the disadvantages of the above two methods, but samples mounted in resin are not favoured for SEM. Finally Woods metal is used as the mounting material. And the sample cutting surface was ground down 2-3mm. During polishing, the polishing direction is very important. For the longitudinal section, it is better to keep the sample longitudinal direction following the polishing wheel rotation direction to avoid scale damage, such as through-thickness cracks.

5.5 Comparison of the scale thickness measurement methods

The scale thickness shown in Fig. 4.35 was measured by optical microscopy, and the scale thickness shown in Fig. 4.37a was measured by the weighing method. The accuracy of these two methods both depends on the numbers of the sample taken for one condition. The more samples were measured, the higher the accuracy. For the first method, the preparation of the sample plays a key role in the measurement accuracy

because it is important to keep the scale without damage and to eliminate the gap between the scale and metal substrate. If the gap between the scale and metal is taken into account in the scale thickness measurement, the scale thickness obtained is larger than its real value. Compared with the first method, the second method is much simpler because the scale thickness is calculated by the weight difference before and after shot blasting. During the shot blasting, there may be some metal losses, which would cause error in the scale thickness, the scale thickness obtained being larger than its real value. Optical microscopy method and weighting method have been used to measure the scale thickness of the same sample on the same area. In general, the data from two methods agree with each other well.

In Swinden Technology Centre, the scale thickness was evaluated from the weight difference before and after chemical pickling. Because there is a minimum metal loss during the chemical pickling due to the careful control of the pickling time, the scale thickness obtained by this method is more accurate than the above two methods.

5.6 Scale fracture mechanisms at room temperature

Under external load, the stress is transferred to the scale from the substrate, and the stress distribution on the rod sample varies in 3 dimensions, the scale cracks and is removed first at the places where the critical strain for scale cracking and removal is satisfied. Because for the stress distribution on the rod shown in Fig. 5.1, only at the top/bottom surface, it is pure tensile/compressive stress. During the laboratory bending tests of steel rods, which includes 4-point bending and cantilever bending, it can be observed that oxide scale is brittle at room temperature and first cracking forms within the elastic limit of the steel grades or at the beginning of plastic deformation. It is also found that the cracking of the oxide scale occurs earlier in compression than in tension.

In tension, the first through-thickness crack forms at the places with highest stress concentration (Fig. 5.2b). The critical strain for scale failure at room temperature depends on the defects size and surface fracture energy (Table 5.1). As soon as the through-thickness crack formed, the stress will relax in the immediate crack area and the distribution of the stress within the oxide scale and also along the oxide/metal

interface changes significantly. The in-plane stress must reduce to zero at the crack faces because the stress cannot be transmitted across these places. Without relaxation, this tensile stress will increase as the distance from the crack face increases and will, due to symmetry, reach a maximum value midway between cracks. Then new cracks will tend to form in this location (Fig. 5.2c). For the same scale thickness, the spacing of through-thickness cracks is uniform and large when the strain is small, and as the strain increases, the new through-thickness cracks form midway between the existing cracks and the spacing of the through-thickness cracks is still uniform but decreases. However, scale thickness also has an effect on crack spacing. It has been shown that the thicker the scale, the larger the cracking spacing (Fig. 4.21). At the same time, the formation of such tensile cracks will also introduce shear stresses along the oxide/metal interface because within the scale fragment the strain distribution significantly relaxes the level of deformation of the oxide scale compared with the surface layer of the metal [Nagl, 1992]. If there is no stress relaxation, these shear stresses will be highest at the edges of the tensile cracks. It is these stresses that keep the islands of oxide in their stretched position [Evans et al. 1994&1995]. These shear stresses can be relaxed by interface cracking and spallation of the scale fragment when the strain increases to a critical level (Fig. 5.2d and 5.2e). But at room temperature, the brittle oxide scale can only occur elastic deformation before fracture and metal substrate can take place plastic deformation before fracture, according to fracture mechanics, the critical scale islands spall off the rod surface by tensile stresses which are produced by the bending moment (Fig 5.3 mode I). This is also proved by FE modelling (Appendix), so the spallation of a portion of the oxide scale requires the development of through-thickness cracks and also decohesion at the oxide/metal interface [Nicholls et al, 1997]. This mechanism is schematically shown in Fig. 2.4, which was found by Nagl [1992] in the failure of nickel oxide scale in tension by 4-point bending tests. FEM simulation (Appendix) of the scale cracking behaviour in tension also shows the same mechanism (Fig. 4 showing the through-thickness cracking in scale and Fig. 6 showing the shorter the scale fragment, the easier to remove it). Furthermore, the inner sub-layer of multi-layer oxide scale can adhere the metal surface after cantilever bending while the upper, brittle sub-layer is spalled due to delamination within the scale. This phenomenon has been found in the samples supplied by Cardiff Rod Mill with the cooling condition by

turning off all of the fans in the Stelmor process, i.e. a thin layer of magnetite (below $1\mu\text{m}$) identified by EBSD (Fig. 4.46) is left on the descaled rod surface. The FEM result (Fig. 5 in Appendix) also reveals this mechanism.

From the observation of oxide scale cracking and removal on the compressive side during 4-point bending or cantilever bending, it can be found that the scale failure is similar to that in tension from a macro-view, i.e. during the bending, when the compressive strain is small, the spacing between through-thickness cracks is large, and as the compressive strain increases, new cracks are formed between the existing cracks and the crack spacing decreases until scale islands spall off the rod surface. However, the mechanism of oxide scale failure in compression is a more complicated than that in tension. In general, from the viewpoint of fracture mechanics, scale fails in mode II, shown in Fig. 5.3, but there are two kinds of failure modes, which depend on whether the scale/metal interface is strong. When the scale/metal interface is weak, such as when there are pre-existing defects (Fig. 4.43) or sulphur segregation, buckling of the oxide may become easier in compression (Fig. 5.4b and Fig. 9 in Appendix). This mechanism is preferred by thin oxide scale. When the oxide scale is relatively thick, the oxide/metal interface is strong, i.e. the adhesion at the oxide/metal interface is good, and through-thickness shear cracks may form from pre-existing defects or due to failure of oxide following the slip systems of the underlying substrate next to the interface because of the interface constraint (Fig. 5.4a and Fig. 8 in Appendix). Further increasing the compressive strain then induces the development of a tensile wedge cracks at the oxide/metal interface. Spallation occurs when the growth of this crack becomes unstable or when it meets another crack growing in the opposite direction (Fig. 8 in Appendix). Other sources of initiation of through-thickness cracking under compression are convex sites on the metal surface. At these sites, the oxide scale is lifted from the metal and because the scale is brittle, through-thickness cracking is initiated (Fig. 5.4c). These mechanisms were identified by Nagl [1992] in iron oxide and nickel oxide failure at room temperature.

In the area near the neutral plane, it is found that the scale cracks formed $\pm 45^\circ$ to the neutral plane at the places where the shear stress is a maximum. This crack pattern can be attributed to shear deformation or failure of the oxide following the slip systems

of the underlying substrate next to the interface because of the interface constraint. The affected oxide area either buckled at higher strains or showed shear cracks within the oxide along which the oxide was wedged out.

Kendall [1978] regarded brittleness as a size-dependent concept. A critical scale thickness h_c is calculated from the yield stress σ_y below which the oxide does not fail by cracking, but in a ductile manner at high temperature. However, for this project, scale cracks and fractures at room temperature. So it cannot be used to explain why few scale patches still left on descaled rod surface at room temperature. There is a reason that can explain why scale islands are left on the metal surface. This is when the stress in the oxide scale is higher than the substrate yield stress, but less than its fracture stress, or the stress in the substrate can continue to increase, but the stress in oxide scale is still higher than the substrate work-hardened stress, but less than its fracture stress, the scale islands can still keep their continuity and attach on the substrate surface without further breaking.

5.7 Factors affecting the descaling properties

Table 5.1 summarises the critical strains for scale failure under tensile and compressive stress. From the equations listed in Table 5.1, it can be seen that the parameters, such as Young's Modulus, E_{ox} , oxide surface energy, γ_{ox} , or oxide/metal interface energy, $\gamma_{interface}$, and scale thickness, h , etc. play important roles in the prediction of scale failure. In industrial production, these parameters are determined by the steel grades, rod surface roughness, manufacturing conditions such as laying temperature, cooling condition, environmental humidity, etc..

While the billet passes through many stands, scale is repeatedly formed and peeled [Tominaga, 1982]. Therefore laying temperature and cooling rate have the largest effect on the formation of the residual scale.

5.7.1 Laying temperature

From Fig. 4.35 and Fig. 4.37a, it can be seen that as laying temperature increases, the scale thickness increases, even though the data in Fig. 4.35 were obtained from the samples supplied by Scunthorpe Rod Mill and the data in Fig. 4.37a were obtained from

the samples supplied by Cardiff Rod Mill. By comparing the experimental results in Fig. 4.34, Fig. 4.36 and Fig. 4.37b, it can be found that the laying temperature (scale thickness) has a larger effect on descalability than that of cooling condition or ageing time. From the literature, it is known that oxide scale often displays brittle characteristics, at least at intermediate and room temperature [Crouch & Dooley 1976, Hancock & Nicholls 1988, Nagl et al 1963 & 1993, Schütze 1991, Banks et al 1994] and brittleness is regarded as a size-dependent concept [Schütze, 1995], Fig. 4.34 shows this again, which illustrates that as laying temperature increases, the strain for 100% scale removal decreases, i.e. the higher the laying temperature, the easier the descaling. But too high laying temperature also leads to metal losses that are not what the wire industry wants. From the equations for the critical strain for spallation in compression (Route I) and for the through-scale cracking in tension that are listed in Table 5.1, it can be seen that as scale thickness increases, the strain for scale spalling or cracking decreases, i.e. the thicker the scale, the easier the removal of the scale.

5.7.2 Cooling condition

In this project, the samples except those supplied by Roundwood with a diameter of $\phi 14\text{mm}$ which were cooled by the conventional cooling process, the others, no matter whether supplied by Scunthorpe Rod Mill or Cardiff Rod Mill, were all cooled in the Stelmor process with the cooling rate being controlled by the numbers of fans turned on or off and the travelling speed of the conveyor.

In conventional cooling, the cooling rate is slow, so the scale grows quickly and is thicker.

In the Stelmor process, the wire rod is laid via the laying tube in non-concentric rings on moving conveyor chains rather than into the reel as a compact coil. Thus the single rings are separated and cooled faster in a controlled manner in several consecutive zones by adjustable air volumes. With the conveyors at full speed and with the highest air volume, 5.5mm-diameter rod is cooled between 800 and 500°C at 20°C/s. By shutting off the air and with the conveyor moving slowly at 0.2m/s, the cooling speed is decreased to about 4°C/s [Beck, 1981]. By reason of this range, the Stelmor process in its standard form makes it feasible to adjust the structure and mechanical properties of the wire rod to the demands of processing to a great degree.

Two phenomena may happen during the cooling process. One is the scale thickening, another is phase transformation such as from wüstite to magnetite. For the sample supplied by Scunthorpe Rod Mill, the cooling rate in the Stelmor process from 700°C is 13°C/s at the centre and 7°C/s at the bunched edges. At this cooling condition, Fe₃O₄ has not been found at the scale/metal surface. The higher the laying temperature, the cleaner the descaled rod surfaces. For the samples supplied by Cardiff Rod Mill, for the cooling condition with all fans off in the Stelmor process, Fe₃O₄ formed by the transformation of wüstite is found by EBSD at the boundary between the scale and metal on the descaled rod surfaces with laying temperature 870°C and 900°C. The transformation from FeO to Fe₃O₄ at the interface between scale and metal relaxes the residual stress at the interface [Tominaga, 1982] and worsens the descalability of the steel rod. After descaling, a very thin layer (less than 1µm) is left on the rod surface.

By comparing Fig. 4.34 and Fig. 4.37b, it can be revealed that at the same laying temperature such as 870°C or 900°C, because the cooling conditions for the samples supplied by Scunthorpe Rod Mill and Cardiff Rod Mill are different, the scale thickness for these samples is different (Table 5.2). Therefore the strains for 100% scale removal are different (Table 5.3). In Scunthorpe Rod Mill, the cooling rate in the Stelmor process from 700°C is 13°C/s at the open centre and 7°C/s at the bunched edges, but in Cardiff Rod Mill, the starting cooling temperature is not known, and the scale thickness of the rod samples supplied by two rod mills are measured by two different methods, which have been discussed in section 5.5. Because, first, the differences between the scale thickness of the samples supplied by two rod mills with the same nominal laying temperature but different cooling rate are very small, and second, there are many uncertainties involved between the two rod mills, it is difficult to draw any conclusions about the effect of the cooling rate on the scale thickness based on these samples.

However, for the samples supplied by Cardiff Rod Mill and taken from the same laying temperature, but different cooling conditions, except that phase transformation may take place at a certain cooling rate, if cooling rate is large, scale thickness increases less; if cooling rate is small, scale thickness increases more (Fig. 4.37a). By comparing Table 5.3 with Table 5.2, it shows again that the thicker the scale, the smaller the strain

for 100% scale removal no matter the scale thickness increases due to higher laying temperature or low cooling rate.

5.7.3 Steel grade

The effect of steel grades on descalability was studied by 4-point bending tests at the beginning of the project.

By comparing the deformation of the different steel grade rods in 4-point bending tests (Fig.4.6, Fig. 4.9-4.12), it can be found that because of the different work hardening of the materials, the extent of the plastic hinge formed on the rods is different. For the same diameter rods, the plastic hinge of low carbon steel rods (K08, R09, B03, etc.) is more serious than that of high carbon steel rod (K58). For different diameter rods, the plastic hinge of large diameter rod ($\phi 14$, mild steel) is less serious than that of small diameter rod (K58, high carbon steel) even though their carbon contents are different (Table 3.1). For cold wire drawing, the softer the material, the more appreciated because of the consideration to keep energy consumption, die wear and the work hardening of materials as low as possible. Comparison of Fig. 4.14-4.17 also illustrates the effect of chemical composition and steelmaking process on descalability. From the literature, the descalability of high carbon or high silicon steel is worse. Here the percentage scale removed from R09 rod (low silicon and low carbon steel) after bending is higher than that of K08+B rod (high silicon and low carbon steel), and the percentage scale removed from K58 rod (high carbon steel) is lower than that of R09 and K08+B rods (low carbon steel), i.e. the experimental results agree with the literature. By X-ray element mapping (Fig. 4.48b), silicon was found in the interface between the scale and metal but within the scale side on the descaled K08-F rod sample surface. It is believed that silicon forms the liquid phase fayalite ($2\text{FeO}\cdot\text{SiO}_2$) at temperature above 1170°C , which binds the innermost layer of the scale to the steel surface and worsens the descalability [Sachs & Tuck, 1967, Marston, 1995 and Asai et al, 1997]. This implies that the primary scale could not be totally removed by the first hydraulic descaling, and an inner residual scale is left which is “glued” to the surface of the metal. This residual scale oxidises further to form the secondary scale, and in this case, there is no gap between the secondary scale and metal, which means that the secondary scale could not be removed totally even by a second hydraulic

descaling. Then tertiary scale forms further from this residual scale. After mechanical descaling, it still cannot be removed totally because this inner glued layer.

In wiredrawing applications, electric arc furnace (EAF) steels are increasingly being used for products previously supplied by BOS (basic oxygen steel) [Franks, 1997]. With the right steelmaking equipment, and iron sources, there is almost no restriction to the grades, which can be replaced by electric arc steel. The use of a wholly scrap-based furnace charge does have limitations, but these are increasingly being overcome in the commercial wiredrawing markets. The main disadvantage of a scrap-based route as opposed to BOS is as follows:

- The scrap-based route generally produces higher levels of residual elements in the steel, which makes the descaled rod surface of EAF steel appear significantly dark compared with the bright surface of descaled rod of BOS steels. For EAF steel, scrap is used as raw material, the residual element such as Cu is high in the steel. X-ray element map study (Fig. 49b) found that Cu enriched in the interface between the scale and metal substrate and within the metal substrate side, which makes the descaled rod surface look dark red in colour. This is because iron oxidises to form scale first, leaving Cu in the metal substrate.

For the EAF steel rods K08-A supplied by Scunthorpe Rod Mill and K08+B supplied by Cardiff Rod Mill, they are low carbon and high silicon steels and the only difference is with and without boron. For K08-A, it is without boron, for K08+B, it is with boron. Franks [1997] studied the effect of boron on the properties of electric arc-sourced plain carbon wiredrawing qualities, including the descalability, and found that:

- Boron treated electric arc steel can be used to successfully replace BOS steels in low carbon drawing application.

- Boron addition to electric arc drawing quality rods has been shown to be effective in reducing rod strength, reducing work hardening rate and reducing strain ageing.

- Boron treated electric arc steels with relatively high residual levels can give drawing behaviour similar to BOS steels, providing other factors such as internal cleanliness and surface quality are also controlled.

- Dark sub-scale films on high residual steels can be reduced by the careful control of cooling conditions in rod cooling.

5.7.4 Position in the coil

For the samples supplied by Roundwood Rod Mill, they were taken from different positions of the coil. In Roundwood Rod Mill, the conventional cooling process is used. The coil is cooled by the air blown in the centre of the coil from the bottom. From Fig. 4.39, it is found that the scale thicknesses of the samples taken from the different levels and different positions of the coil are different. Because the temperature distribution is very complicated, it is difficult to draw any conclusion.

For the samples supplied by Scunthorpe Rod Mill and Cardiff Rod Mill, they were cut from the waps that were trimmed from the back end of the coil. In order to know the effect of the positions in a ring of the coil on the scale thickness, centre and edge positions were marked in a ring before sample cutting, and samples were cut from the exactly symmetry positions of a ring in order to keep the same sample temperature distribution. Samples were taken from four positions in a ring (Fig. 3.16). From Fig. 4.40, it can be found that the scale thickness at the edge of the coil is higher than that at the centre of the coil. This agrees with the temperature distribution of coil in the Stelmor process.

On the other hand, even though there is a difference between the scale thicknesses of the samples taken from different positions in the coil, from Fig. 4.40, it can be found that the difference is not very large and it is in the same order of the 95% confidence limit of five samples with four measurements on each sample.

In general, the position of the sample taken has an effect on the scale thickness, but in the Stelmor process, the position effect is not very large, and at one condition, if the number of samples taken is large enough, the error caused by the position difference will be reduced and can be ignored.

5.7.5 Ageing time

Fig. 4.37 shows the effect of ageing time on descalability, it can be seen that ageing time has an effect on the strain for 100% scale removal, but the effect is relatively small. From the figure, it also can be seen that the curves are wavy. In fact,

these results may involve the effect of humidity, because the ageing time tests were done in the open air in the laboratory in December 1999 and lasted nearly one month's time in the winter. From the weather forecast data, the relative humidity was around 70% on the average for that period, but its relative difference within one day could be 20-30%, such as, when it was raining, the relative humidity was about 70%, when it was not raining on the same day, the relative humidity was around 50-60%. Of course the wire rods were stored inside the building of the workshop, there might be difference for the relative humidity inside and outside, but the relative humidity inside of building is influenced by weather outside. Furthermore, ageing at room temperature just could relax a very small part of the residual stress, which formed during the cooling of the rod and was relatively small in our case. So the relative humidity could account for the wavy nature of the data in ageing time tests.

5.7.6 Humidity and temperature

Fig. 4.41 shows the effect of relative humidity on the strain for 100% scale removal. Humidity changes the scale property such as Young's modulus E and furthermore changes the critical strain of scale failure. When the relative humidity is high, water vapour diffuses into the porosity of the scale, softens and roughens the scale, i.e. reduces the brittleness of scale and increases the critical strain of scale failure. However, when the relative humidity is low, such as in silica gel of 5% relative humidity (Fig. 4.41a), the dry environment makes the scale become more brittle and easier to remove.

The effect of porosity on Young's modulus E was studied by Spriggs [1961], Wang [1984] and Phani [1986] and can be represented by semiempirical formulae such as

$$E = E_0(1 - p)^3 \quad (5.1)$$

and Rice [1977] reviewed the above equation as follows

$$E = E_0 \exp(-bp) \quad (5.2)$$

where E_0 is the modulus of the fully compact solid, p is the porosity, and $b \approx 3$. Birchall et al. [1981] have shown that when porosity consists of both large and small pores, the small pores reduce E as in equations (2.43) and (2.44) and the large pores act

as flaws or stress concentrators and weaken the materials towards fracture. From the above equations, it can be concluded that as porosity decreases, Young's modulus increases, according to the equations in Table 5.1, the critical strain for scale failure decreases. From this viewpoint, the phenomena reflected in Fig. 4.41 can be explained as follows: by comparing Fig. 4.41d and e, for the almost the same relative humidity, when the environmental temperature is lower, vapour diffuses more slowly, and it needs more time to fill in all of the porosity of the scale. From Fig. 4.41d, it is found that it needs 4 days to reach the maximum strain to remove 100% scale. As holding time increases, the descalability of the steel rod becomes worse, but there is a critical value, when all of the porosity of the scale is full of water vapour. Any more holding time does not have any effect on descalability. When the environmental temperature is higher, the water vapour diffuses faster. As the holding time increases, it needs shorter time to fill in all of the porosity of the scale. So the critical time is shorter than that at lower environmental temperature. In Fig. 4.41e, it needs 3 days to reach the maximum strain to remove 100% scale. After the porosity is saturated by water vapour, any more holding time does not further affect descalability. For Fig. 4.41e, only one sample was taken for each condition, so it is difficult to draw any conclusion about the significance of differences between the curves. However, from Fig. 4.41 a-d it is clear that after 5 days holding at room temperature, increasing humidity has a deleterious effect on descalability. The relationship between relative humidity and true strain for 100% scale removal after holding 5 days is drawn in Fig. 5.6, it can be found that as relative humidity increases, the true strain increases, which means that the descalability decreases.

CHAPTER SIX

CONCLUSIONS AND FUTURE WORK

6.1 Conclusions

In the laboratory, bending techniques to remove the scale on wire rod of commercial steels have been developed. Assessment of local strain has also been carried out. The factors influencing descalability have been investigated. Post metallographic examinations have been conducted to establish the failure mechanism operating in the scale.

The main conclusions are:

1. 4-point bending could be used to study the initial scale cracking behaviour, but could not be used to study the removal of the scale from the surface of the steel rods used in this project because plastic hinges formed in 4-point bending tests.
2. The cantilever bending test could be used effectively to study scale cracking and removal behaviour.
3. Compared with the scribe and shadowgraph methods, the Cyclone scanner method was more accurate and efficient in the evaluation of the critical strains for scale cracking and removal.
4. The critical strain for 100% scale removal was in the range 4-8%.
5. FE models calculating the strain distribution of the rod sample after 4-point bending, cantilever bending and constrained bending tests were developed. Calculated strain agreed well with measured strain.
6. As laying temperature increased, the scale thickness increased and the strain for 100% scale removal decreased.
7. At the same laying temperature, as cooling rate increased, scale thickness decreased and the strain for 100% scale removal increased.
8. Ageing time had an effect on the strain for 100% scale removal, but it is relatively small.

9. The thickness of the scale at different coil positions was different. As the number of the samples taken at one position increased, the error caused by positions decreased.
10. Relative humidity and temperature had an effect on descalability, but it depended on the holding time. Beyond a critical holding time, time had no further effect on descalability. The higher the environmental temperature, the less the critical holding time. After the critical holding time, e.g. 5 days, increasing humidity reduced descalability.
11. The residual sub-layer of scale left on the descaled rod surface of the sample supplied by Cardiff Rod Mill (EAF steel), was identified as magnetite by EBSD.
12. Copper enrichment was found by X-ray element mapping at the scale/metal interface but within metal side, and silicon enrichment was found at the scale/metal interface but within scale side for the sample with sub-layer left on the descaled rod surface and supplied by Cardiff Rod Mill (EAF steel).
13. Failure in tension started with first cracks formed at the place with high stress concentration. As tensile strain increased, new cracks formed midway between the existing cracks. Crack spacing kept uniform but decreased until scale segments spalled off the rod surface. The crack spacing increased with increase in scale thickness and decreased with increase in strain applied.
14. Four failure mechanisms were found for the failure of the three layers under compressive stress. (i) Oxide scale of around $10\mu\text{m}$ in thickness showed interface delaminating and buckling within the main area of oxide, which was characteristic of Route II mechanism for weak interface/strong oxide cohesion. (ii) Thicker oxide failed by interface delamination initiated at the edge of oxide area, which was due to bending curvature. (iii) Oxide scale of $25\mu\text{m}$ in thickness showed failure with wedging which was characteristic of Route I mechanism for strong interface/weak oxide cohesion. (iv) Oxide scale lying in the area near the neutral plane of the rod showed shear failure with buckling and wedging along fracture zones, which formed a regular pattern.

15. The scale cracking and removal mechanism in compression depended on the relative shear strength of the oxide, the buckling stability of the layer and the relative shear strength of the interface. Spallation always required the propagation of a crack at the interface.

6.2 Future Work

1. So far, the descalability of mild steel rods has only been investigated. Therefore future work should extend to the descalability tests to alloy steel and high carbon steel rods.
2. The data processing of the bending strain by the Cyclone scanner method should be programmed by C or C++ language to increase the efficiency further.
3. Electron microscopy characterization of the scale structure and composition should be carried out further.
4. Scale cracking and removal mechanisms should be studied in detail.
5. The effect of relative humidity and temperature on descalability, especially the effect of environmental temperature of the same relative humidity on descalability should be studied in more detail.
6. FE simulation of scale cracking and removal behaviour at room temperature should be continued.

REFERENCES

- Annual Book of ASTM Standards, 1994, Section 3, Metal Test Methods and Analytical Procedures, V.03.01, Metal-Mechanical Testing; Elevated and Low-Temperature Tests; Metallography, p655-656.
- Asia, T., Soshiroda, T. and Miyahara, M., 1997, *ISIJ Int.* 37, 3, 271-277.
- Armitt J., Holmes D. R., Manning M. I., Meadowcroft D. B. and Metcalfe E., 1978, Report FP-686. Palo Alto: Electric Power Research Institute (EPRI).
- Aubry A., Armanet F., Beranger G., Lebrun J.L. and Maeder G., 1988, *Acta. Metall.*, 36, 2779-2786.
- Banks, J. P., Evans, H. E. Hall, D. J. and Saunders, S. R. J., 1994, In: *Materials for Advanced Power Engineering, Part II* (Coutsouradis, D. et al. (eds)) Kluwer Academic Publi. Dordrecht, Netherlands, 543.
- Banks J.P., Gohil D. D., Evans H. E., Hall D. J., and Saunders S. R. J., 1957, presented at "Materials for Advanced Power Engineering", Liège.
- Banks J.P., Gohil D. D., Evans H. E., Hall D. J., and Saunders S. R. J., 1994, in: "Materials for advanced power engineering", Part II, (ed. D. Coutsouradis et al.), 1543-1552; The Netherlands, Kluwer Academic Publ.
- Barbehön J., 1988, *Das Verhalten von Oxidschichten auf Metallen bei Zug-, Druck- und zyklischer Verformung.* Fortschritt-Berichte VDI Reihe 5Nr, 138. Germany: VDI-Verlag.
- Barnes J. J., Goedjen J. G. and Shores D. A., 1989, *Oxid. Met.*, 32, 449-469.
- Baroux M, 1979, *J. Wire Int.*, 62, May.
- Beck H., 1981, *Proceeding of An International Conference Organized by the Metal Society and Held at the Royal Hotel, London on 13-14 May.*
- Berchtold L., Sockel H. G. and Ilschner B., 1980, In: *Behaviour of High Temperature Alloys in Aggressive Environments.* London: Metal Soc., pp. 927-941.
- Birchall J. D., Howard A. J. and Kendall K., 1981, *Nature*, 289, 388.

- Borie B., Sparks C. J. and Cathcart J.V., 1962, *Acta. Metall.*, 10, 691-697.
- Buresch P.E. and Bollenrath F., 1962, *J. Nucl. Mater.*, 24, 270-280.
- Burton B., 1982, *Single Cryst. Prop.*, B1, 1-48.
- Confente M., Genève D, Resiak B. and Michel Jallon, 1995, *J. Wire Int.*, February, 238-242.
- Cook, E. A. and Rasmussen, K. E., 1970, *Iron and Steel Engineer*, March, 380-385.
- Crouch, A. G. and Dooley, R. B. *Corros. Sci.*, 1976, 16, 341.
- Delauney D., Huntz A. M. and Lacombe P., 1980, *Corros Sci.*, 20, 1109-1117.
- Dieter G. E., 1988, *Mechanical Metallurgy, Mat. Sci & Met.*, ISBN 0-07-100406-8. 266.
- Donaldson A. T., in 'Zirconium in the nuclear industry, 9th Int. Symp.', (ed. C. M. Eucken and A. M. Garde), STP 1132, 177-197; 1991, Philadelphia, PA, ASTM.
- Donaldson A. T. and Evans H. E., 1981, *J. Nucl. Mater.*, 99, 38-46.
- Donaldson A. T. and Evans H. E., 1981, *J. Nucl. Mater.*, 99, 47-56.
- Donaldson A. T. and Evans H. E., 1981, *J. Nucl. Mater.*, 99, 57-65.
- Eisenblatter J., 1979, In: *Proc. of a Meeting on Acoustic Emission. Germany: Deutsche Gesellschaft fur Metallkunde*, 189-204.
- Evans A. G., Crumley G. B. and Demaray R. E., 1983, *Oxid. Met.*, 20, 193-216.
- Evans A. G. and Cannon R. M., 1989, *Mater. Sci. Forum*, 43, 243-268.
- Evans H. E., 1988, *Mater. Sci. & Technol.*, 4, 415-420.
- Evans H. E., 1989, *Mater. Sci. Eng.*, A120, 139-146.
- Evand H. E., 1994, *Mater. at High Temp.*, Vol. 12, 219-227.
- Evans H. E., 1995, *Int. Mat. Rev.*, Vol. 40, No. 1, 1-39.
- Evans H. E., 1996, *CMMT(A)22*, National Physical Laboratory, ISSN 1361-4061, 1-17.
- Evans H. E. and Huntz A. M., 1994, *Mater. at High Temp.*, Vol. 12, No. 2-3, 111-118.
- Evans H. E. and Lobb R. C., 1984, *Corros. Sci.*, 24, 209-222.

- Evans H. E., Nicholls J. R. and Saunders S. R. J., 1995, *Solid State Phen.*, Vol. 41, 137-156.
- Evans U. R., 1948, 'Symposium on International Stress in Metals and Alloys', 295-310.
- Fisher K, 1998, final year project, the University of Sheffield, Department of Engineering Materials.
- Francis J.M. and Whitlow W. E., 1965, *ISIJ*, 203, 468-473.
- Frank Anthony R and Kirkcaldy Andrew, 1997, *Proceedings of Annual Convention of the Wire Association International*, 1-14.
- Fresnedo C. and Ruiz J. M., 1996, *J. Wire Int.*, January, 70-73.
- Frost H. J. and Ashby M. F.: *Deformation-mechanism maps: 1982*, Oxford, Pergamon Press.
- Garber, S., and Sturgeon, G. M., 1961, *Wire Ind*, 3, 257.
- Genève D and Francois M., 1994, *J. Wire Int.*, May, 54-60.
- Grosskreutz J. C. and McNeil M. B., 1969, *J. Appl. Phys.*, 40, 355-359.
- Goedjen J.G., Stout, J.H., Guo Q. and Shores D. A., 1994, *Mater. Sci. Eng.*, A115-124.
- Hall D. J., Booth S. and Evan W. T. 1988, May, 4, 391-397.
- Hancock, P. and Nicholls, J. R., 1988, *Mater. Sci. Tech.*, 4, 398.
- Hancock, P. and Nicholls, J. R. *Mater. at High Temp.*, 1994, 12 (2-3), 209-218.
- Heizer J., 1990, *Int. J. Fracture.*, 46, 271-295.
- Hessenbruch, W. and Rohn, W., 1923, *Heraeus Vacuumschmelze*, 33, 247.
- Hideo Sugisawa, Japanese patent application (No. 38-39769)
- Hopkinson J., 1993, M.S. thesis, Sheffield Hallam and University of Sheffield Joint Masters Programme.
- Hou P. Y. and Stringer J., 1991, *Acta. Metall. Mater.*, 39, 841-849.
- Huntz A. M., 1988, *Mater. Sci. & Technol*, 4, 1079-1087.
- Huntz A. M., Liu C., Kornmeier M. Lebrun J. L., 1993, *Corros. Sci.*, 35, 989-997.

- Huntz A. M. and Schüze M., 1995, *Mater. at High Temp.*, special issue, 151-162.
- Huntz A. M. and Zhao J. G., 1987, *Mater. Sci. Eng.*, 1987, 88, 213-219.
- Huntz A. M., Zhao J. G., Boumaza, Moulin G., 1988, *Mater. Sci. & Tech.*, May, Vol. 4, 470-478.
- Kelly A. and McMillan N. H., 1986, *Strong Solids* (Oxford University Press, Oxford).
- Kendall K., 1978, *Nature*, 272, 710.
- Kubaschewski, O., and Hopkins, B. E., 1962, *Oxid. Met. and Alloys*, (2 edn); London, Butterworths.
- Li T. and Li M. 1989, *Mater. Sci. Eng.*, A120, 239-244.
- Luyckx, L. and Lorang, F., 1965, *C.N.R.M.*, No. 2, January, 3-8.
- Manning M. I., 1981, in: "Corrosion and mechanical stress", (ed. V. Guttman and M. Merz), 323; London, Applied Science.
- Manning M. I., 1983, in: "Aufbau von Oxidschichten auf Hochtem-peraturwerkstoffen" (ed. A. Rahmel), 283; Oberursel, Deutsche Gesellschaft für Metallkunde.
- Marston, H. F., 1995, 1st international conference "Hydraulic Descaling in Rolling Mills", 9-10, Oct., Painters Hall, London, UK, The Institute of Materials.
- Mecholsky J. J., Freeman S. W. and Rice R. W., 1976, *J. Mater. Sci.* 11, 1310.
- Moulin G., Huntze A. M. and Rousselet, 1989, *Mater. Sci. Eng.*, 1989, A120, 221-228.
- Murahashi M, Oki Y, et al., 1993, *J. Wire Int.*, November, 50-57.
- Nagl M. M., Saunders S. R. J., and Hall D. J., *Corros. Sci.*, 1963, 35, 965.
- Nagl M. M., Evans W. E., Saunders S. R. J. and Hall D. J., 1992, *Mater. Sci. & Tech.*, November, 8, 1043-1049.
- Nagl M. M., Evans W. T., Hall D. J., and Saunders S. R. J., 1993, *J. de Phys. IV, Colloq. C9, Supp.* 1993, 13 3, 932.
- Nagl, M. M., Evans, W. T., Hall D. J. and Saunders, S. R. J., 1993, *J. Phys IV, Colloq. C9, Suppl.* 13, 3, 932.

- Nagl M. M., Evans W. E., Saunders S. R. J. and Hall D. J., 1993, *Corro. Sci.*, vol. 35, Nos5-8, 965-977.
- Nagl M. M., Evans W. E., Saunders S. R. J. and Hall D. J., 1994, *Oxid. Met.*, vol.42, Nos5/6, 431-449.
- Nicholls J. R. and Saunders S. R. J., 1990, In: Phys-Jones T. N., ed. *Surface Stability*, London: Institute of Metals, 95-144.
- Nicholls J. R., Evans H. E. and Saunders S. R. J., 1997, *Mater. Sci. & Tech.*, 5-13.
- Noden J. D., Knights C. J., and Thomas M. W., 1968, *Br. Corros. J.*, 3, 47-55.
- Pawel R. E. and Campbell J. J., 1975, in 'Stress effects and oxidation of metals', (ed. J. V. Cathcart), 330-351; New York, AIME.
- Pawel R. E. and Campbell J. J., 1966, *Acta Metall.*, 14, 1827-1833.
- Phani K. K., 1986, *J. Mater. Sci. Lett.*, 5, 747.
- Pilling N. B. and Bedworth R.E., 1923, *J. Inst. Metals*, 529-582.
- Reinaido Heitor Batista Queiroga, Ricardo José Macedo dos Santos, and Dagoberto Brandão Santos, 1995, *J. Wire Int.*, October, 56-63.
- Rhines F. N. and Wolf J. S., 1970, *Metall. Trans.*, 1, 1701-1710.
- Rice R. W., 1977, in: "Treatise in materials science and technology", vol. 11, (ed. R. K. MacCrone), 200; New York, Academic press.
- Rice R. W., 1984, Pores as Fracture Origins in Ceramics. *J. Mater. Sci.*, 19, 895-914.
- Robertson J. and Manning M. I., 1990, *Mater. Sci. & Tech.*, 6, 81-91.
- Roy C. and Burgess B., 1970, 2, 235-261.
- Ruth Chatterjee-Fischer, 1978, *Met. Trans.*, Nov., Vol. 9A, 1553.
- Sachs, K and Jay, G. T., 1959, *ISIJ*, September, 34-44.
- Sachs, K., and Tuck, C. W., 1967, Conference on " Reheating for Hot Working", The Iron and Steel Institute, London, pp. 1-17.

- Saunders S. R. J. and Nicholls J. R., 1996, Oxidation, Hot Corrosion and Protection of Metallic Materials, chapter 14, (ed. R. W. Cahn and P. Haasent), Physical Metallurgy; fourth revised and enhanced edition, Elsevier Science BV.
- Schell, E. and Kiwit, K., 1936, Arch. Eisenh. 9, 405.
- Schütze, M., 1985, Oxid. Met., 24, 199-232.
- Schütze M., 1988, Mater. Sci. & Tech., May, Vol. 4, P407-414.
- Schütze, M., 1990, Mater. Sci & Technol., 6, 32-38.
- Schütze, M., 1991, Int. J. Pres. Ves. & Piping, 47, 293.
- Schütze, M., 1995, Oxid. Met., 44, Nos. 1/2.
- Seybolt A. U., 1954, Trans. AIME, 200, 774.
- Spriggs R., 1961, J. Am. Ceram. Soc., 44, 628.
- Stalson S. L. and Hurat L. T., 1965, Wire and Wire Productions, November, Vol. 40, No. 11, 1731-17952.
- Stringer J., 1970, Corros. Sci., 10, 513-543.
- Tien J. K. and Davidson J. M., 1974, In: Cathcart J. V., ed. Pro. Symp. On Stress Effects and the Oxidation of Metals. USA: AIME, 200-219.
- Tien J. K. and Davidson J. M., 1975, In: 'Stress effects and the oxidation of metals', (ed. J. V. Cathcart), 200-219; New York, AIME.
- Timoshenko S. and Goodier J. N., 1969, " Theory of elasticity", 3rd Edition. New York, McGraw-Hill, 408.
- Tominaga J., Wakimoto K., Mori T., Murakami M. and Yoshimura T., 1982, Transactions ISIJ, 1982,22, 646-656.
- Tucker M. O., Brown A. F. and Healey T., 1978, J. Nucl. Mater., 74, 41-47.
- Walter M., 1991, Verhalten ausgewählter System Werkstoff/Oxidschicht bei Temperaturewechselbelastung. Doctoral Thesis. Germany: Technische Hochschule Aachen.
- Wang J. C., 1984, J. Mater. Sci., 18, 801.

Wasilewski R. J., 1953, Am. Chem. Soc., 75, 1001-1002.

Weirick, L. J., 1975, in: "Stress Effects and the Oxidation of Metals" (Ed. J.V.

Wells C. H., Follansbee P. S. and Dils R. R., 1974, In: Cathcart J. V. e. pro. Symp. On Stress Effects and the Oxidation of Metals. USA: AIME., 220-244.

Cathcart), Metallurgical Society of AIME, Warrendale, PA, 299.

William M. B., Miller E. T., Haney D. 1952, Wire, July, 672-711.

Yasuhiko Miyosi, 1971, Technical Report of Fuji Steel, Vol. 13, No. 1, 164.

Yalamanchili B., Power P. M. and Jr. Nelson J. B., 1999, J. Wire Int., May, 100-106.

Zhao J. G. and Huntze A. M., 1984, J. Mater. Sci., 19, 3166-3172.

Zhao J. G. and Zhang Y. J., 1989, Mater. Sci. Eng., A120, 245-250.

Appendix

This appendix reports micro-FE modeling work carried out by M. Krzyzanowski in collaboration with the Author as part of the research within IMPETUS on mechanical descaling, supported by the Materials Forum

ANALYSIS OF OXIDE SCALE FAILURE DURING MECHANICAL DESCALING: NUMERICAL SIMULATION

M. Krzyzanowski

INTRODUCTION

A thermal-mechanical model has been applied to simulate the behaviour of oxide on the surface of steel rod during mechanical descaling. The model uses the finite element method with detailed modelling of the rod and an oxide layer on the stock. Initially, the numerical approach has been developed for analysis of influence of oxide scale failure in hot rolling on friction and heat transfer. It allows for the analysis of deformation, viscous sliding along the oxide/metal interface, cracking and spallation of the oxide scale from the metal surface [1-9]. The oxide scale failure is predicted taking into account temperature dependence of the main physical phenomena, namely thermal expansion, stress-directed diffusion, fracture and adhesion. Then, the approach has been broadening for analysis of oxide scale failure in hot rolling on subsequent hydraulic descaling. A thermal solid model has been developed to simulate the behaviour of secondary oxide on the surface of the strip during hydraulic descaling [10]. For this purpose, a water jet impinging on a hot stock surface with oxide scales, cracked and partly spalled after the rolling pass, is simulated as transient boundary conditions for pressure and heat transfer on the basis of available results of experimental investigations and theoretical assumptions of hydraulic descaling. The boundary conditions are dependent on descaling conditions, such as spraying pressure, discharge rate, spray angle and spraying distance. It allowed for investigation of the mechanism of descaling from the analysis of operational factors in hot strip rolling. An investigation was made of the temperature fields during hydraulic descaling of heated steel strip and the associated thermal stresses contributing to separation the scale from the metal surface. It has been shown that the descalability of steel is strongly influenced by the state of failure in the scale after rolling, characterised by the presence of through-thickness cracks and partly spalled scale fragments. The measurement of separation loads, critical for the modelling of through-thickness cracking or failure due to crack propagation along the oxide/metal interface, was also discussed [10]. The aim of this investigation is assess the applicability of the numerical approach to the analysis of oxide failure during mechanical descaling when bending and tension at room temperature are operational factors influencing scale spallation.

MATHEMATICAL MODEL

The main assumptions of the mathematical model for hot, flat rolling related to oxide scale have been described in previous papers [3, 6] and are broadened here for a more complex multi-layered oxide scale. The thermal and mechanical properties of the oxide scale used for the modelling are tabulated in Table I. The model comprises a macro-level that computes the strains, strain rates and stresses in the specimen during bending and a micro-level to model oxide scale failure. There were two macro-models used for the analysis. One of them (Figure 1), included just one or two oxide scale fragments (solid or multi-layer) but has an adjusted finite element mesh around the scale for more precise calculation of crack propagation. Another one (Figure 2), having relatively coarse finite element mesh but large number of the scale fragments, was used to evaluate crack spacing during bending. Oxide scale failure is predicted taking into account the main physical phenomena (Table II). The finite element (FE) model is rigorously thermo-mechanically coupled and all the mechanical and thermal properties are included as functions of temperature. The commercial MARC K7.2 FE code was used for solving the non-steady state two-dimensional problem of the metal/scale flow, heat transfer, viscous sliding and failure of the oxide scale during testing. The specific heat, thermal conductivity, density and thermal expansion coefficient of the mild steel, necessary for heat transfer calculation during cooling, were introduced on the basis of available experimental data. The mechanical properties of the steel rod were measured during this investigation then introduced into the model as the strain-stress relationship. The radiative cooling of heated surfaces was simulated by prescribing the energy balance for the boundary surface.

The oxide scale was simulated as consisting of scale fragments joined together along the metal surface to form a continuum scale layer. The length of each scale fragment was less than that observed in the laboratory tests to allow for sensitivity of the model to crack spacing prediction. Each scale fragment consisted of four- and three-node, isoparametric, arbitrary plane strain elements. It has to be noted that the length of scale fragment, number of scale sublayers, type of element and their number for the scale fragment depend on the conditions being analysed.

To demonstrate the ability of the modelling approach two types of oxide scale have been chosen, which were observed in experiments: the homogeneous one scale layer model with the possibility of spallation along the scale/metal interface (Figure 3a) and the non-homogeneous three scale layer model with the additional possibility of delamination within

the scale between the sublayers (Figure 3b). The scale and metal surface were assumed to be adherent when they were within a contact tolerance distance, taken to be 1 μm . The available experimental data showed unstable crack propagation for the test conditions when through-thickness oxide scale cracking occurred, favouring the assumption of linear elastic fracture mechanics for the model. A critical failure strain was used as the criterion for the through-thickness cracking and was applied perpendicular to the crack faces. Assuming that the critical failure strain related to the fracture due to shear loading parallel to the crack faces exceeds the corresponding value for the tensile mode, the normal and tangential separation stresses were calculated in the model using the deformable-deformable contact procedure implemented in the MARC code. Tangential viscous sliding of the oxide scale over the metal surface was allowed when the scale and the metal surface were adherent. The viscous sliding arose as a result of the shear stress transmitted from the underlying metal to the scale in a manner analogous to grain boundary sliding in high-temperature creep. Although the viscous sliding is more significant at high temperatures, it can influence the crack spacing in low temperature when relatively low strain rate applied. This kind of sliding is different from frictional sliding of the separated scale fragment when separation stresses are exceeded.

Table I. Thermal and mechanical properties of oxide scale and interface used for calculation

Parameter	Function	Ref. [3, 10]
Density, kg/m^3	$\rho = 5.7 \times 10^3$	Ranta et al., 1993
Specific Heat Capacity, J/kg deg	$c_p = 674.959 + 0.297 \cdot T - 4.367 \cdot 10^{-5} \cdot T^2$ for $T \in 600 - 1100^\circ\text{C}$	Ranta et al., 1993
Thermal Conductivity, W/mK	$\lambda = 1 + 7.833 \cdot 10^{-4} \cdot T$ for $T \in 600 - 1200^\circ\text{C}$	Ranta et al., 1993
Young's Modulus, GPa	$E = E_{\text{ox}}^0 (1 + n(T-25))$ $n = -4.7 \times 10^{-4}$; $E_{\text{ox}}^0 = 240 \text{ GPa}$;	Morrel, 1987
Poisson's Ratio	$\nu = 0.3$	Robertson and Manning, 1990
Heat transfer coefficient at oxide/metal interface, $\text{W/m}^2\text{K}$	$\alpha = 30000$	Pietrzyk and Lenard, 1991
Surface diffusion coefficient times effective surface thickness, m^3/s	$\delta_s D_s = \delta_s D_{\text{os}} \exp(-Q_s / RT)$ $\delta_s D_{\text{os}} = 1.10 \cdot 10^{-10} \text{ m}^3/\text{s}$; $Q_s = 220 \text{ kJ/mole}$	Swinkels and Ashby, 1981
Volume (lattice) diffusion coefficient, m^2/s	$D_v = D_{\text{ov}} \exp(-Q_v / RT)$ $D_{\text{ov}} = 1.80 \cdot 10^{-4} \text{ m}^2/\text{s}$; $Q_v = 159 \text{ kJ/mole}$	Swinkels and Ashby, 1981
Stress intensity factor, $\text{MN m}^{-3/2}$	$K = a_0 + a_1 T + a_2 T^2 + a_3 T^3 + a_4 T^4 + a_5 T^5$ for $20 - 820^\circ\text{C}$ $a_0 = 1.425$; $a_1 = -8.897 \cdot 10^{-3}$; $a_2 = -8.21 \cdot 10^{-5}$; $a_3 = 3.176 \cdot 10^{-7}$; $a_4 = -5.455 \cdot 10^{-10}$; $a_5 = 3.437 \cdot 10^{-13}$	Hancock and Nicholls, 1988
Linear Coefficient of Thermal Expansion, $\times 10^{-6} \text{ deg}^{-1}$	$\alpha_{\text{ox}} = 15.0 (\text{FeO}); 12.0 (\text{Fe}_3\text{O}_4); 13.0 (\text{Fe}_2\text{O}_3)$	Robertson and Manning, 1990

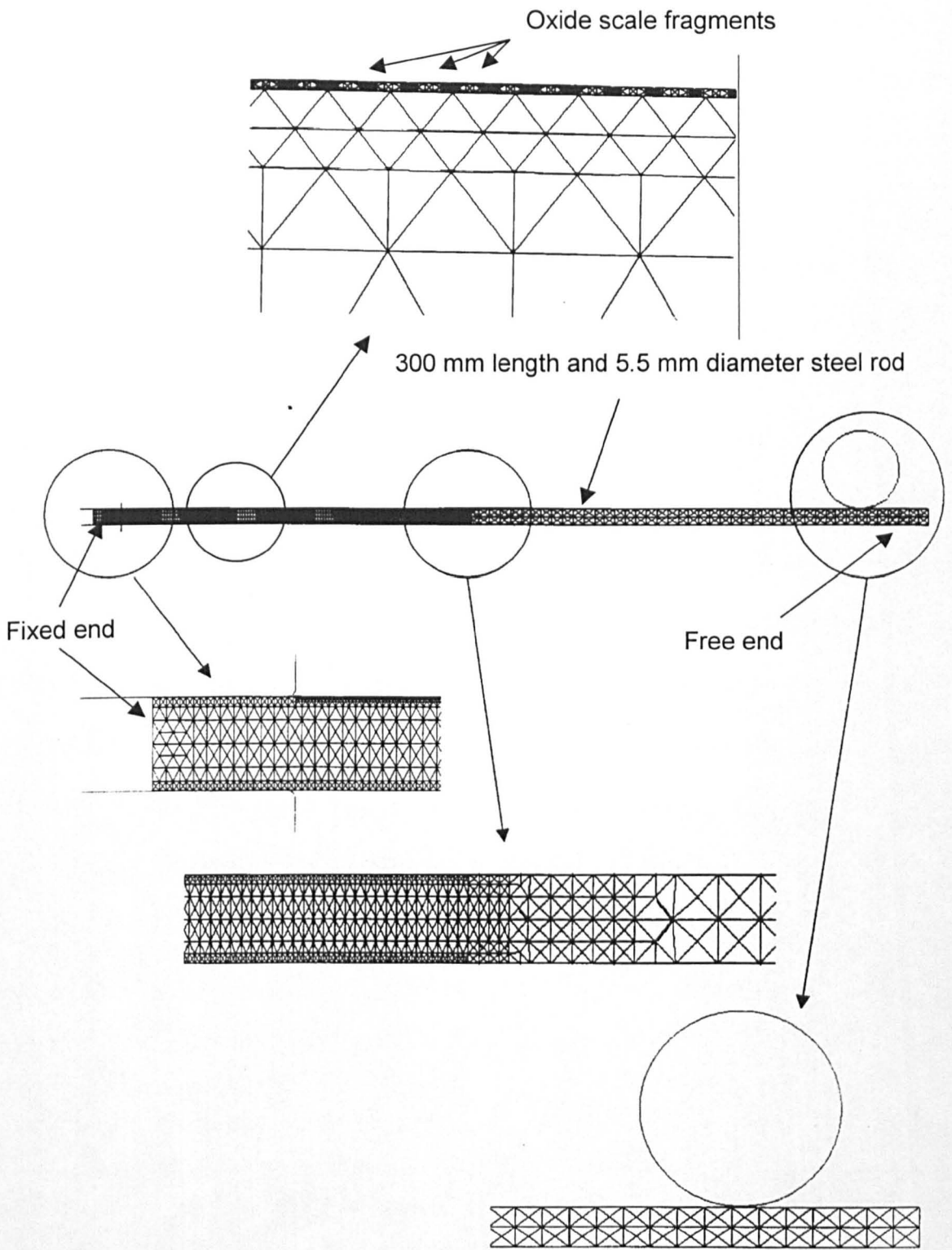


Fig. 2 Mathematical model N2 - schematic representation of the finite element mesh and the model setup.

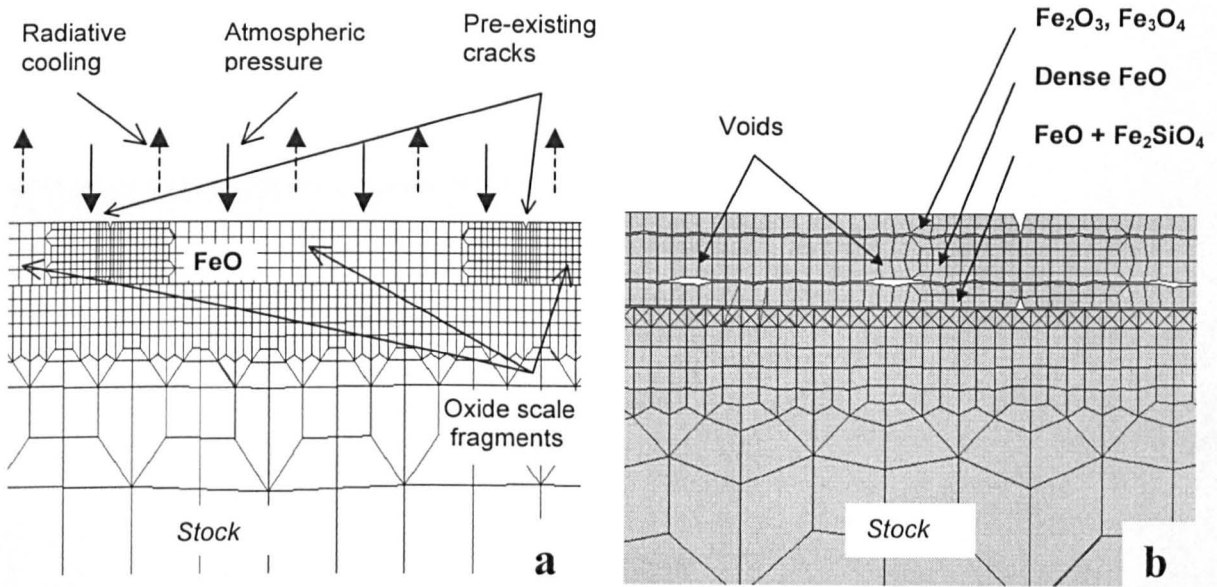


Fig. 3 Micro part of the model N1 - schematic representation of oxide scale model.

a) one layer oxide scale model; b) multi-layer oxide scale model.

RESULTS AND DISCUSSION

Figure 4 shows the oxide scale failed due to tension in a through-thickness crack mode, typical for the low temperature range. It was assumed that the scale deforms elastically such that the possible forms of stress relaxation were fracture, viscous sliding along the interface, and spallation. At room temperature and at relatively high strain rates within the time interval of testing about 15 s, the contribution of viscous sliding is negligible. Through-thickness cracks develop from pre-existing defects located at the outer surface of the oxide layer (Figure 3). The critical failure strain (Table II) can vary for the given temperature depending on both the parameters of the defects and the surface fracture energy, γ . It has been shown that the length c can be calculated as an effective composite value made up of the sum of the sizes of discrete voids whose stress fields overlap [11]. The formation of tensile cracks through the thickness of the oxide scale produces considerable redistribution of the stress within the scale and also at the oxide/metal interface. The stress concentration at the crack zone near the interface can lead to the onset of cracking along the interface. The in-plane stress cannot transfer across the crack and becomes zero at each of the crack faces. By symmetry it reaches a maximum value midway between the cracks. Within the scale

fragment the strain distribution significantly relaxes the level of deformation of the oxide scale compared with the surface layer of the metal. The formation of the crack through the thickness of the oxide scale develops shear stresses at the interface. At low temperatures in

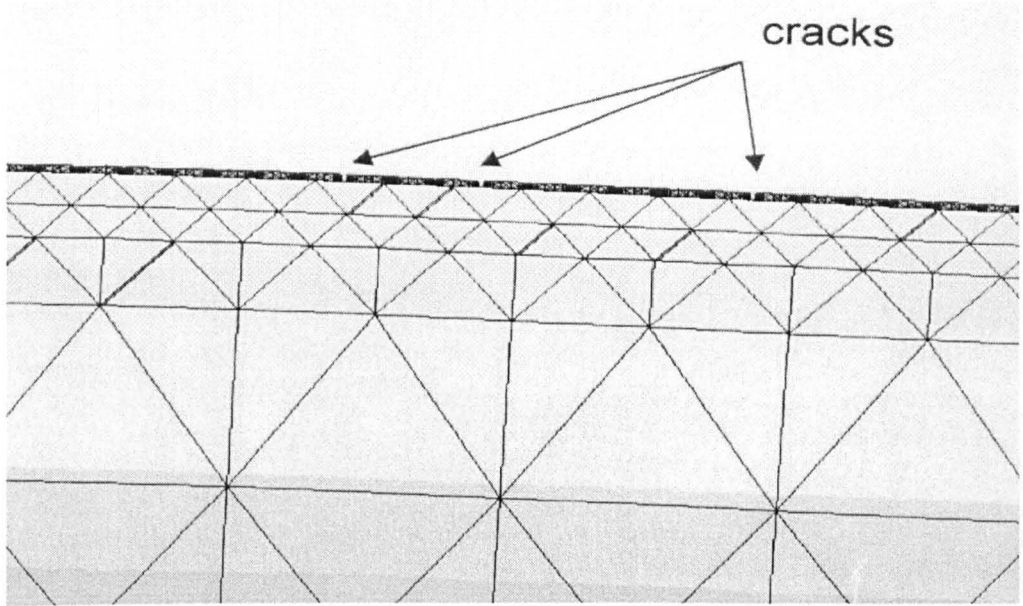


Fig. 4 Prediction of through-thickness crack formation at the convex surface of the steel rod.

the absence of relaxation by viscous sliding, these stresses have a maximum at the edges of the cracks. Relaxation of shear stresses can occur by interface cracking and spallation of the scale fragment when the strain increase critical level (Figure 5). As also can be seen from Figure 5, the more ductile inner sub-layer of multi-layer oxide scale can adhere the metal surface after bending while upper brittle sub-layer is spalled due to delamination within the scale.

There is a possibility of changing the extent of longitudinal tension at the steel rod in commercial mechanical descaling practice. Such change inevitably will influence the spacing between the neighbour through-thickness cracks formed at the earlier stages of bending. Another process parameter, which can be varied in practice, is the scale thickness. It was therefore important to investigate the influence both of them have on descalability of oxide fragments. Figure 6 shows two oxide scale fragments of the same 50 μm thickness after bending. The longer 5 mm length scale fragment adhered the metal surface even after more significant bending while the 0.8 mm length fragment showed better descalability. At the same time, the thinner scale fragment having the same 0.8 length but 25 μm thickness did not

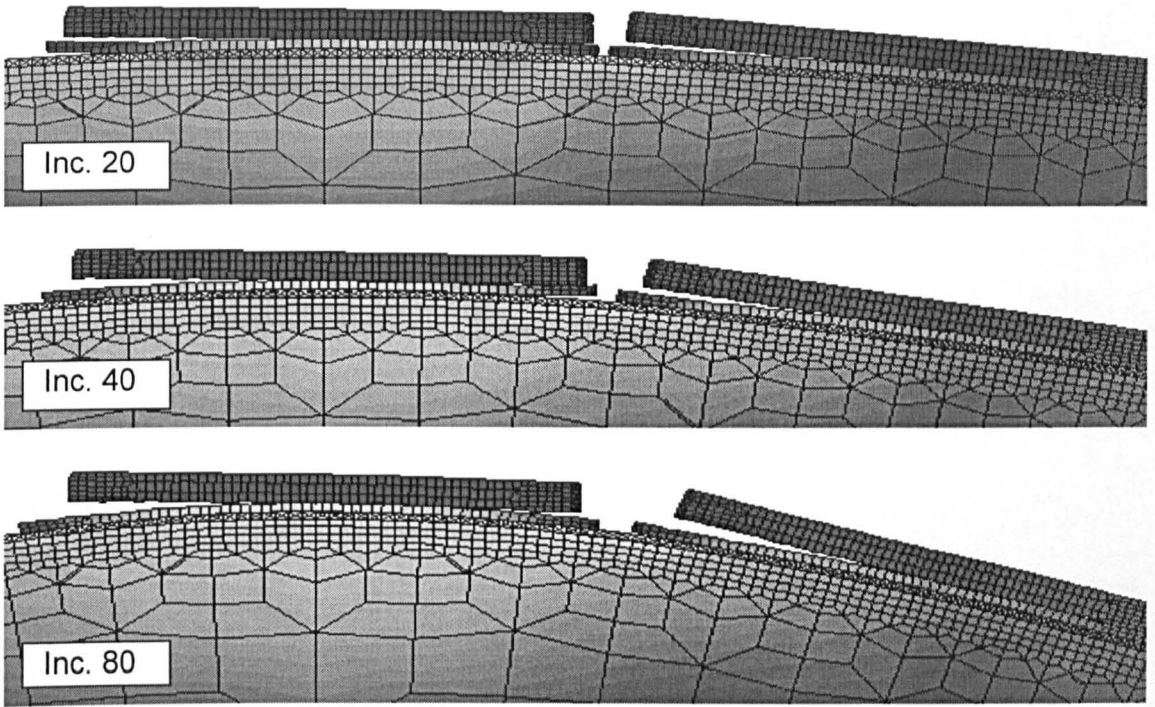


Fig. 5 Prediction of delamination within multi-layer oxide scale and spallation of the upper sub-layers at the convex surface of the steel rod for the different time increments.

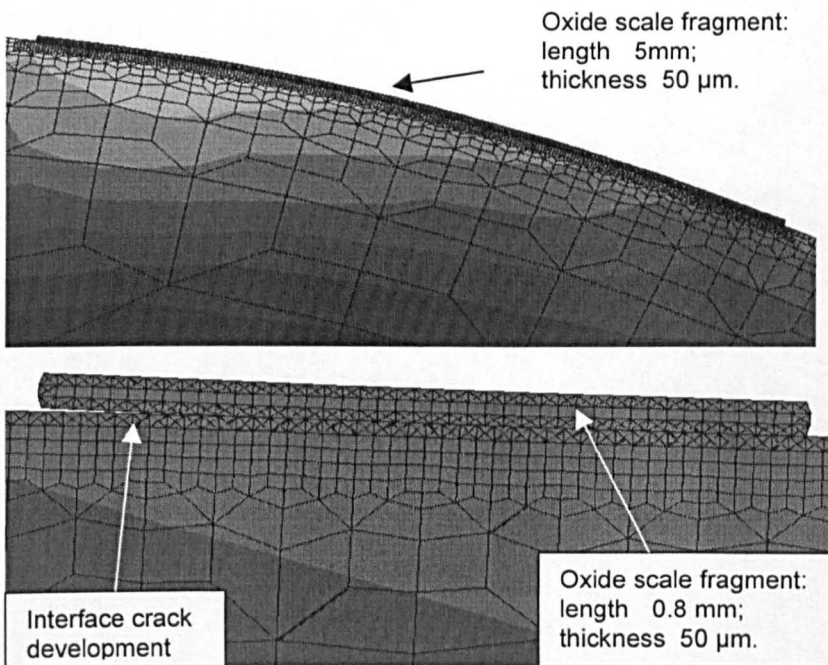


Fig. 6 Prediction of spallation of one layer FeO scale during bending. Note better descalability of the shorter scale fragment.

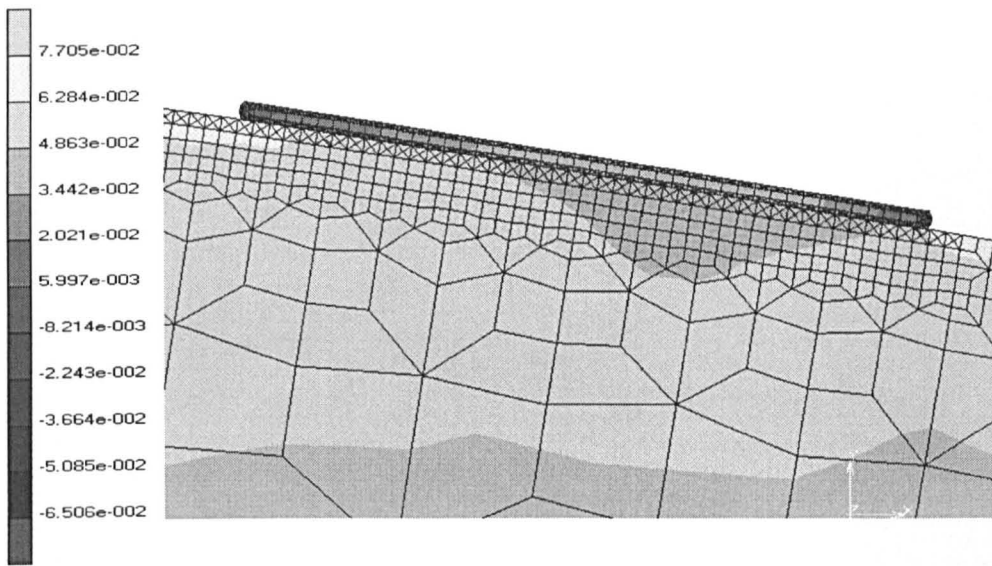


Fig. 7 Distribution of the longitudinal component of the total strain predicted for one layer FeO scale of 25 μm thickness during bending. Note adherence of the scale fragment to the metal surface.

loose adherence to the metal surface at much higher deformation (Figure 7). These results can favour the conclusion that, in order to improve the descalability during mechanical descaling on the convex part of a steel rod, both decreasing the length and increasing the thickness of the scale fragments are beneficial. Taking into account that the properties both of the oxide scale and the scale/metal interface are to a great extent dependent on the chemical content of steel and the scale growth conditions, implementation of the finite element model with the data for the particular steel grade becomes critical. The method of measurement of the oxide scale failure properties has been developed and discussed in [10].

The mechanism of oxide scale spallation for the opposite concave side of the steel rod, where longitudinal compression stresses are developed, is different. For an ideally smooth scale adhered to the smooth metal surface, the interfacial stresses, which can influence spallation, are close to zero provided that there are no discontinuities in the scale. Real scales and wavy interfaces with defects contain sites where, owing to inhomogeneous deformation, the new formation of defects or the growth of existing defects is facilitated when the scale is under compression acting parallel to the interface. It has been shown [12], that the initiation of local decohesion and through-thickness cracks may be due to grain boundary sliding of the underlying metal resulting from deformation by external forces. Other sources of the initiation of local decohesion under compression are convex sites on

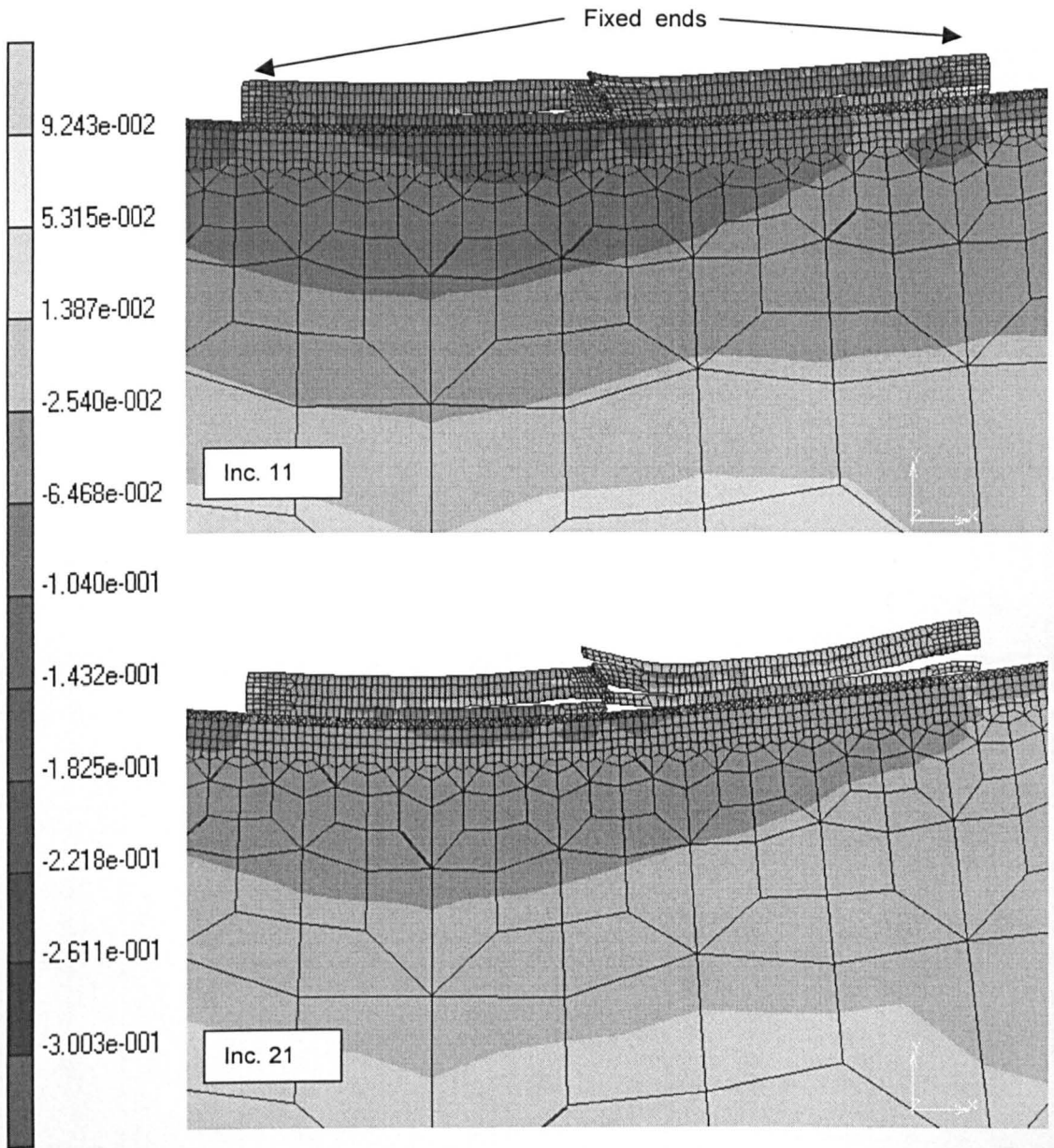


Fig. 8 Distribution of the longitudinal component of the total strain predicted for the multi-layer oxide scale of 100 μm thickness during bending. Note spallation of the scale sub-layers due to “wedge” mechanism.

the metal surface. At these sites, the oxide scale is lifted from the metal and scale separation is initiated. Once either a through-thickness crack or local buckling of a critical size has formed, spalling will occur under compressive longitudinal stresses during bending. As can be seen from the figure 8, spallation in a “wedge” mode at the concave side of the rod can occur during bending. To mimic the continuous oxide scale layer for the modelling, the left and right edges of the scale fragments were fixed to the metal surface in terms of zero

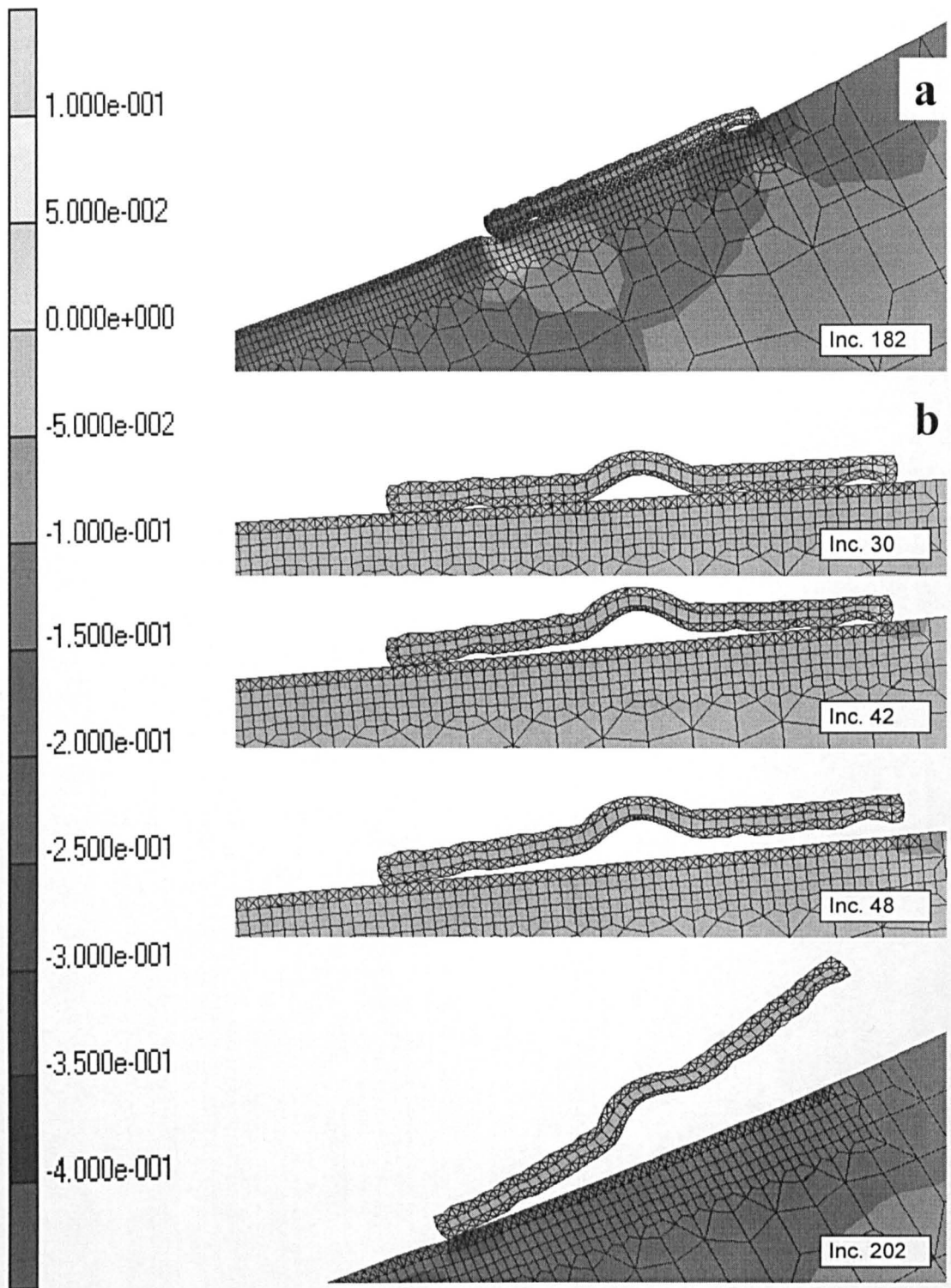


Fig. 9 Distribution of the longitudinal component of the total strain predicted for one layer FeO scale of 100 μm thickness during bending. Note spallation of the scale when oxide ridge of critical size has formed.

freedom in longitudinal direction. Figure 9 illustrates development of spallation from local buckling. If the buckling of the scale is below the critical level, the compressive stresses in the scale not lead to tensile stresses perpendicular to the interface (Figure 9a) and spalling does not occur. An initial separation leading to formation of oxide ridges of critical size is necessary for spalling under compressive stresses in the scale (Figure 9b).

CONCLUSIONS

1. The numerical approach has been developed for investigation of the mechanism of mechanical descaling by bending from the analysis of operational factors and the study of oxide scale and oxide/metal interface.
2. There are different mechanisms of oxide spallation for the concave and convex sides of the steel rod.
3. In order to improve the descalability during mechanical descaling on a convex side of the steel rod, both decreasing of the length and increasing of the thickness of the scale fragments are beneficial.
4. Spalling on a concave side of the steel rod under compressive longitudinal stresses during bending occurs when either a through-thickness crack or local buckling of a critical size has formed.

REFERENCES

1. Krzyzanowski M., Beynon J.H. and Sellars C.M.: Analysis of secondary oxide scale failure at entry into the roll gap, *Metallurgical and Materials Transactions A*, 2000 in print.
2. Krzyzanowski M. and Beynon J.H.: Modelling the boundary conditions for thermo-mechanical processing - oxide scale behaviour and composition effects, *Modelling and Simulation in Materials Science and Engineering*, 2000 in print.
3. M. Krzyzanowski and J.H. Beynon: Finite element model of steel oxide failure during tensile testing under hot rolling conditions, *Materials Science and Technology*, vol. 15, 1999, pp. 1191-1198.
4. M. Krzyzanowski and J.H. Beynon: The tensile failure of mild steel oxides under hot rolling conditions, *Steel Research*, vol. 70, issue 1/99, 1999, pp. 22-27.
5. Y.H. Li, M. Krzyzanowski, J.H. Beynon and C.M. Sellars: Physical simulation of interfacial conditions in hot forming of steels, *Acta Metallurgica Sinica*, vol. 13, No. 1, 2000, pp. 359-368.
6. Beynon J.H. and Krzyzanowski M.: Finite-element model of steel oxide failure during flat hot rolling process, *Proc. Int. Conf. Modelling of Metal*

Rolling Processes 3, 13-15 December, 1999, London, IOM Communications Ltd, London, UK, 1999, pp. 360-369.

7. Krzyzanowski M. and Beynon J.H.: Steel compositional effect on oxide scale failure during hot rolling of steel, *Proc. 8th International Conference on Metal Forming*, Krakow, Poland, September 3-7, 2000 in print.
8. Beynon J.H., Li Y.H., Krzyzanowski M. and Sellars C.M.: Measuring, modelling and understanding friction in the hot rolling of steel, *Proc. 8th International Conference on Metal Forming*, Krakow, Poland, September 3-7, 2000 in print.
9. Krzyzanowski M. and Beynon J.H.: Micro-finite element modelling of oxide scale effect on friction and heat transfer during hot rolling of steel, *Proc. International Conference on Processing & Manufacturing of Advanced Materials THERMEC '2000*, December 4-8, 2000, Las Vegas, USA, in print.
10. Krzyzanowski M. and Beynon J.H.: Effect of oxide scale failure in hot steel rolling on subsequent hydraulic descaling: Numerical simulation, *Proc. 3rd Int. Conf. Hydraulic Descaling*, 14-15 September, 2000, London, IOM Communications Ltd. in print.
11. Schütze M.: Mechanical Properties of Oxide Scales, *Oxidation of Metals*, Vol. 44, Nos. 1 / 2, 1995, pp. 29-61.
12. Schütze M.: Stresses and decohesion of oxide scales, *Materials Science and Technology*, Vol. 4, 1988, pp. 407-414.

Tables

Table 2.1 Oxide scale composition

Name	Symbol	%Composition at 620°C	Visual appearance	Microscopical appearance
Hematite	Fe ₂ O ₃	0-5	Red	White
Magnetite	Fe ₃ O ₄	5-10	Black/blue	Light grey
Wustite	FeO	90-95	Grey	Dark grey

* Wustite is the softest and most acid soluble of the phases, hematite is the hardest and most insoluble [Hopkinson, 1993]

Table 2.2 Summary of deviation from classic scale growth [Sachs and Tuck, 1967]

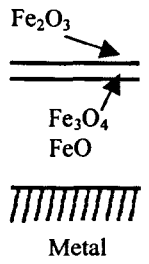
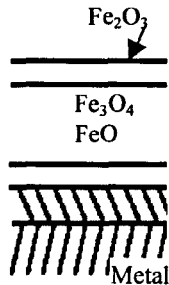
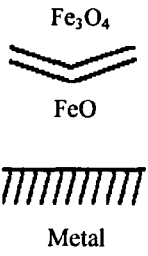
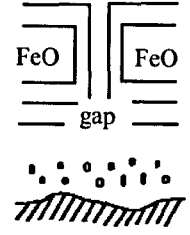
	1	2	3	4	5	6	7
	Classical	Gap formation	Surface reaction	Pseudo-classical	Gas-phase transport	Stable cracks and gaps	Gaps, blisters transverse & lateral cracks
Structure	 <p>Diagram 1: Classical scale growth. Layers of Fe_2O_3, Fe_3O_4, and FeO are shown on a metal substrate.</p>	 <p>Diagram 2: Gap formation. A gap is shown between the Fe_2O_3 and FeO layers.</p>	 <p>Diagram 3: Surface reaction. A wavy surface is shown on the metal substrate.</p>	 <p>Diagram 4: Pseudo-classical scale growth. A V-shaped Fe_3O_4 layer is shown on a metal substrate.</p>	 <p>Diagram 5: Gas-phase transport. Gas bubbles are shown on the metal substrate.</p>	 <p>Diagram 6: Stable cracks and gaps. A crack is shown in the scale layer.</p>	 <p>Diagram 7: Gaps, blisters, transverse & lateral cracks. A complex crack network is shown, including gaps and blisters.</p>
Kinetics	Parabolic	Parabolic-slower than parabolic	Linear-transitional	Parabolic	Parabolic	Parabolic	Parabolic/linear
Mechanism	Diffusion of iron ions through wustite	Diffusion of iron ions in wustite followed by conversion of FeO to higher oxides	Phase-boundary diffusion with changing boundary conditions	Iron ion diffusion	Iron ion diffusion and inward transport of oxygen	Escape of C-bearing gases Separation of scale from substrate Stabilization by N_2 local-lized diffusion through high oxygen layers	Bursting of scale. Separation from metal. Iron-ion diffusion and inward transport of oxygen.

Table 2.3 Summary of deviation from classical scale growth [Sachs and Tuck, 1967]

Materials	Atomosphere	Time initial	Short-term	Long-term
Pure iron	oxygen	Not evident at high temperature	Classical (1)	Gap formation (2)
	air			
	CO ₂	Surface reactions(3)	Psedo-classical (4)	Gas-phase transport (5)
	H ₂ O			
Carbon steel	oxygen	As pure iron	Classical: as pure iron but shorter duration (1)	Earlier gap formation (2)
	air	As pure iron	Cracks and gaps (6)	Gaps, blisters, transverse and lateral cracks (7)
	CO ₂	Surface reaction (3)	Gap-phase transport (5)	Gas-phase transport (5)
	H ₂ O			

Table 2.4 Summary of the scale failure mechanism in compression [Nagl,1992]

Designation	Critical initiation condition	Schematic diagram of failure mechanism
Case A: Route I (shear failure by wedging)	Critical shear strength	
Case B: Route II (buckling)	Critical buckling stability	
Case C: (Shear failure)	Critical shear strength	
Case D	Substrate yielding	
Case E	Critical buckling stability	

Table2.5 Summary of oxide properties

Oxide	γ (J/m ²)	E (Gpa)	K_{IC} (MPa \sqrt{m})	ν
FeO	3.0	130	0.9	0.36
Fe ₂ O ₃	6.0	219	1.6	0.19
Fe ₃ O ₄	4.5	208	1.4	0.29

* γ surface fracture energies, E Young modulus, ν Poisson ratio and K_{IC} fracture toughness (calculated values) at room temperature [Robertson&Manning, 1990]

Table 2.6 Processes for cooling wire rod from the rolling heat [Beck, 1981]

	Cooling medium	Wire rod shape	Designation	In operation since
1	Still air	Coil	Conventional	About 1850
2	Lead bath	Single wire	Lead patenting	1854
3	Cold water	Coil	Water quench	about 1890
4	Salt	Open coil	Salt patenting	1942
5	Flowing air	Single ring	Stelmor	1964
6	Flowing air	Coil	Reel cooling	1967
7	Sand Fluidized bed	Single ring	HOAG-Kobe	1967
8	Still air	Single ring	Schloemann	1969
9	Salt bath	Single ring	Arpat	1970
10	Flowing air	Single ring	Demag-Yawat	1970
11	Still air	Single ring	Ashlow	1972
12	Cold water	Single wire	Salzgitter	1973
13	Boiling water	Single ring	ED/EDC	1974
14	Flowing air	Single ring	Krupp	1974
15	Still air	Single ring	Stelmor, slow	1976
16	Still air	Single ring	Stelmor, retarded	1976
17	Water or oil	Vibrating coil	Röchling vibration hardening	In development

Table3.1 The chemical compositions of all steel grades used in the experiments (wt. %) and the related information

Steel grades	Chemical composition									Dia. (mm)	Steel-making	Testing application	Analyzed in	Supplier
	C	Si	Mn	P	S	Cr	Mo	Ni	Cu					
R09	0.032	0.02	0.24	0.017	0.017	0.02	<0.02	0.03	0.04	6.5	BOS	3-/4-point bending	university	#SRM
K08-A	0.055	0.18	0.60	0.017	0.032	0.05	<0.02	0.08	0.18	6.5	EAF	3-/4-point bending	university	SRM
K58	0.59	0.21	0.59	0.013	0.011	0.02	<0.02	0.02	0.04	5.5	BOS	3-/4-point bending	university	SRM
D12	0.11	0.21	0.58	0.016	0.041	0.02	<0.02	0.03	0.04	6.5	BOS	3-/4-point bending	university	SRM
B03	0.03	0.04	0.23	0.013	0.15					6.5	BOS	3-/4-point bending	industry	SRM
*K08+B	0.057	0.187	0.60	0.013	0.022	0.092	0.008	0.082	0.237	6.5	♣EAF	3-/4-point bending	industry	•CRM
φ14	0.23	0.20	0.61	0.005	0.027	0.03	0.004	0.030	0.05	14	♦BOS	Coil position test	industry	**RRM
K08-B	0.07	0.20	0.52	0.024	0.007					5.5	BOS	LT test (950°C)	industry	SRM
K08-C	0.07	0.19	0.54	0.017	0.007					5.5	BOS	LT test (890°C)	industry	SRM
K08-D	0.08	0.16	0.54	0.012	0.07					5.5	BOS	LT test (830°C)	industry	SRM
K08-E	0.070	0.220	0.530	0.018	0.016	0.021	0.003	0.020	0.016	5.5	BOS	Ageing time test	industry	SRM
K08-F	0.06	0.16	0.57	0.012	0.019	0.10	0.02	0.09	0.25	6.5	♣EAF	Cooling con. test	industry	•CRM
K08-G	0.04	0.047	0.23	0.010	0.014	0.011	0.002	0.020	0.010	6.5	BOS	Effect of Si element	industry	SRM

*steel grade K08+B contains B 0.007%. ♦ BOS - Basic Oxygen Steelmaking. ♣EAF - Electric Arc Furnace. #SRM – Scunthorpe Rod Mill. **RRM – Roundwood Rod Mill. •CRM – Cardiff Rod Mill.

Table 3.2 3-point bending test parameters for low carbon flat samples (1000°C×2, 5, 10, 20min with gas protection)

Sample	Span (mm)	Deflection (mm)
1 [#] (2min)	87	7
5 [#] (2min)	87	3.5
2 [#] (5min)	87	random
3 [#] (10min)	87	5
4 [#] (20min)	87	10

Table 3.3 3-point bending test parameters for D12 rod samples as received from Scunthorpe Rod Mill ($\phi 6.5\text{mm}$)

Sample	Span (mm)	Deflection (mm)
21 [#]	75	3.5
22 [#]	65	3.5
23 [#]	55	3.5
24 [#]	85	7

Table 3.4 Parameters used in 4-point bending test for steel grade (K08) rod samples supplied by Scunthorpe Rod Mill ($\phi 6.5\text{mm}$)

Sample (No.)	u (mm)	s (mm)	δ (mm)	f (mm/min)
1	20	80	4	5
2	20	80	5	5
3	30	80	9	5
4	30	90	9	5
5	15	90	9	5
6	20	80	9	5
7	30	90	9	4
8	30	90	9	3
9	30	90	9	2
10	30	90	9	1

* u: the distance between inner and outer rollers (mm),
s: the distance between outer rollers (mm),
 δ : deflection in 4-point bending test (mm),
f: cross head speed (mm/min)

Table 3.5 Parameters used in 4-point bending test for steel grades (R09, B03, K08+B) rod samples supplied by Scunthorpe Rod Mill ($\phi 6.5\text{mm}$)

Sample (No.)	u (mm)	s (mm)	δ (mm)	f (mm/min)
1	20	80	3.3	5
2	20	80	4.9	5
3	20	80	6.55	5
4	20	80	8.2	5
5	20	80	9.85	5
6	20	80	11.15	5
7	20	80	13.15	5

Table 3.6 Parameters used in 4-point bending test for steel grade (K58) rod samples supplied by Scunthorpe Rod Mill ($\phi 6.5\text{mm}$)

Sample (No.)	u (mm)	s (mm)	δ (mm)	f (mm/min)
1	20	90	8	5
2	20	90	8.75	5
3	20	90	10	5
4	20	90	11.65	5
5	20	90	14	5
6	20	90	17.5	5

Table 3.7 Specification of Cyclone scanner

Axial travel	600×500×400mm nominal
Maximum workpiece weight	200kg
Accuracy	50μm
Resolution	7μm
Scanning speed	up to 3m/min
Rapid speed	6m/min
Scanning rate	140points/sec
Scale and Readheads	5μm
Probe	Reinshaw 3 axis analogue probe
Probe rate	1N/mm nominal
Stylus	Ceramic, M4×100mm, φ6mmtip
Controller	PC resident transputer board
Weight	162Kg without PC
Colour	Royalite Grey and black
Table	Granite tile with grid of M8 holes
Operating temperature range	10°C to 38°C
Storage temperature range	-10°C to 50°C
Machine supplies: Power supply	240/110v ac 50/60Hz
Power consumption	200W
Air pressure	5Bar
Air consumption	40litre/min at atmospheric pressure
Noise	56dB(A)
Software	Reinshaw TRACECUT(capture, manipulation and part program generation).
Optical accessories	Scanning styli kit, styli, anti-vibration feet and additional clamp kit

Table 3.8 Ageing times in ageing time tests, K08 steel rod supplied by Scunthorpe Rod Mill ($\phi 6.5\text{mm}$)

LT($^{\circ}\text{C}$)	Ageing time (hour)												
950	0.5	1	2	4	8	16	32	48	72	96	120		
890	0.5		2	4		16	32	48	72	96	120	360	504

* LT: laying temperature

Table 3.9 Cooling conditions in cooling condition tests, K08 steel rod supplied by Cardiff Rod Mill ($\phi 6.5\text{mm}$)

LT($^{\circ}\text{C}$)	Cooling conditions	
900	all fans off	all fans on
870	all fans off	all fans on

Table 4.1 Primary scale formed in the laboratory furnace

Heat treatment	Notes
900°C×5, 10, 20min, without gas protection, air cooling	the oxide scales separate from all the sample surfaces even in the furnace
1000°C×2, 5, 10, 20min, with gas protection, air cooling	even with gas protection, for heating times of 5min., the oxide scale separated from the sample surfaces even in the furnace
820°C×6min, with gas protection, air cooling	
1000°C×1.5, 2min, without gas protection, air cooling	for heating times of 2min., the oxide scale separated from the sample surfaces even in the furnace
820°C×6min, without gas protection, air cooling	can see a little oxide separated from sample surface

Table 4.2 3-Point Bending Test Parameters for the samples (1000°C×2, 5, 10, 20min with gas protection)

Sample	Span (mm)	Deflection (mm)	Notes
1 [#] (2min)	87	7	when deflection was 3mm, cracking began
5 [#] (2min)	87	3.5	when deflection was 3mm or so cracking began
2 [#] (5min)	87	random	
3 [#] (10min)	87	5	no visible cracking could be seen
4 [#] (20min)	87	10	when deflection was 6mm, cracking began

Table 4.3 3-Point Bending Test Parameters for D12 samples

Sample	Span (mm)	Deflection (mm)
21	75	3.5
22	65	3.5
23	55	3.5
24	85	7

Table 5.1 Summary of strain for scale cracking and spalling

Strain for scale cracking and spalling	
Compression	Route I (strong interface, weak oxide) $\varepsilon_I^{init} = \sqrt{\frac{G_{IC}^{cohesive}}{k_1 h E_{ox} (1-\nu)}} \qquad \varepsilon_I^{spall} = \sqrt{\frac{G_{IC}^{interface}}{k_2 E_{ox} h (1-\nu)}}$ $G_{IC}^{cohesion} = G_{IC}^{interface} = 2\gamma \text{ [Robertson and Manning, 1990]}$
	Route II (weak interface, strong oxide) $\varepsilon_{II}^{init} = \frac{1.22}{(1-\nu^2)} \left(\frac{h}{R}\right)^2 \qquad \varepsilon_{II}^{spall} = \sqrt{\frac{1.052h^4}{R^4} + \frac{1.041G_{IC}}{E_{ox} h}}$ $G_{IC} = 2\gamma \text{ [Robertson and Manning, 1990]}$
Tension	$\varepsilon_c = \sqrt{\frac{2\gamma}{F^2 \pi E c}} \qquad c = kh \text{ [Robertson and Manning, 1990]}$

* G_{IC} : energy release rate, h: the oxide scale thickness, R: the initial radius of the zone of decohesion, E: Young modulus, ν : Poison ratio, γ : the fracture surface energy, c: the defect size, F and k: constants

Table 5.2 Average scale thickness at different cooling conditions

Laying temperature (°C)	Average Scale Thickness(micron)		
	Sample from Scunthorpe Rod Mill	Sample from Cardiff Rod Mill	
		all fans on	all fans off
870 °C	12.5	9	11
900 °C	13.75	10.5	11.5

Table 5.3 Average strains for 100% removal of the scale formed at different cooling conditions

Laying	Average Strain for 100% Scale Removal					
temperature	Sample from Scunthorpe		Sample from Cardiff Rod Mill			
(°C)	Rod Mill		In ten.		In com.	
	In ten.	In com.	fans on	fans off	fans on	fans off
870 °C	0.033	0.036	0.037	0.0425	0.036	0.0375
900 °C	0.03	0.032	0.036	0.0375	0.034	0.036

Figures

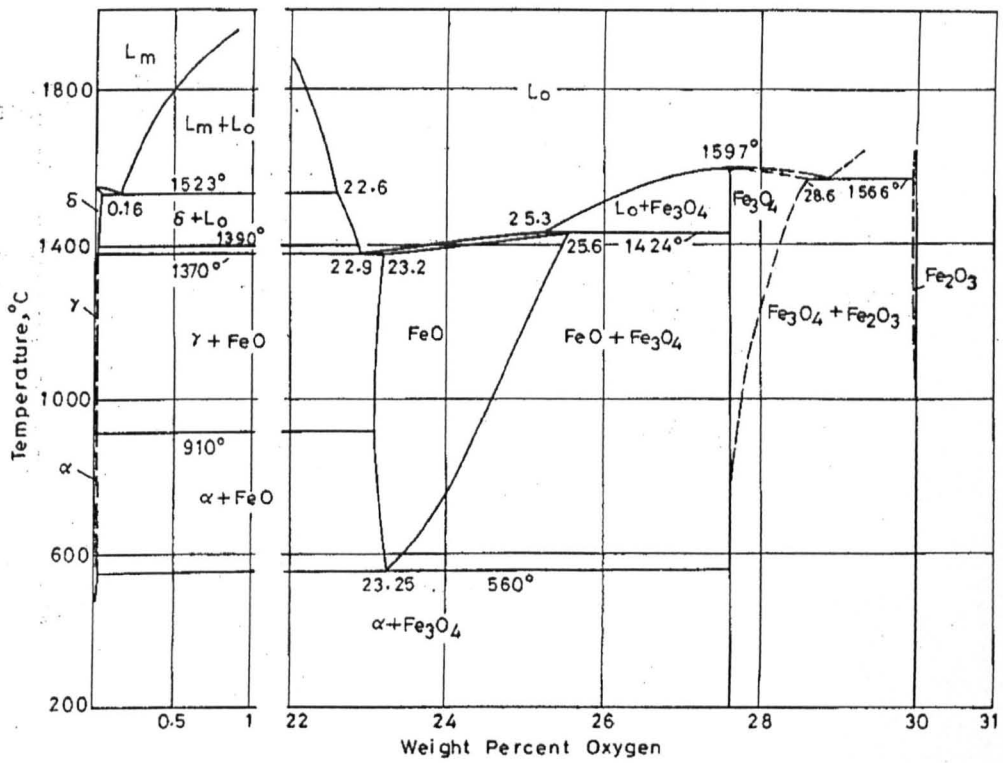


Fig. 2.1 Fe-O equilibrium phase diagram (after Tekko Binran, ed., 1962)
[Tominaga, 1982]

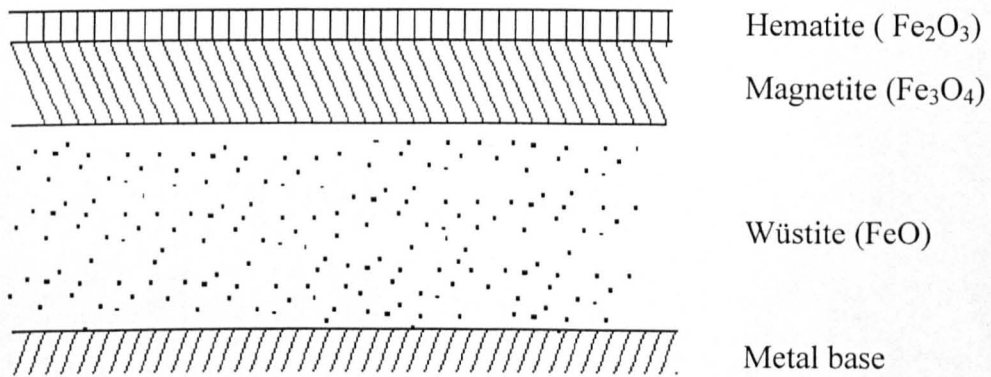


Fig. 2.2 Schematic representation of mill scale [Tominaga, 1982]

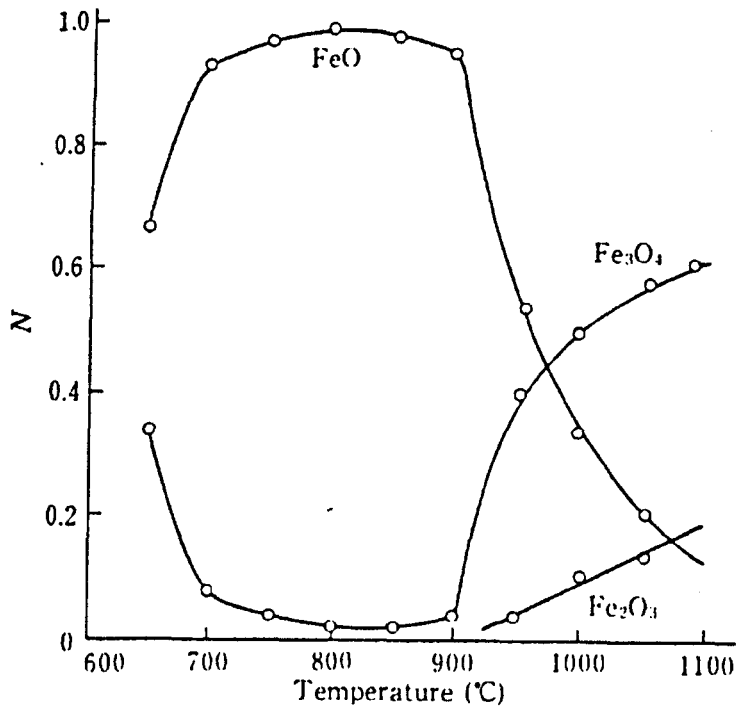


Fig. 2.3 Effect of temperature on the proportions of Fe-oxides (mole ratio) formed in scale [Tominaga, 1982]

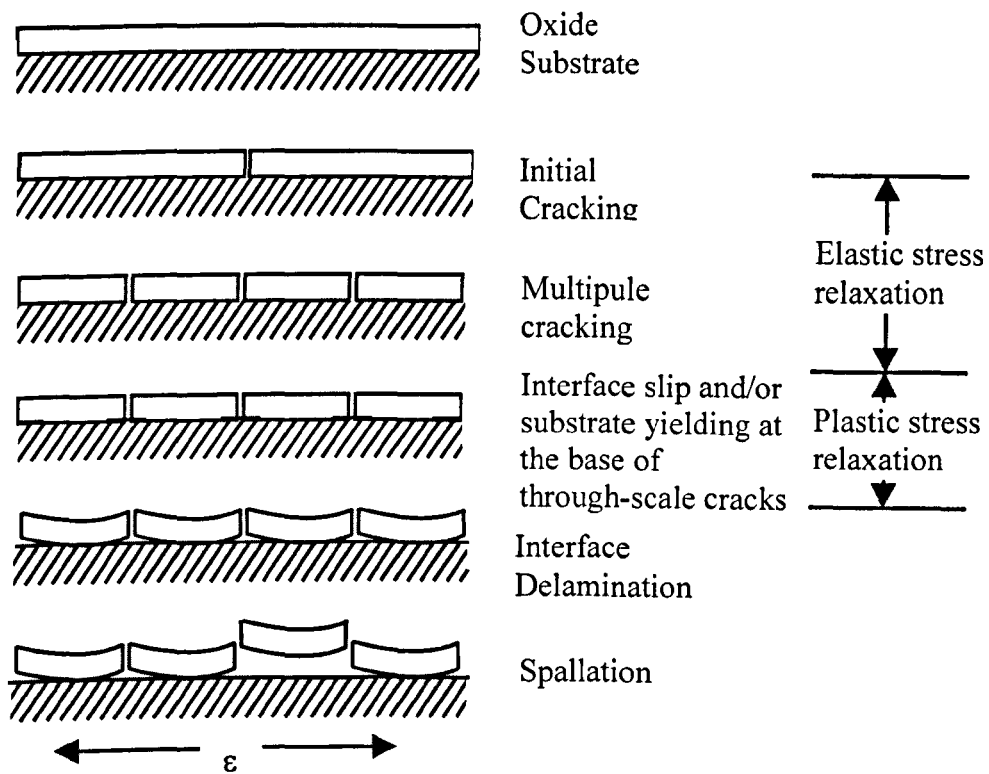


Fig. 2.4 Schematic diagram of tensile failure of oxide scale [Evans, 1988].

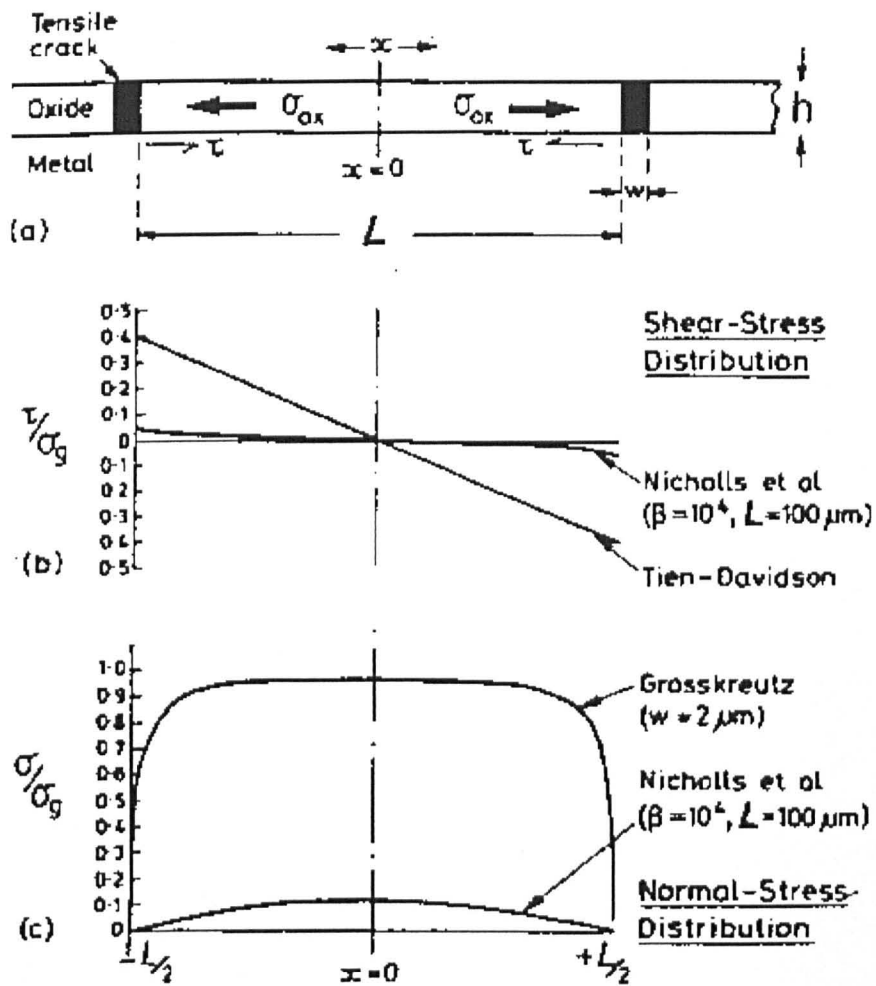


Fig. 2.5 Schematic of through-thickness tensile cracks in the oxide layer (a).

These cracks perturb the distribution of shear stress along the scale/metal interface (b), and in-plane tensile stress reducing it to zero at the crack faces and produce a maximum value midway between cracks (c).

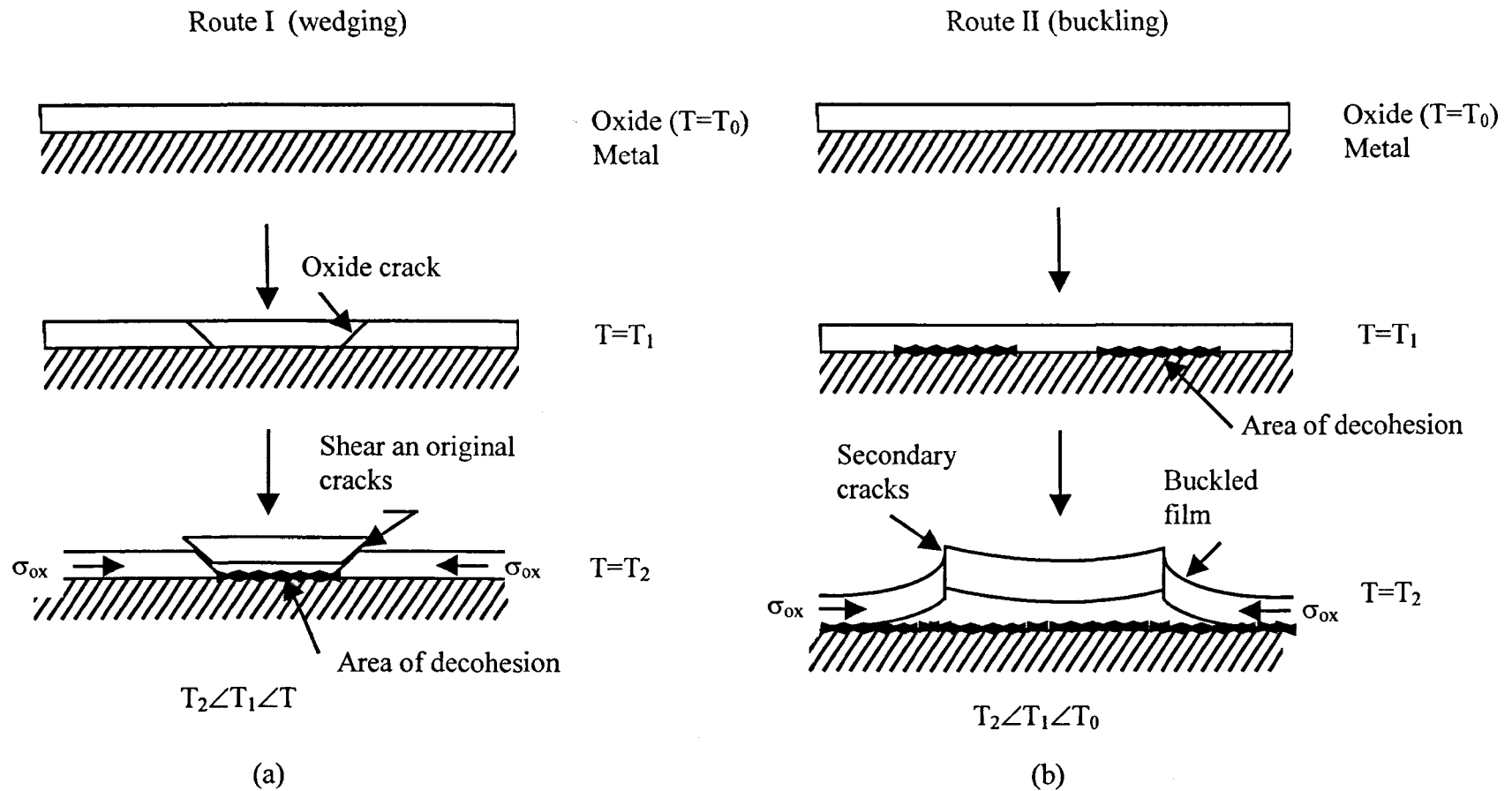


Fig. 2.6 Schematic diagram of compressive failure of oxide scale: (a) Route I and (b) Route II (Evans et al, 1993)

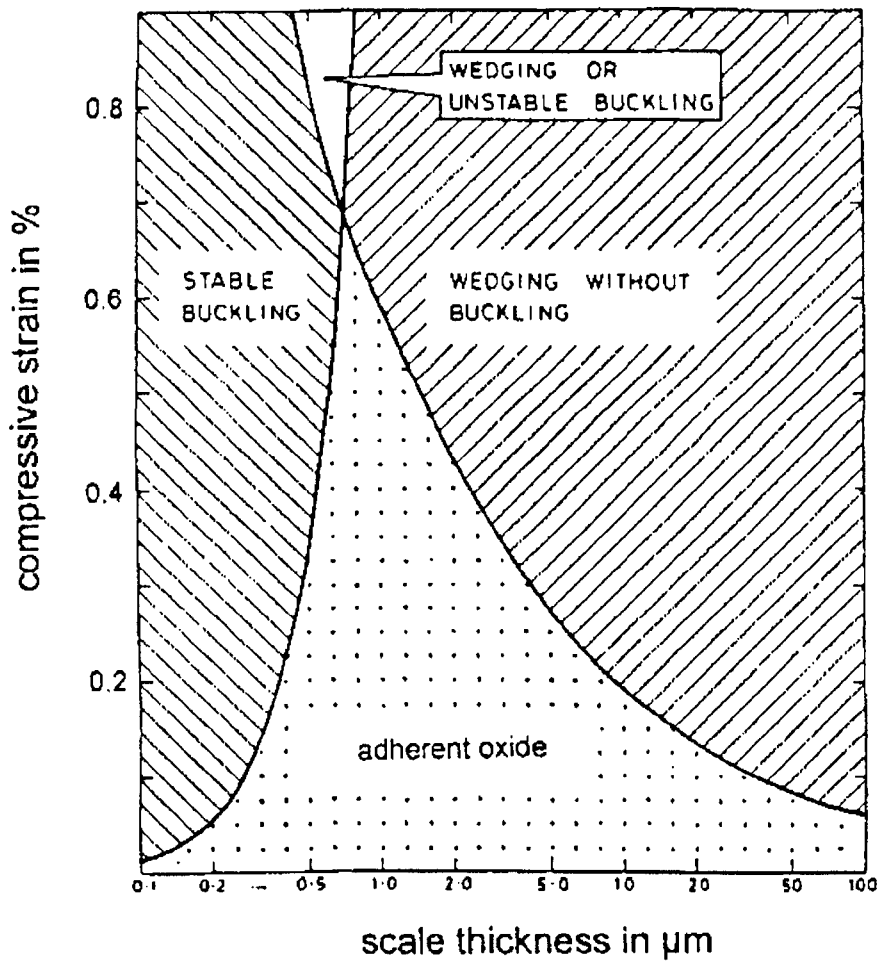


Fig. 2.7 Scale failure mode diagram for chromia on a 20Cr-25Ni-Nb stabilized steel [Schütze, 1995]

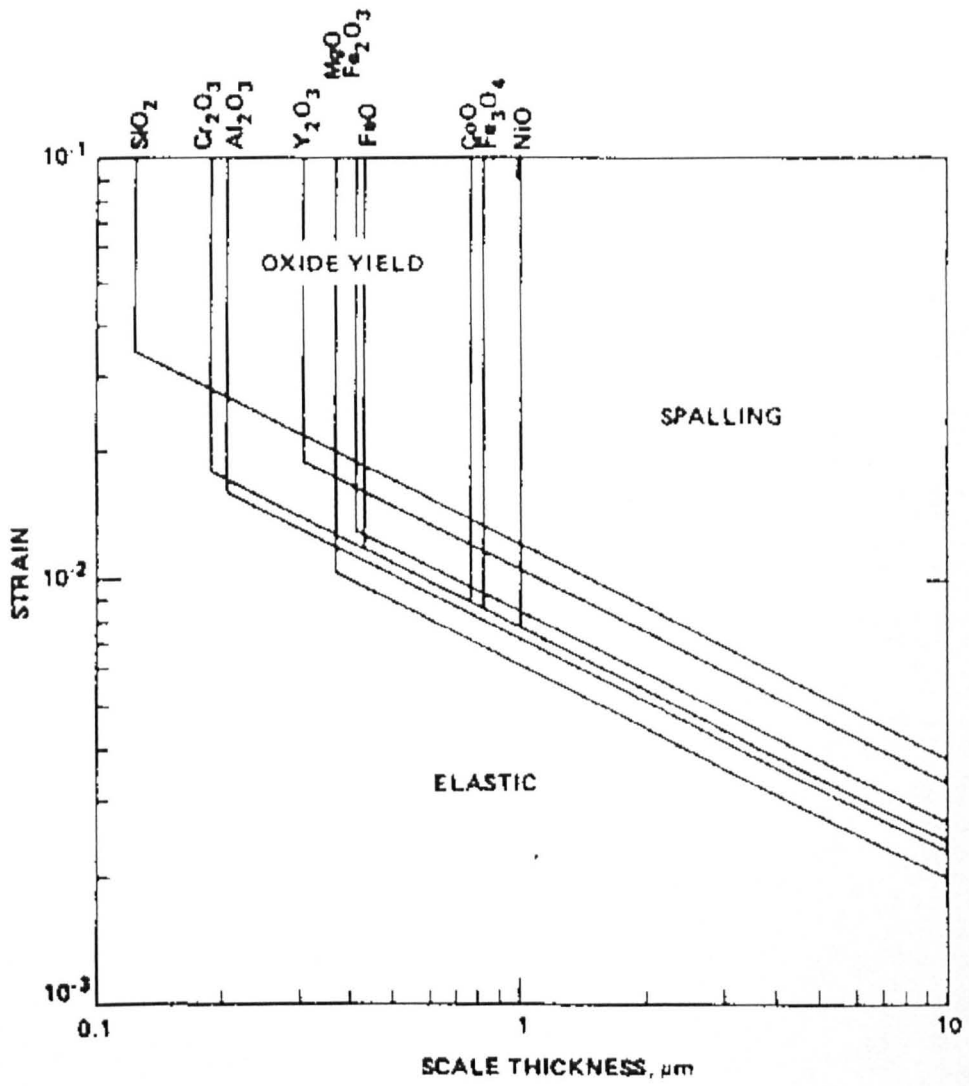


Fig. 2.8 Scale failure mode diagram showing fields of intact oxide (elastic) and of oxide failure (spalling) as a function of compressive strain and scale thickness for several oxides [Schütze, 1995]

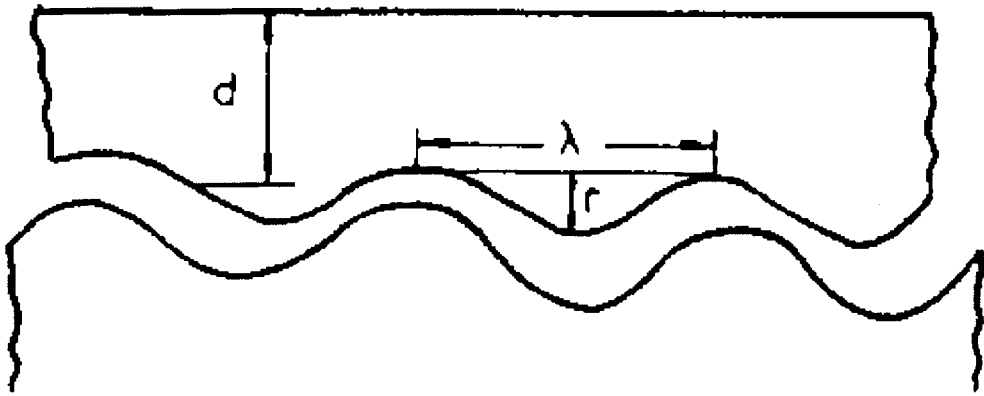


Fig. 2.9 Schematic description of the situation at a rough interface [Evans and Crumley, 1993]

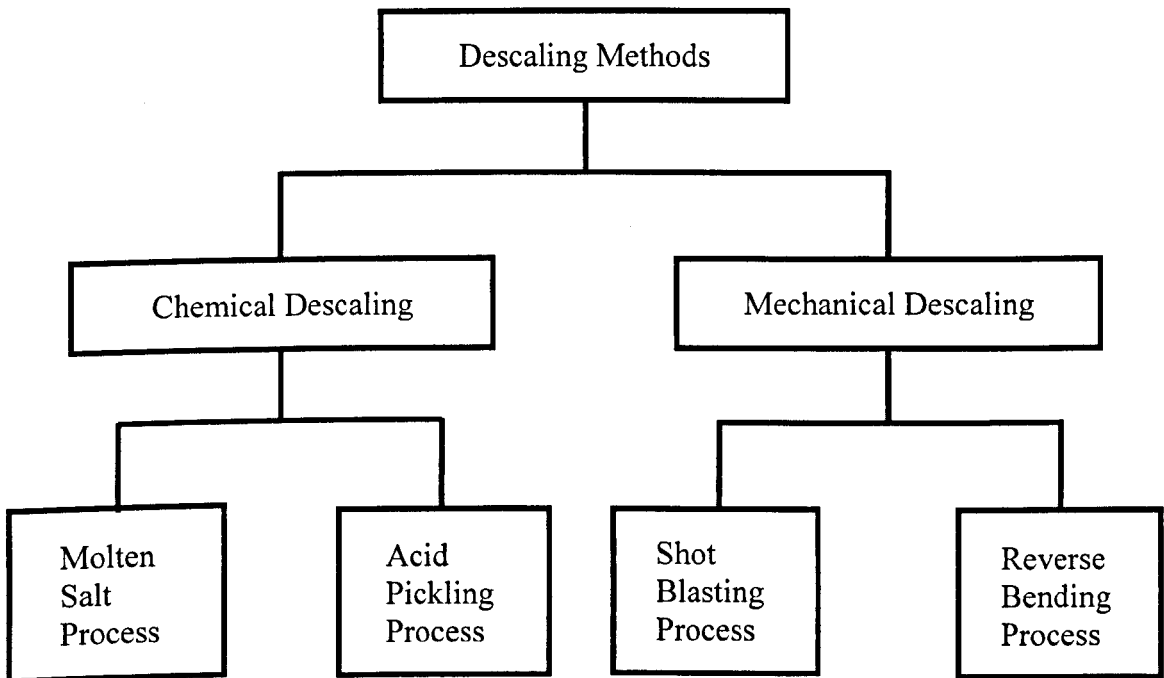


Fig. 2.10 Descaling methods block diagram

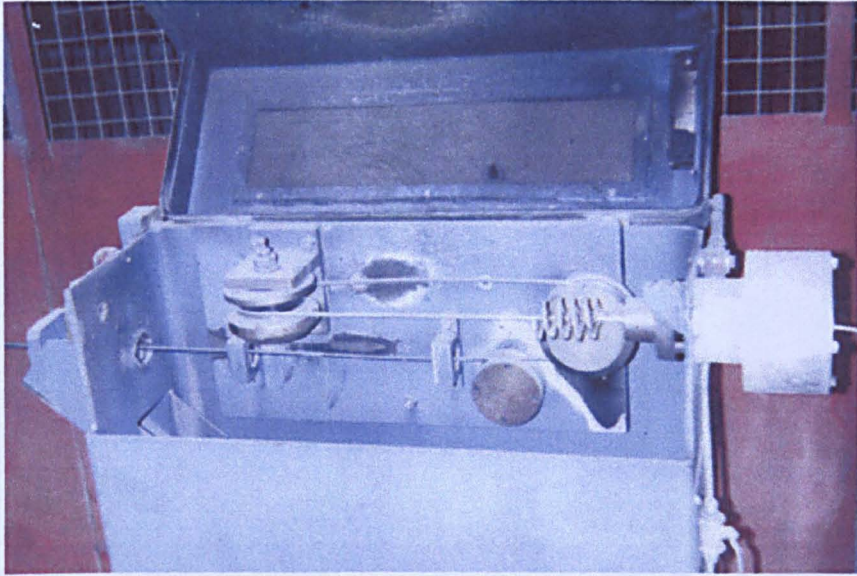


Fig. 2.11 Mechanical Descaling System of Tinsley Wire-Sheffield Ltd

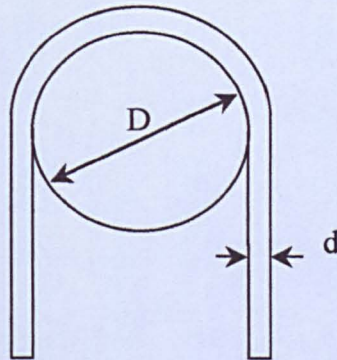


Fig. 2.12 Calculation for elongation in bending

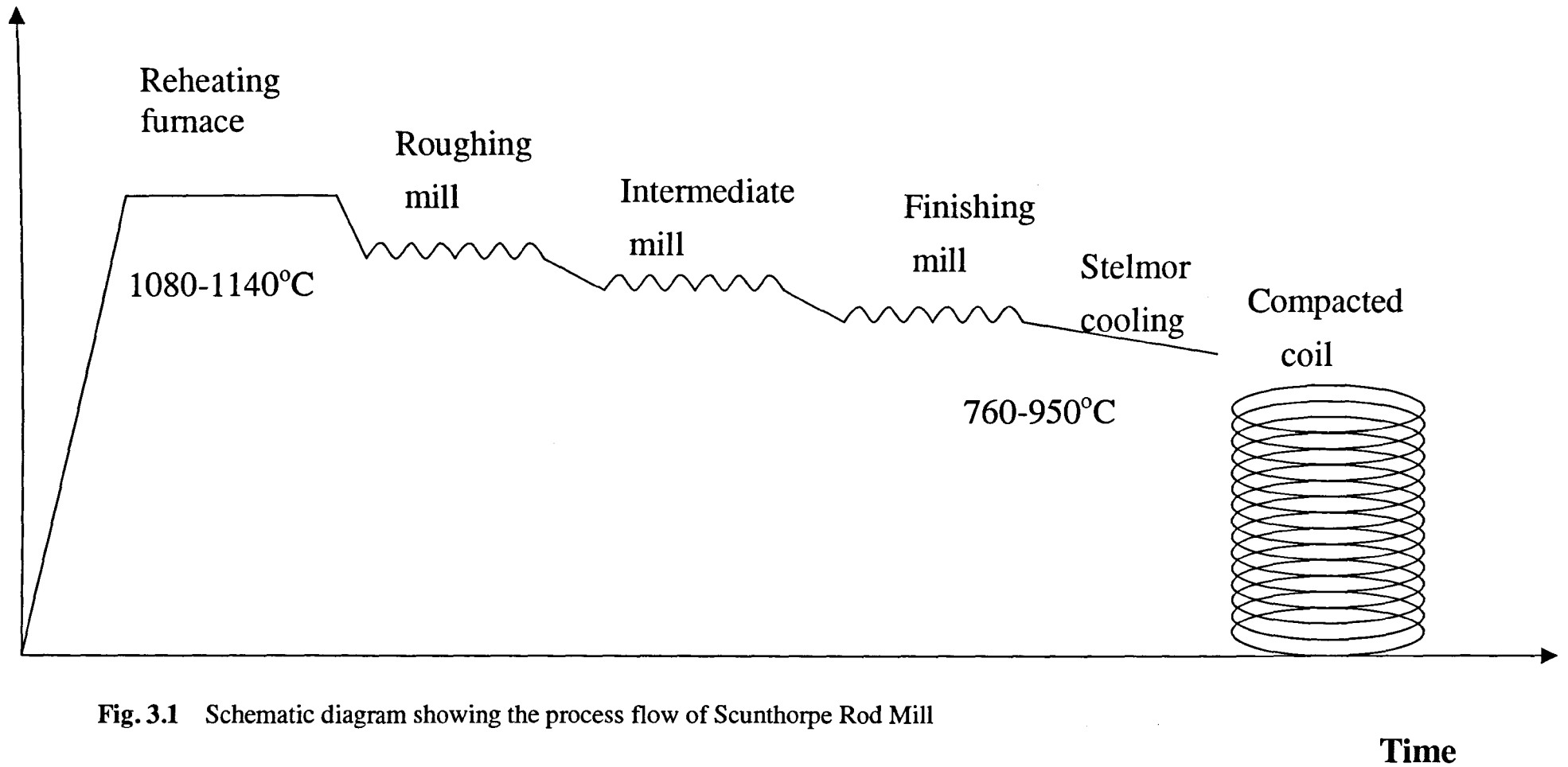


Fig. 3.1 Schematic diagram showing the process flow of Scunthorpe Rod Mill

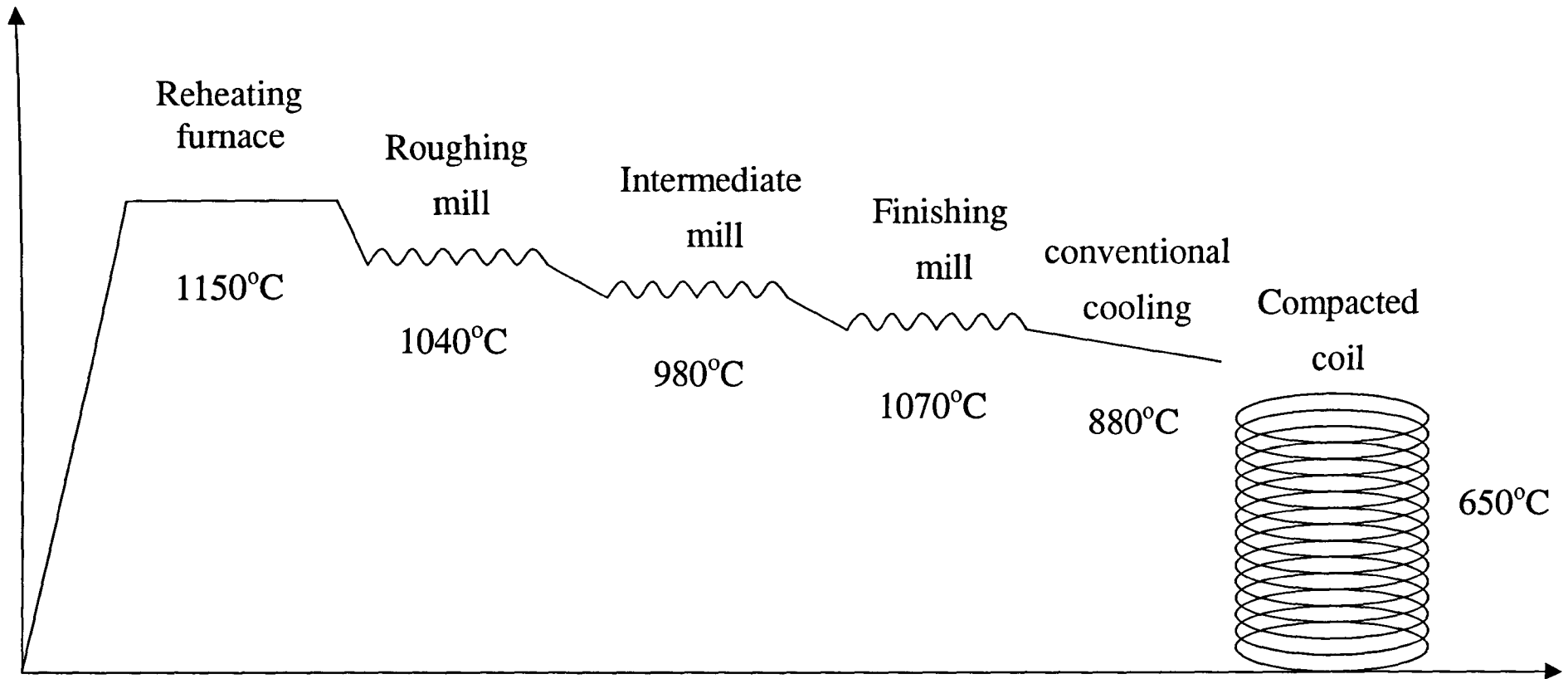


Fig. 3.2 Schematic diagram showing the process flow of Roundwood Rod Mill

Time

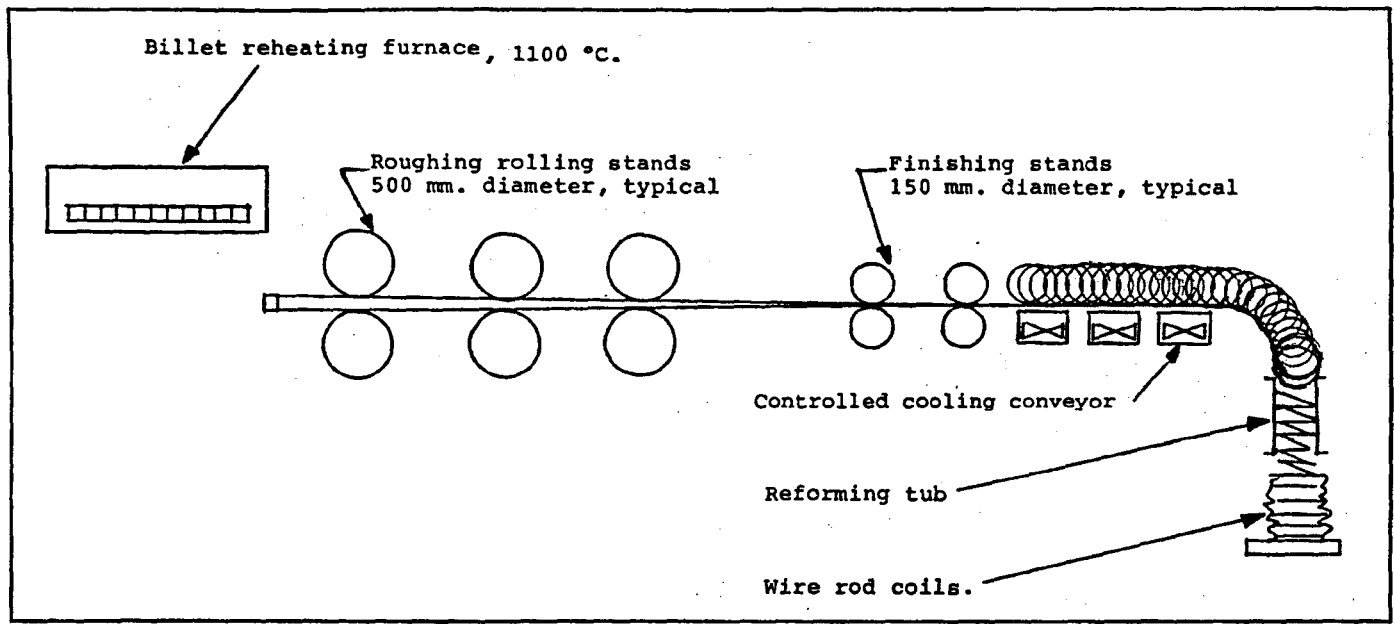


Fig. 3.3 Schematic diagram showing the rolling and coiling process in SRM and CRM.

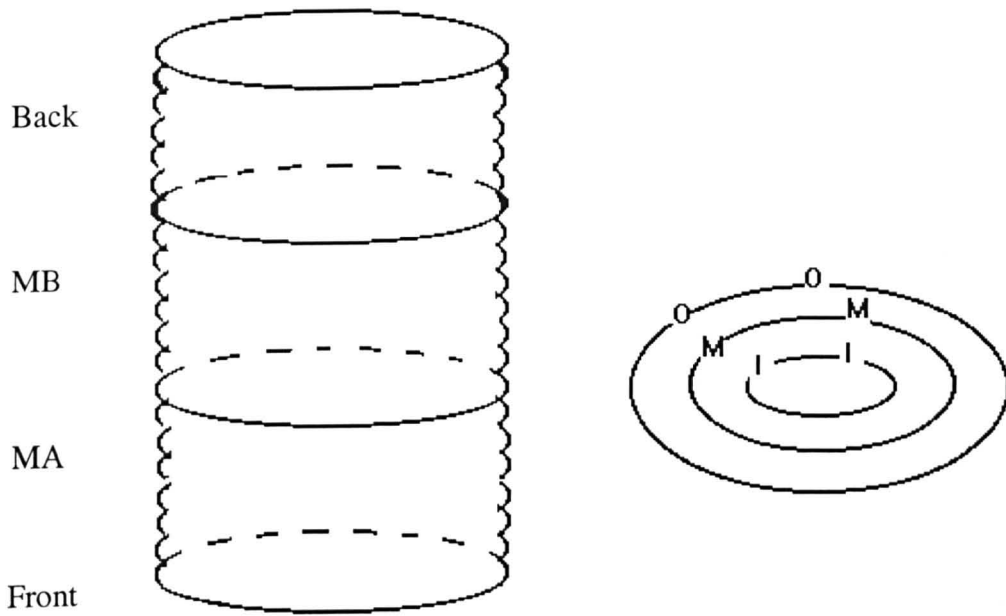
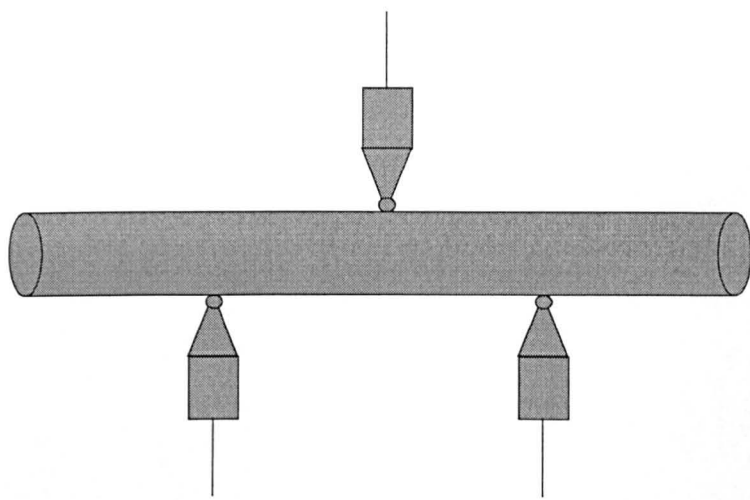
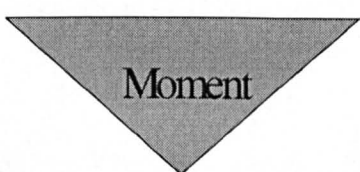


Fig. 3.4 Schematic diagram showing sampling positions in Roundwood Rod Mill

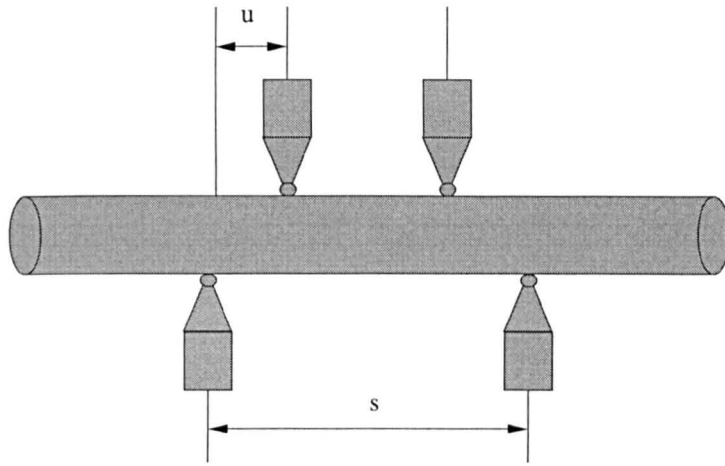


(a)

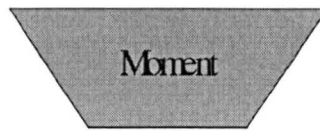


(b)

Fig. 3.5 Schematic illustration of 3-point bending test (a) and its bending moment distribution (b).



(a)



(b)

Fig. 3.6 Schematic diagram of 4-point bending test (a) and its bending moment distribution (b)

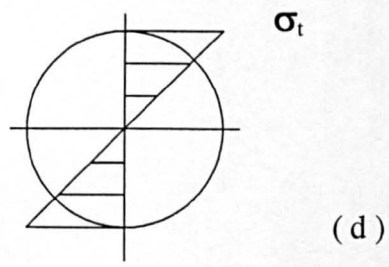
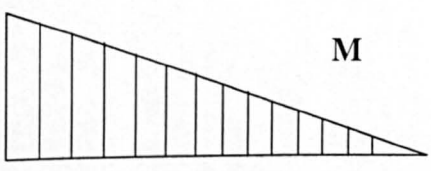
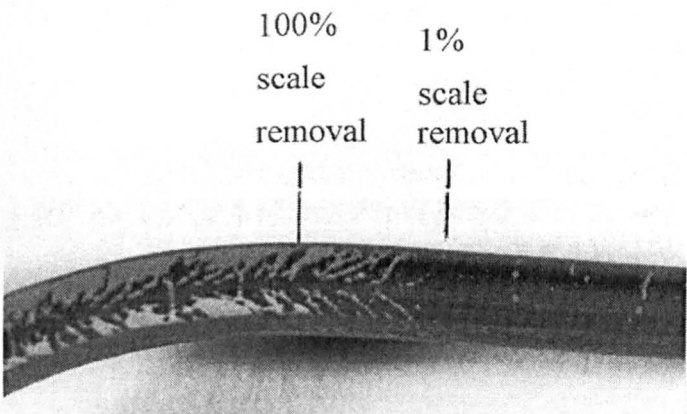
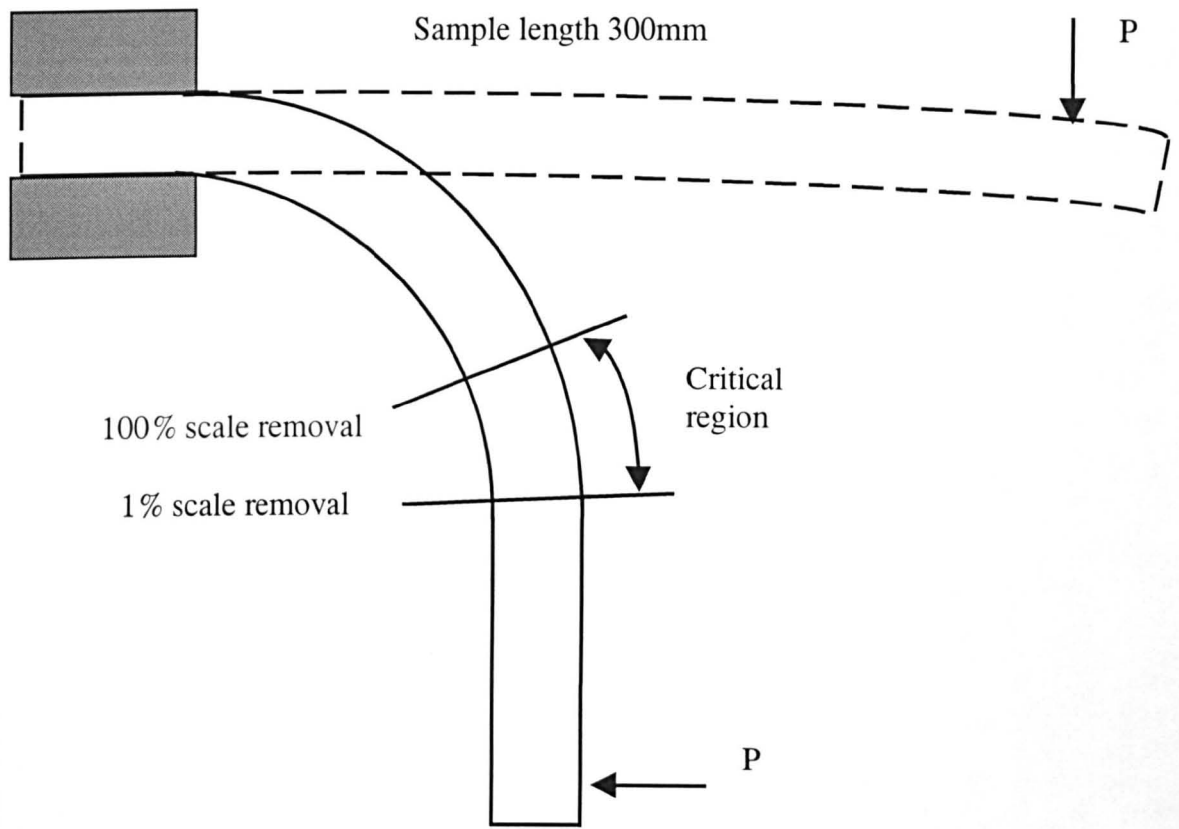


Fig. 3.7 Schematic representation of simple cantilever test (a), the definition of critical area (b), its bending moment distribution (c) and stress distribution in the cross section (d).

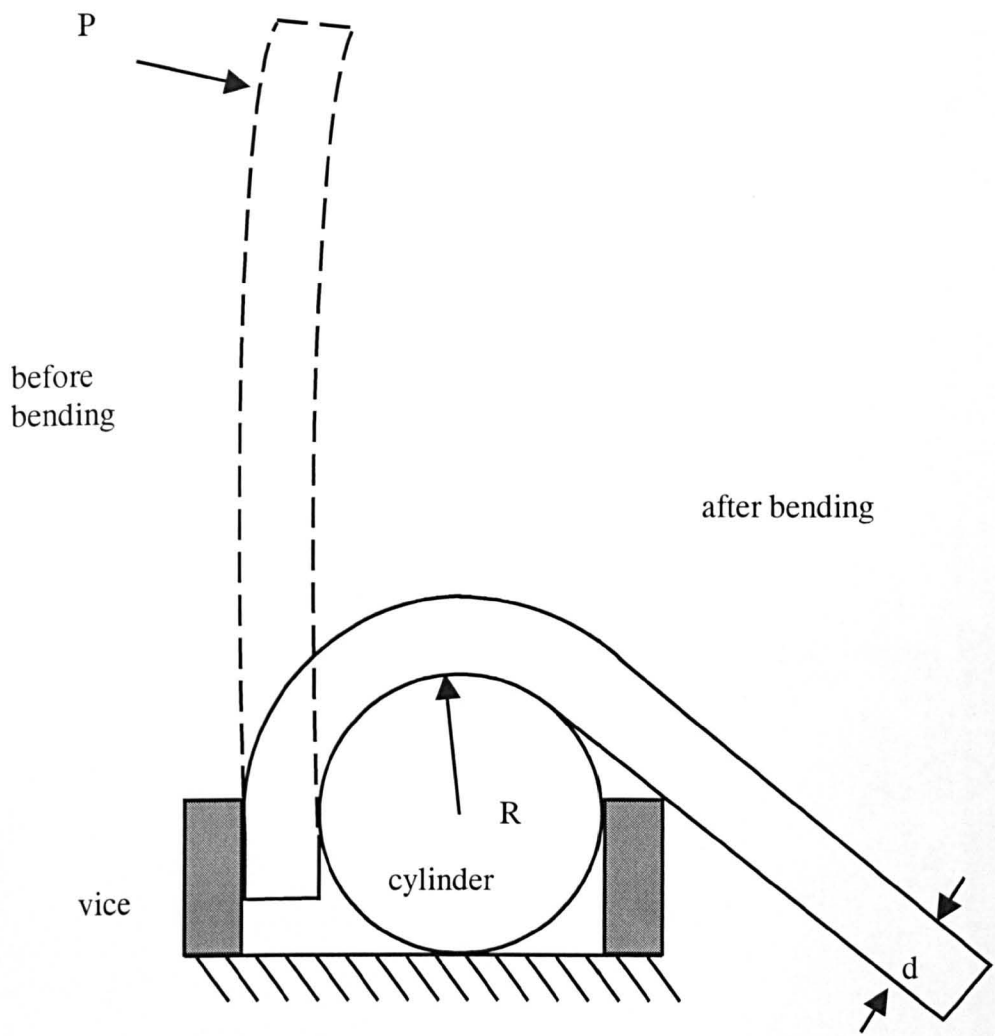


Fig. 3.8 Schematic diagram of constrained bending

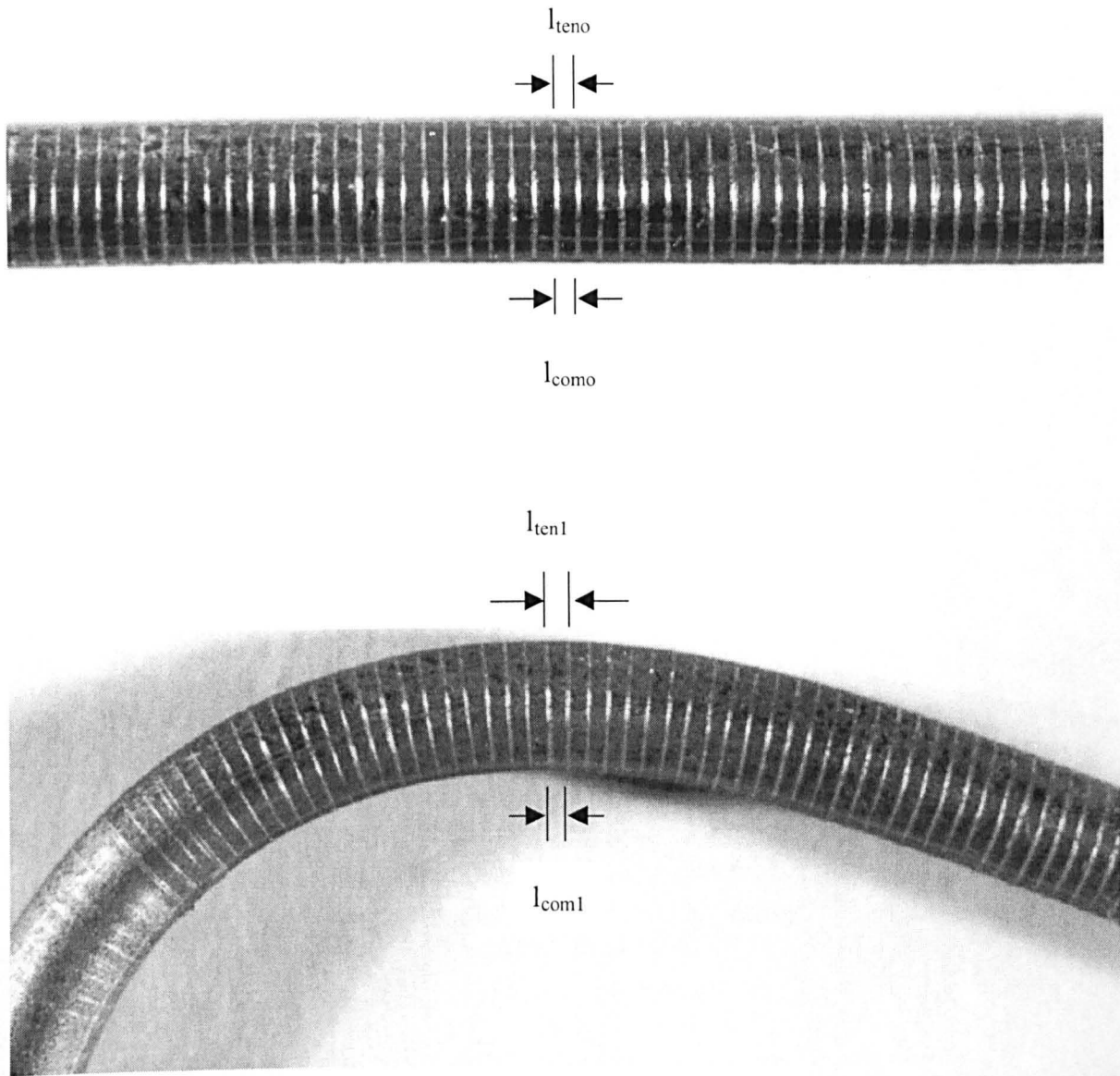


Fig. 3.9 Schematic illustration of scriber method

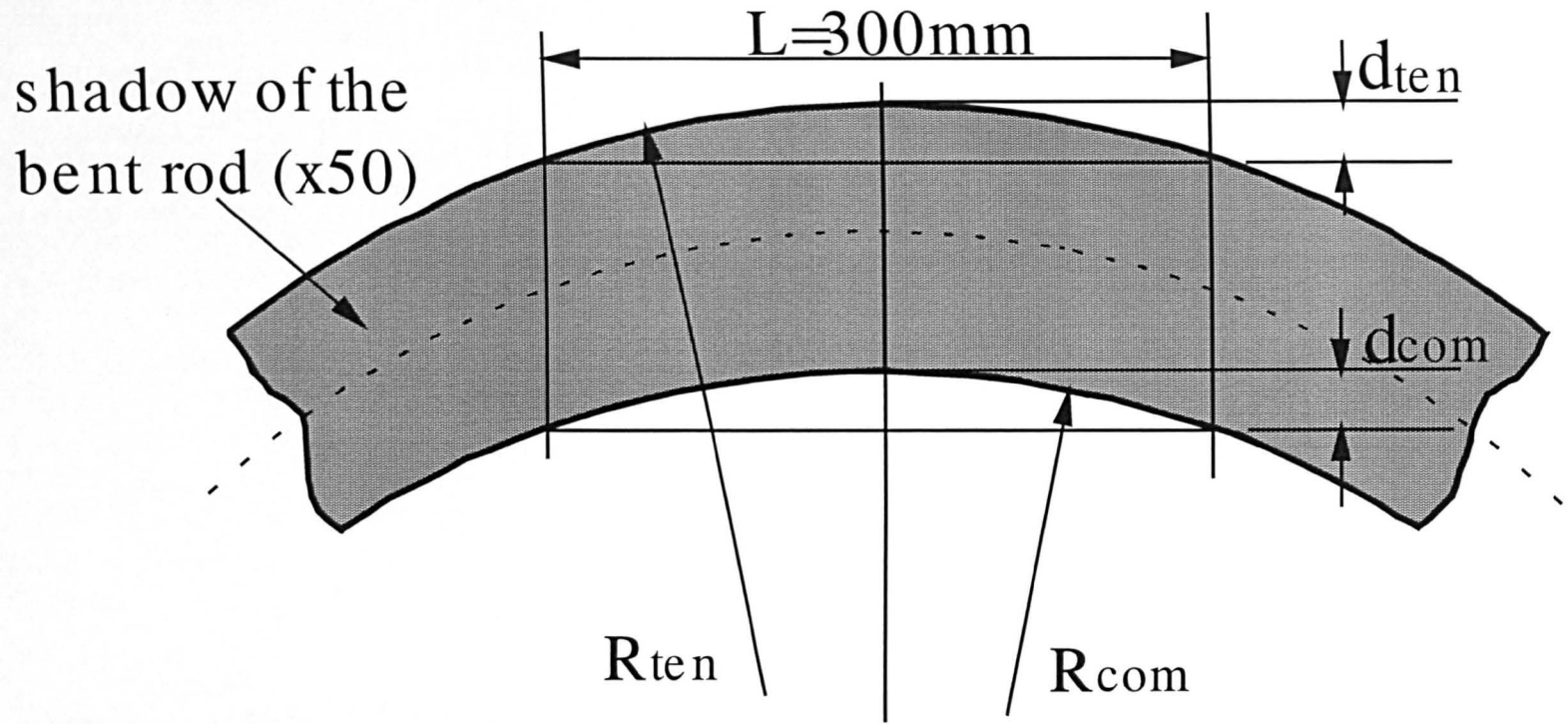
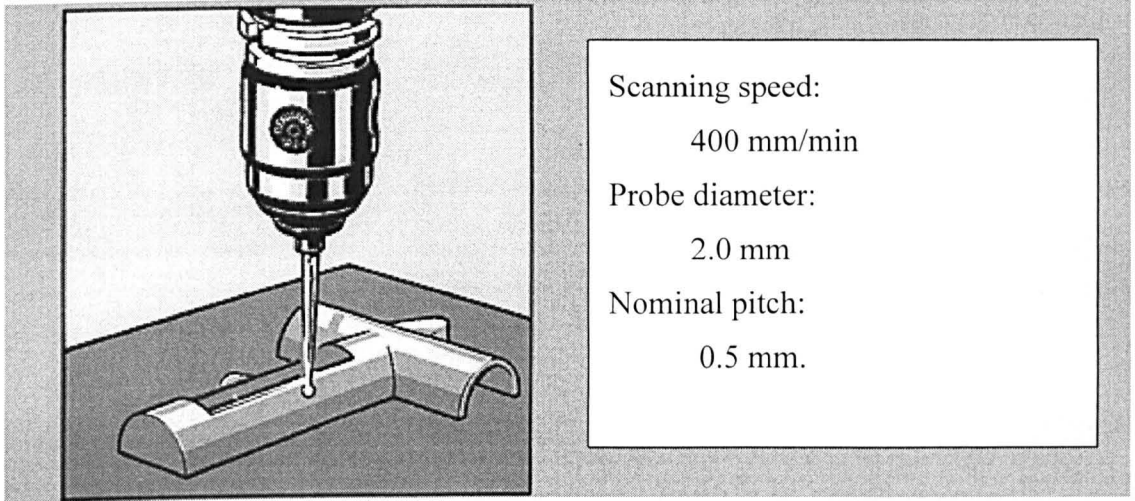
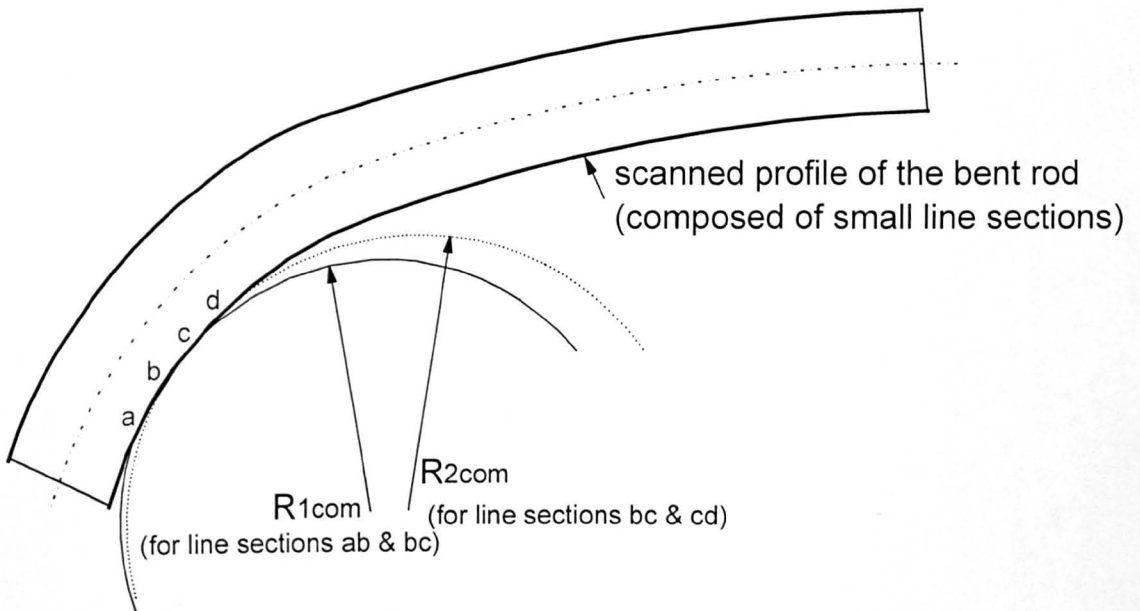


Fig. 3.10 Schematic representative of the relationship between R_{ten}/R_{com} , L and d_{ten}/d_{com} in shadowgraph method



(a)



(b)

Fig. 3.11 Schematic representation of scanning system

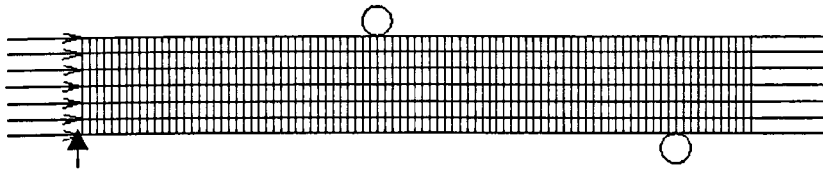


Fig.3.12 4-point bending model: schematic representation of finite element mesh and boundary conditions

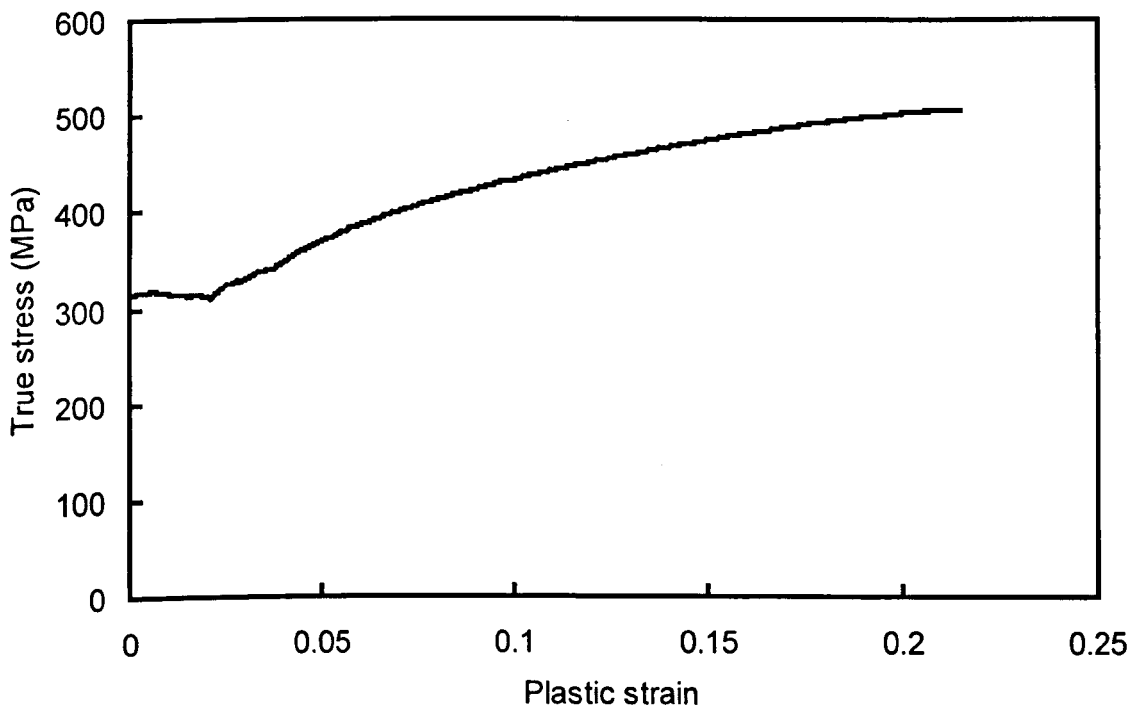


Fig. 3.13 Work hardening curve of K08 steel

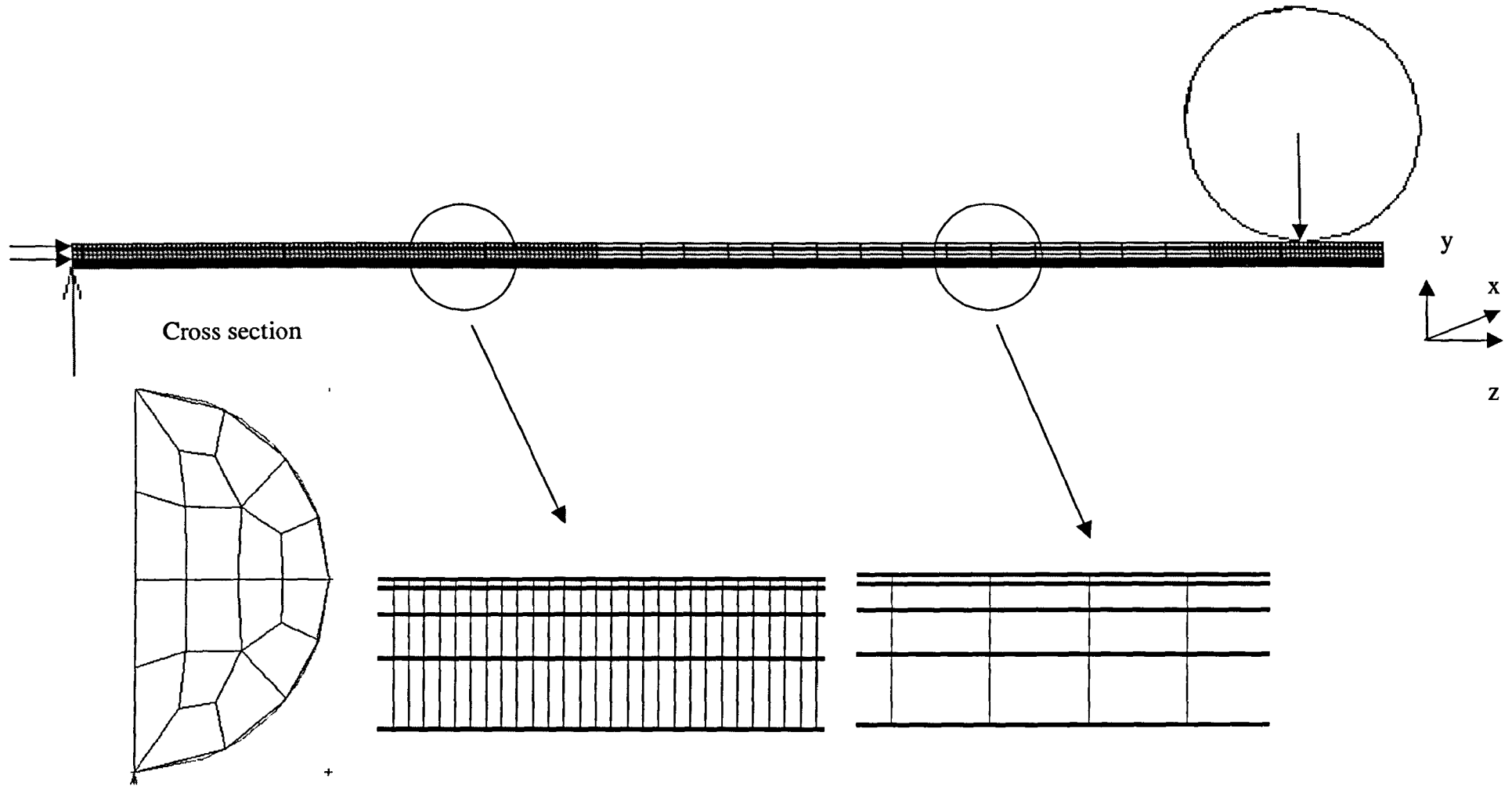


Fig.3.14 Cantilever bending test model: schematic representation of finite element mesh and boundary condition

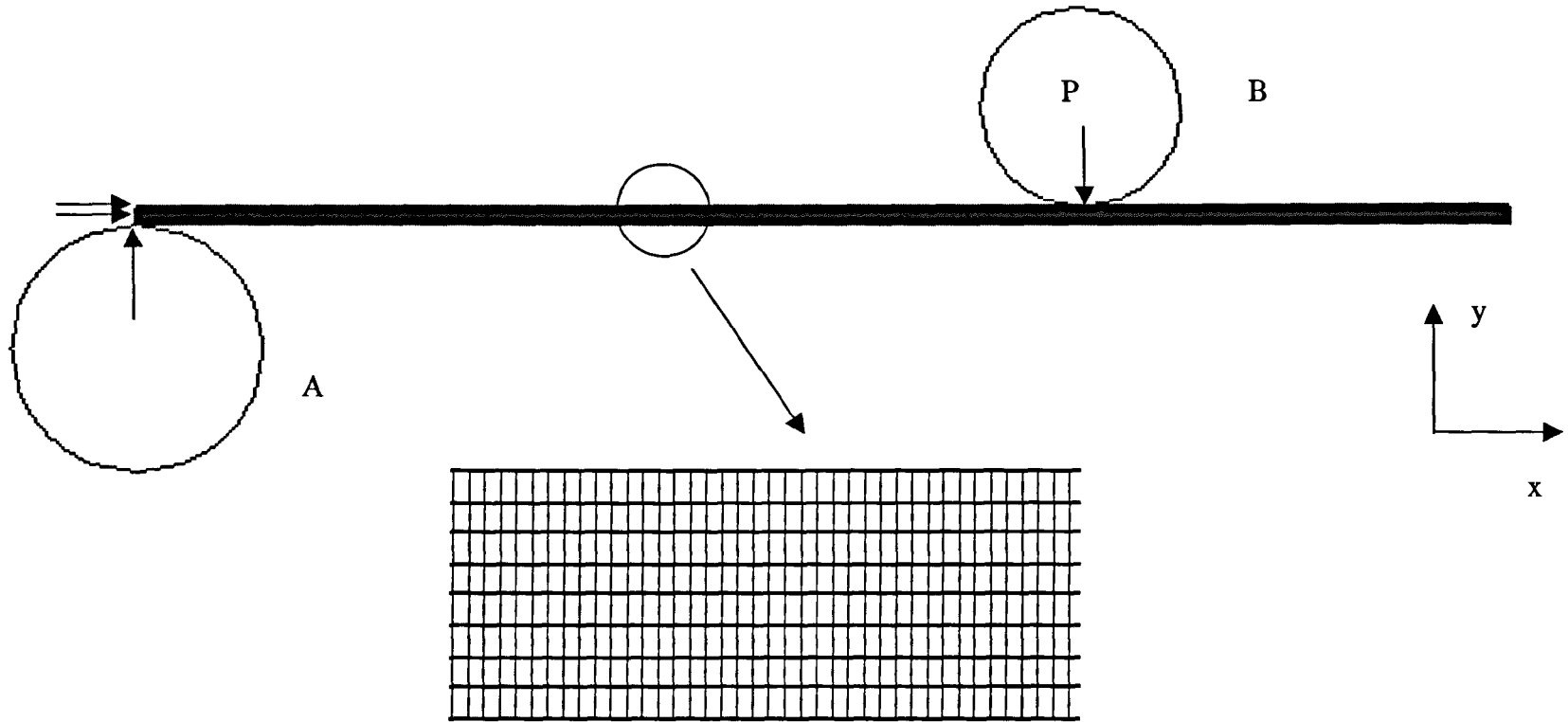


Fig.3.15 Constrained bending test model: schematic representation of the finite element mesh and boundary condition

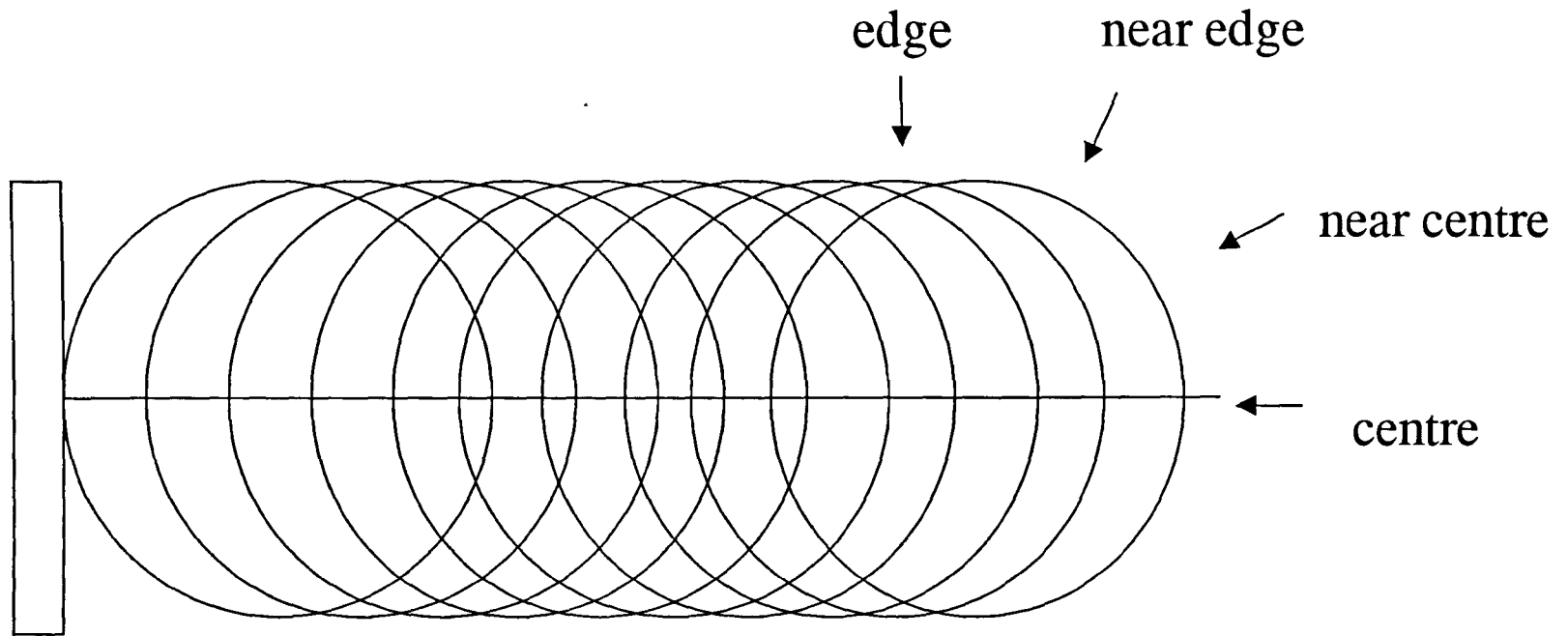


Fig. 3.16 Schematic diagram showing sampling positions in aging time test and scale thickness measurement

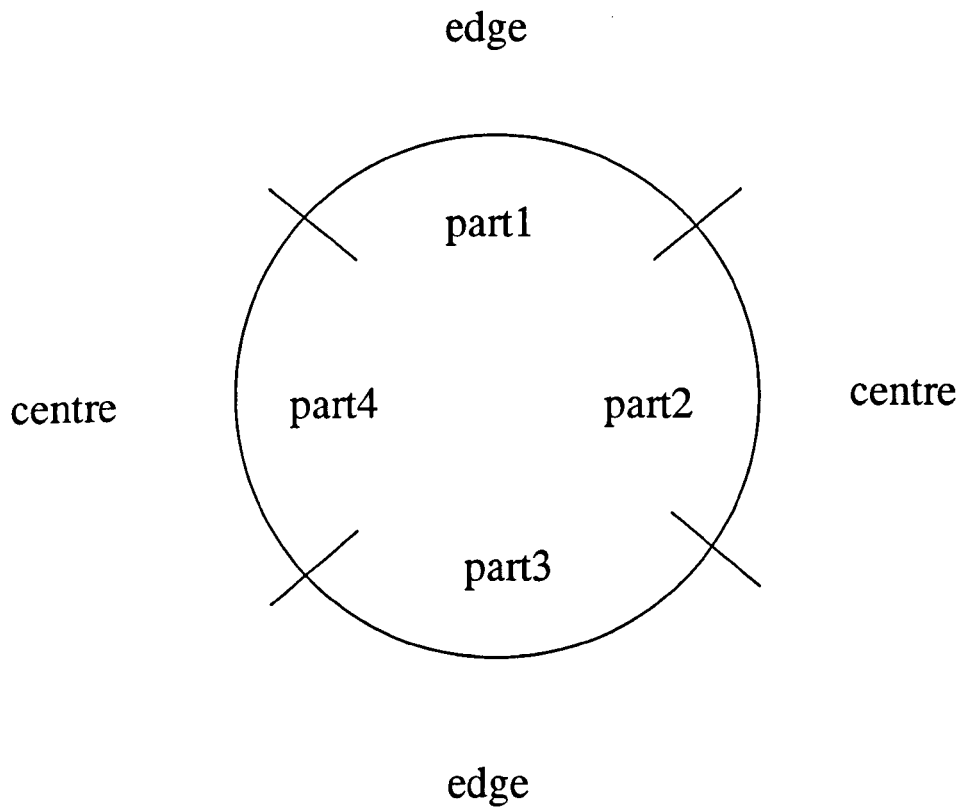


Fig. 3.17 Schematic illustration of sampling position in ageing time test

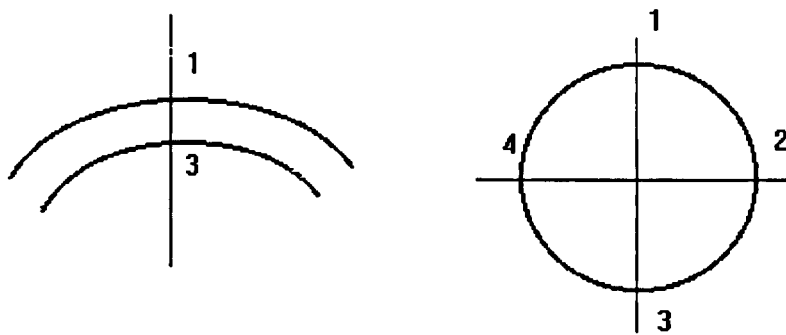


Fig. 3.18 Schematic representation of the measured points for scale thickness of the rod sample supplied by Roundwood Rod Mill in cross section



900°C×10min
without gas
protection



900°C×5min
without gas
protection



900°C×20min
without gas
protection

(a) top view



900°C×10min
without gas
protection



900°C×5min
without gas
protection



900°C×20min
without gas
protection

(b) bottom view

Fig. 4.1 Primary scale formed on the low carbon steel flat sample surfaces in the laboratory furnace (a) top view, (b) bottom view

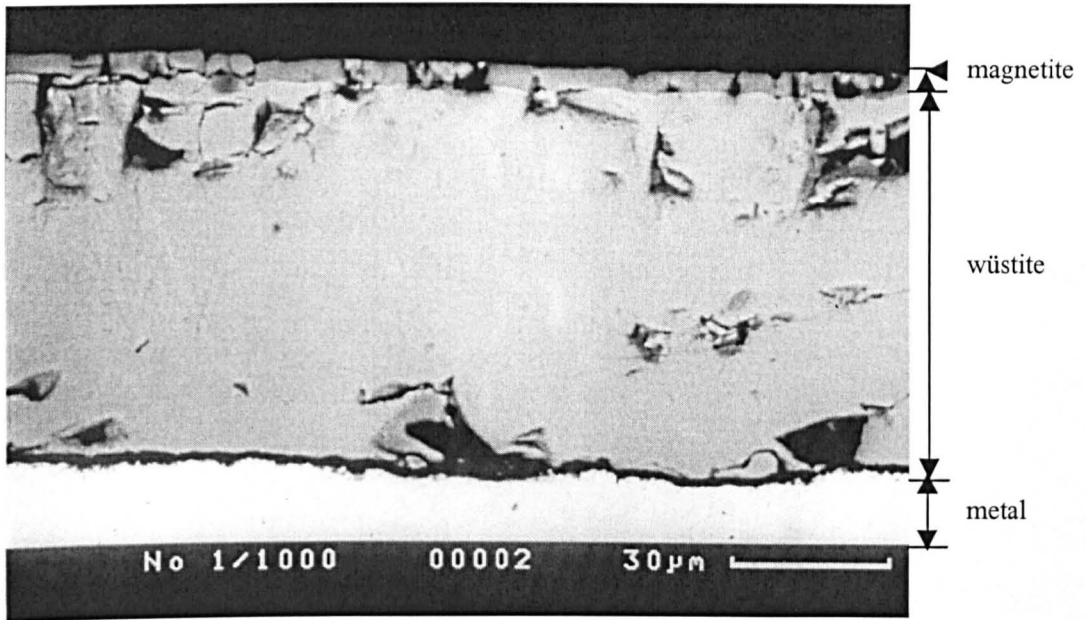
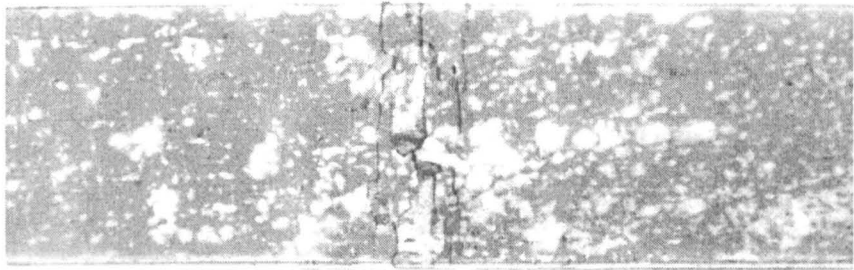
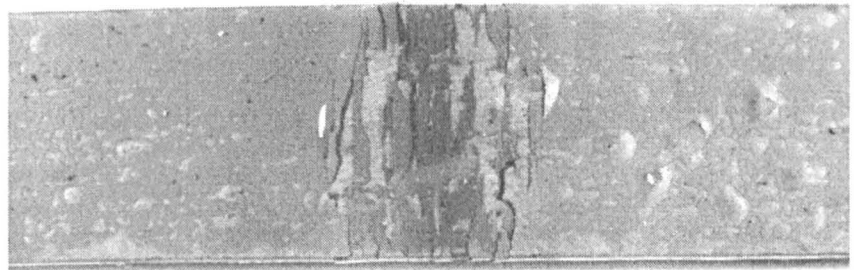


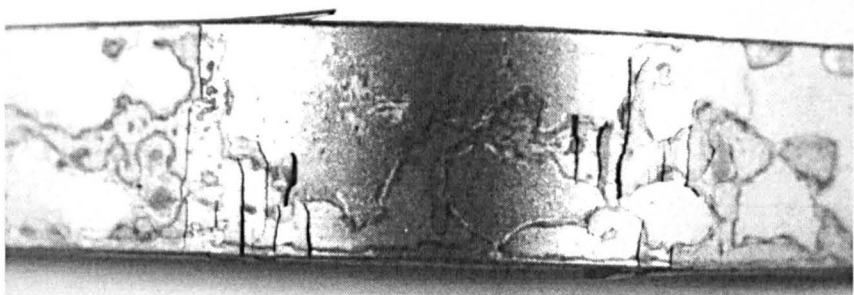
Fig. 4.2 Cross-sectional BEI (Back-scattered electron image) SEM micrograph of the scale on the low carbon steel flat sample surface (formed in the laboratory furnace, 1000°C×2min with gas protection and air cooled)



(a) 1000°C×2min span=87mm
with gas protection deflection =3.5mm



(b) 1000°C×2min span=87mm
with gas protection deflection =7mm



(c) 1000°C×5min span=87mm
with gas protection deflection =large

Fig.4.3 The cracking and removal behaviour of the scale on the low carbon steel flat sample surface under different strains in 3-point bending tests

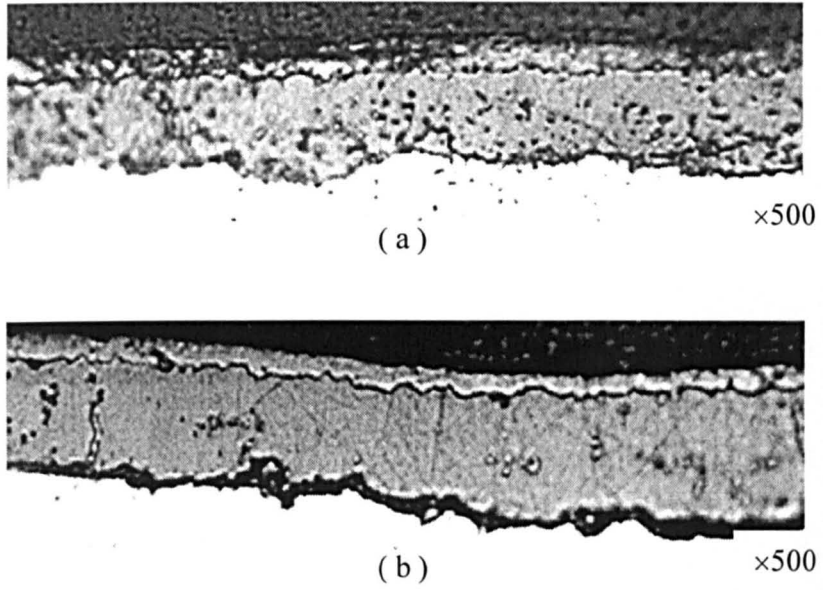
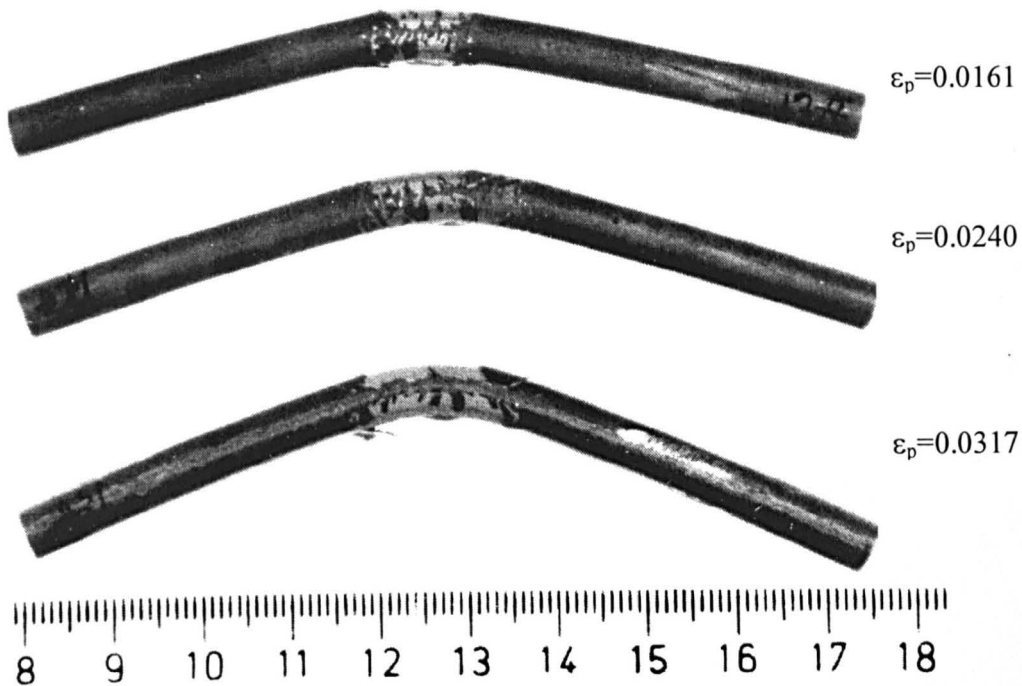
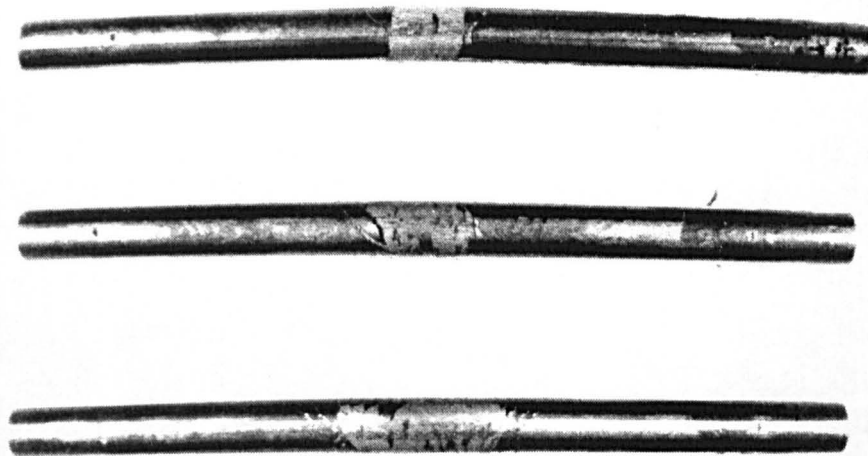


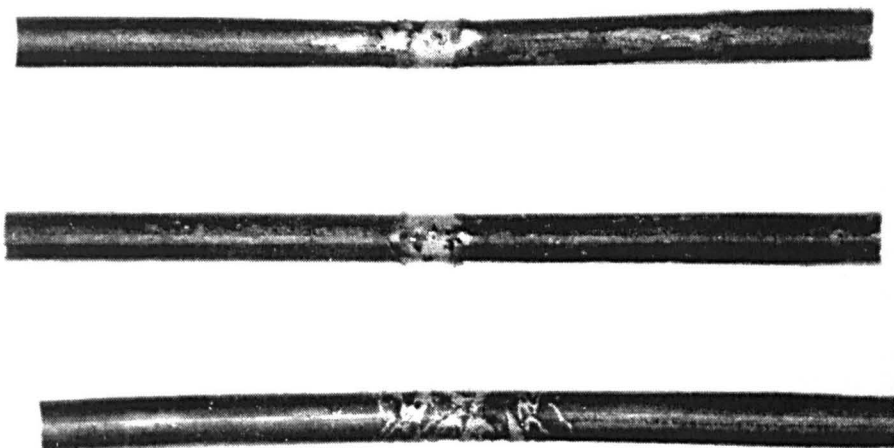
Fig. 4.4 Etched cross-sectional optical micrograph of the scale on the surfaces of the commercial steel (a) K58 and (b) K08 rods, supplied by Scunthorpe Rod Mill (the samples were etched by 2% HCl in alcohol for 15 seconds before the photographs were taken).



(a) side view



(b) top view



(c) bottom view

Fig. 4.5 Scale cracking and removal behaviour on commercial steel rod (D12) surface in 3-point bending tests (deflection and spans between two anvils were shown in Table 4.3), rods ($\phi 6.5\text{mm}$) were supplied by Scunthorpe Rod Mill.

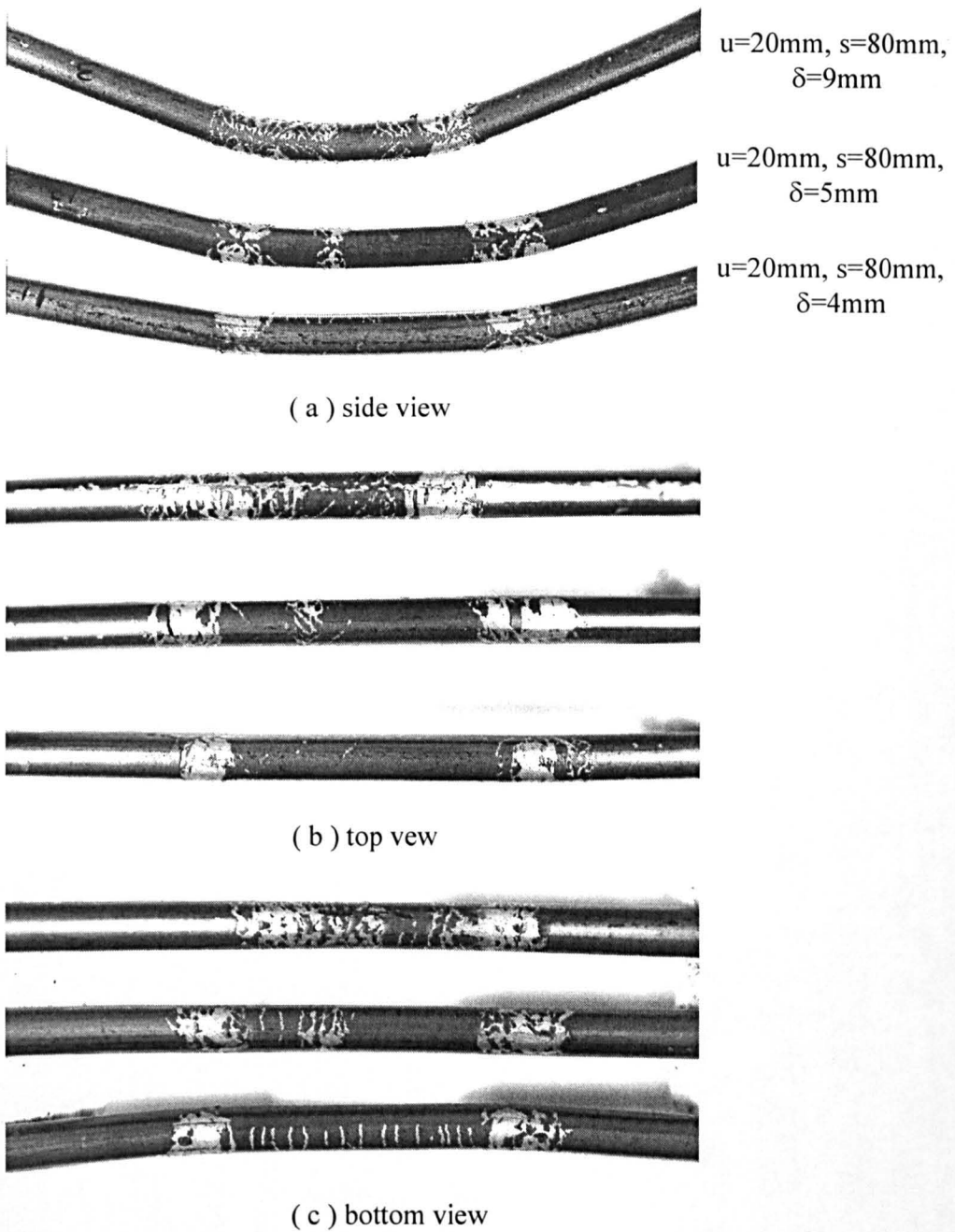
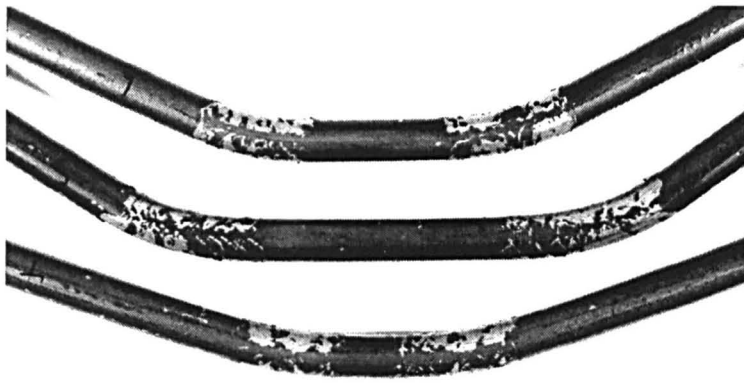


Fig. 4.6 The effect of deflections on the scale cracking and removal behaviour of K08 steel rod in 4-point bending tests ($f=5\text{mm/min}$), rods ($\phi 6.5\text{mm}$) were supplied by Scunthorpe Rod Mill, laying temperature 830°C .

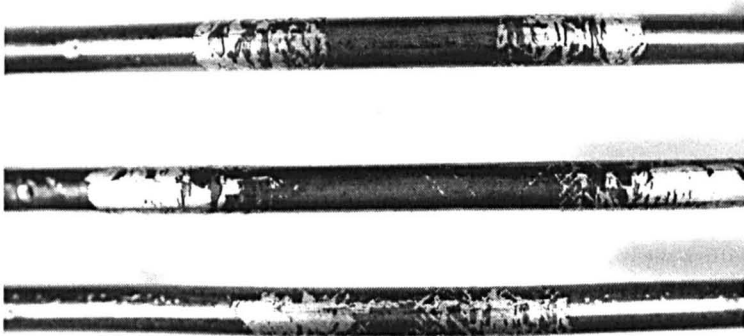


$u=20\text{mm}$, $s=80\text{mm}$,
 $\delta=9\text{mm}$

$u=15\text{mm}$, $s=90\text{mm}$,
 $\delta=9\text{mm}$

$u=30\text{mm}$, $s=90\text{mm}$,
 $\delta=9\text{mm}$

(a) side view

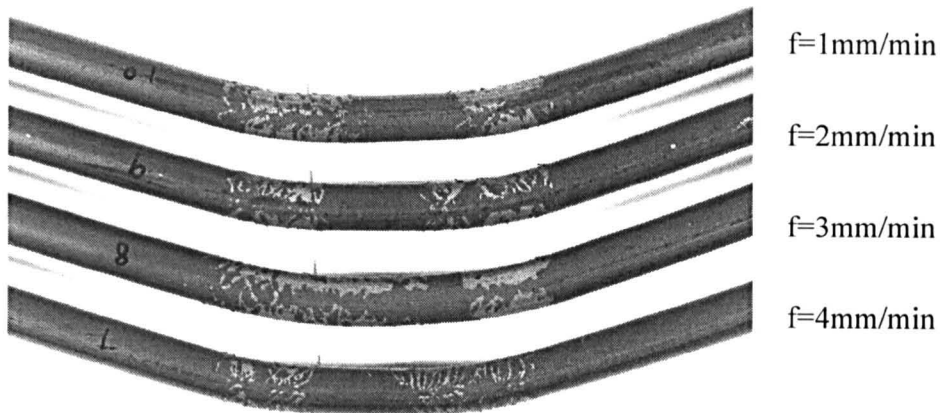


(b) top view

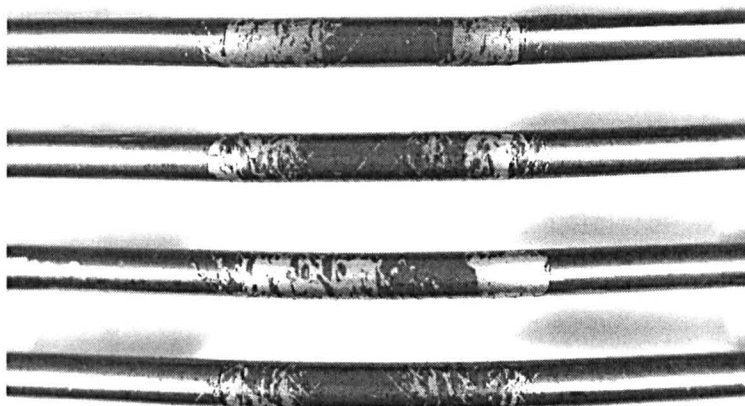


(c) bottom view

Fig 4.7 The effect of the distance between inner and outer rollers on the scale cracking and removal behaviour of K08 steel rod in 4-point bending tests ($f=5\text{mm/min}$), rods ($\phi 6.5\text{mm}$) were supplied by Scunthorpe Rod Mill, laying temperature 830°C .



(a) side view



(b) top view



(c) bottom view

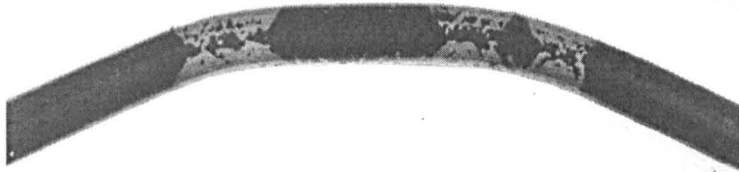
Fig.4.8 The effect of cross head speed on the scale cracking and removal behaviour of K08 steel rod in 4-point bending tests ($u=30\text{mm}$, $s=90\text{mm}$, $\delta=9\text{mm}$), rods ($\phi 6.5\text{mm}$) were supplied by Scunthorpe Rod Mill, laying temperature 830°C .



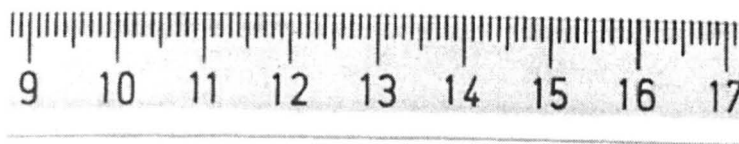
$u=20\text{mm}$, $s=80\text{mm}$,
 $\delta=3.3\text{mm}$, $\epsilon_p=0.0284$



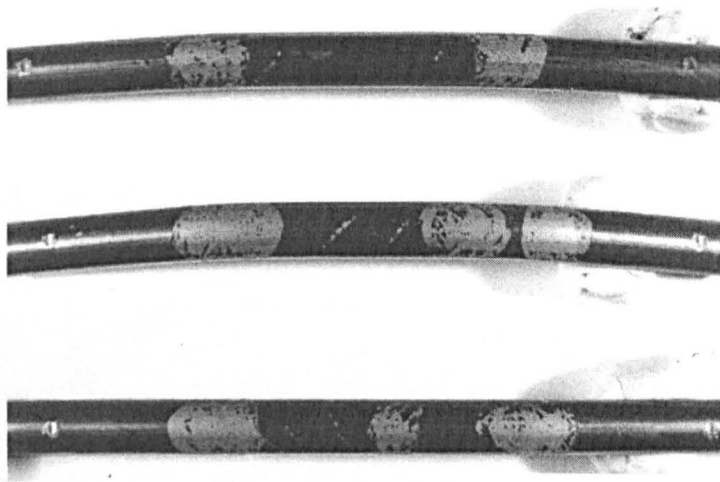
$u=20\text{mm}$, $s=80\text{mm}$,
 $\delta=4.9\text{mm}$, $\epsilon_p=0.0473$



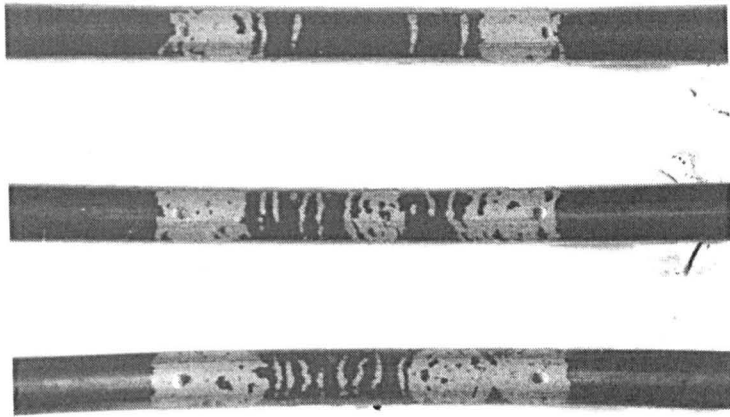
$u=20\text{mm}$, $s=80\text{mm}$,
 $\delta=6.55\text{mm}$, $\epsilon_p=0.0552$



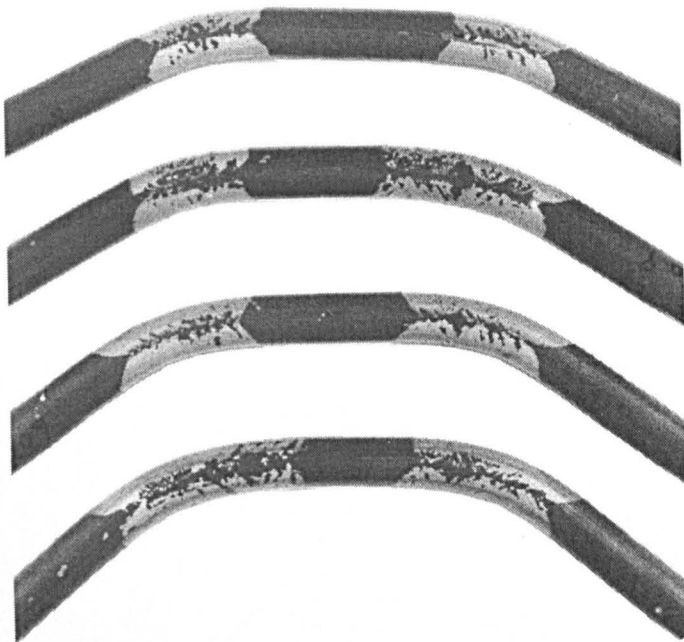
(a) side view



(b) top view



(c) bottom view

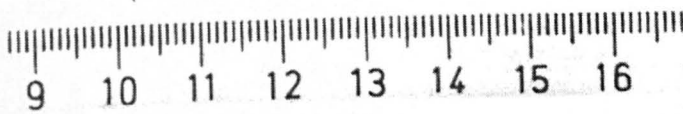


$u=20\text{mm}$, $s=80\text{mm}$,
 $\delta=8.2\text{mm}$, $\epsilon_p=0.0911$

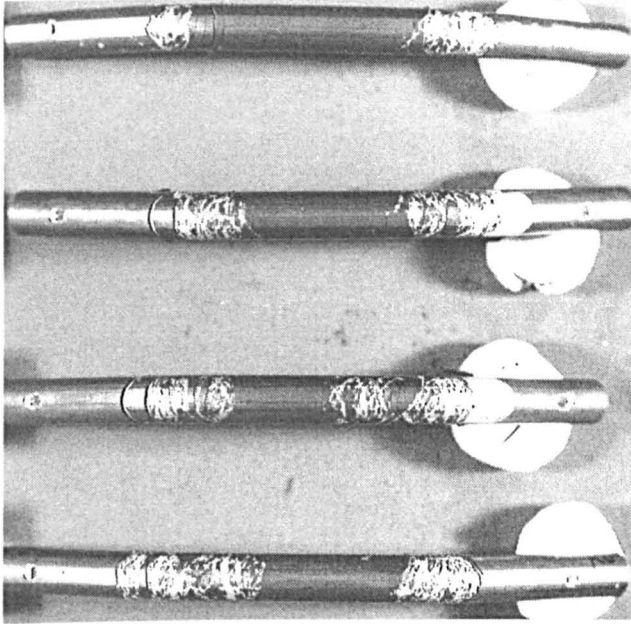
$u=20\text{mm}$, $s=80\text{mm}$,
 $\delta=9.85\text{mm}$, $\epsilon_p=0.1073$

$u=20\text{mm}$, $s=80\text{mm}$,
 $\delta=11.15\text{mm}$, $\epsilon_p=0.1178$

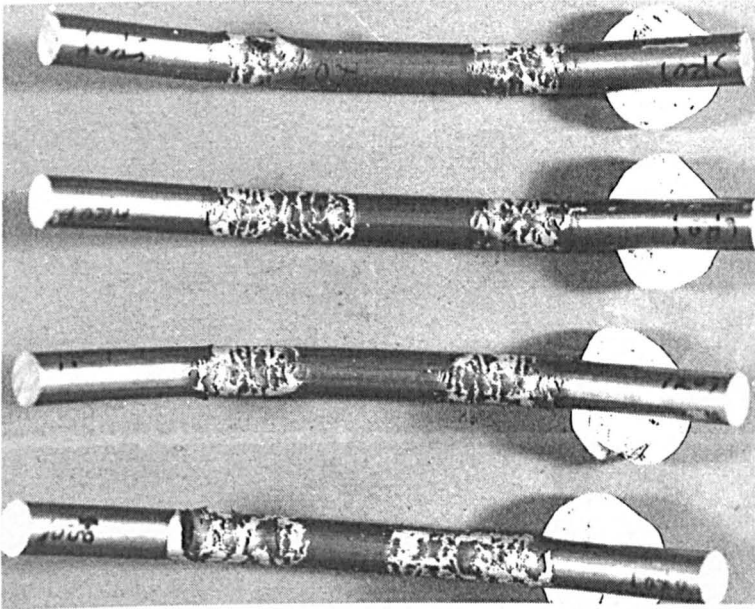
$u=20\text{mm}$, $s=80\text{mm}$,
 $\delta=13.15\text{mm}$, $\epsilon_p=0.1229$



(d) side view

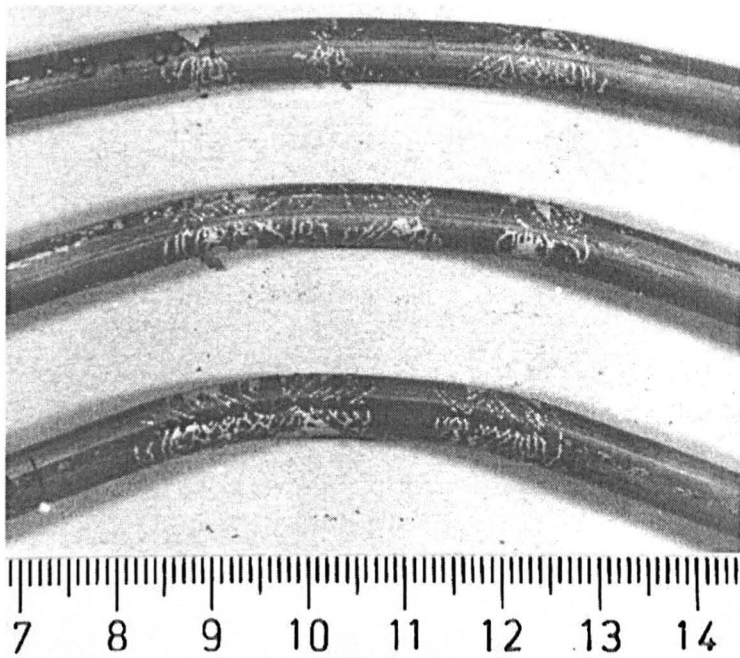


(e) top view



(f) bottom view

Fig. 4.9 The scale cracking and removal behaviour of R09 steel rod in 4-point bending tests, rods ($\phi 6.5\text{mm}$) were supplied by Scunthorpe Rod Mill.

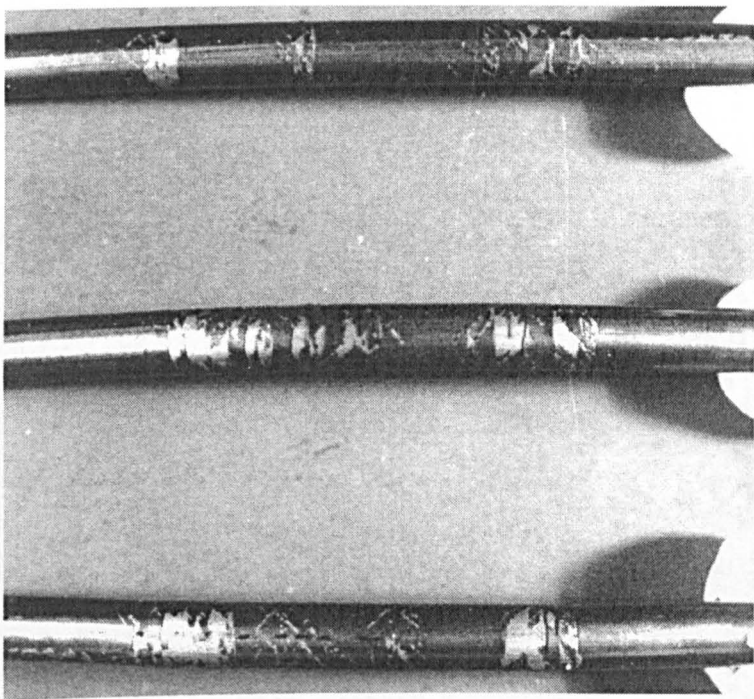


$u=20\text{mm}$, $s=80\text{mm}$,
 $\delta=3.3\text{mm}$, $\epsilon_p=0.0284$

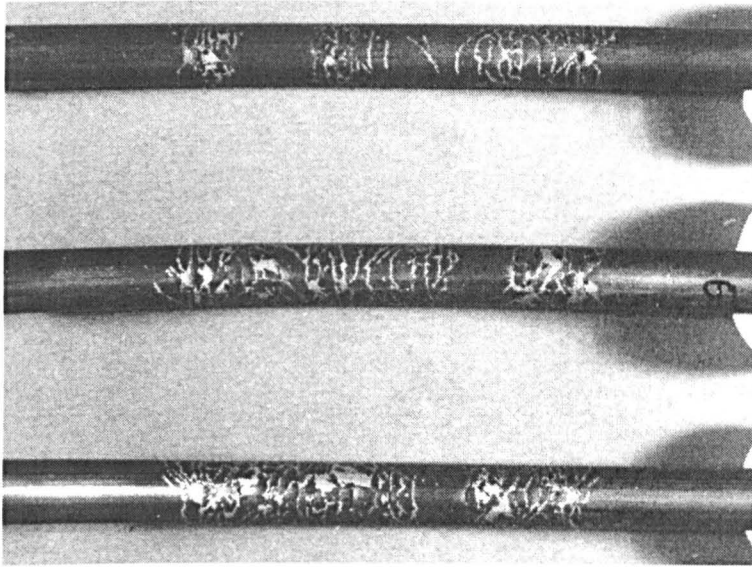
$u=20\text{mm}$, $s=80\text{mm}$,
 $\delta=4.9\text{mm}$, $\epsilon_p=0.0473$

$u=20\text{mm}$, $s=80\text{mm}$,
 $\delta=6.55\text{mm}$, $\epsilon_p=0.0552$

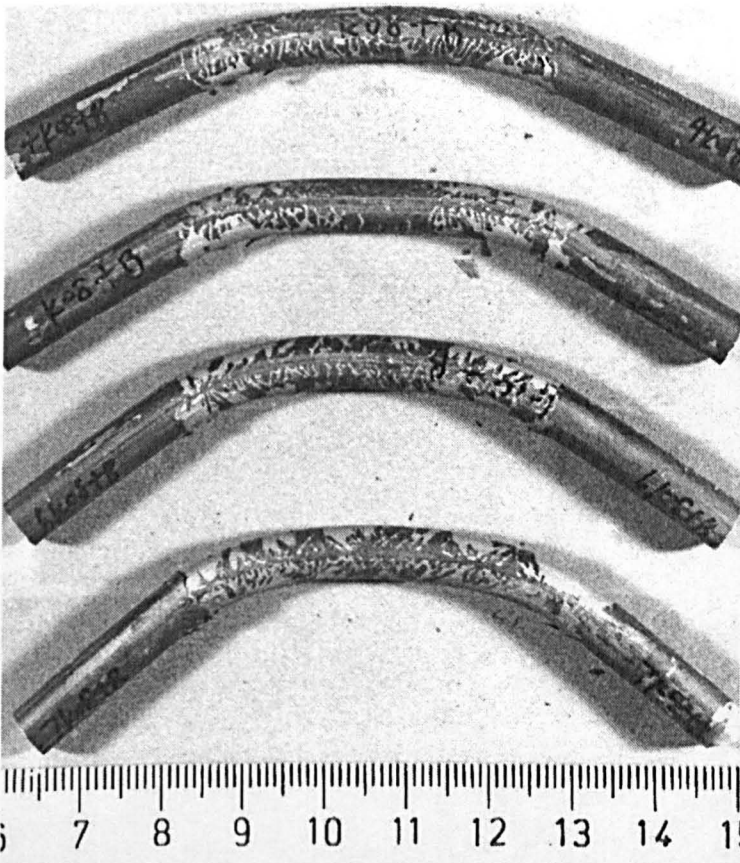
(a) side view



(b) top view



(c) bottom view



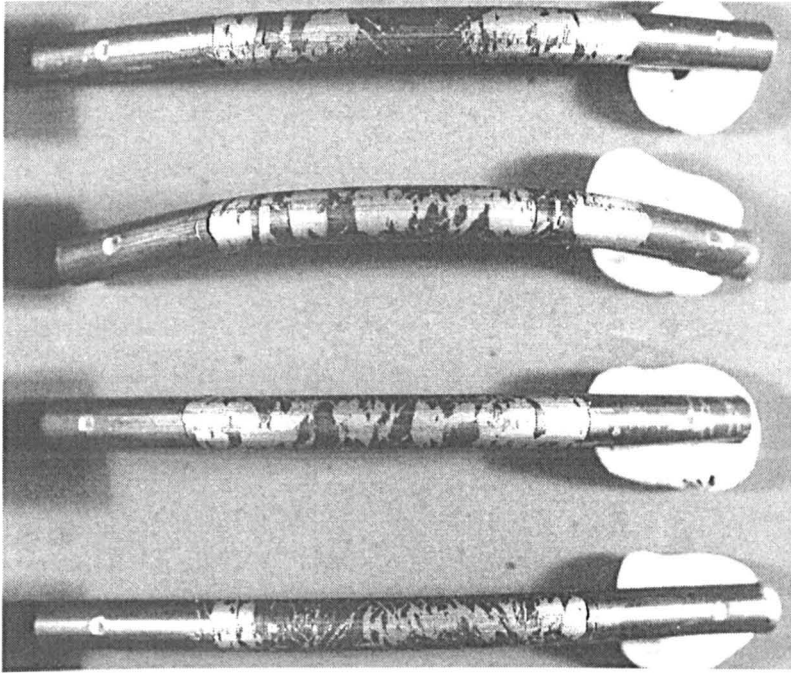
$u=20\text{mm}$, $s=80\text{mm}$,
 $\delta=8.2\text{mm}$, $\epsilon_p=0.0911$

$u=20\text{mm}$, $s=80\text{mm}$,
 $\delta=9.85\text{mm}$, $\epsilon_p=0.1073$

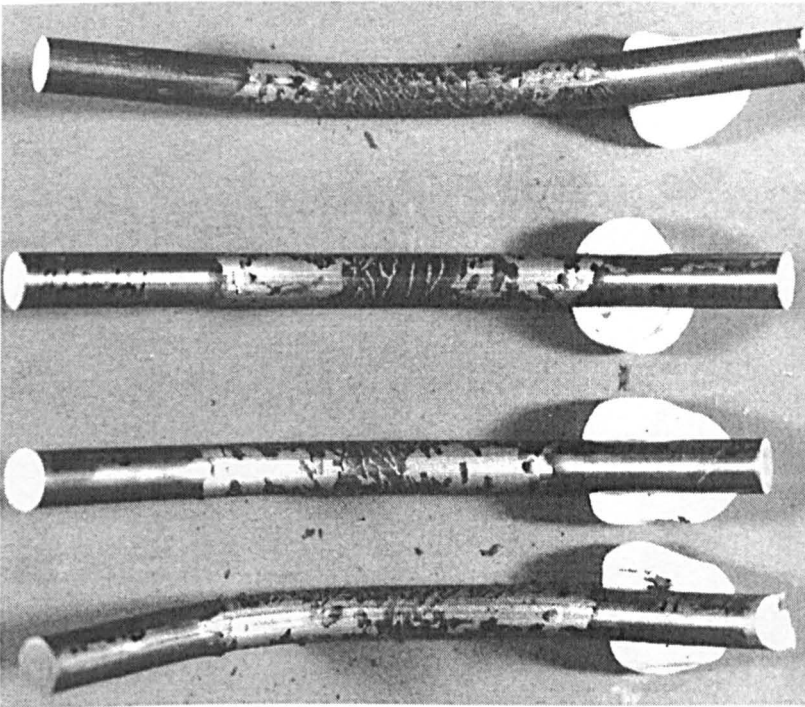
$u=20\text{mm}$, $s=80\text{mm}$,
 $\delta=11.15\text{mm}$, $\epsilon_p=0.1178$

$u=20\text{mm}$, $s=80\text{mm}$,
 $\delta=13.15\text{mm}$, $\epsilon_p=0.1229$

(d) side view

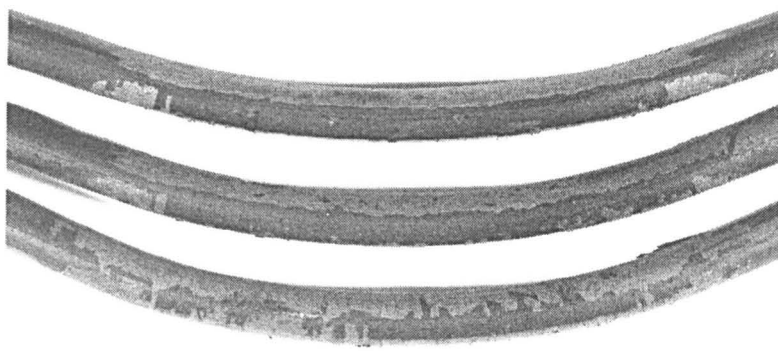


(e) top view



(f) bottom view

Fig. 4.10 The scale cracking and removal behaviour of K08+B steel rods in 4-point bending tests, rods ($\phi 6.5\text{mm}$) were supplied by Scunthorpe Rod Mill.

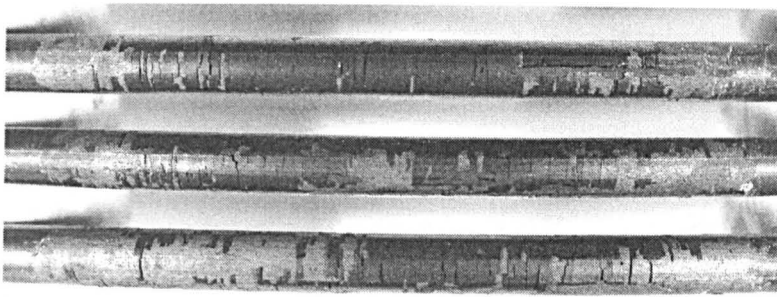


$u=20\text{mm}$, $s=90\text{mm}$,
 $\delta=8\text{mm}$, $\epsilon_p=0.038$

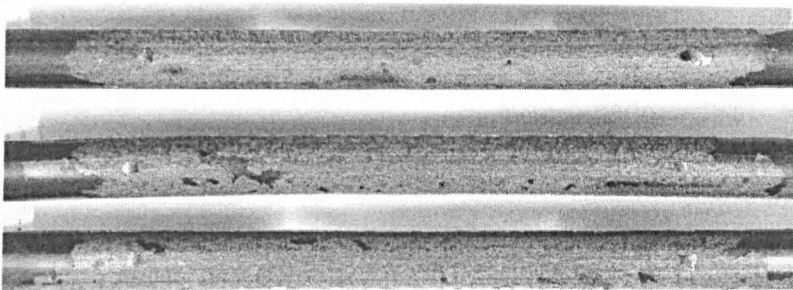
$u=20\text{mm}$, $s=90\text{mm}$,
 $\delta=10\text{mm}$, $\epsilon_p=0.04$

$u=20\text{mm}$, $s=90\text{mm}$,
 $\delta=8.75\text{mm}$, $\epsilon_p=0.05$

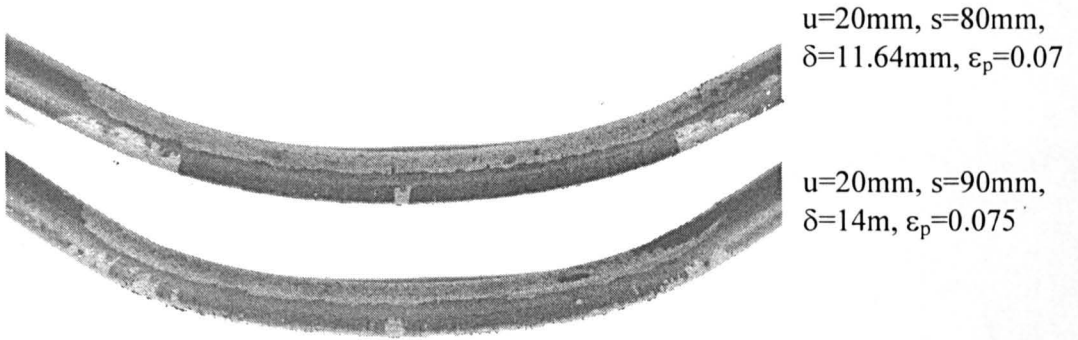
(a) side view



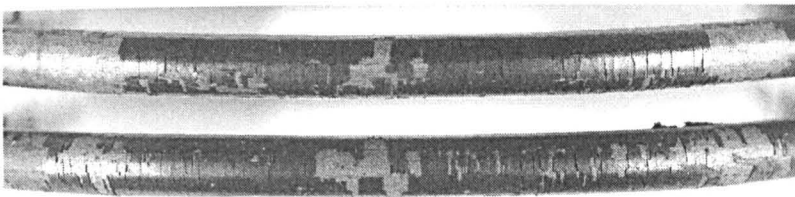
(b) top view



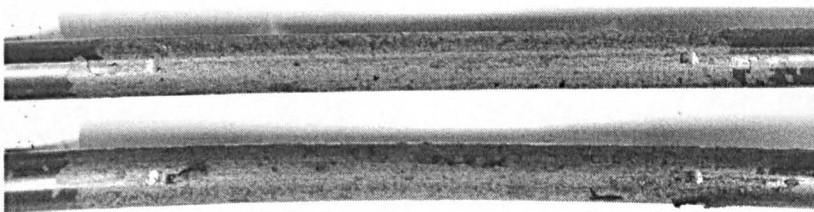
(c) bottom view



(d) side view

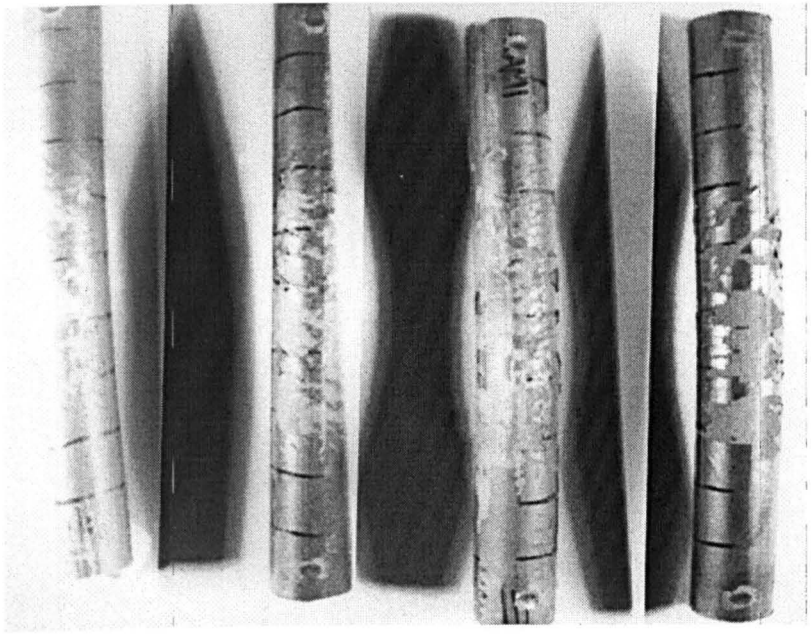


(e) top view

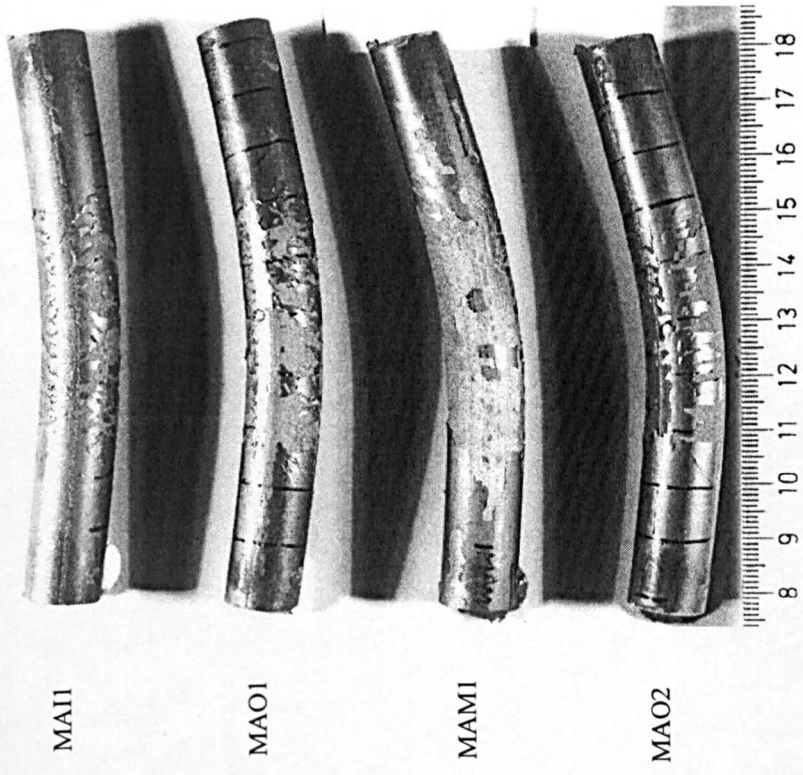


(f) bottom view

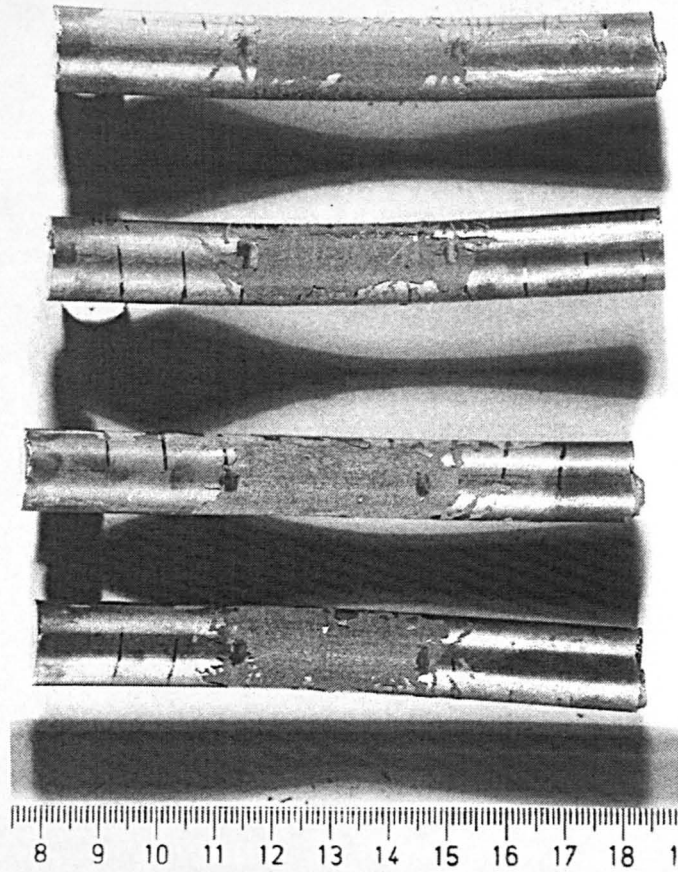
Fig.4.11 The scale cracking and removal behaviour of K58 steel rods in 4-point bending tests, rods ($\phi 6.5\text{mm}$) were supplied by Scunthorpe Rod Mill.



(b) top view



(a) side view



(c) bottom view

Fig.4.12 The scale cracking and removal behaviour of $\phi 14$ rods in 4-point bending test, rods were supplied by Roundwood Rod Mill and taken from different coil positions (Fig.3.4) ($u=20\text{mm}$, $s=90\text{mm}$, $\delta=4.57\text{mm}$, $\epsilon_p=0.0369$)

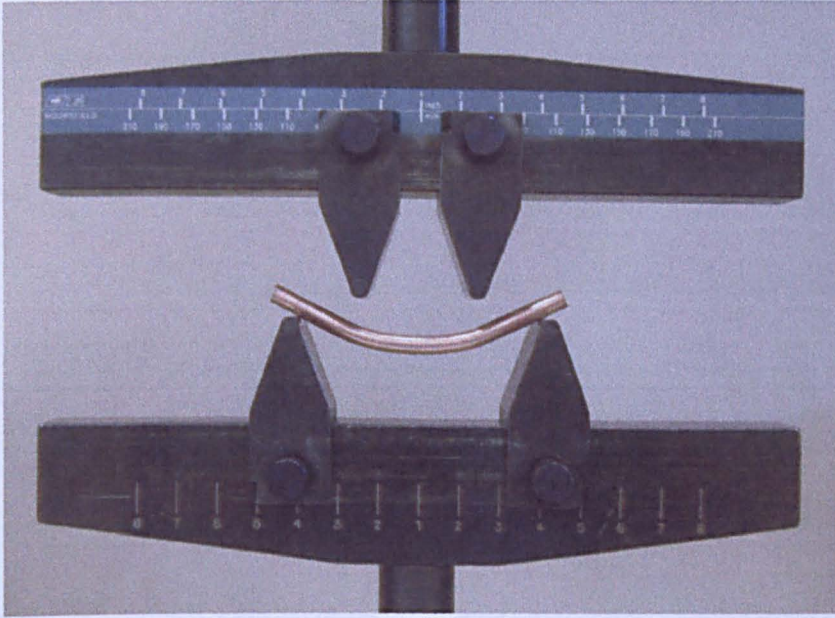


Fig. 4.13 Copper rod sample in 4-point bending test showing no plastic hinge ($u=20\text{mm}$, $s=80\text{mm}$ and $\delta=10\text{mm}$).

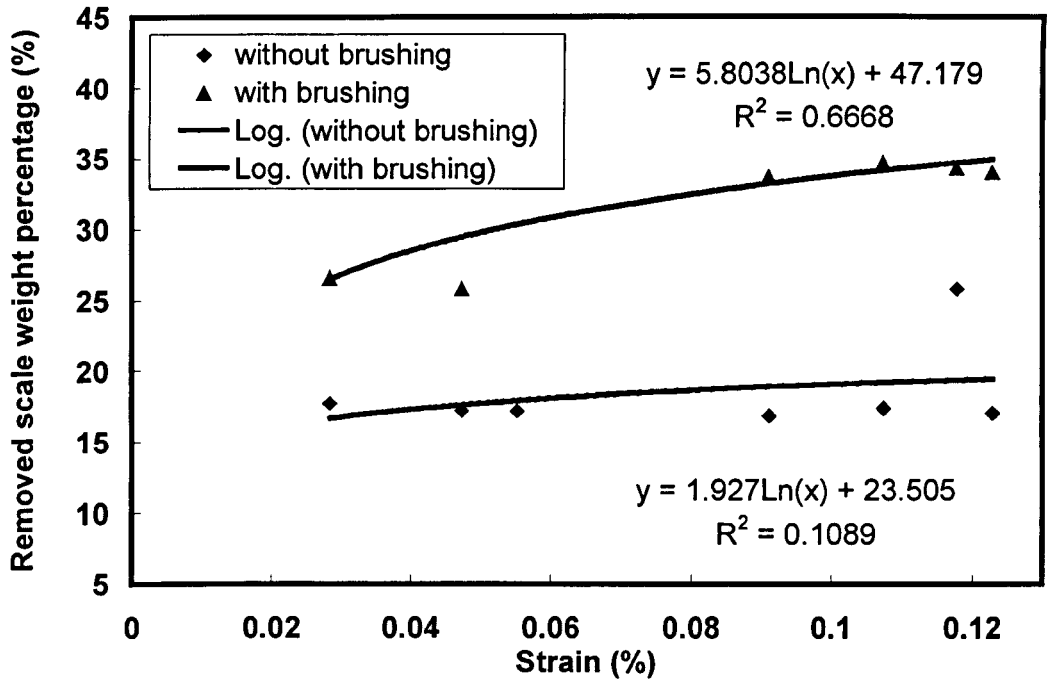


Fig.4.14 Variation of removed scale weight percentage with strain for K08+B after 4-point bending

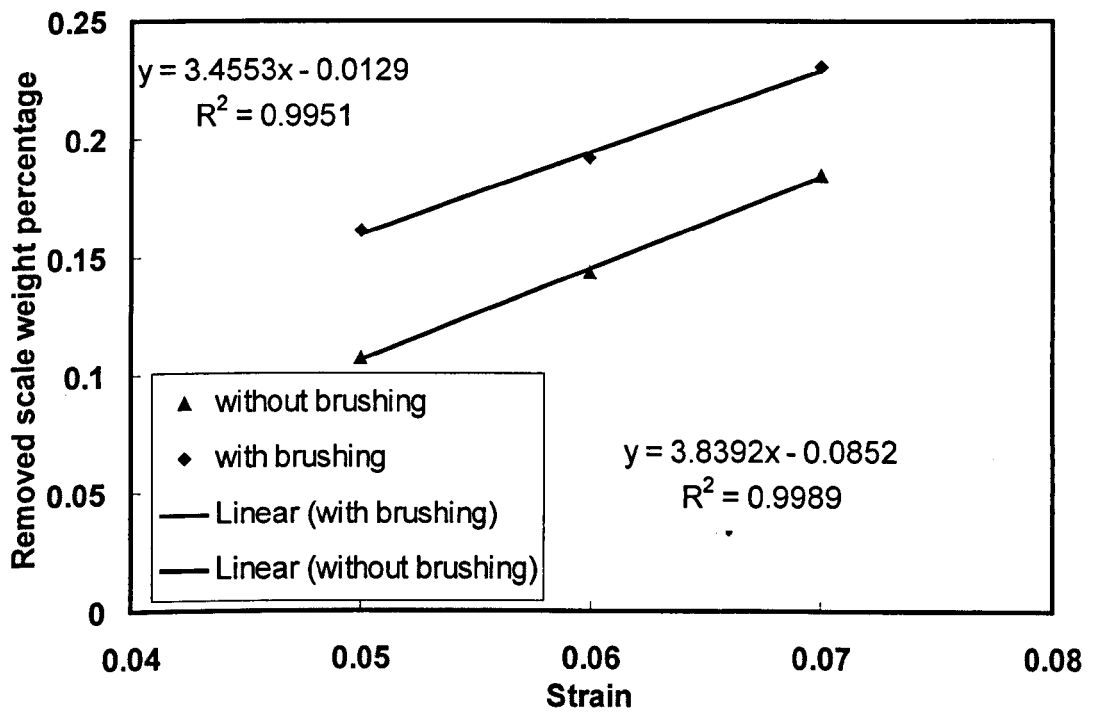


Fig. 4.15 Variation of removed scale weight percentage with strain for K08(EAF) after 4-point bending

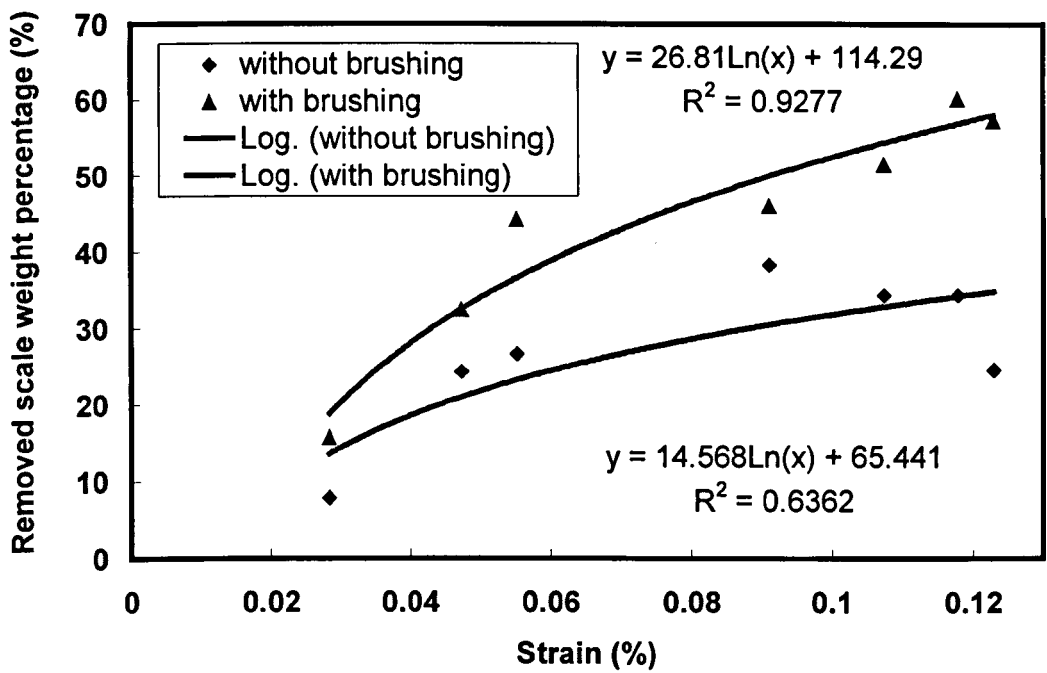


Fig.4.16 Variation of removed scale weight percentage with strain for R09 after 4-point bending

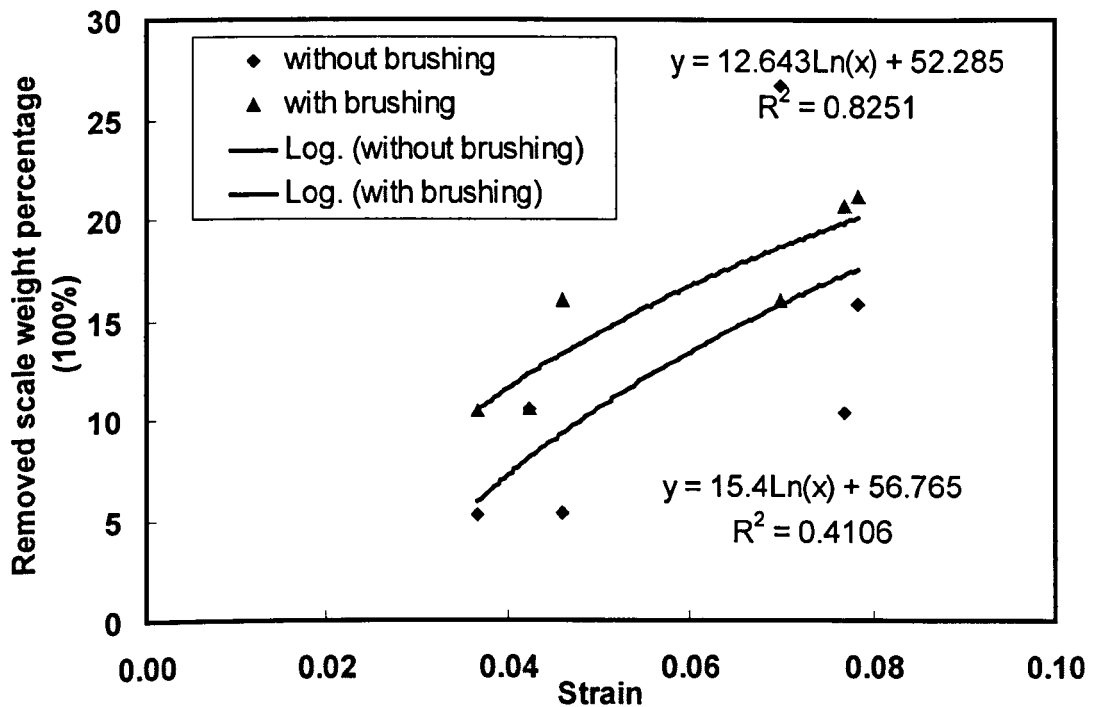


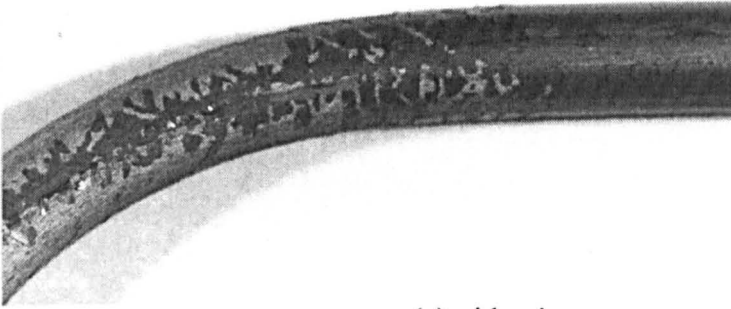
Fig. 4.17 Variation of removed scale weight percentage with strain for K58 after 4-point bending



Stage 1

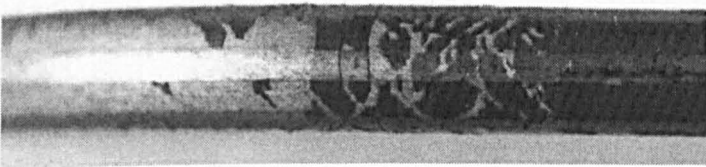
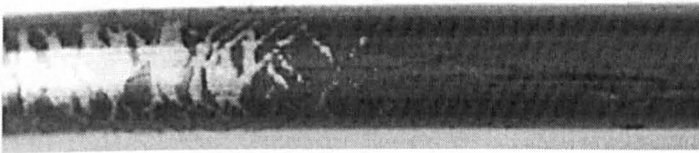
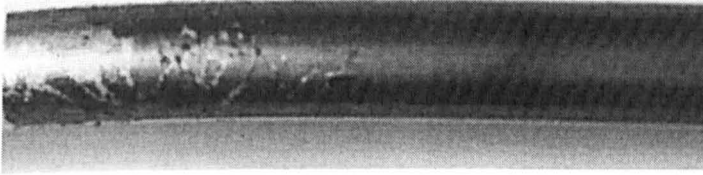


Stage 2

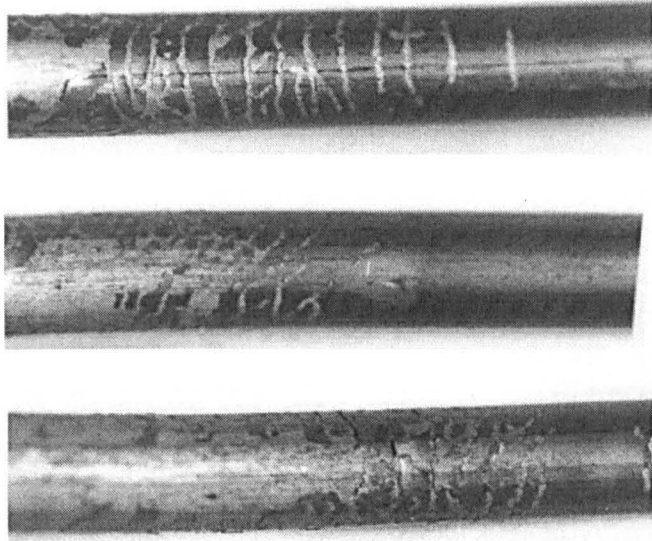


Stage 3

(a) side view

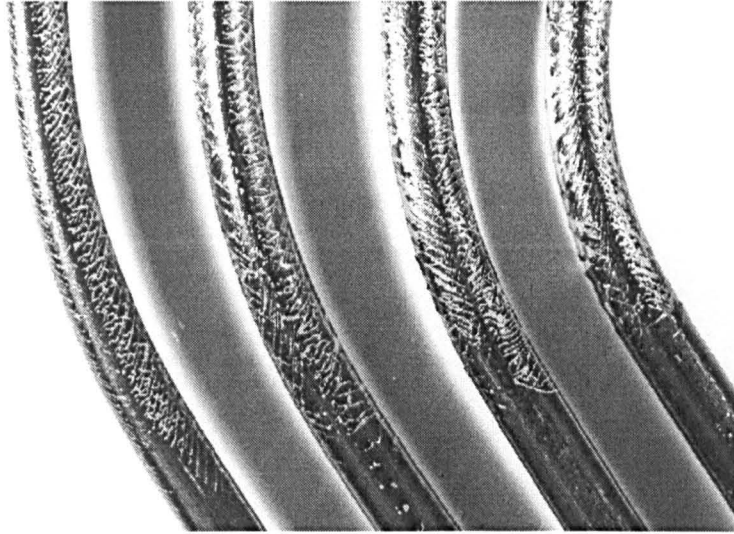


(b) top view

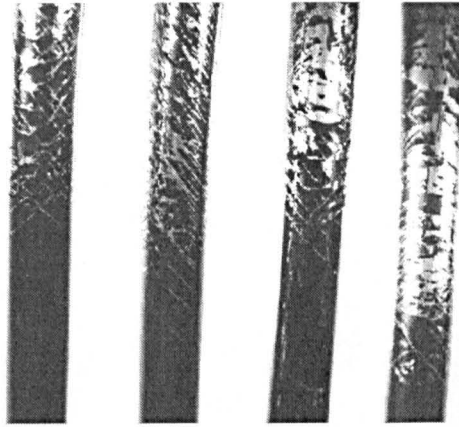


(c) bottom view

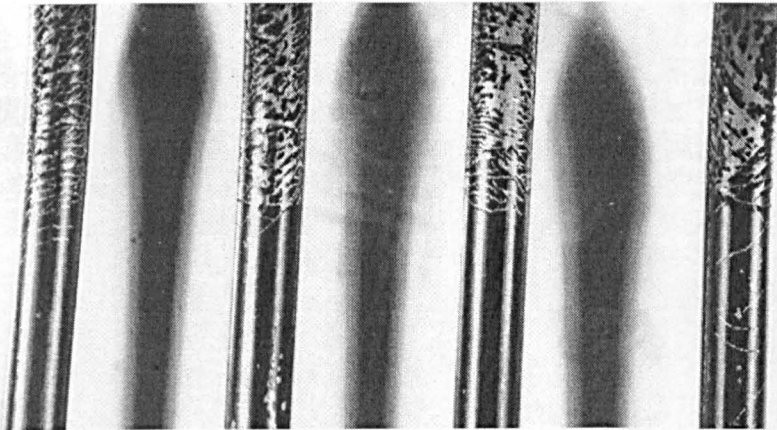
Fig. 4.18 The scale cracking and removal behaviour of steel rod samples under gradually increased strain (stage 1-3) in the cantilever bending tests (a) side view, (b) top view and (c) bottom view



(a) side view

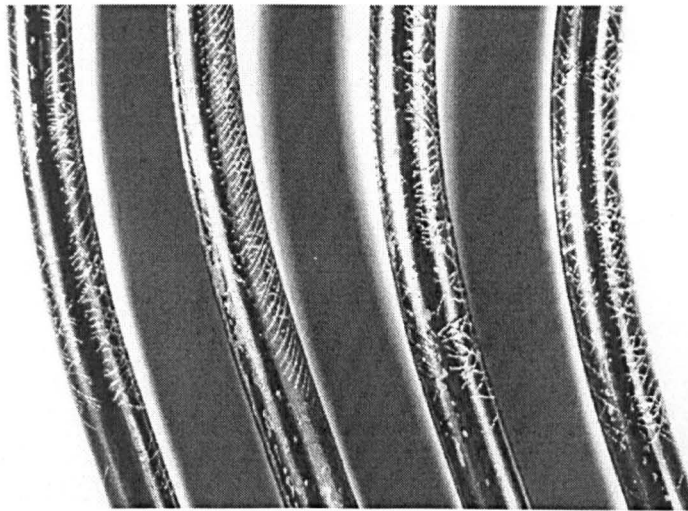


(b) top view

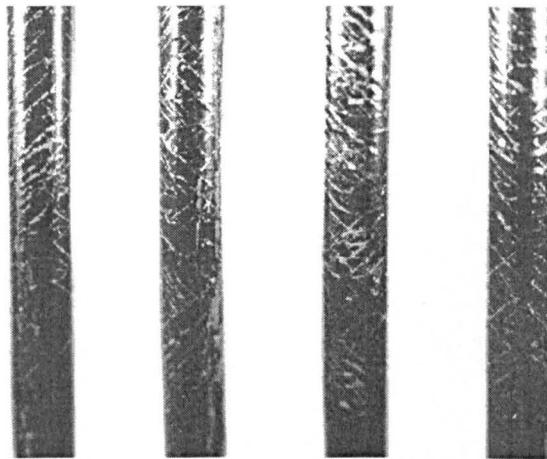


(c) bottom view

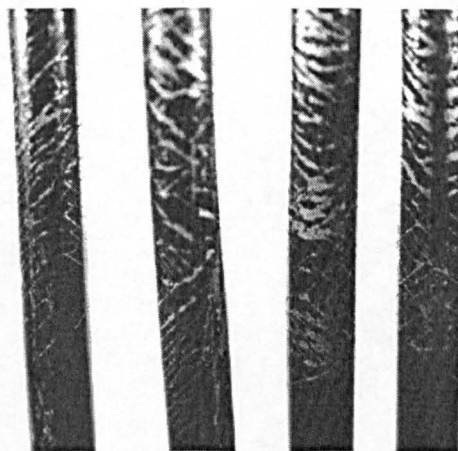
Fig. 4.19 The scale cracking and removal behaviour of K08 steel rods in constrained bending test before brushing (cylinder diameter is 51, 74, 92, 102mm from right to left respectively), rods ($\phi 6.5\text{mm}$) were supplied by Scunthorpe Rod Mill, laying temperature 830°C



(d) side view

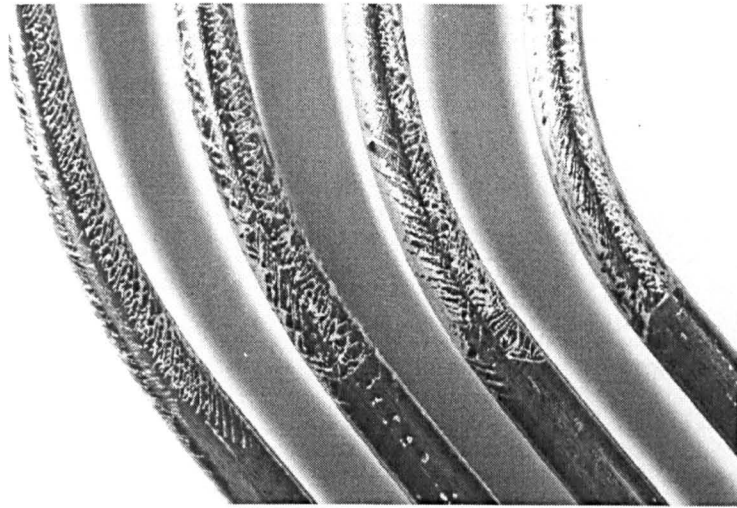


(e) top view

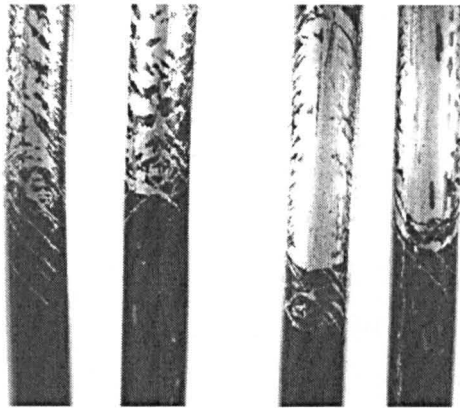


(f) bottom view

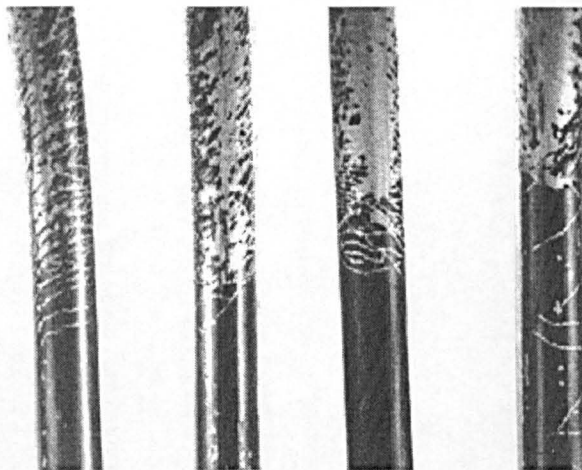
Fig. 4.19 Continued (cylinder diameter are 143, 160, 180, 215 mm from right to left)



(a) side view

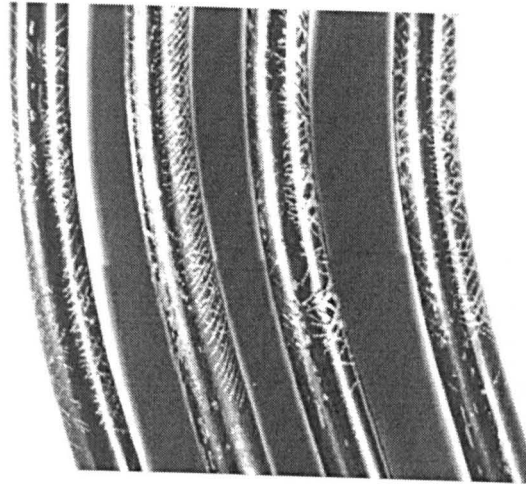


(b) top view

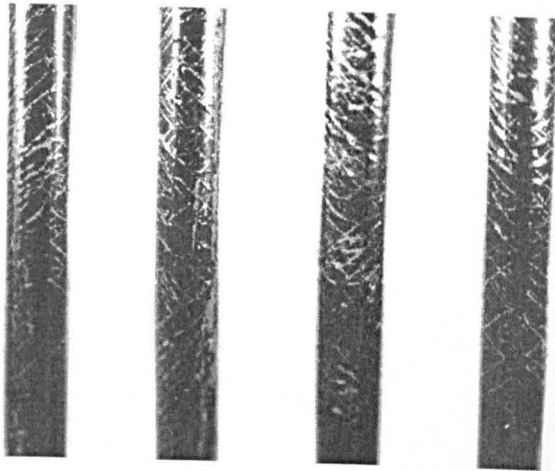


(c) bottom view

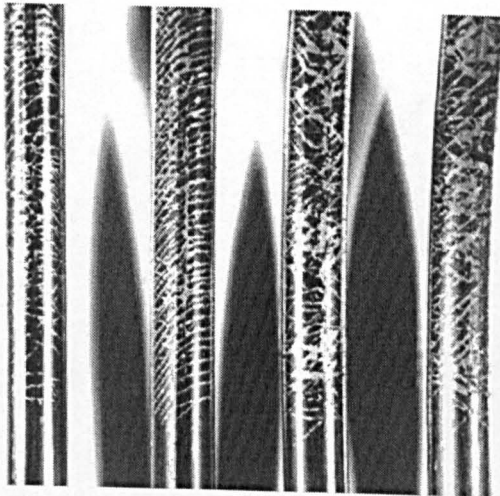
Fig. 4.20 The scale cracking and removal behaviour of K08 steel rods in constrained bending test after brushing (cylinder diameter is 51, 74, 92, 102mm from right to left respectively), rods ($\phi 6.5\text{mm}$) were supplied by Scunthorpe Rod Mill, laying temperature 830°C



(d) side view



(e) top view

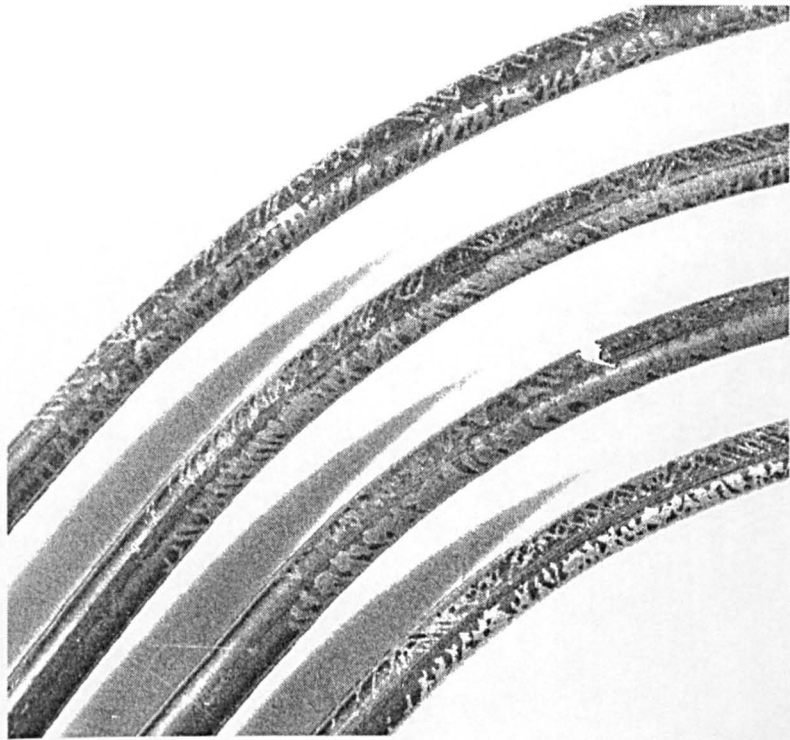


(f) bottom view

Fig. 4.20 Continued (cylinder diameters are 143, 160, 180, 215 mm from right to left)



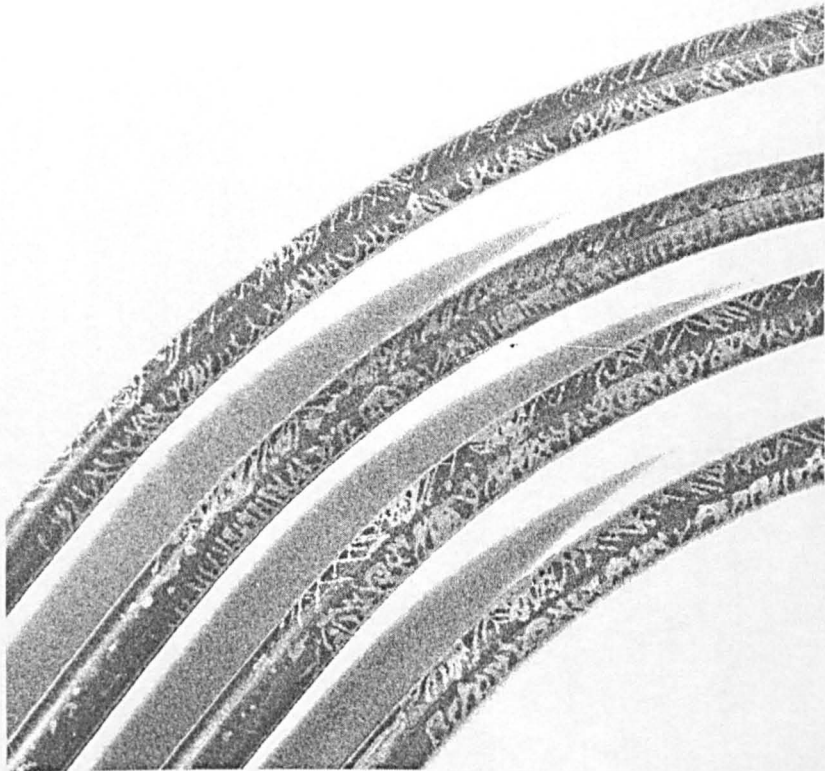
(a) laying temperature 950°



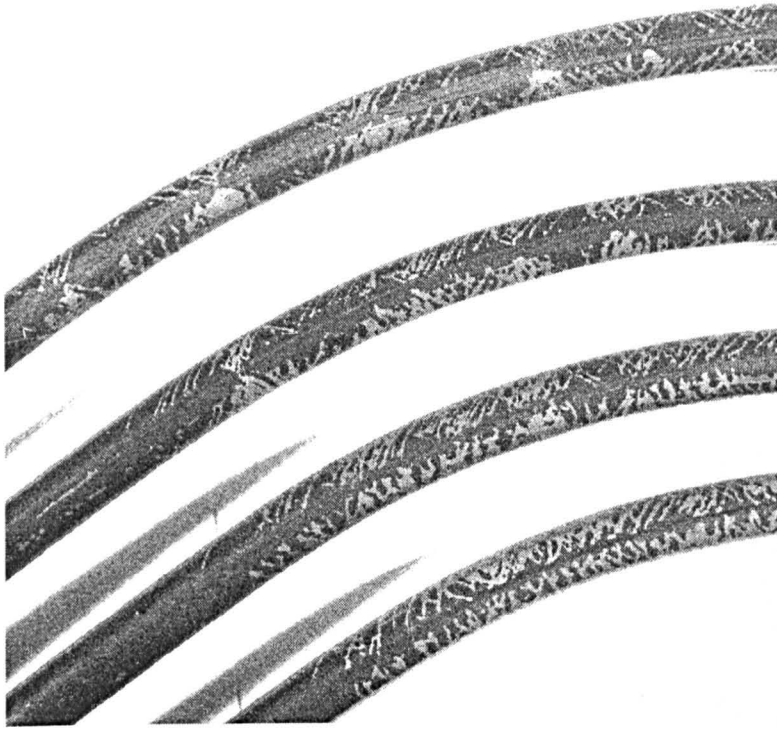
(b) laying temperature 900°C with all fans off in Stelmor process



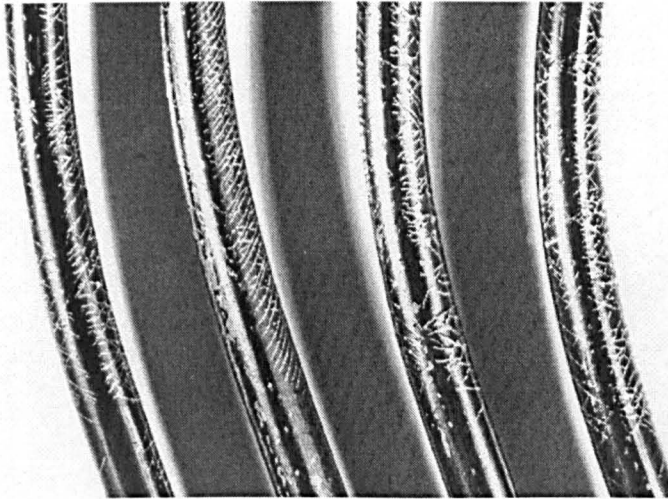
(c) laying temperature 900°C with all fans on in Stelmor process



(d) laying temperature 870°C with all fans off in Stelmor process

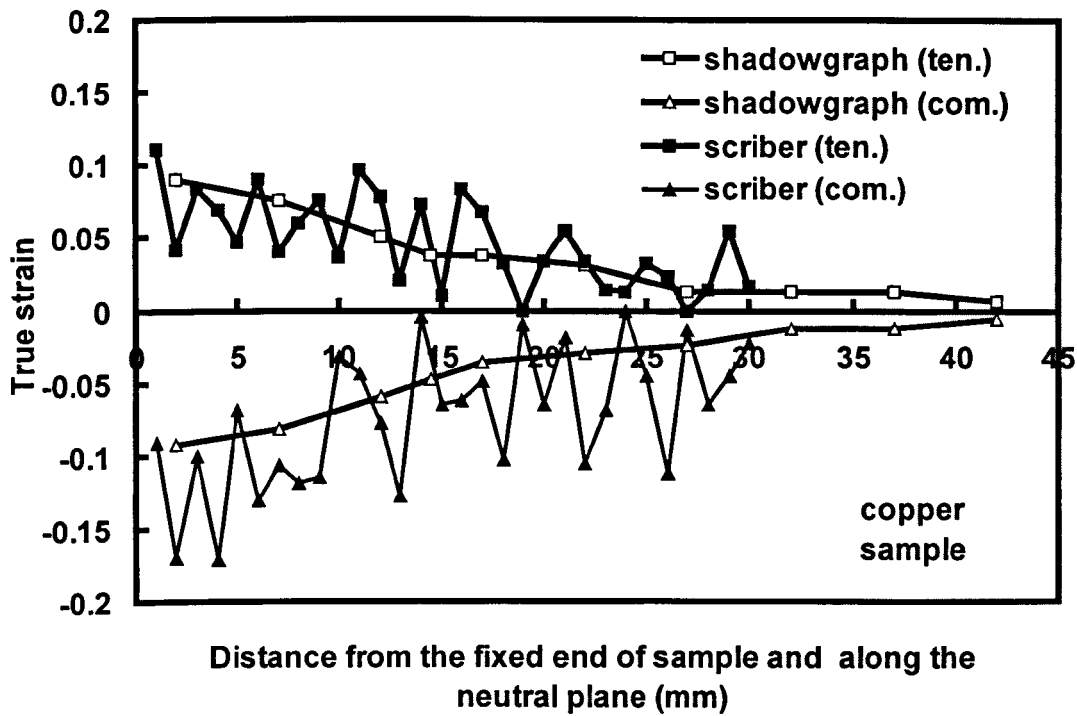


(e) laying temperature 870°C with all fans on in Stelmor process

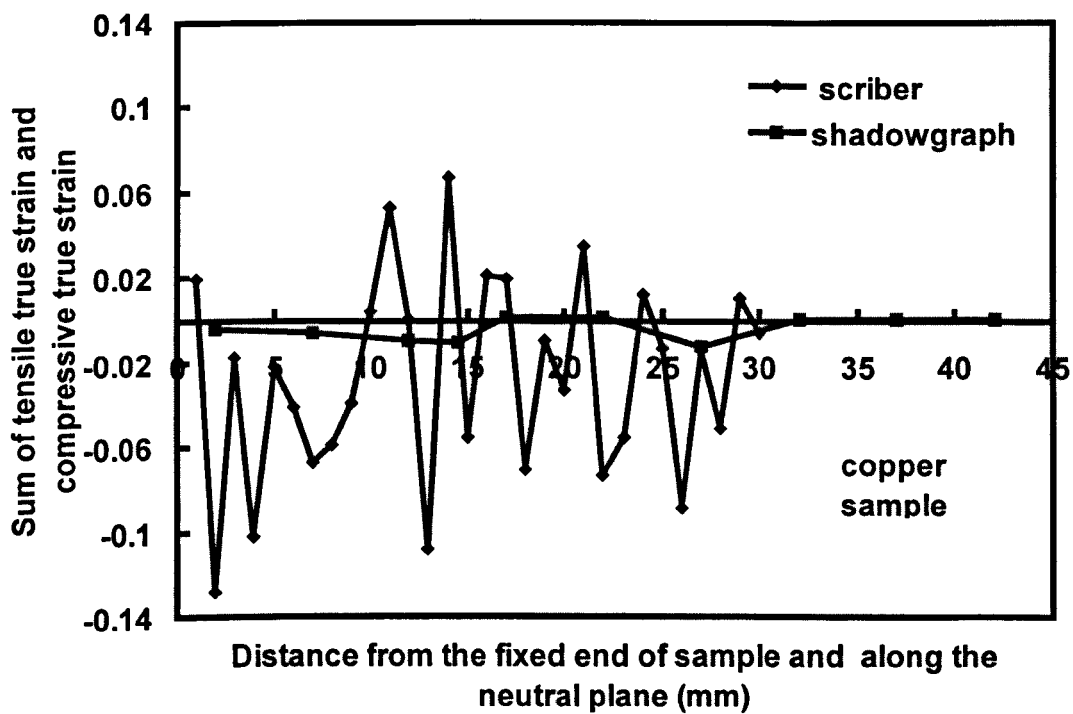


(f) laying temperature 830°C

Fig. 4.21 The side view of the rod samples ($\phi 6.5$) with different laying temperatures in constrained bending tests (cylinder diameter are 143, 160, 180, 215mm from bottom/right to top/left).

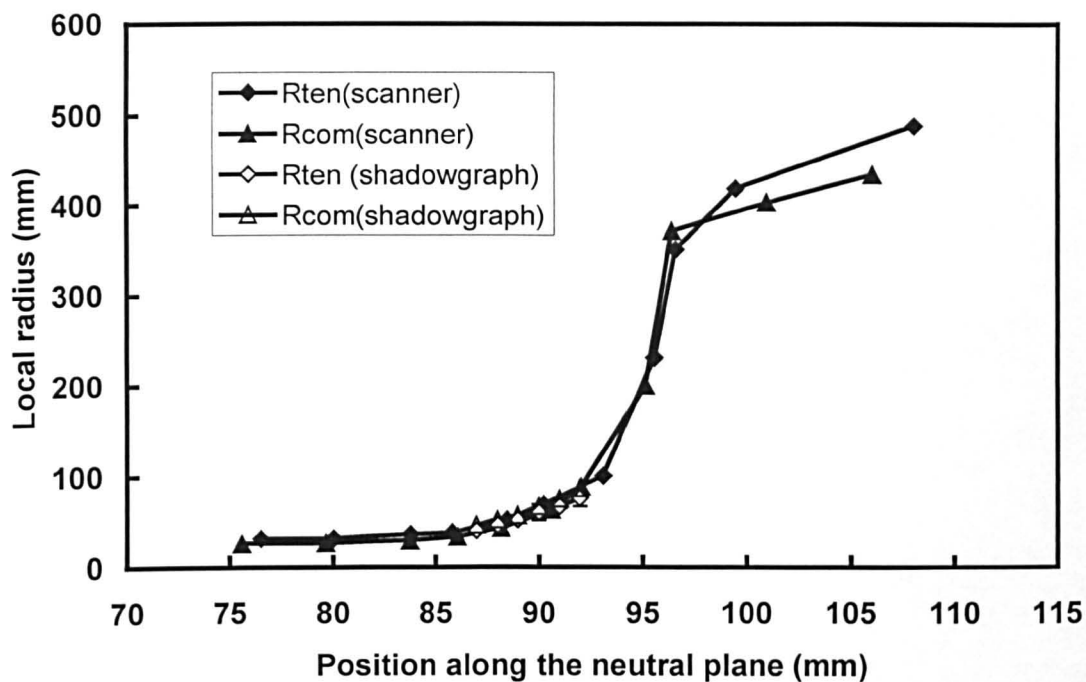


(a) true strain

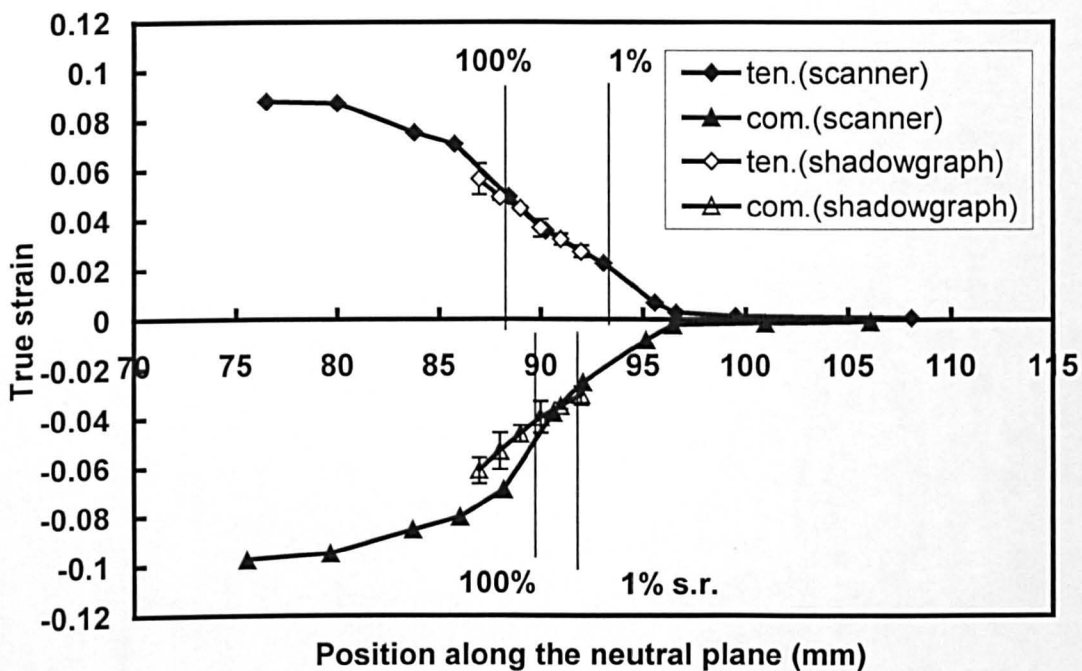


(b) sum of tensile and compressive true strain

Fig. 4.22 Comparison of the data obtained by scriber and shadowgraph methods



(a) local radius



(b) true strain

Fig. 4.23 Comparison of the data obtained by shadowgraph and scanner methods on steel rod.

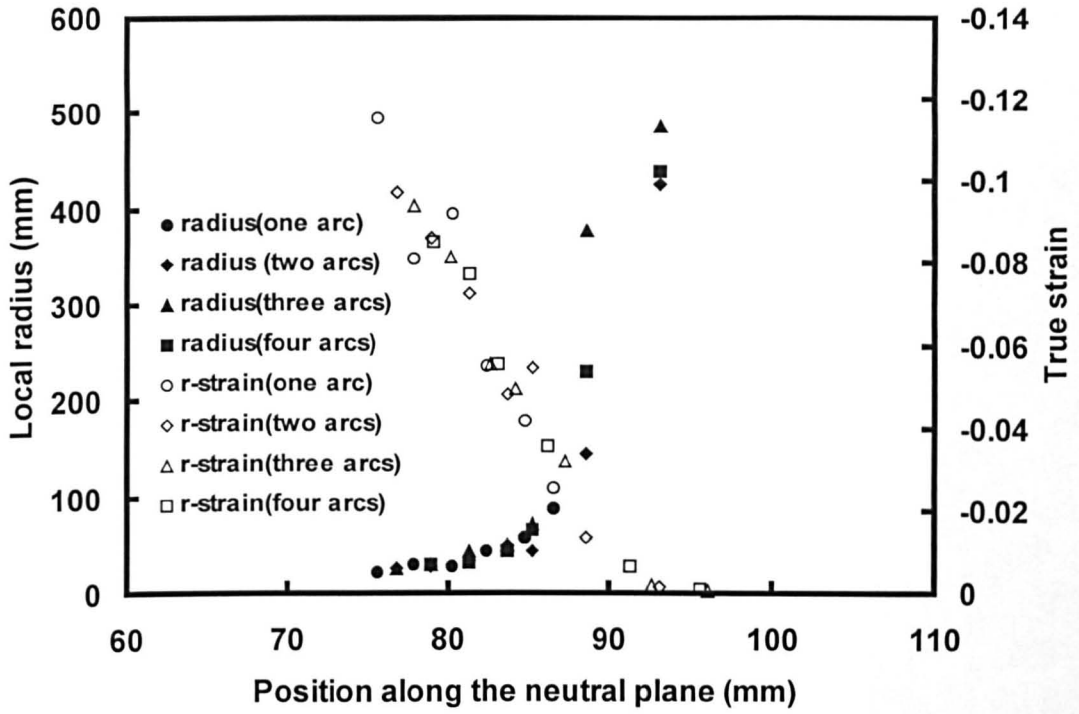
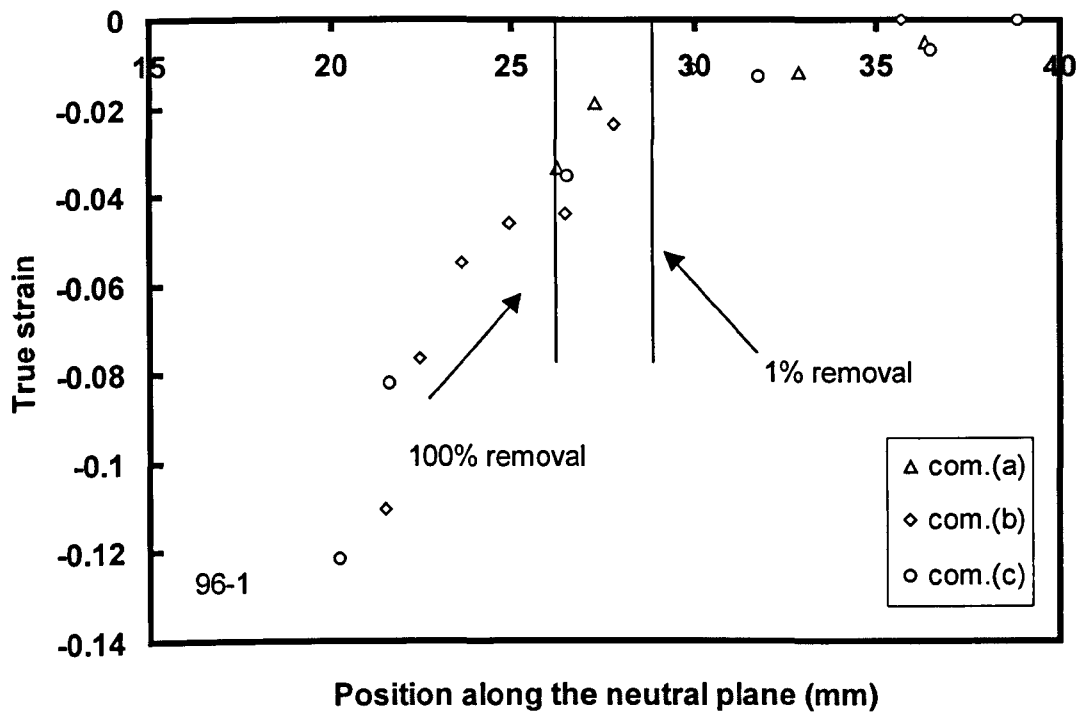
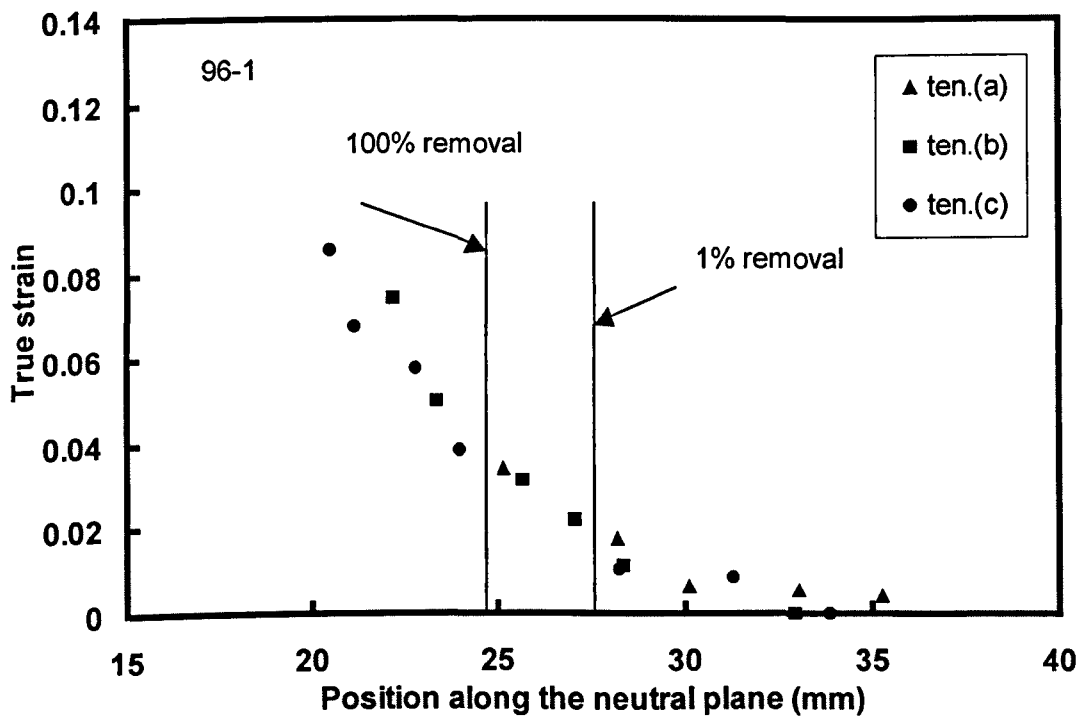


Fig. 4.24 The relationship between the local radius and true strain and the position along the neutral plane (sample 8300)

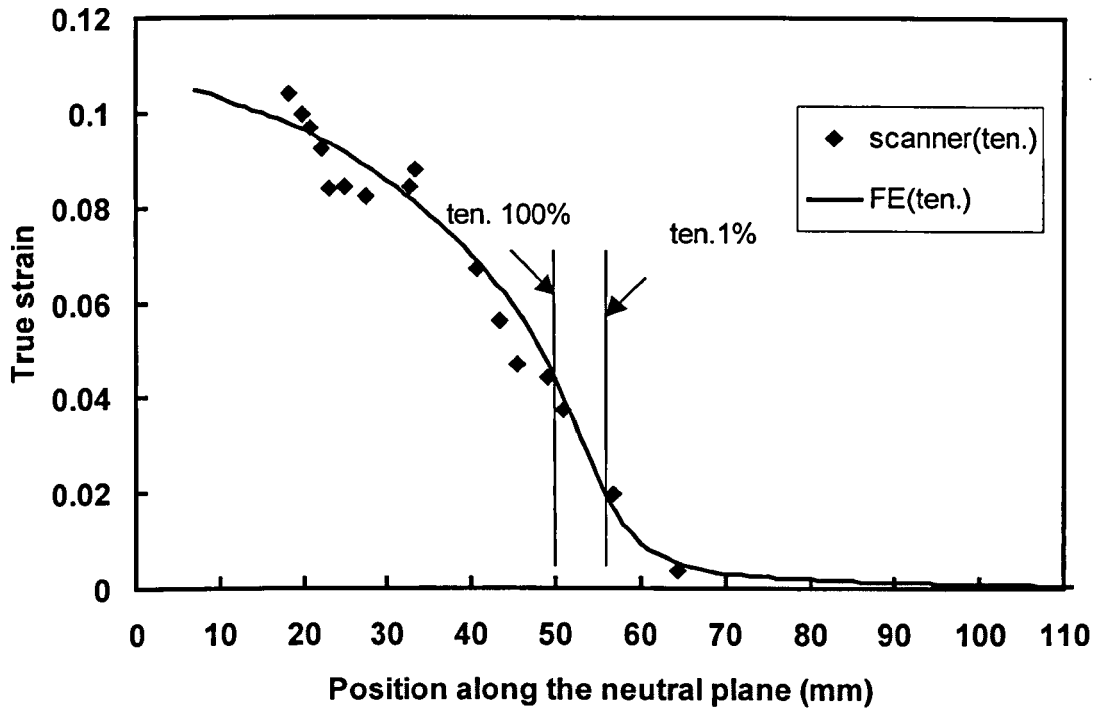


(a)

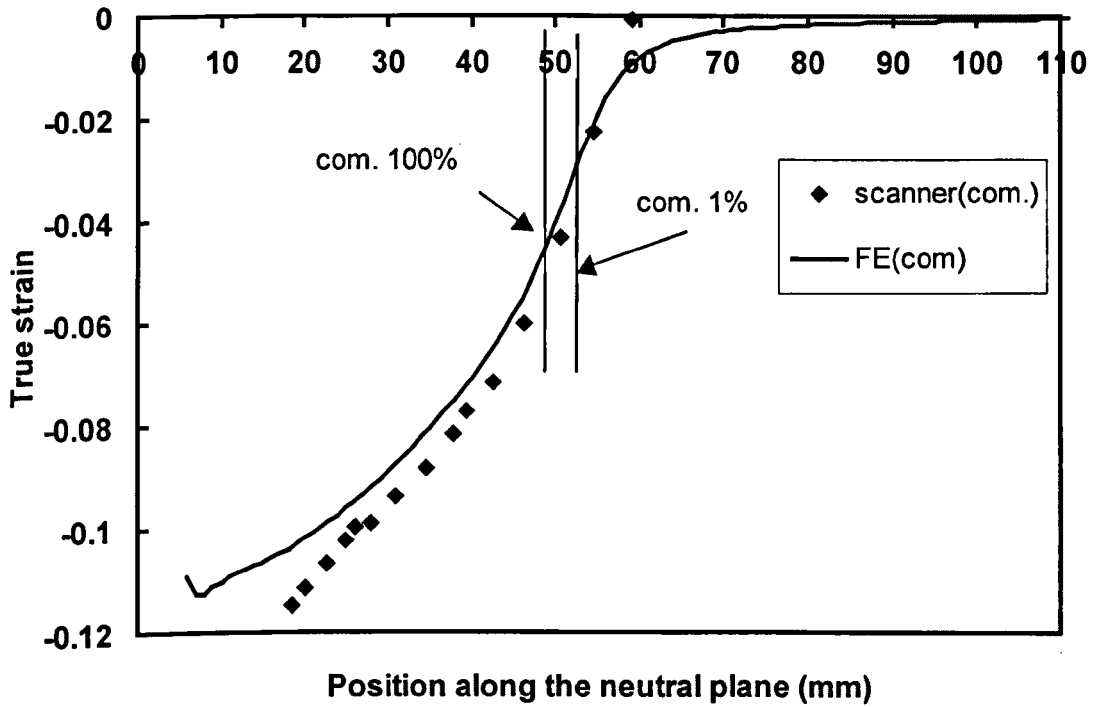


(b)

Fig. 4.25 The test data for one sample, re-scan three times by the scanner, (a) tensile surface, (b) compressive surface (sample 8300)

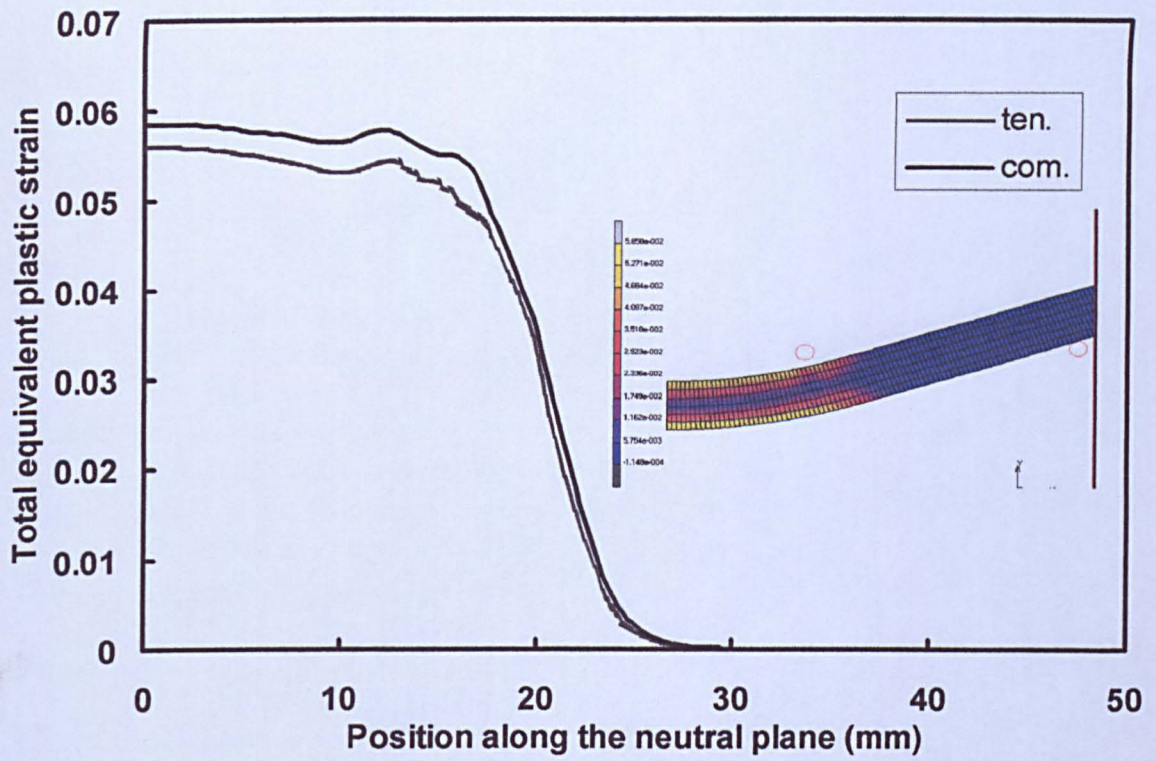


(a)

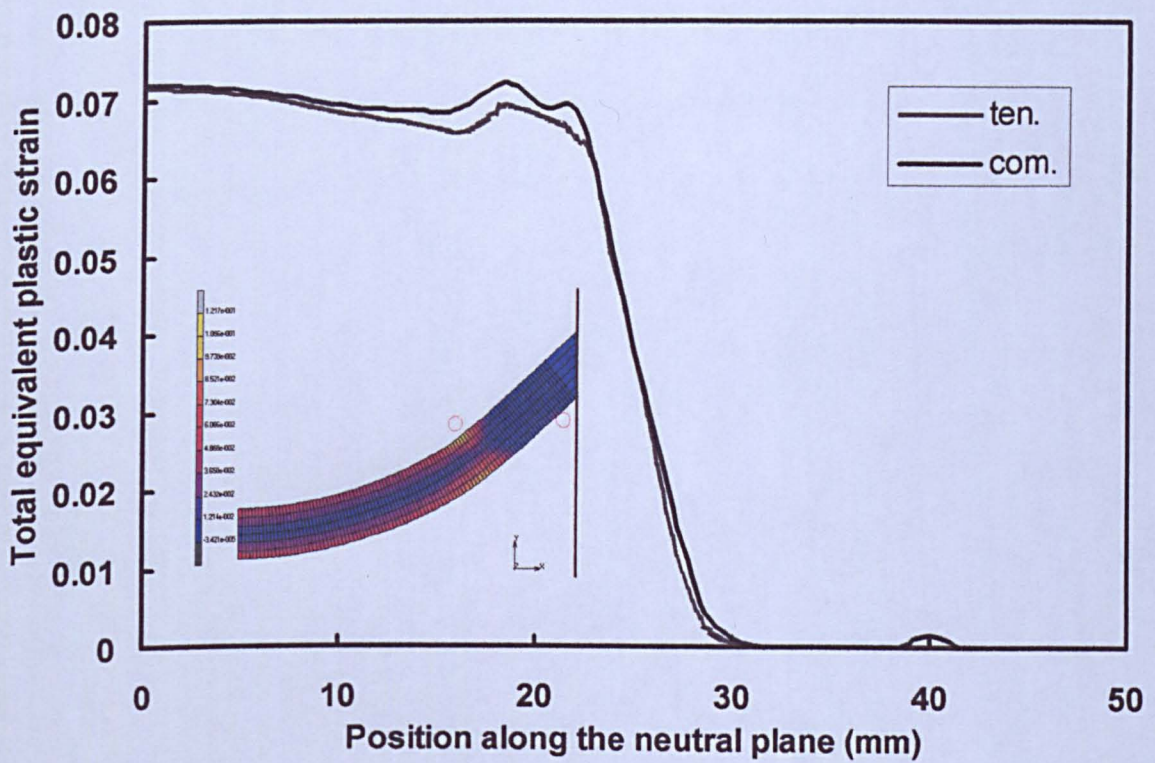


(b)

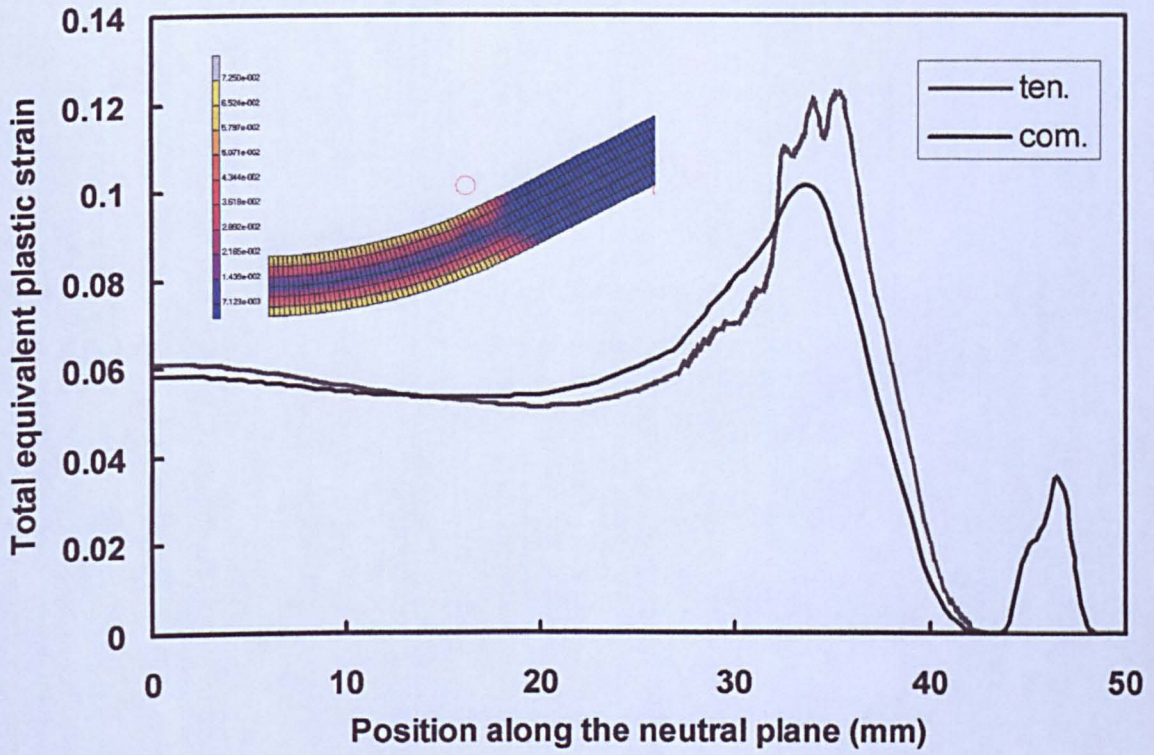
Fig. 4.26 Comparison of results obtained by FE modelling and scanner method (a) in tension and (b) in compression



(a) $u=30\text{mm}$, $s=90\text{mm}$, $\delta=10\text{mm}$

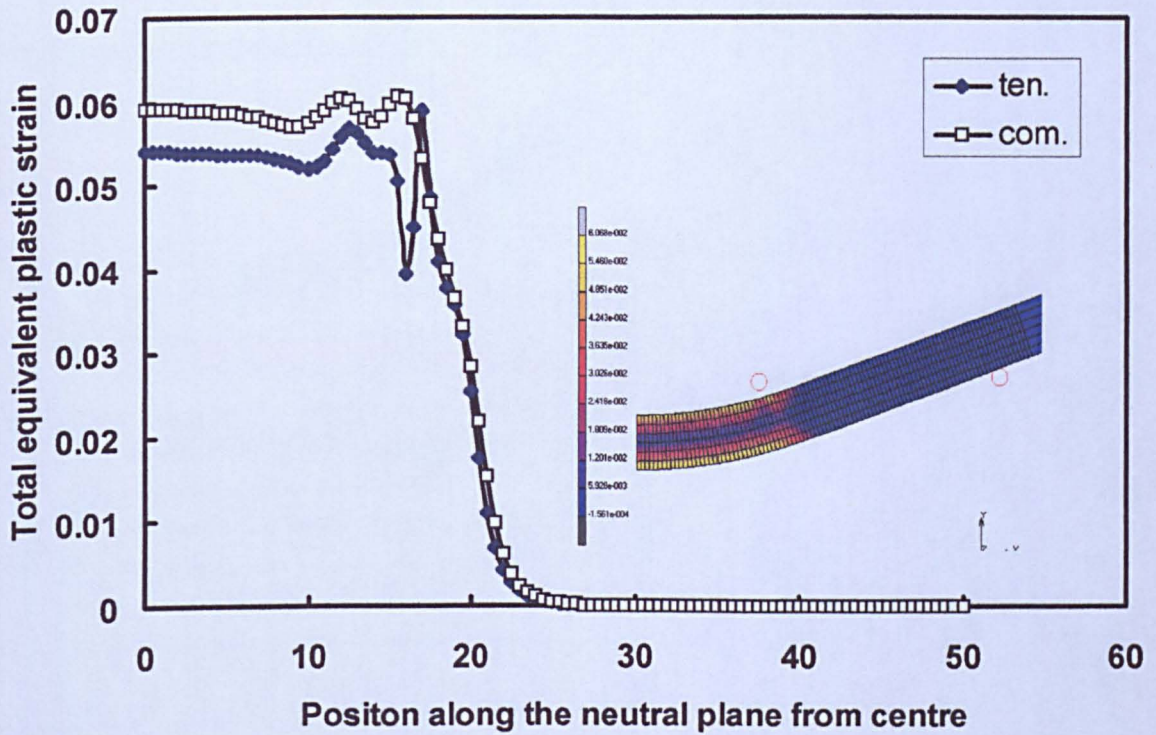


(b) $u=20\text{mm}$, $s=80\text{mm}$, $\delta=10\text{mm}$

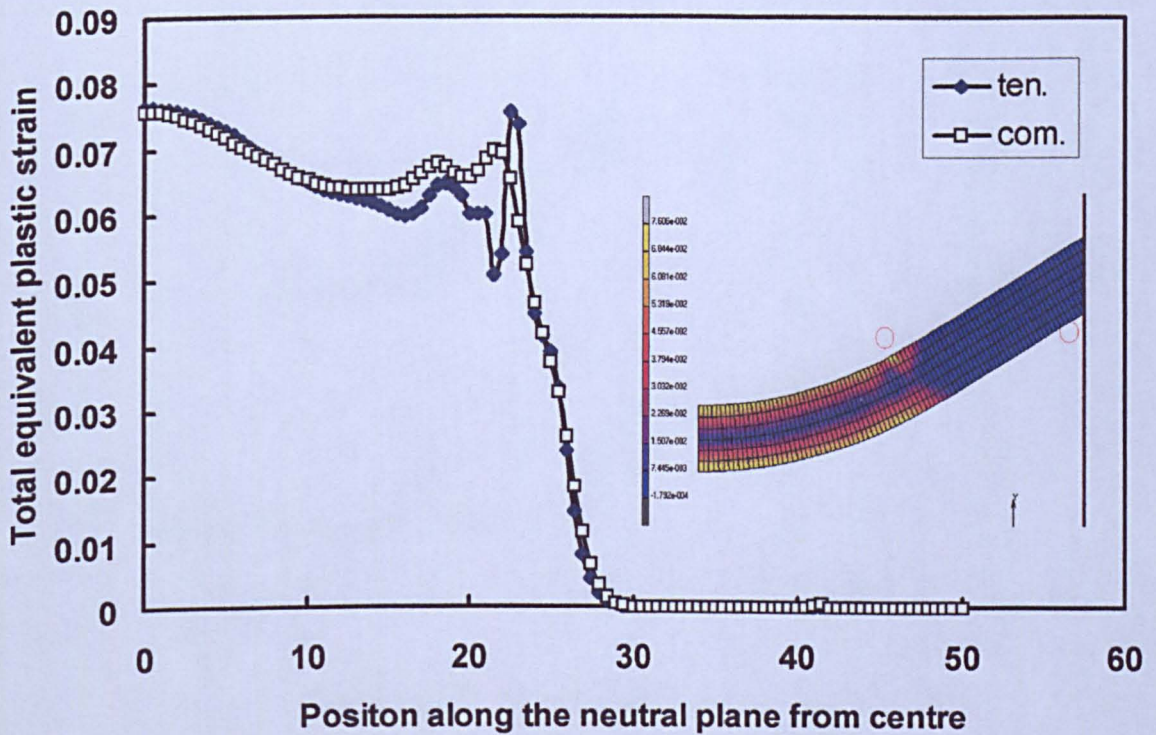


(c) $u=15$, $s=90$, $\delta=10\text{mm}$

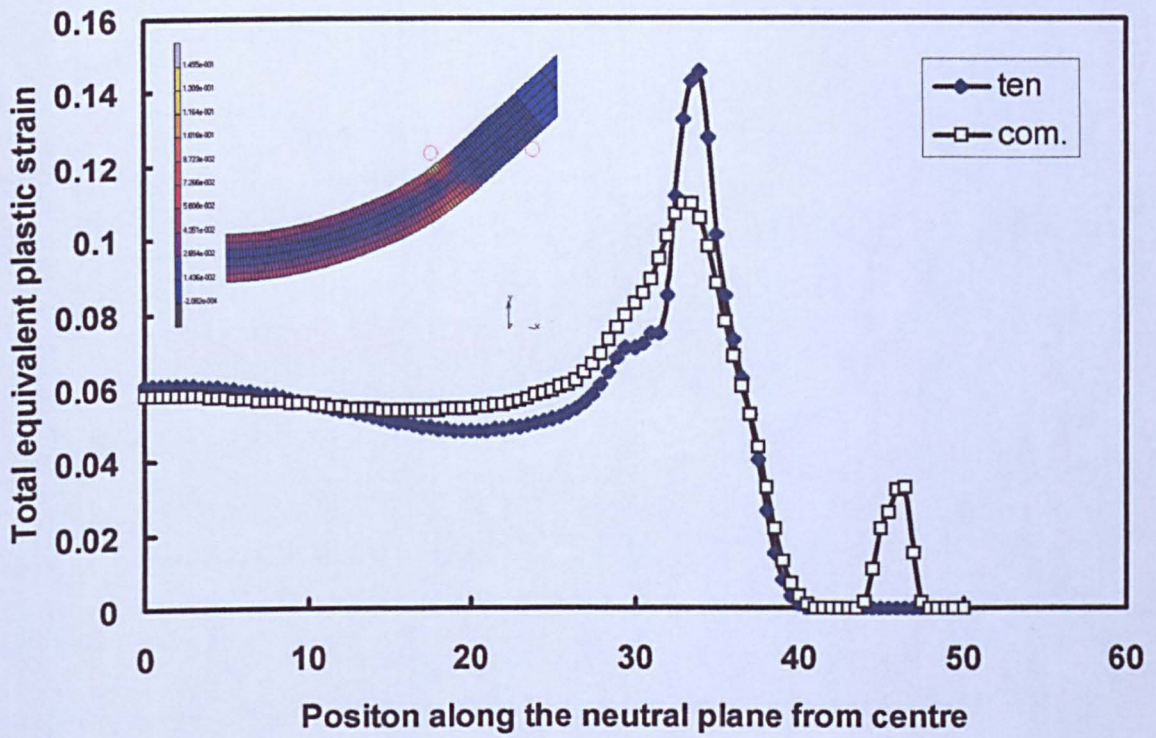
Fig. 4.27 FE model result of copper rod sample in 4-point bending showing no plastic hinges formed in three settings



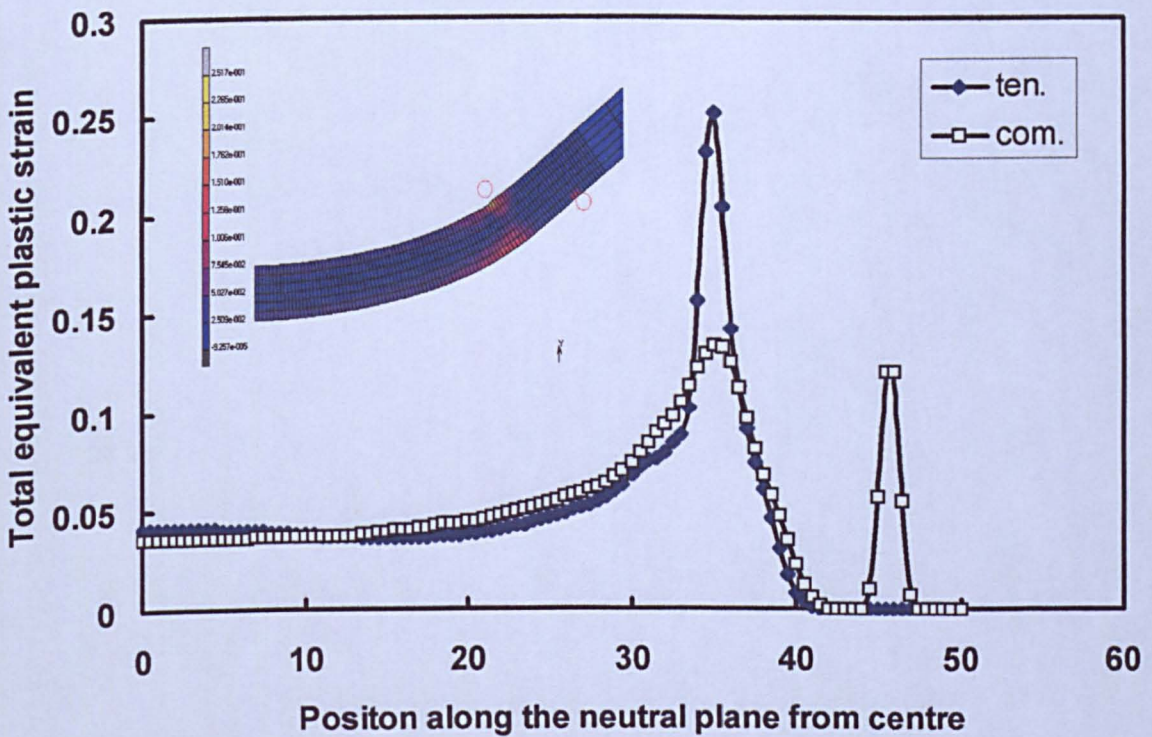
(a) $u=30\text{mm}$, $s=90\text{mm}$, $\delta=10\text{mm}$



(b) $u=20\text{mm}$, $s=80\text{mm}$, $\delta=10\text{mm}$

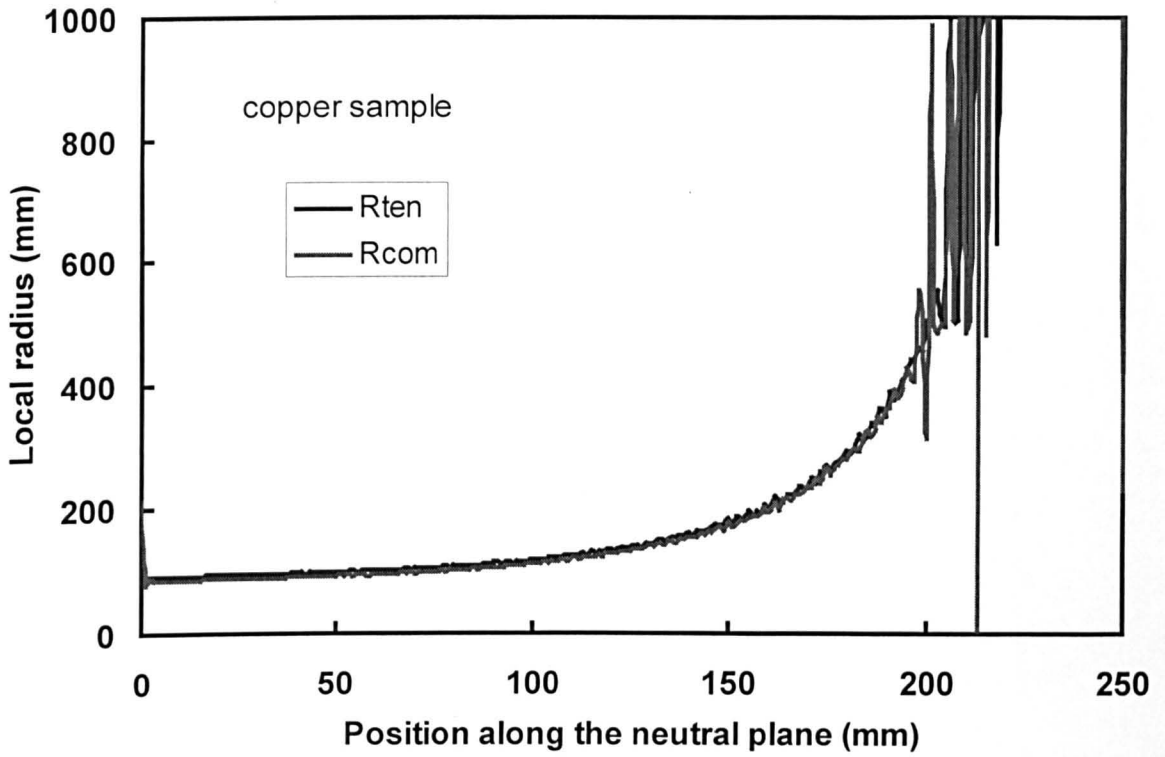


(c) $u=15\text{mm}$, $s=90\text{mm}$, $\delta=10\text{mm}$

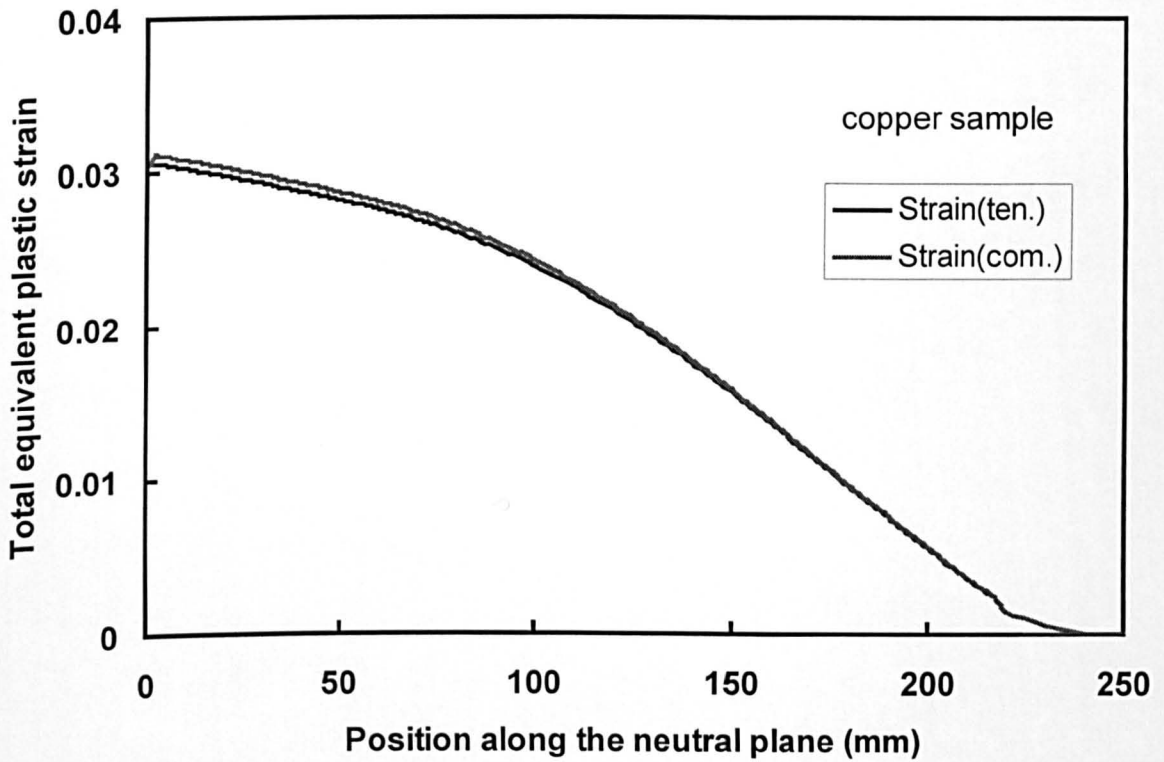


(d) $u=10\text{mm}$, $s=90\text{mm}$, $\delta=8\text{mm}$

Fig. 4.28 FE model result of steel rod sample in 4-point bending showing plastic hinges appeared under large strain

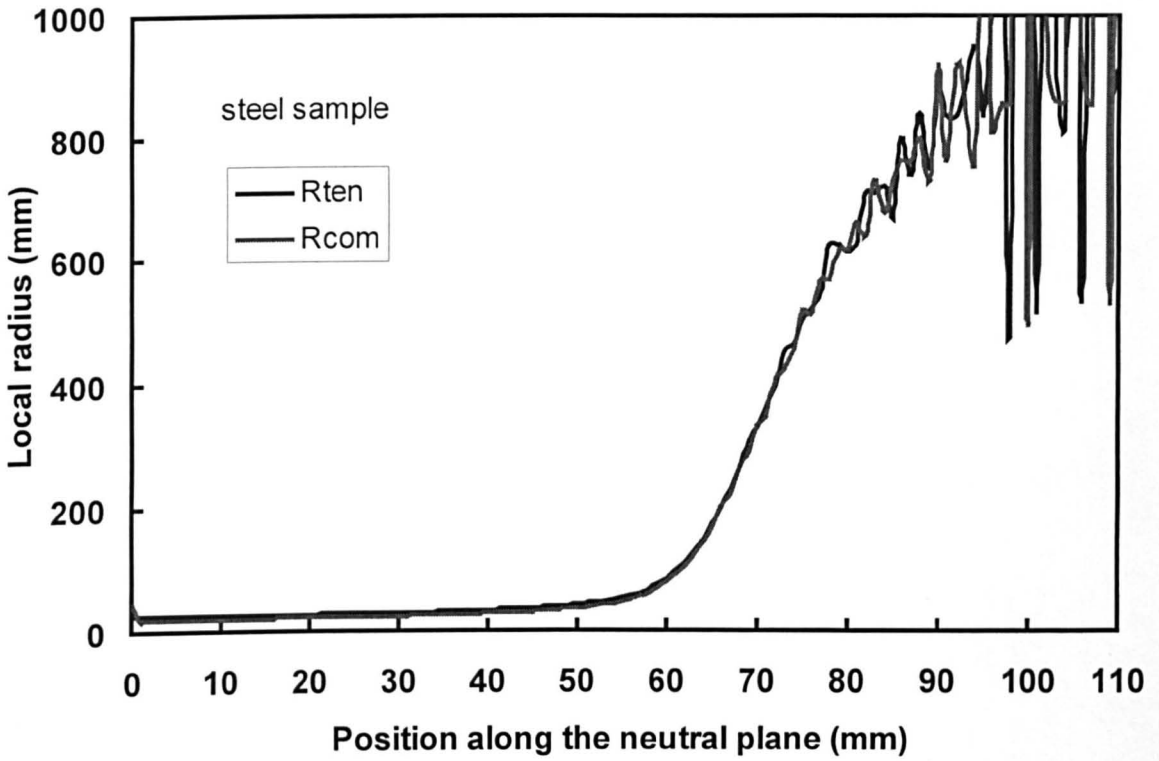


(a) local radius

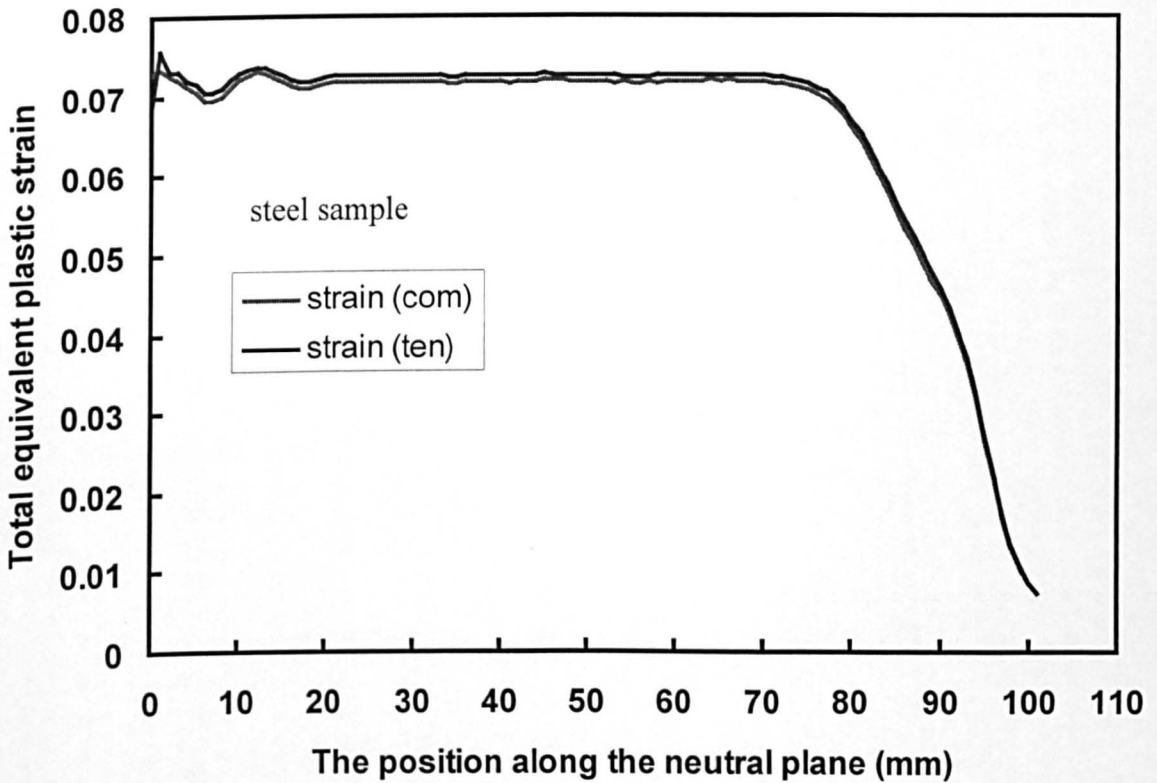


(b) total equivalent plastic strain

Fig. 4.29 FE modeling result of copper rod sample in cantilever bending test

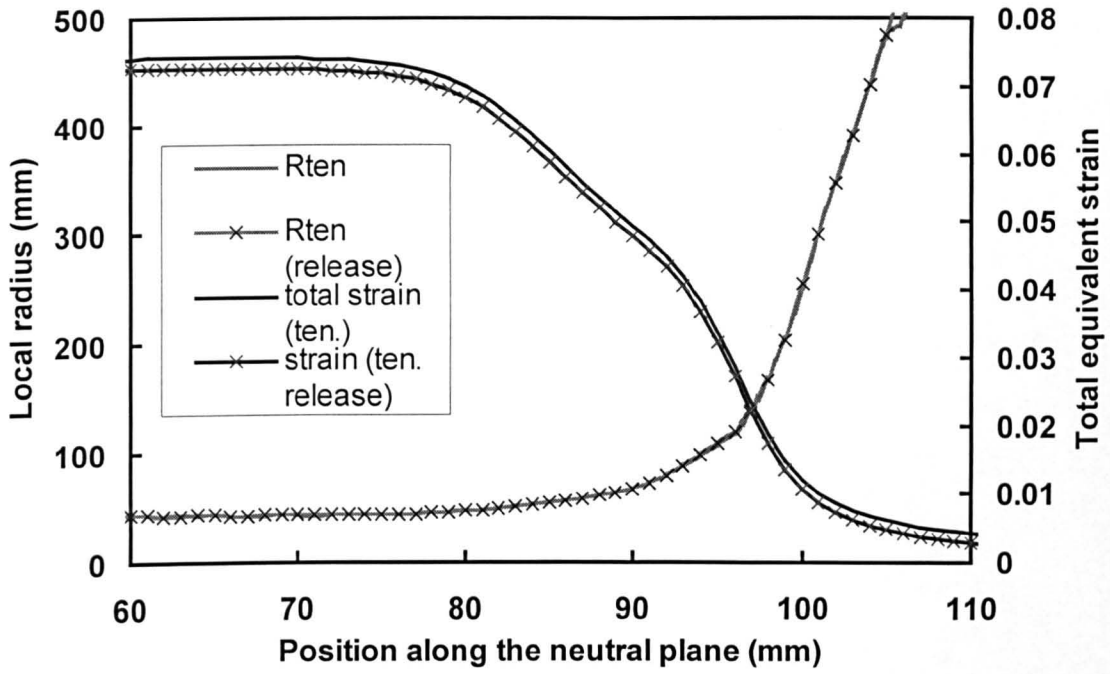


(a) local radius

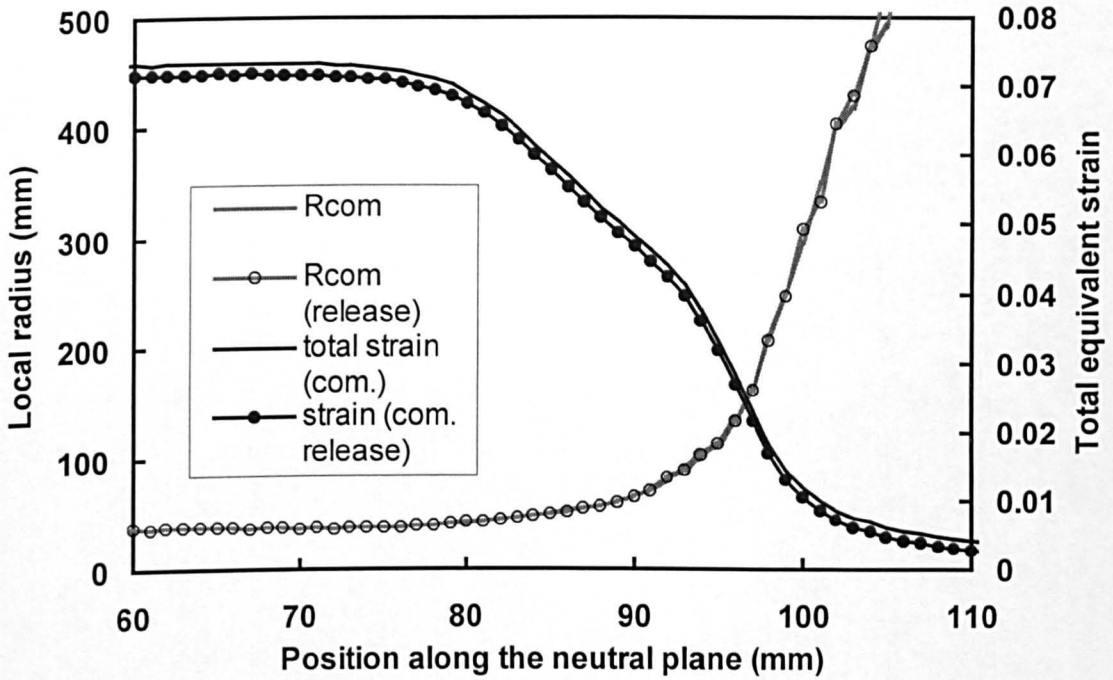


(b) total equivalent plastic strain

Fig. 4.30 FE modeling result of steel rod sample in cantilever bending test

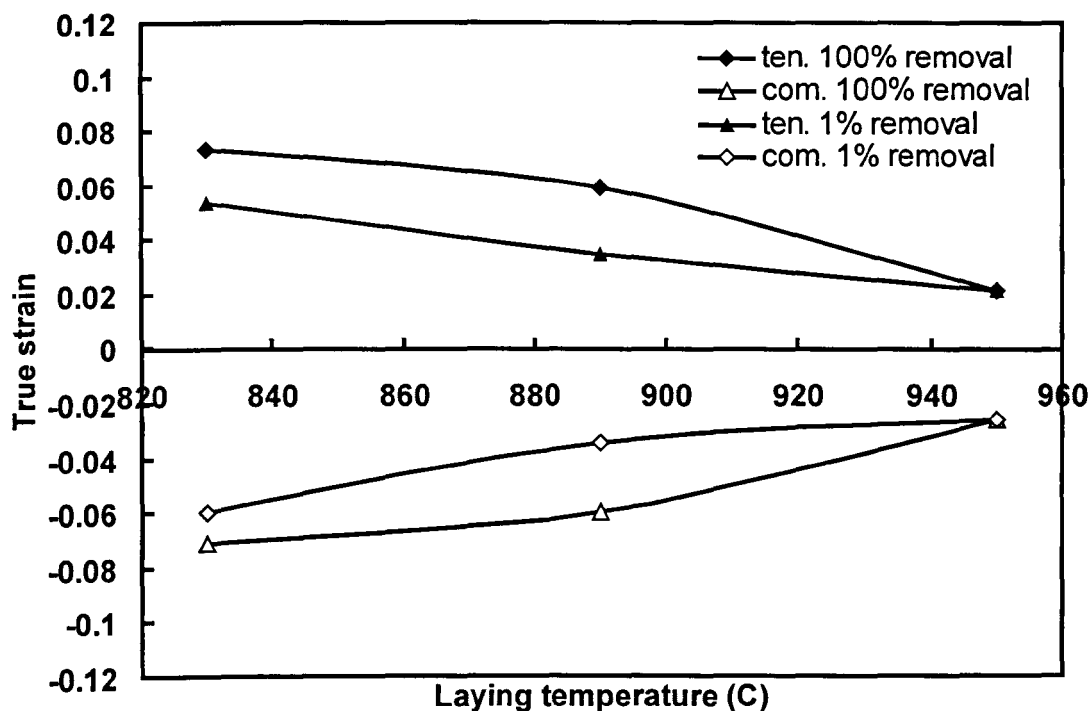


(a) in tension

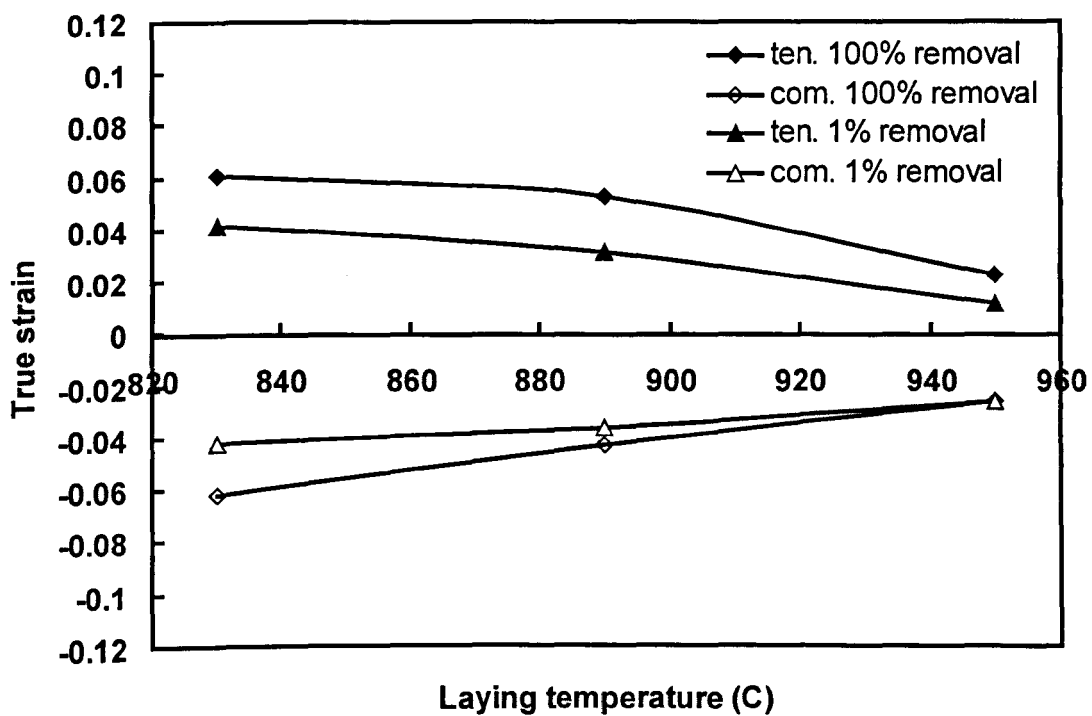


(b) in compression

Fig. 4.31 FE modeling result of steel rod sample in constrained bending test



(a) sample 1



(b) sample 2

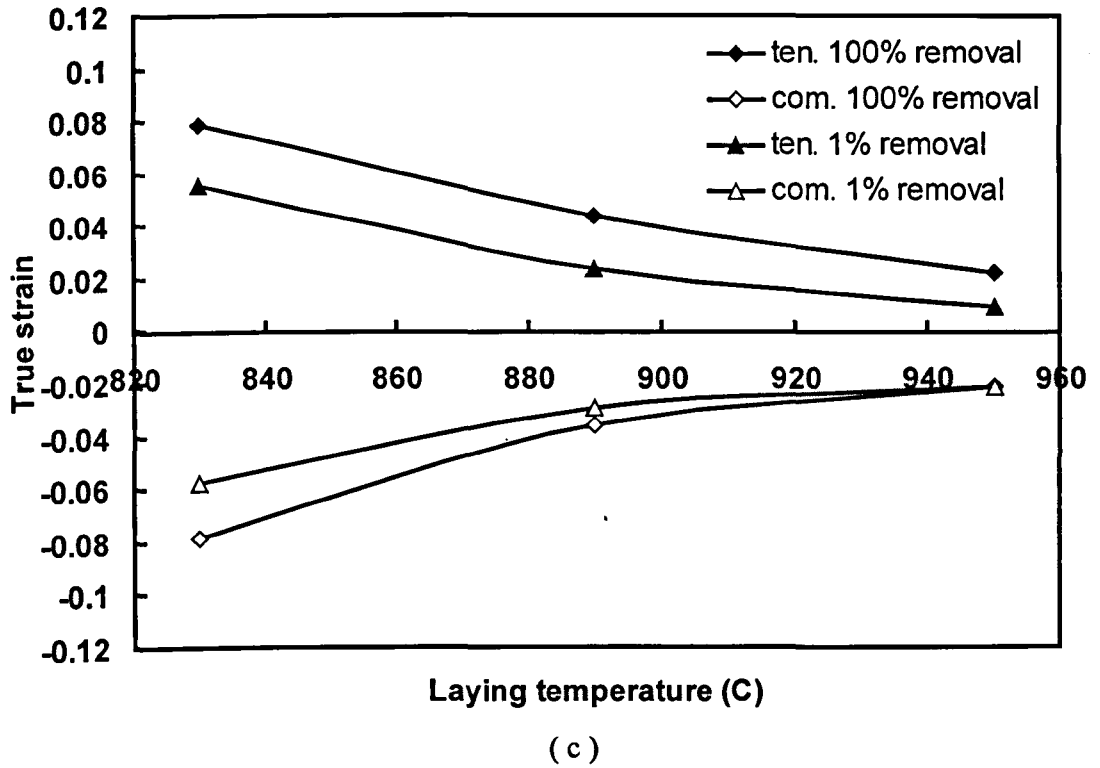


Fig. 4.32 Effect of laying temperature on true strain for scale cracking and removal

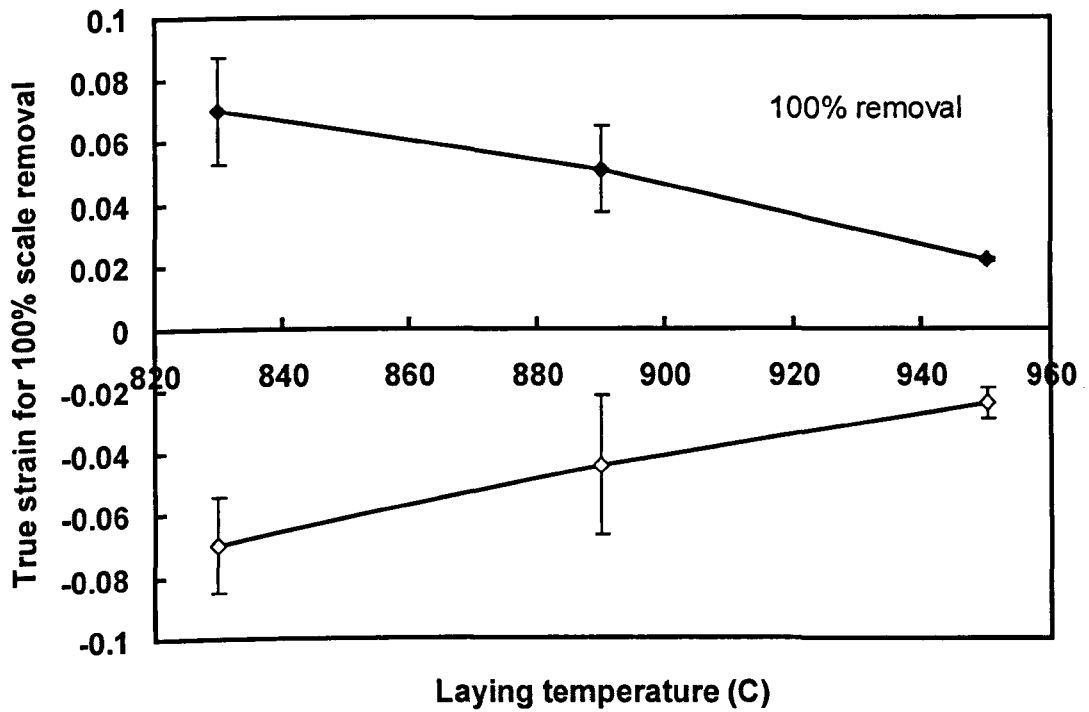


Fig. 4.33 Variation of the strain for 100% scale removal with laying temperature, averaged for three samples (plus 95% confidence limits)

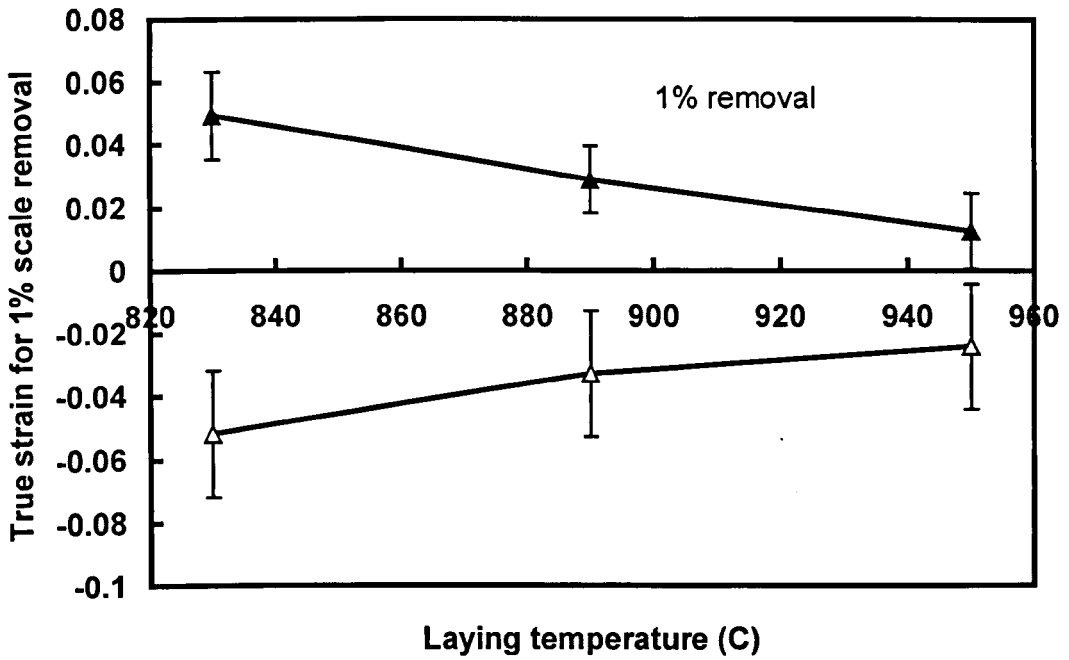


Fig. 4.34 Variation of critical strain for 1% scale removal with laying temperature, averaged for three samples (plus 95% confidence limits).

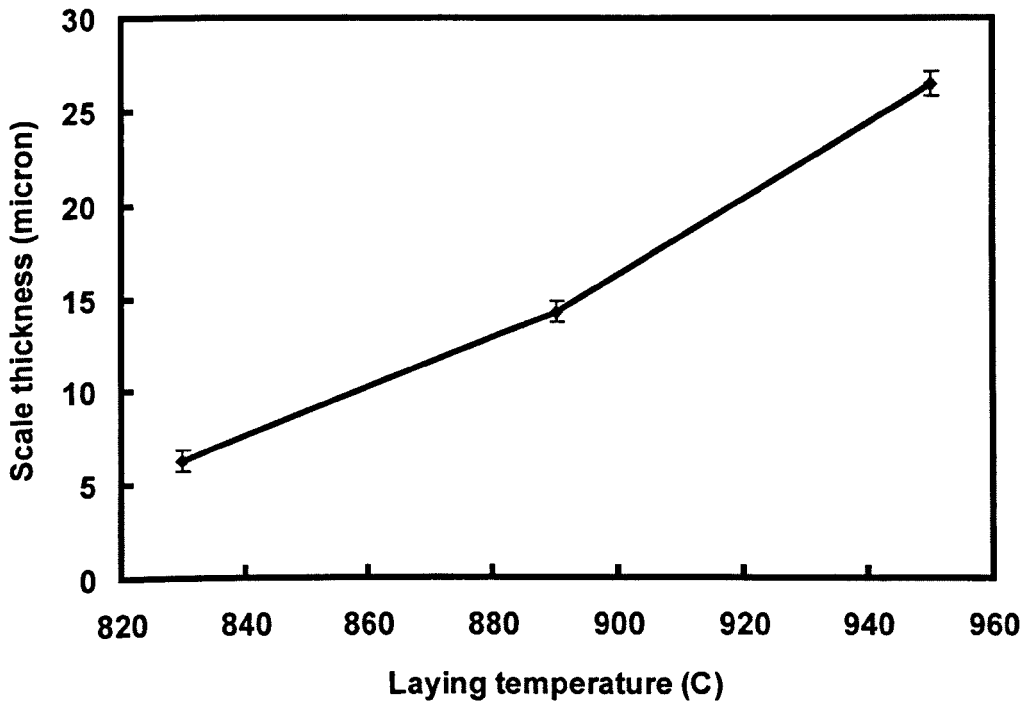
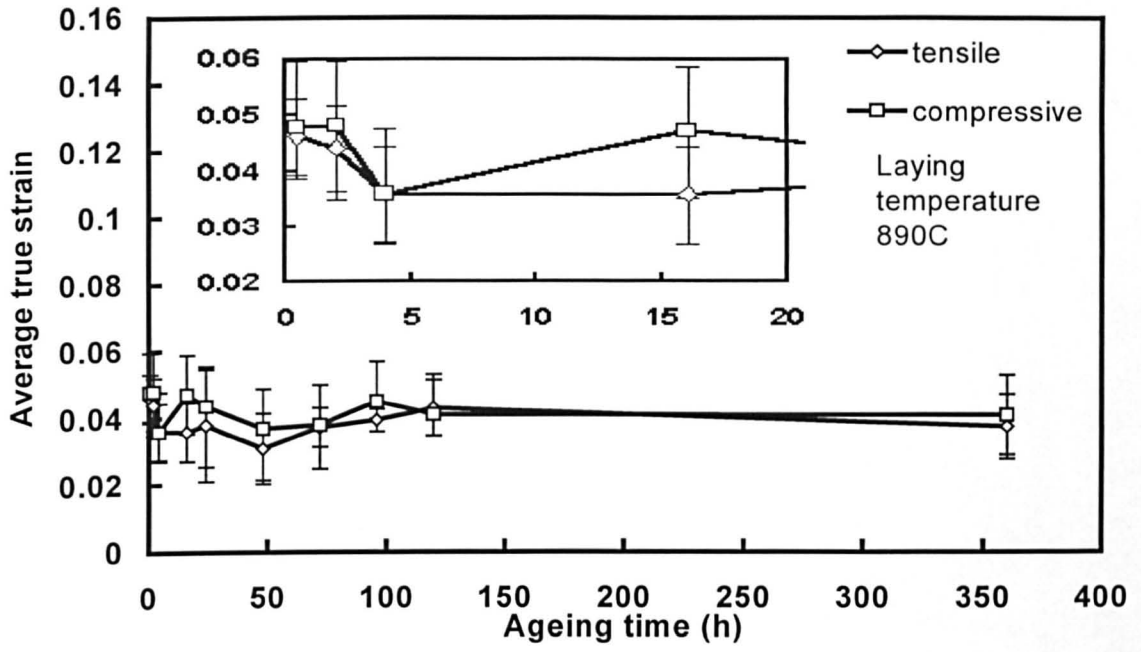
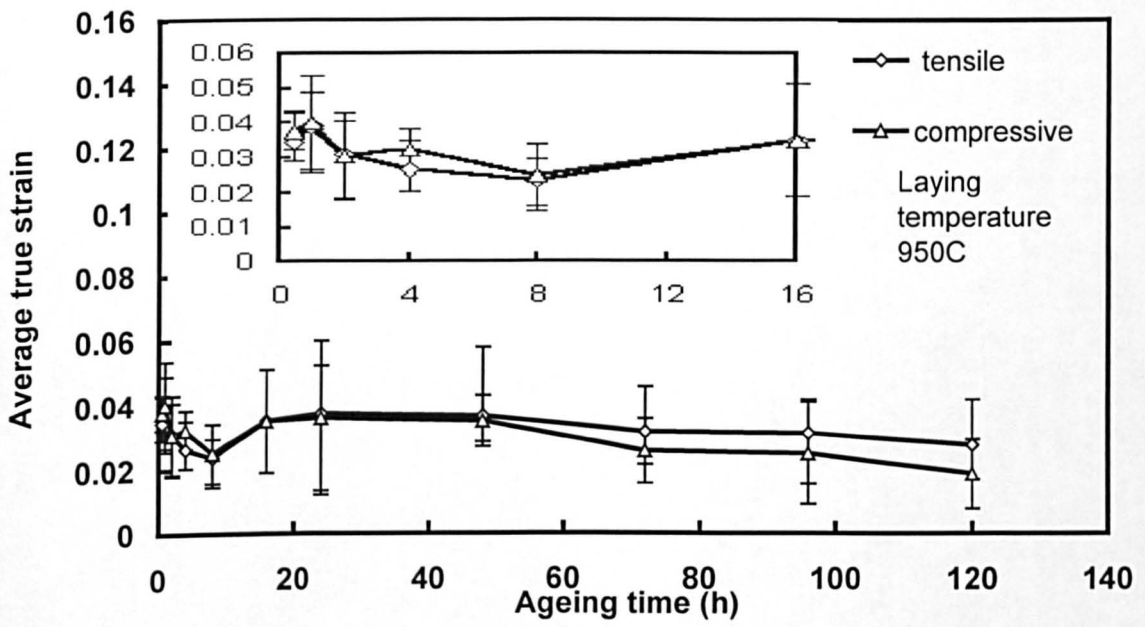


Fig. 4.35 The relationship between laying temperature and scale thickness of K08 ($\phi 5.5\text{mm}$) (4 measurements taken from 5 samples in each case.)

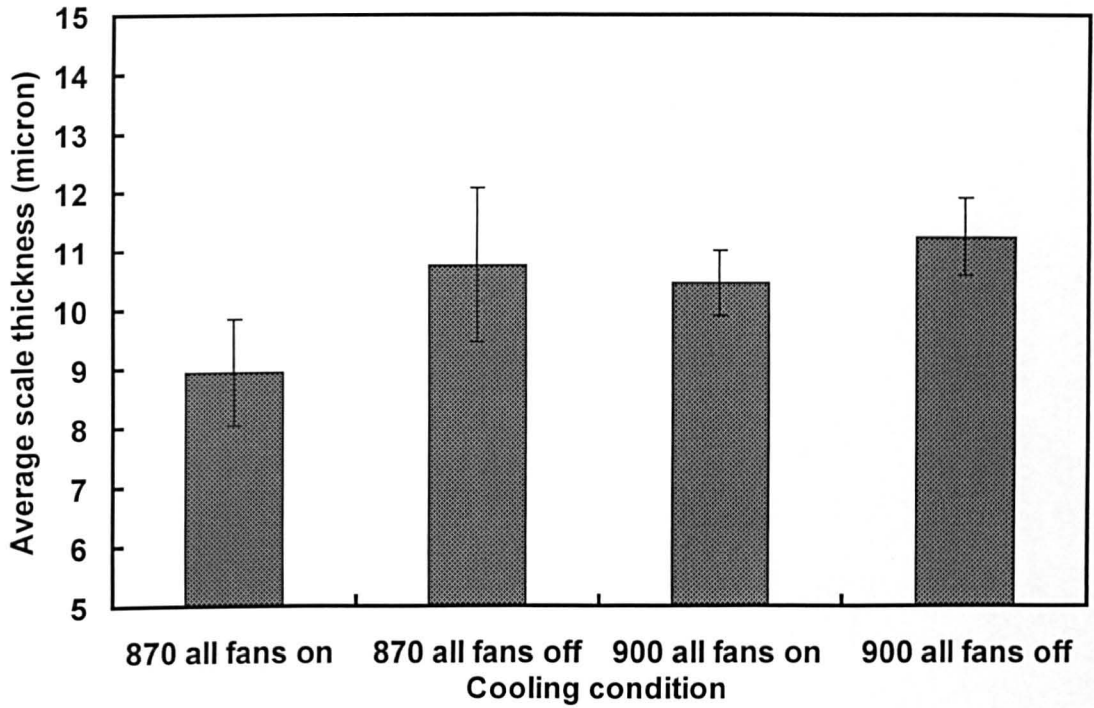


(a) laying temperature 950°C

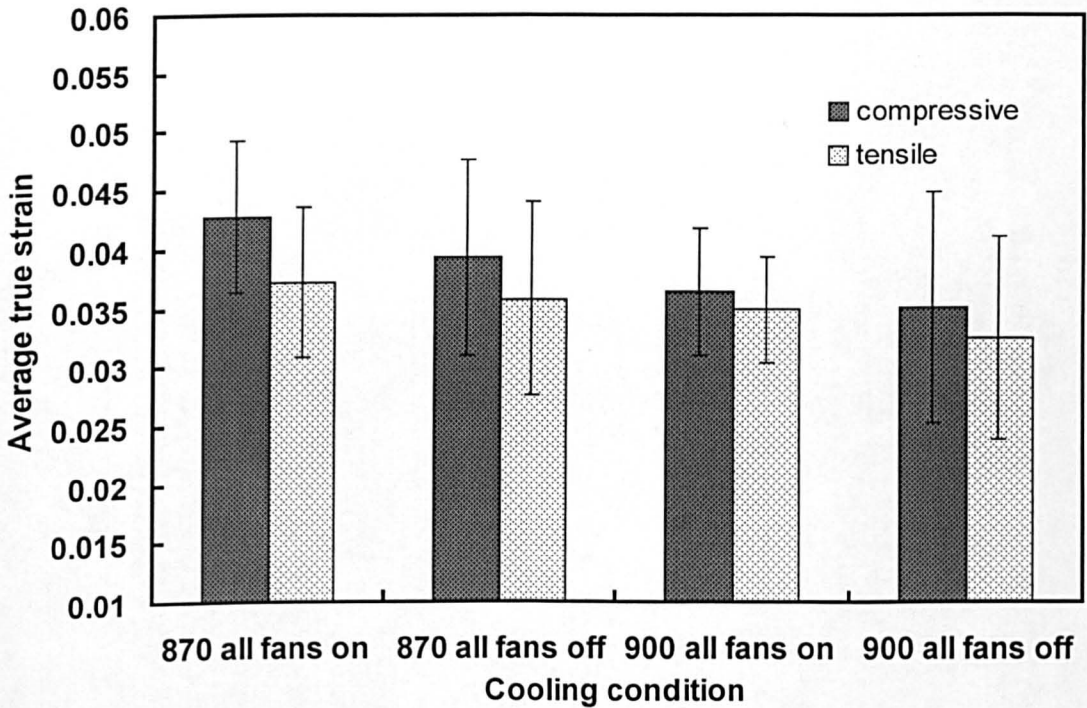


(b) laying temperature 890°C

Fig. 4.36 The effect of ageing time on the average true strain for 100% scale removal (a) laying temperature 950°C and (b) laying temperature 890°C



(a) average scale thickness



(b) average true strain

Fig.4.37 The effect of cooling condition on (a) scale thickness and (b) the average true strain for 100% scale removal.

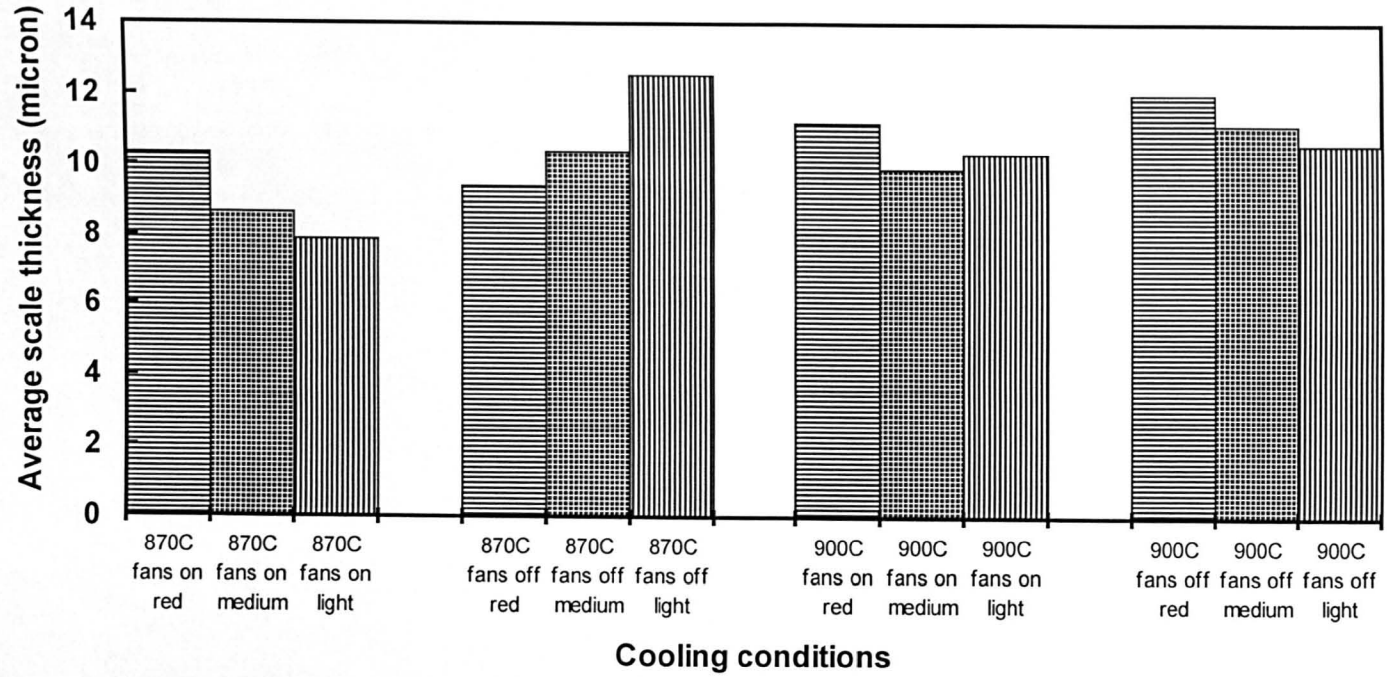


Fig. 4.38 The relationship between the scale colour and the true strain for 100% scale removal (averaged by four samples) in cooling condition test.

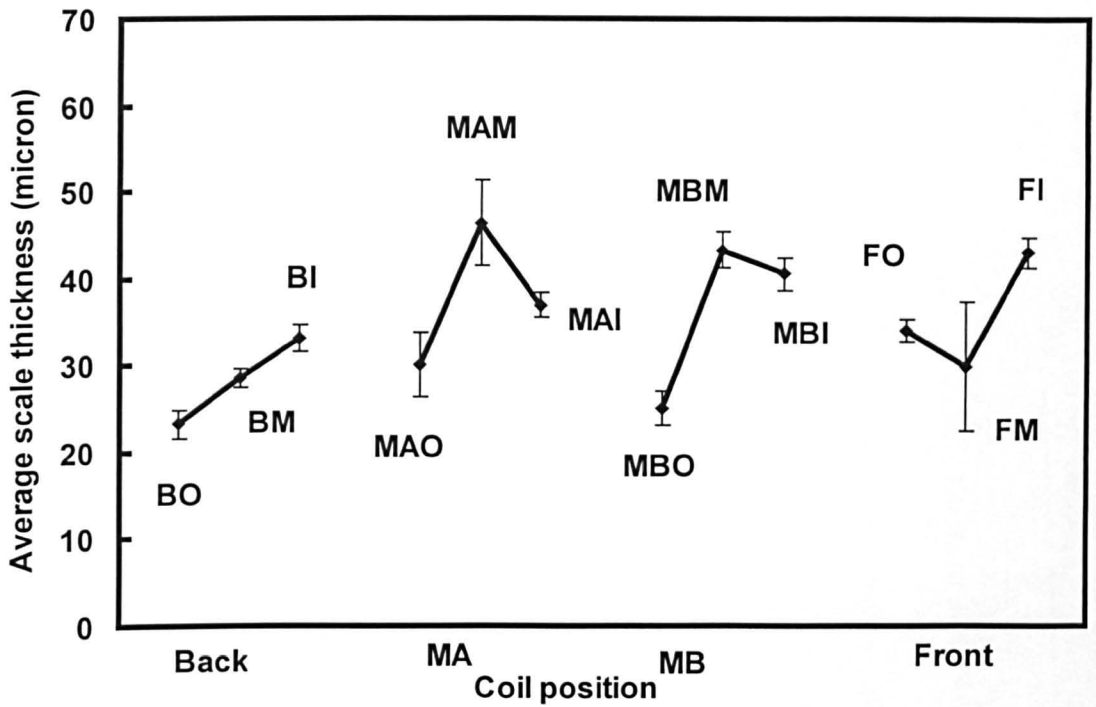


Fig. 4.39 The effect of coil positions on the scale thickness, 4 measurements were taken for each sample and 5 samples were taken from each coil position

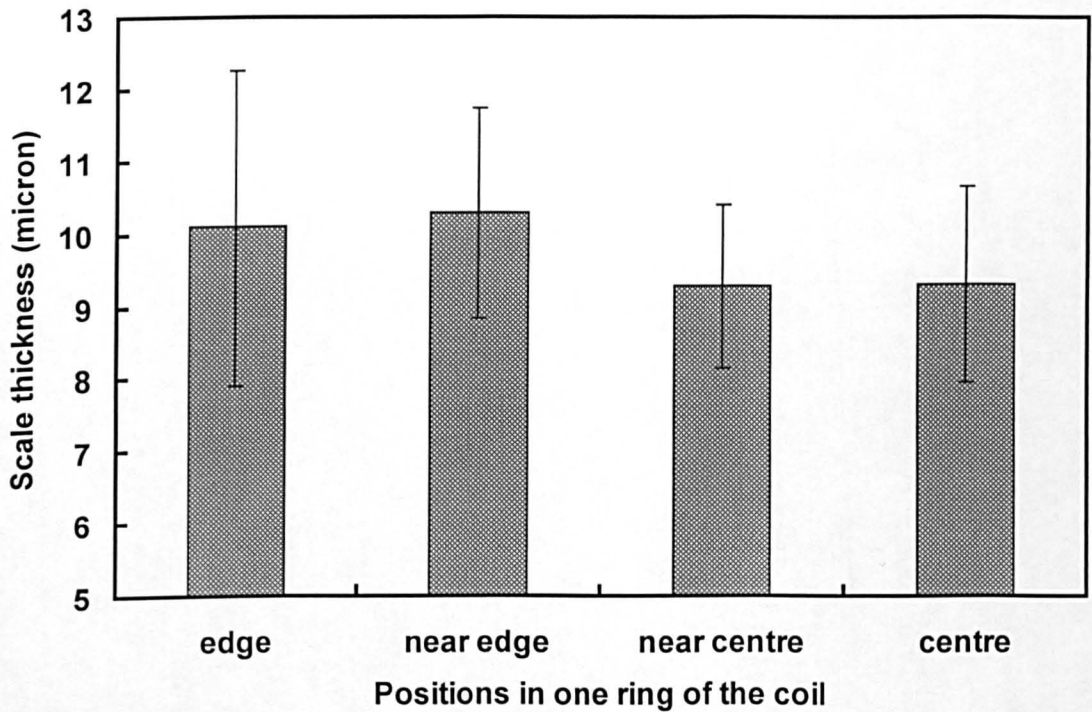
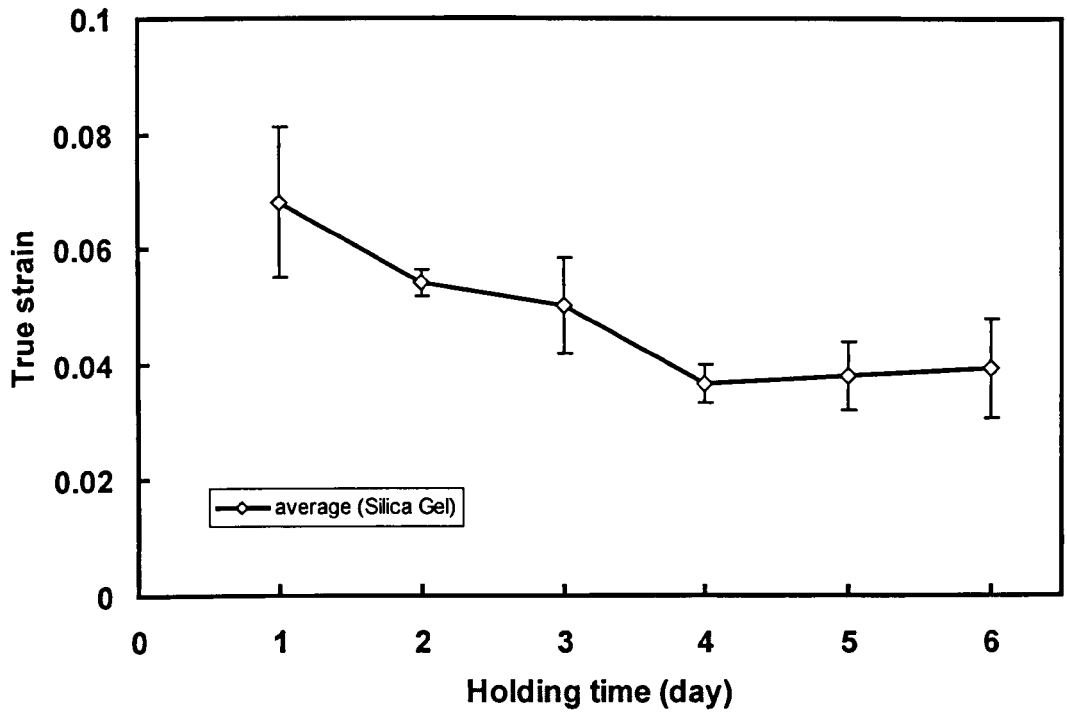
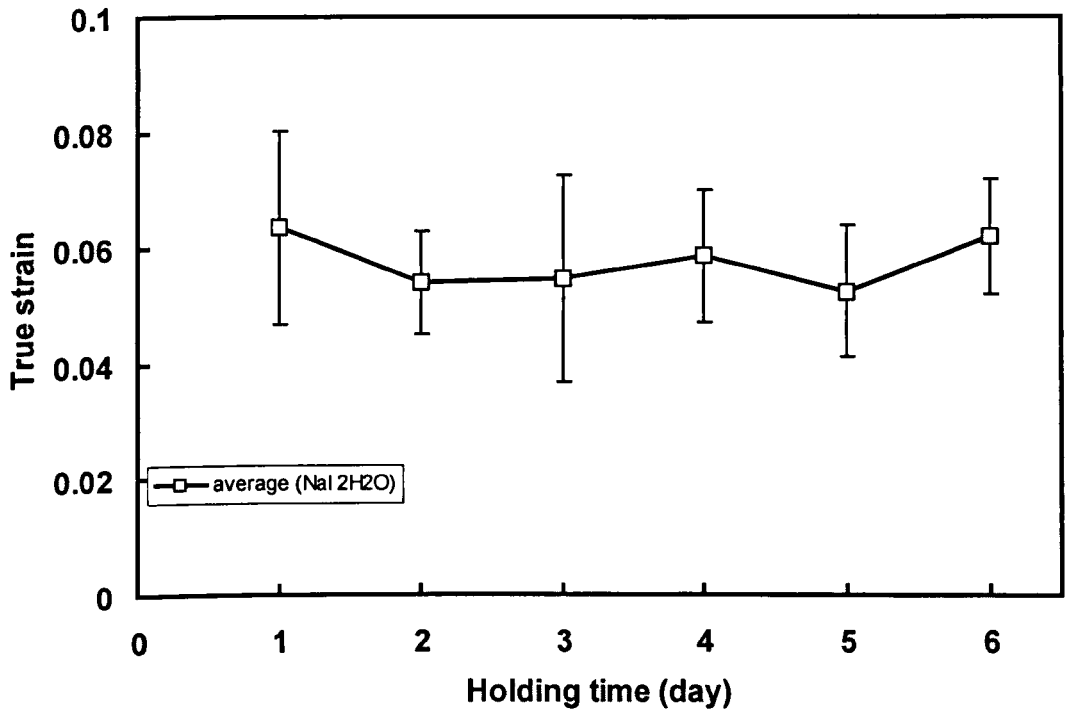


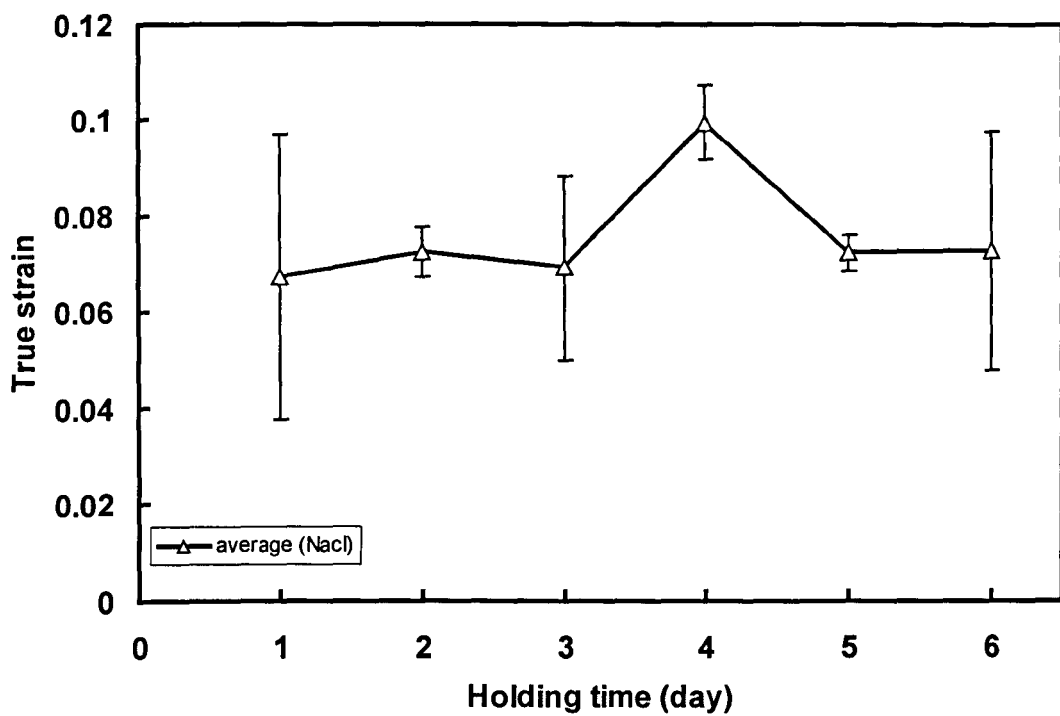
Fig. 4.40 The effect of the positions in one ring of the coil on the scale thickness, four measurements were taken for each sample and 4 samples were taken from each coil position



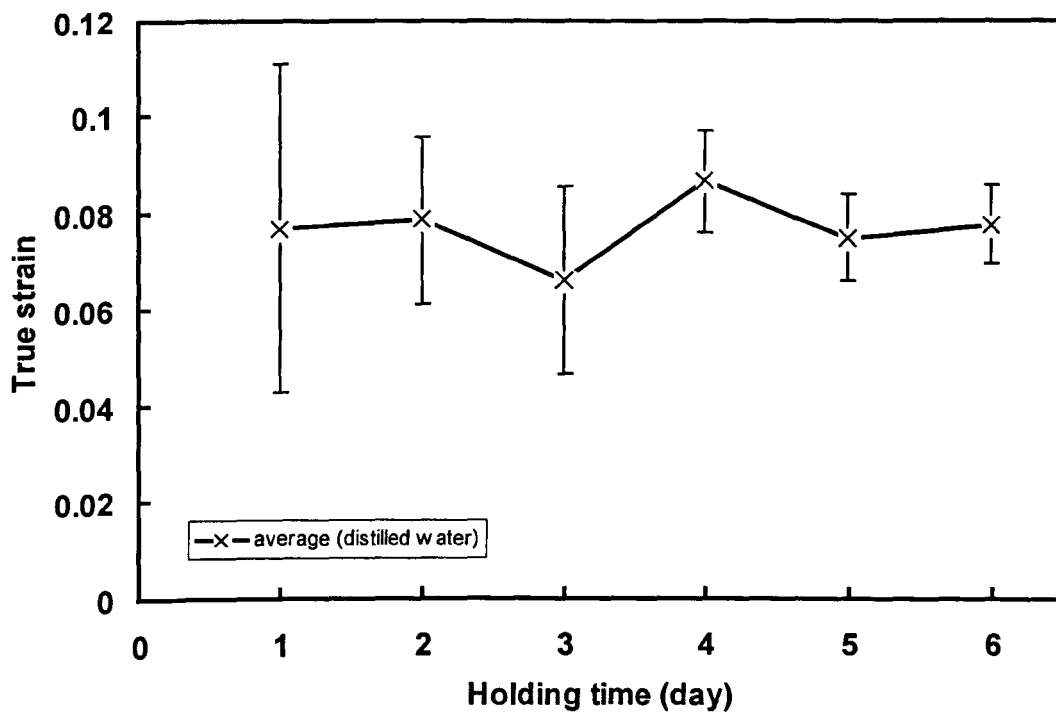
(a)



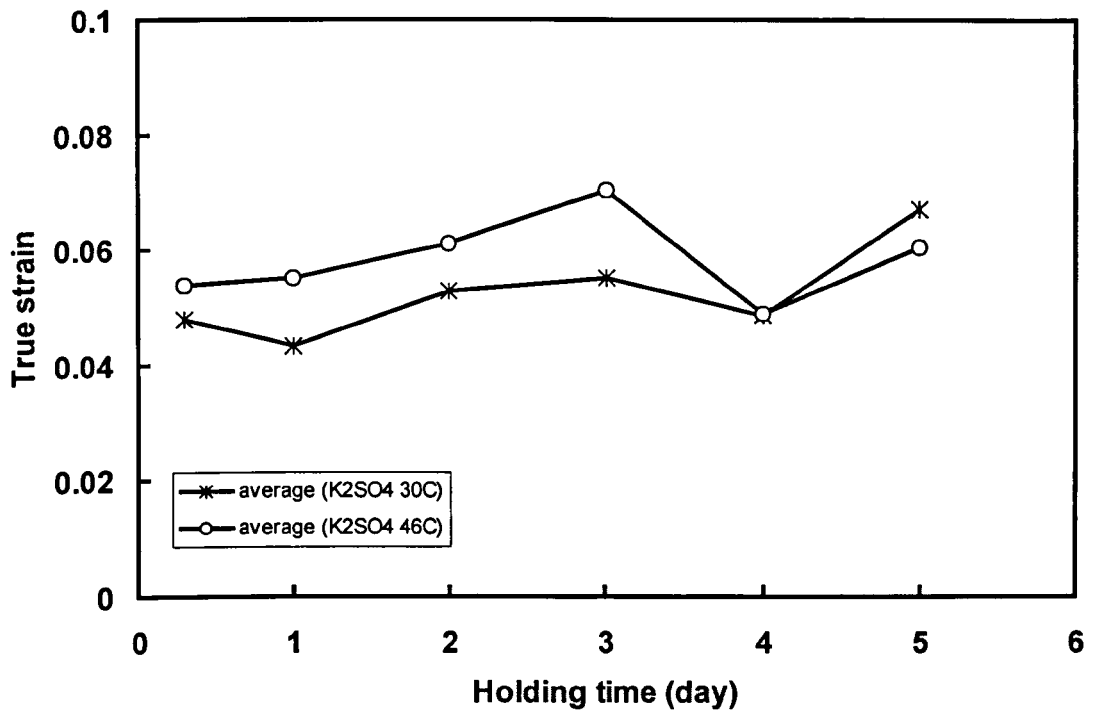
(b)



(c)

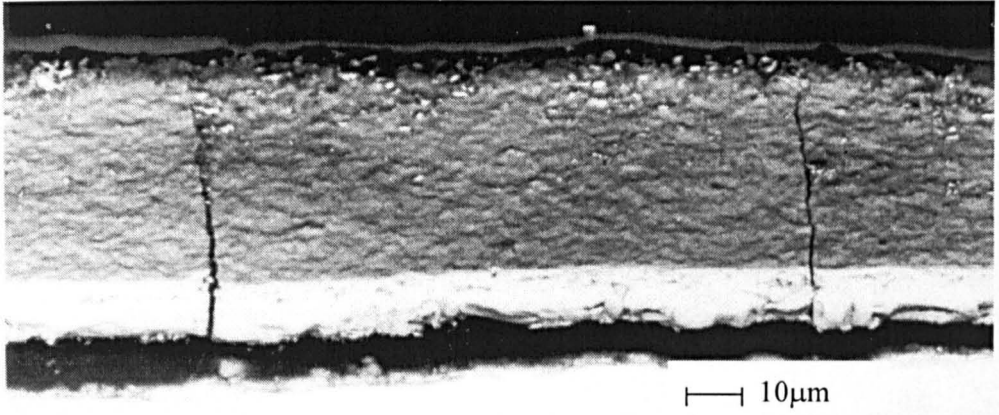


(d)

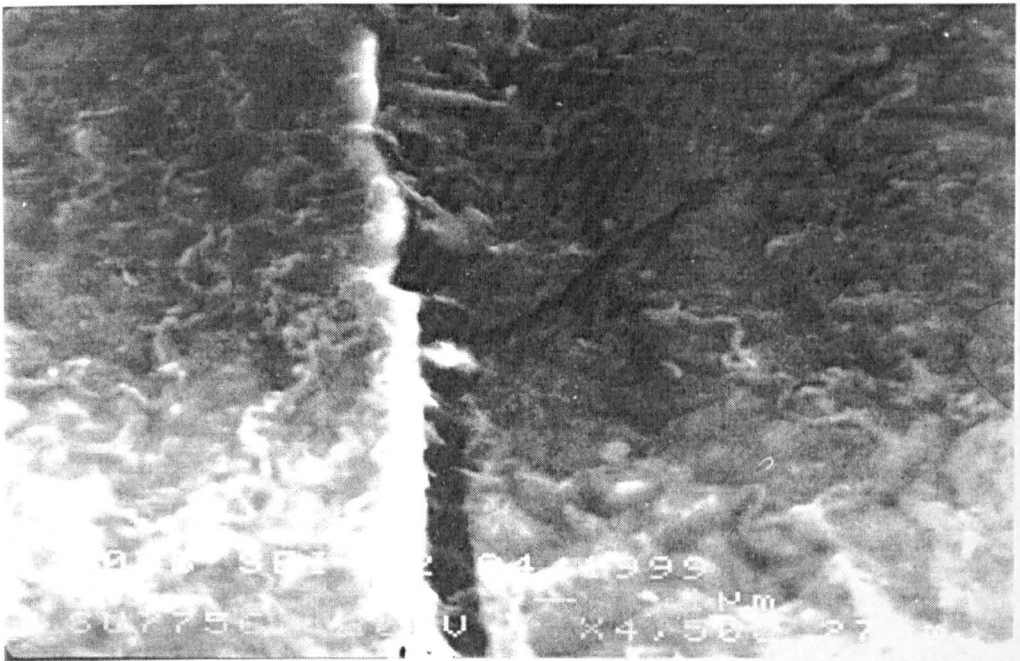


(e)

Fig. 4.41. The effect of relative humidity on the strain for 100% scale removal, (a) Silica Gel, R. H.=5% at room temperature, (b) NaI· 2H₂O, R. H. =40% at room temperature, (c) NaCl, R. H. =70% at room temperature, (d) distilled water , R. H. =100% at room temperature and (e) K₂SO₄, R. H.=97%, oven temperature 30°C and 46°C



(a)

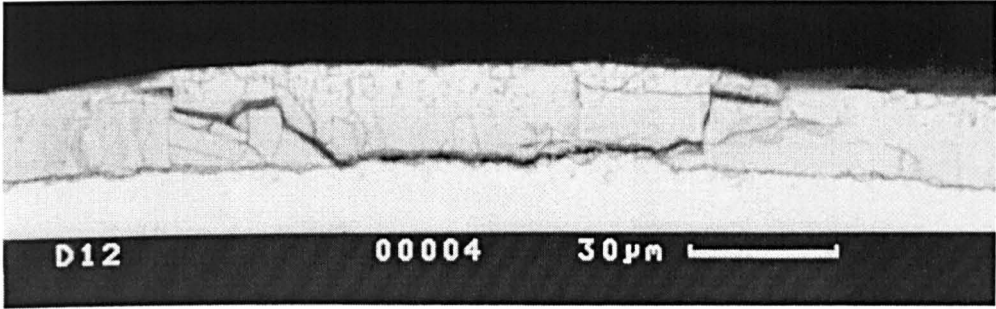


(b)

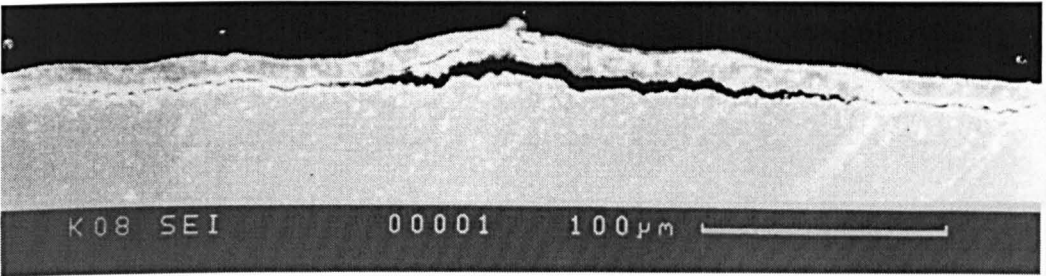


(c)

Fig. 4.42 Scale cracks in tension, (a) Through-thickness cracking, (b) and (c) micro-cracks



(a) Wedging



(b) Buckling

Fig. 4.43 Scale cracking behaviour in compression

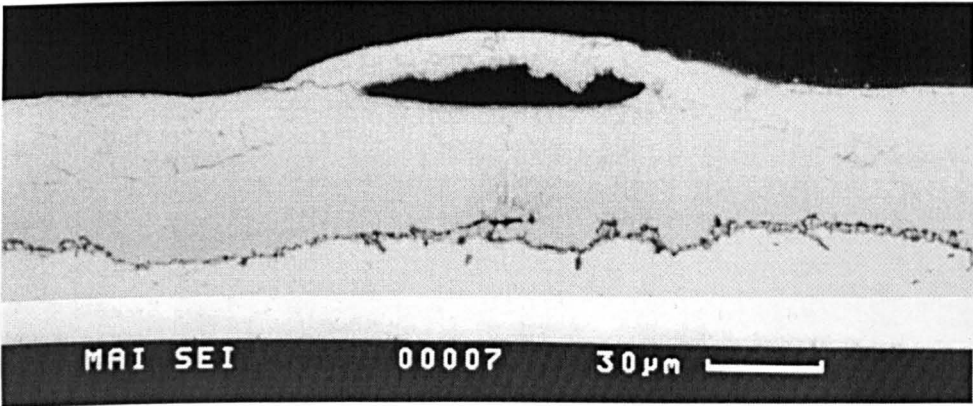
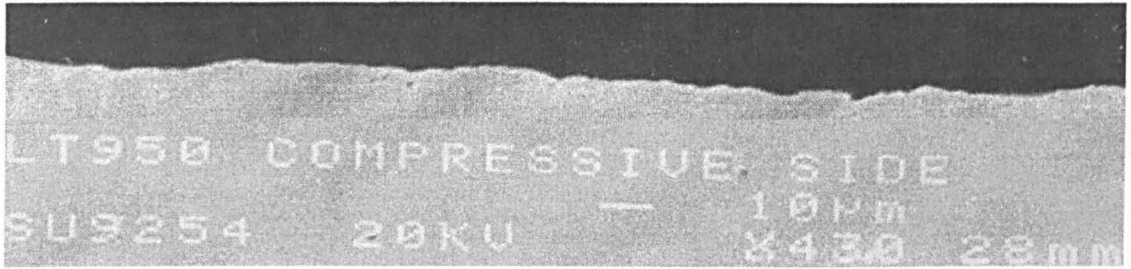
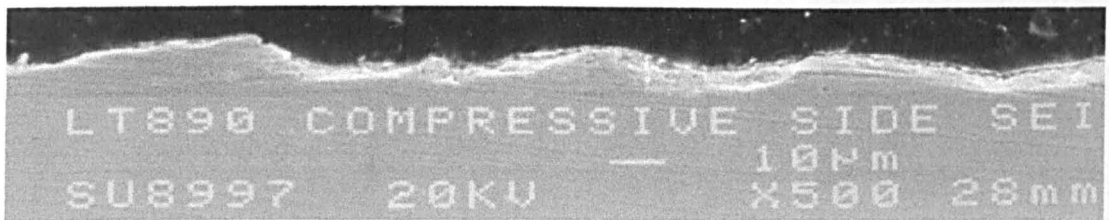


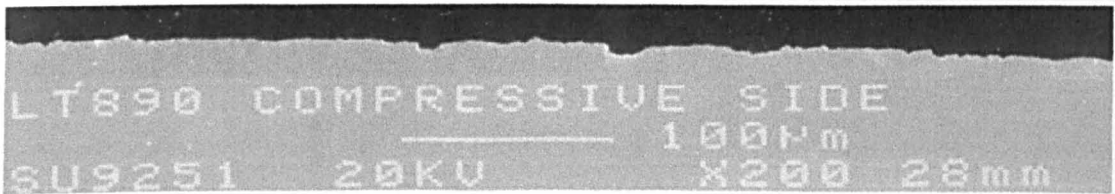
Fig. 4.44 Blister presented in the upper layer of scale in compression



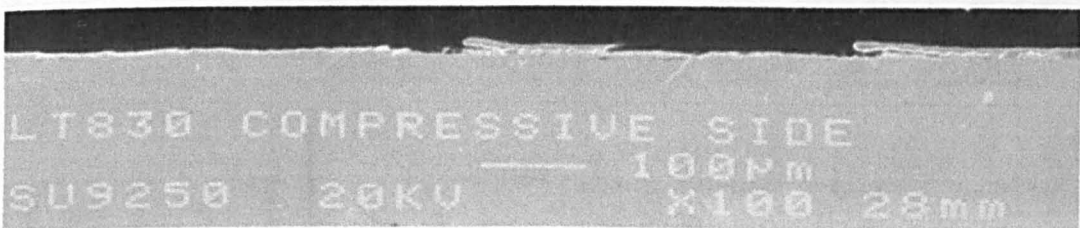
(a) Material: K08, laying temperature 950°C, under high magnification



(b) Materials: K08, laying temperature 890°C, under high magnification

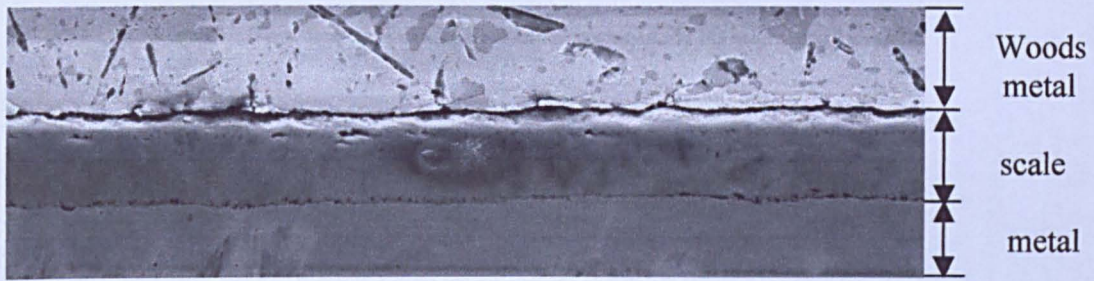


(c) Material: K08, laying temperature 890°C, under low magnification

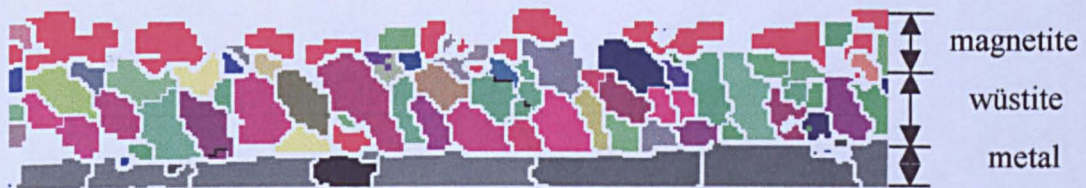


(d) Material: K08, laying temperature 830°C, under low magnification

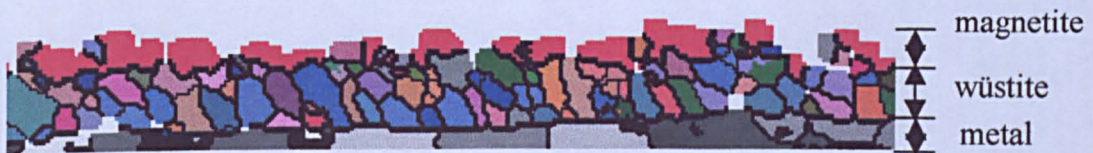
Fig. 4.45 SEM micrographs of descaled rod surface



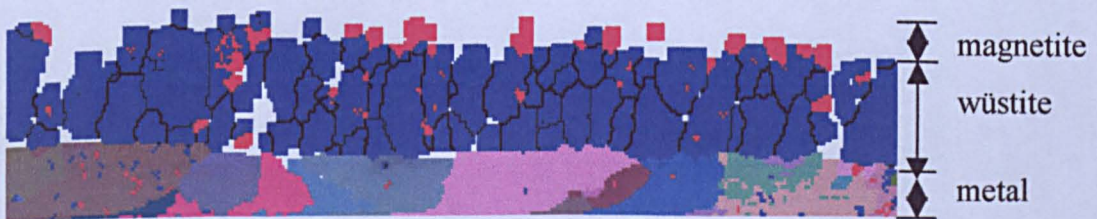
(a) The data collecting area in EBSD



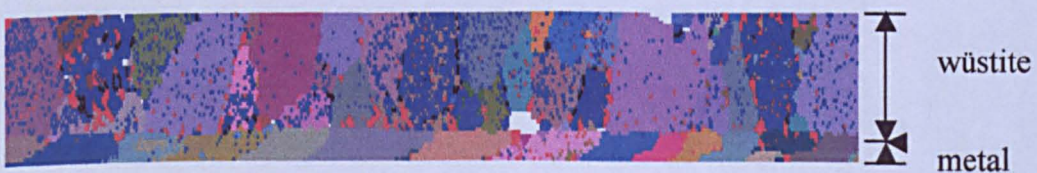
(b) EBSD map of the scale on K08 steel rod surface (LT950°C), sample was supplied by Scunthorpe Rod Mill (scale thickness is 26µm)



(c) EBSD map of the scale on K08 rod surface (LT890°C), sample was supplied by Scunthorpe Rod Mill (scale thickness is 13µm)

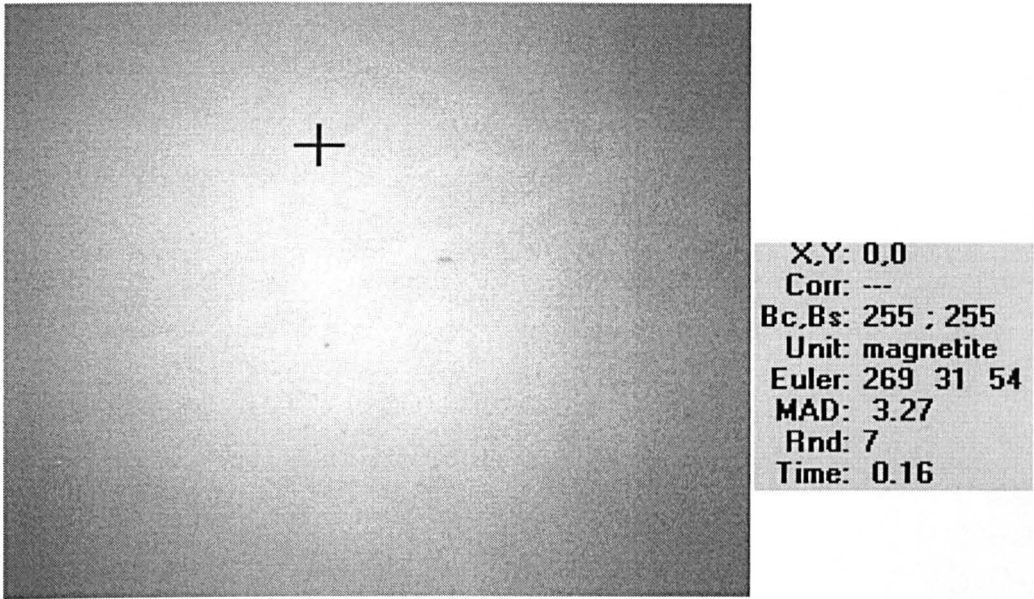


(d) EBSD map of the scale on the rod surface (LT 900°C fans off red), sample was supplied by Cardiff Rod Mill (scale thickness is 15µm)

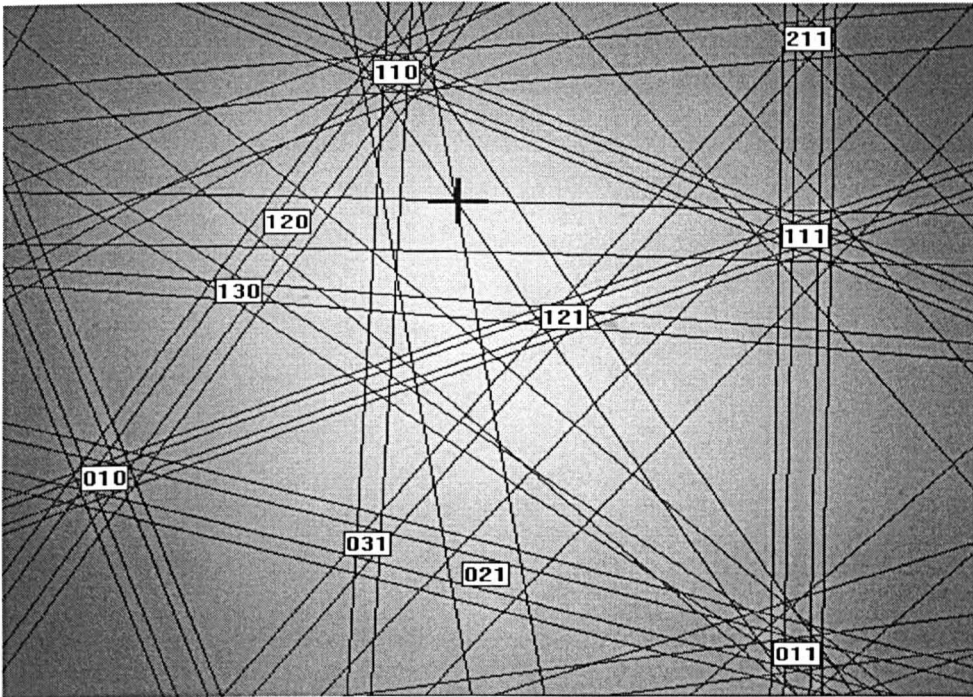


(e) EBSD map of the scale on K08 rod surface (LT 950°C ageing 30mins), sample was supplied by Scunthorpe Rod Mill (scale thickness is 26µm). Here red spots distributed in the scale/metal interface and the wüstite grain boundaries are magnetite.

Fig. 4.46 EBSD map of the scale on the rod surface

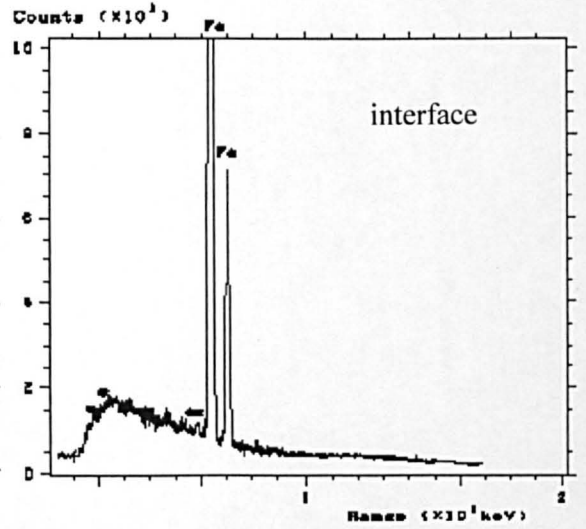
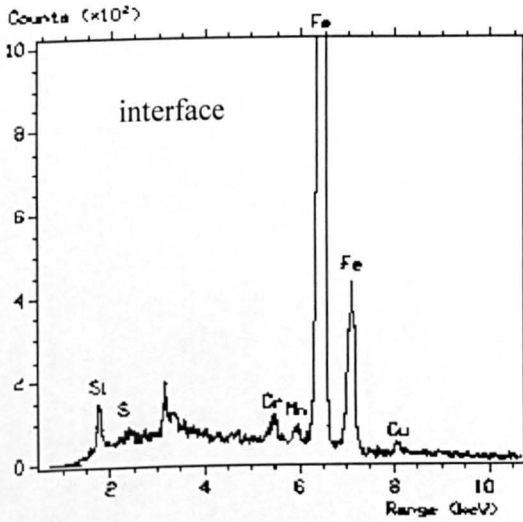
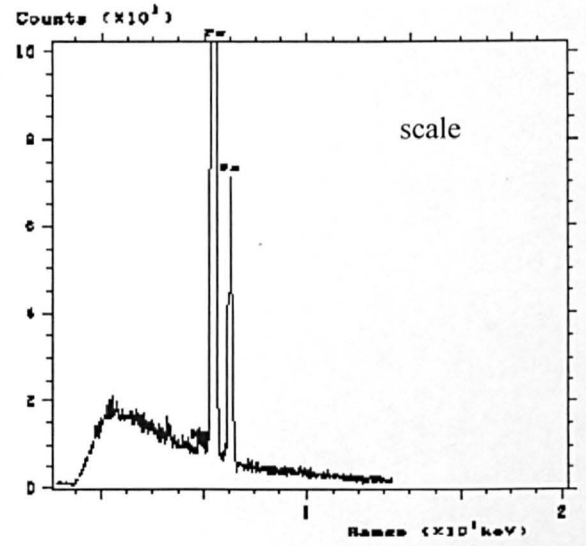
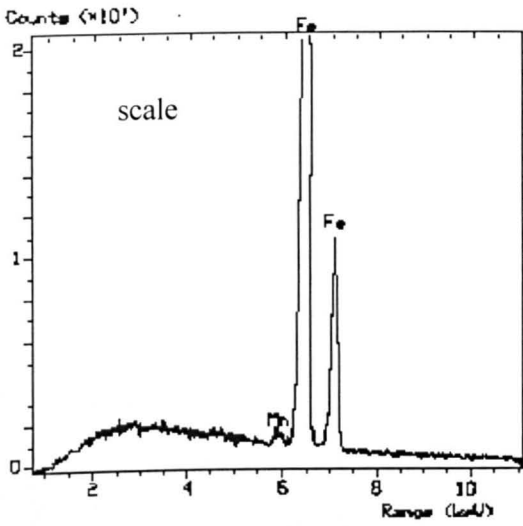
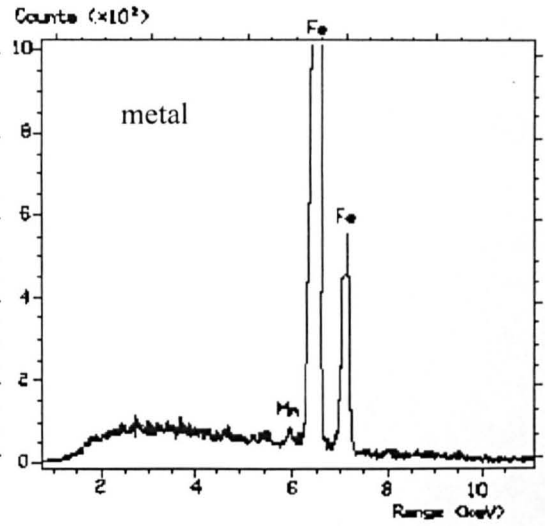
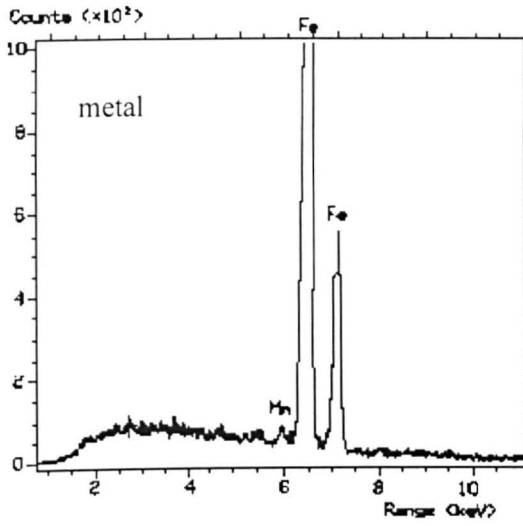


(a) Kichuchi pattern of the residual scale on K08 rod surface(LT900, fans off)



(b) Standard Kichuchi pattern of Magnetite

Fig. 4.47 EBSD identification of the residual scale left on K08 rod surface (LT900, fans off), sample was supplied by Cardiff Rod Mill



(a) 900°C fans off, red

(b) 870°C fans on, light

Fig. 4.48 EDS spot scanning results of the samples used for cooling condition tests

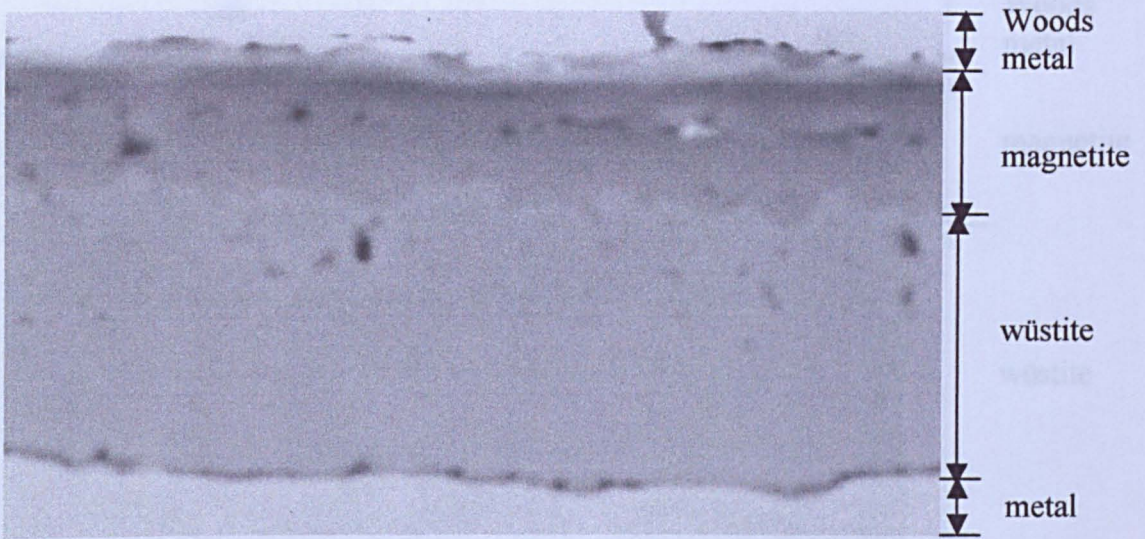


Fig. 4.49 (a) SEM photo of the sample supplied by Scunthorpe Rod Mill (laying temperature 890°C) in longitudinal direction

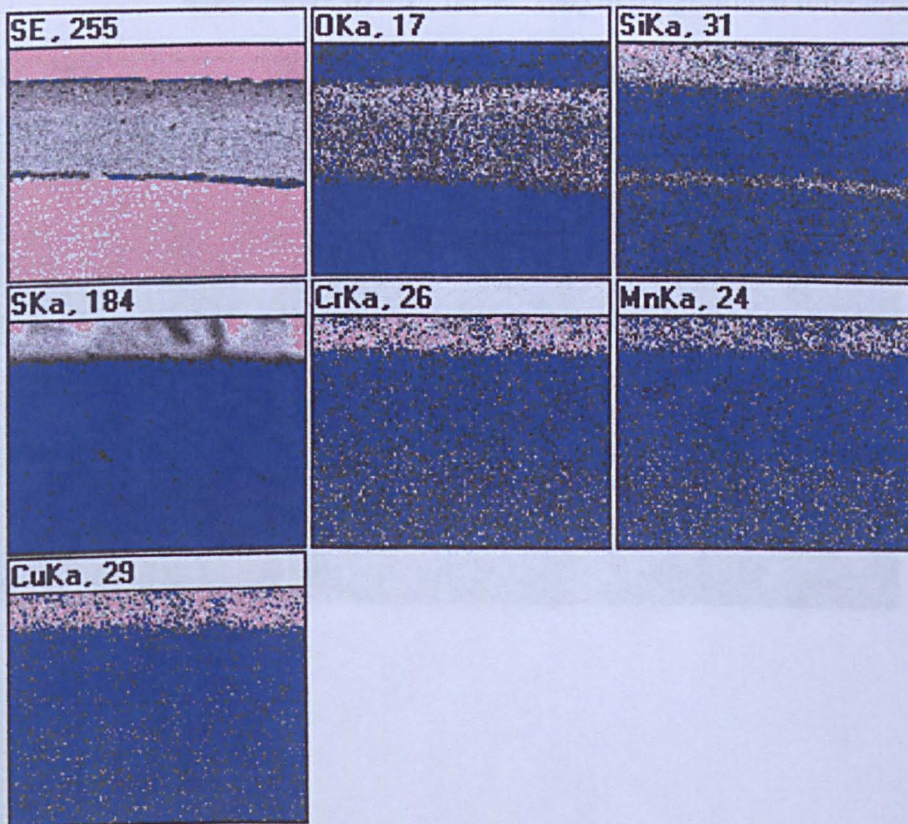


Fig. 4.49 (b) Element mapping of the sample supplied by Scunthorpe Rod Mill (laying temperature 890°C)

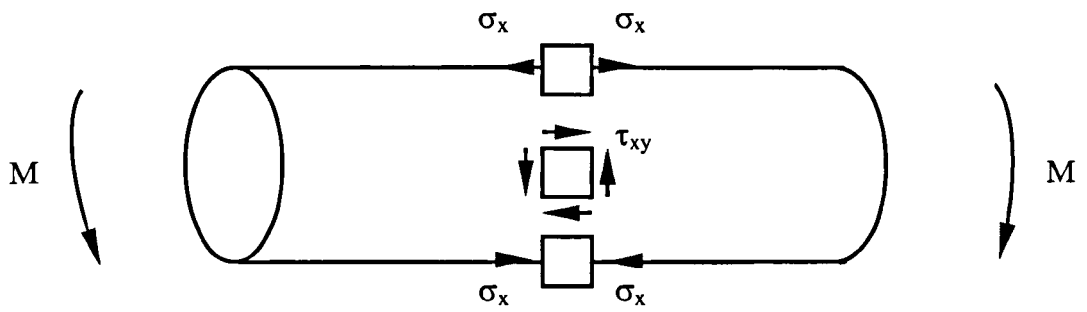


Fig. 5.1 3D stress distribution of the rod after bending showing that only the elements at the top/bottom outer fibres are in tension/compression [Timoshenko, 1969]

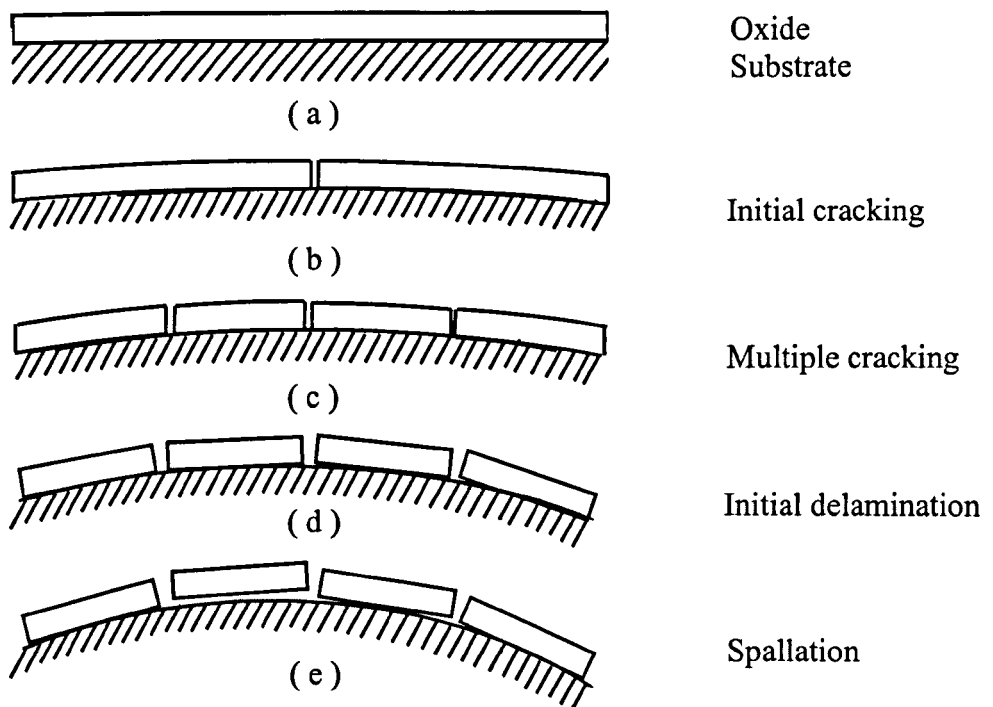


Fig. 5.2 Schematic diagram of scale tensile failure after cantilever bending

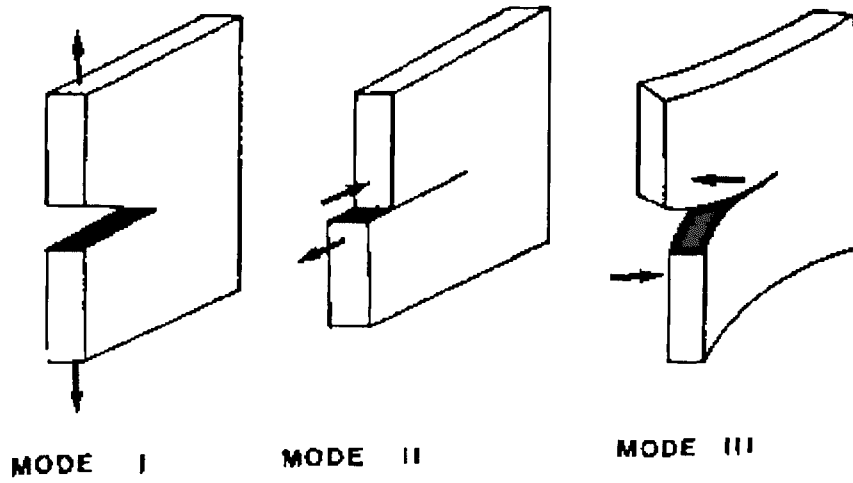


Fig. 5.3 Fracture modes according to fracture mechanics [Dieter G. E., 1988]

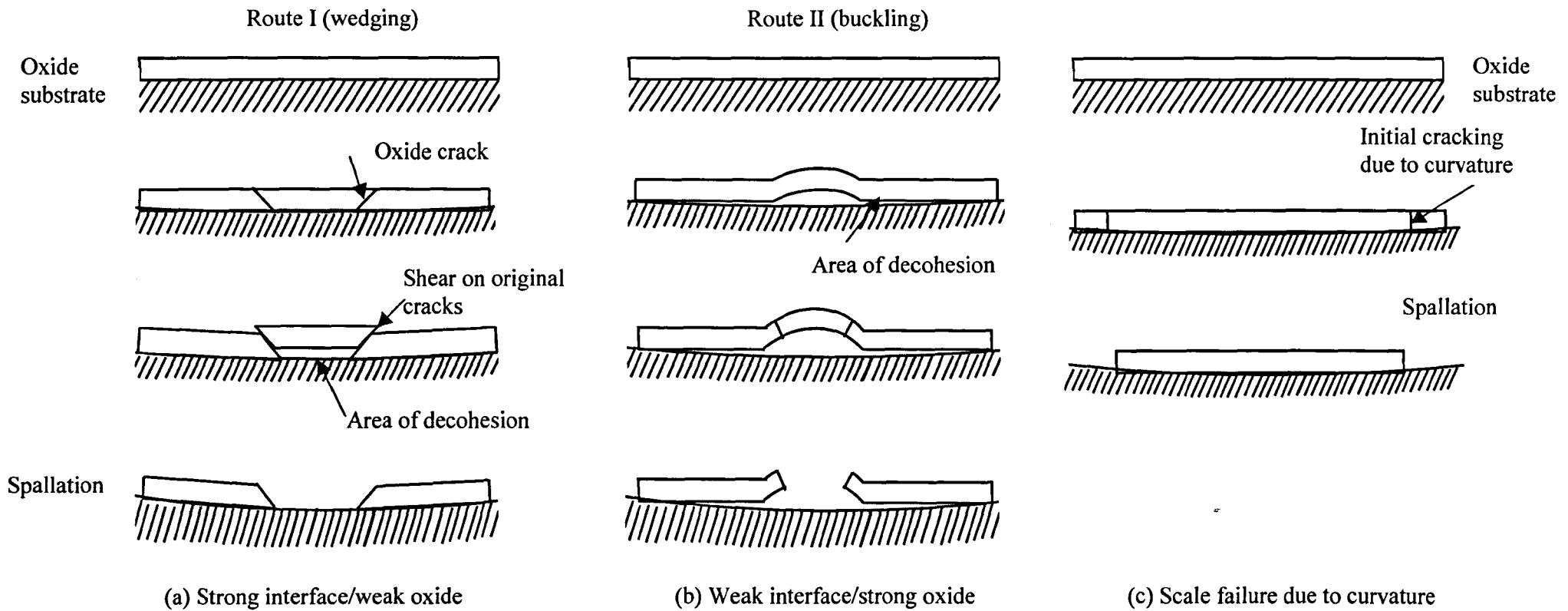


Fig. 5.4 Schematic diagram of scale compressive failure mechanisms after cantilever bending

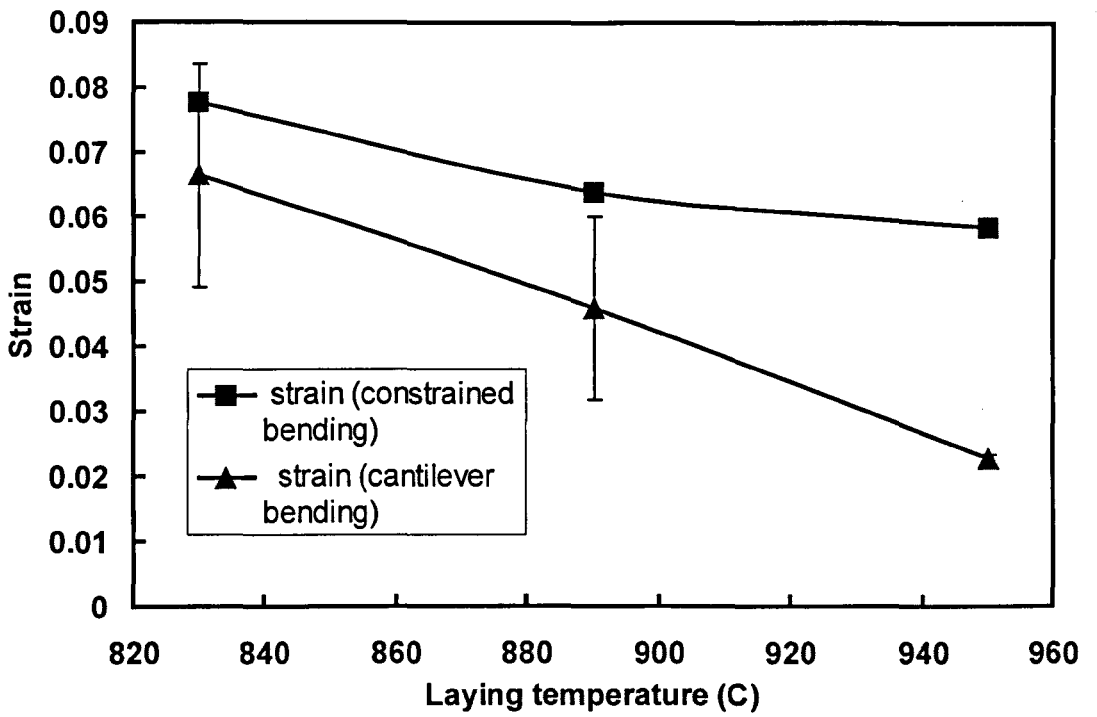


Fig. 5.5 Comparison of the strains calculated after constrained bending and measured by Cyclone scanner after cantilever bending.

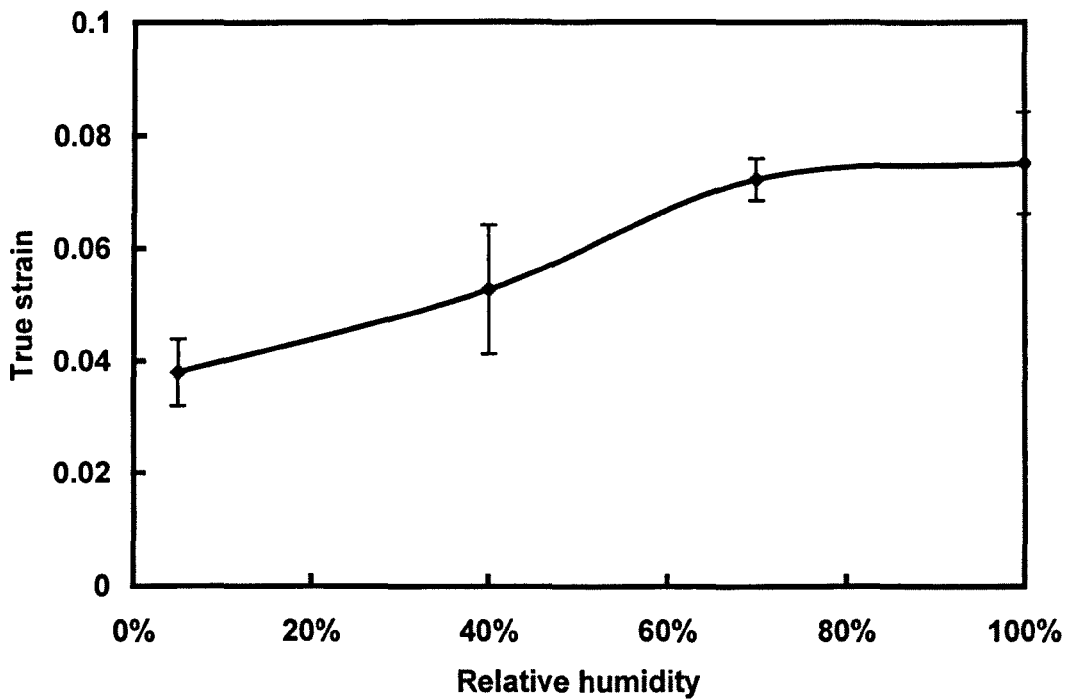


Fig. 5.6 The relationship between true strain and relative humidity after holding 5 days (with 95% confidence)